HAL
open science

# Optical antennas for harvesting solar radiation energy

Waleed Tariq Sethi

## To cite this version:

Waleed Tariq Sethi. Optical antennas for harvesting solar radiation energy. Electronics. Université de Rennes, 2018. English. NNT : 2018REN1S129 . tel-02295386

**HAL Id: tel-02295386**

**https://theses.hal.science/tel-02295386v1**

Submitted on 24 Sep 2019

**HAL** is a multi-disciplinary open access archive for the deposit and dissemination of scientific research documents, whether they are published or not. The documents may come from teaching and research institutions in France or abroad, or from public or private research centers.

L'archive ouverte pluridisciplinaire **HAL**, est destinée au dépôt et à la diffusion de documents scientifiques de niveau recherche, publiés ou non, émanant des établissements d'enseignement et de recherche français ou étrangers, des laboratoires publics ou privés.

**THÈSE / UNIVERSITÉ DE RENNES 1**
*sous le sceau de l'Université Bretagne Loire*

pour le grade de

**DOCTEUR DE L'UNIVERSITÉ DE RENNES 1**

*Mention : Traitement de Signal et Télécommunications*

**Ecole doctorale MathSTIC**

présentée par


# Waleed Tariq Sethi

préparée à l'unité de recherche IETR (UMR 6164)

(Institut d'Electronique et de Télécommunications de Rennes UFR Informatique et Electronique


---

# Optical antennas for harvesting solar radiation energy

**Thèse soutenue à Rennes**

**le 16 Février 2018**

devant le jury composé de :

**Guillaume Ducournau**
IEMN Université Lille 1 / Polytech'Lille, France / *rapporteur*

**Paola Russo**
Università Politecnica delle Marche Ancona, Italy / *rapporteur*

**Olivier Pascal**
Université Paul Sabatier, France / *examinateur*

**Mohamed Himdi**
Université de Rennes 1, Rennes, France / *directeur de thèse*

**Hamsakutty Vettikalladi**
King Saud Université, Saudi Arabia

**Habib Fathallah**
Université de Carthage, Tunisie

# Table of Contents

**Acknowledgments** i

**Chapter 1 General Introduction.....1**

1.1 Introduction to Energy Harvesting.....1

1.2 Photovoltaic solar harvesting vs Radio Frequency energy harvesting.....2

1.3 Plasmonics and Surface Plasmons .....5

1.4 Context and motivation of the study .....7

1.5 Objectives and research contributions .....8

1.6 Thesis Structure.....9

Bibiliography .....11

**Chapter 2 Radio Frequency Energy Harvesting Rectenna** 12

2.1 Introduction to Radio Frequency (RF) Energy Harvesting.....12

2.2 Radio Frequency (RF) Energy Harvesting Principle .....13

2.2.1 Antenna .....14

2.2.2 Impedance matching cricuit .....15

2.2.3 Rectifier .....16

2.3 Literature Review: State-of-the-art Energy Harvesting Rectennas.....18

2.4 Proposed Hexaband antenna .....28

2.4.1 Antenna Design .....28

2.4.2 Antenna Simulation and Experimental Results.....29

2.5 Proposed multiband rectifier.....33

2.5.1 Schottky Diode Selection .....34

2.5.2 Impedacne matching.....35

2.5.3 Complete Rectifier in ADS Simulator.....35

2.6 Experimental Investigation of Rectenna System .....46

2.7 Summary and conclusion .....49

Bibliography.....50

**Chapter 3 Optical Antennas based on Dielectric Resonators (DR)** 52

3.1 Introduction to Optical Antennas/ Nantennas .....52

3.2 Electromagnetic interaction with metals and Maxwell equations .....55

3.2.1 Optical Properties of Metals (Drude Model) ..... 58
3.3 Brief Introduction to Surface Plasmons Polaritons (SPP) and Local Surface Polaritons (LSP) ..... 61
3.3.1 Localized Surface Plasmons (LSP) ..... 62
3.4 Literature Review: Dielectric Resonator (DR) Based Nantennas ..... 63
3.5 Proposed Equilateral Triangular Dielectric Resonator Nantenna [ETDRN] ..... 65
3.5.1 Introduction to Dielectric Resonator antenna (DRA) ..... 65
3.5.2 ETDRN Design Geometry ..... 66
3.5.3 Antenna Simulation and Experimental Results ..... 67
3.5.4 Results and Discussion ..... 73
3.6 Proposed Hexagonal Dielectric Resonator Nantenna [HDRN] ..... 75
3.6.1 HDRN Design Geometry ..... 75
3.6.2 Design Simulation and Optimisation ..... 77
3.6.3 Results and Discussion ..... 80
3.7 Array synthesis ..... 84
3.7.1 Antenna Array Design Geometry ..... 84
3.7.2 Results and Discussion ..... 85
3.7.3 Tuneability of proposed 1x2 ETDRNA Array ..... 87
3.8 Summary and conclusion ..... 90
3.9 Bibliography ..... 91

**Chapter 4 Proposed optical antennas for harvesting infrared energy 94**
4.1 Introduction to Optical Photodetectors (PD) ..... 94
4.2 Optical Photodetector for THz detection ..... 96
4.3 Optical Antenna Design I: Yagi-uda Antenna with Fermionics Photodiode ..... 99
4.3.1 Molybdenum based Yagi-uda Antenna Design ..... 99
4.3.2 Simulation and measurements of proposed yagi-uda nantenna ..... 102
4.3.3 Aluminium based Yagi-uda Antenna Designs ..... 105
(a) Antenna Design with Aluminium Material ..... 105
(b) Array Design with Aluminium Material ..... 109
(c) Experimental realization of Yagi-uda Nantenna Array Aluminium Material ..... 115
4.4 Optical Antenna Design II: Polydimethylsiloxane [PDMS] Lens Antennas ..... 121

4.4.1 PDMS based Lens Antenna Design .....121
(a) PDMS Polymer .....121
(b) Lens Antenna Design Simulations.....122
4.5 Optical Antenna Design III: Thermopiles Antennas.....125
4.5.1 Thermopile antenna detector and geometric design.....125
(a) Principle of thermocouples .....125
(b) Proposed geometric designs and experimental realization:.....127
4.6 Summary and conclusion .....136
Bibliography.....137

**Chapter 5 Conclusion, challengesa nd future work 139**
5.1 Summary of Contributions.....139
5.2 Challenges faced during research .....141
5.3 Future Work .....143

**List of Publications 144**
**List of Figures 145**
**List of Tables 150**
**Abstract 151**
**Résumé 152**

# Chapter 1
# General Introduction

This chapter provides a brief introduction to energy harvesting, its various types and its current importance among the research community. Also a comparison between available photovoltaic harvesting to newly proposed radio frequency harvesting is mentioned. In section 1.3, basics to surface plasmons is given which leads to the motivation of the research work as presented in section 1.4. The objectives and contributions of this work with the layout of the thesis documentation is given in the remaining sections.

## 1.1 Introduction to Energy Harvesting

Over the last few years, worldwide demand for energy has increased by 50 % [1]. Although dependency of the worlds' power is still on the combustion of fossil fuels yet, they are finite and cause environmental hazardous to our planet. An alternate clean renewable sources of energy are required that can fulfill the demands and save our planet in the process. Such solutions are possible either from using nuclear based fission reactions or capturing energy from artificial ambient sources such solar or wind. The former, although offers long lifetime, but it comes with its own dangers, however the artificial ambient sources can be utilized as they are technology based. Various external energy include mechanical vibration, thermal, wind, and Radio Frequency (RF) sources.

The process of collecting the energy from the ambient surroundings and converting it into useable electrical energy is termed as Energy Harvesting (EH). Such sources of energy can be scavenged from man-made devices or from natural available sources [2]. Man-made sources are abundant and they do not harm the environment. With the increase in technological devices mostly for wireless communication, the lifetime of devices needs to increase as well. Batteries that are mostly used as a source of energy for these devices need to be made operationally prolong. One solution is to use the available energy surrounding these devices in the form of radio frequency electromagnetic radiation and convert those abundant energies into a secondary source for these batteries. Hence, momentum in charging of batteries or even battery less systems have recently gained popularity [3–4]. The recharge period for batteries last almost ten years and we need a novel solution to enhance their lifetime. With the increase in wireless devices, which are battery dependent, we need a solution that can cope with the lifetime of these batteries. Energy harvesting offers a solution that can provide uninterrupted power to many applications near and far needed in this modern day and age of wireless communication. The applications for charging or storing energy can vary from monitoring weather stations to traffic control or charging medical implantation devices and cell phones. [5].

## 1.2 Photovoltaic solar harvesting vs Radio Frequency energy harvesting

The most direct and abundant source of energy comes from the Sun. From figure 1.1 it can be seen that the energy which is received on Earth can be divided into; 51 % of which is available at the Earth's surface that can be utilized for various tasks. The heat or energy form the Sun is used to lower the atmosphere temperature or heat its surface, melt the glaciers and then evaporate the water causing rain to appear and provide plants with necessary photosynthesis. Of the remaining 49% energy, reflected back energy is 4%, scattered via particles and clouds is 26% and the gases in the air absorb 19 % of the energy [6]. The solar energy that lies in the visible spectrum, as shown in figure 1.2, is being converted into useable electrical energy by a well-known technology. This technology is based on Photovoltaic (PV) effect which has matured over the years (since mid-70s). From the first silicon based cells to the second and third generation of photovoltaic cells which are based on thin film and multi-junction cells, a tradeoff has been standardized in the market as listed in Table 1.1, providing efficiency compared to its market cost.

| PV Technology | Efficiency | Market Captured |
|---|---|---|
| **1st generation** | 20 | 90 |
| **2nd generation** | 5-12 | 10 |
| **3rd generation** | 40-50 | 10 |

**Table 1.1 Efficiency of PV technology over the years [8]**

Photovoltaic (PV) technology encompasses a basic element that is called a photovoltaic cell. The placement of these cells determine what is needed at the output. If photogenerated current is needed then the cells are aligned in parallel configuration. For maximum voltage to be seen at the output, series configuration is preferred. Photovoltaic cells worked on the principle of photo-electric effect, first discovered in 1839 by Alexander-Edmond Becquerel. The basic principle is the same as photo-electric effect which is based on interaction of photons having energy *hv* with electrons. As shown in figure 1.3, a typical PV cell is made from a semiconductor material. The photoelectric effect occurs in the center of the cell at the junction of two semiconductors. When the light is incident on the PV cell, photons interact with electrons in the valence band of the semiconductor. The photon and its energy is absorbed by the electrons, thus jumping to the conduction band while leaving a vacancy in the valence band in the form of a hole. This whole process is known as photo generation or an electron-hole pair generation which only happens if the energy of the photons are greater or equal to the band gap energy (energy gap between valence and conduction band). The newly created electron-hole pairs by photogeneration process are then driven by the electric field to the depletion region of the PN junction. Here the photovoltage and its subsequent photocurrent is generated when an electric load is connected to the PV cell.

As mentioned earlier, the energy received from the sun on the photovoltaics is utilized in visible region during the day time. At night the energy that is absorbed is not utilized by the solar cells. This released energy at night lies in the infrared region (IR) i.e. 7-17μm spectral range [7] along with some other infrared sources i.e. thermal engines and furnaces. In order to harvest and convert this available infrared energy into something useful as charging devices or batteries, we need some novel capturing devices and conversion electronics that can cope with the generated photovoltaic current technology.

One solution that can utilize this abundant IR energy released from the Earth's surface is to make use of energy harvesting based on Radio Frequency (RF) techniques called rectennas. Rectennas working principle involves two components; (1) an antenna and (2) a rectifier circuit element. The antenna will work following its main principle of operation [9], i.e., receiving electromagnetic waves and resonating at desired frequency bands as per transmission lines or conducting elements shape. The rectifier will then take those alternating currents, pass through some diodes and give results in DC voltages [10]. All these steps will be accomplished keeping the impedance matching check between the antenna and diode. Rectennas offer an alternative and cheap solution to the already existing mature photovoltaics. Table 1.2 shows the comparison difference between both technologies;

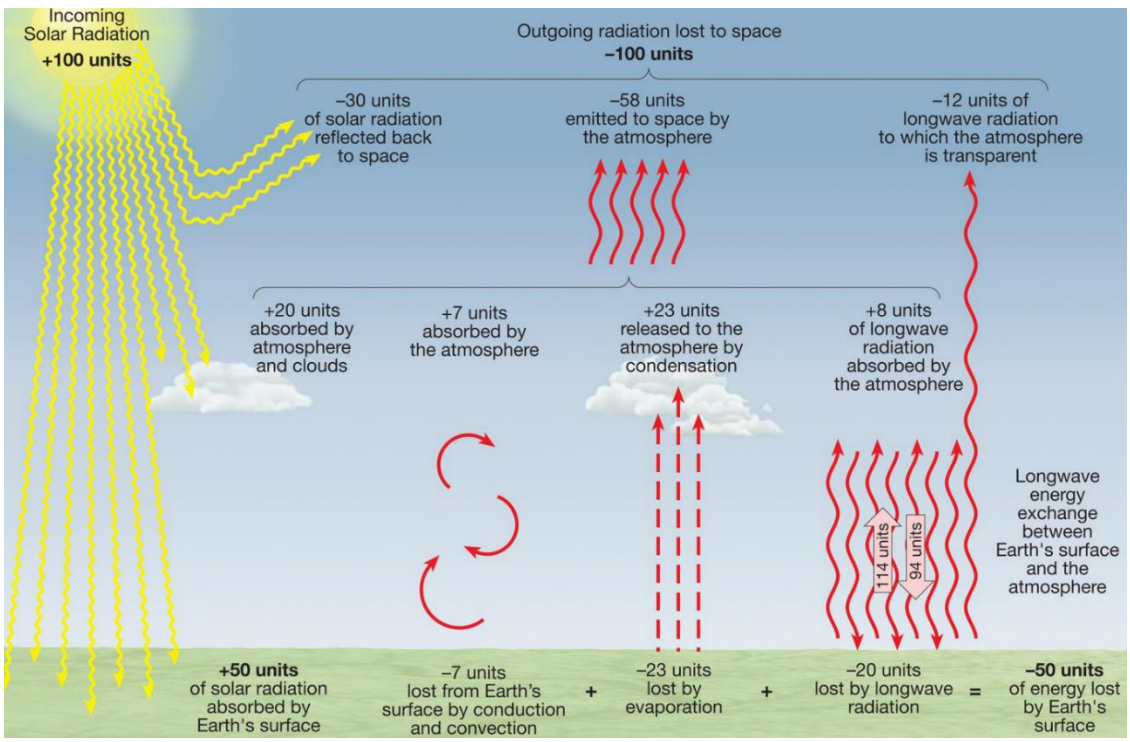


**Figure 1.1 Solar Radiation Energy Distribution on Earth [6]**

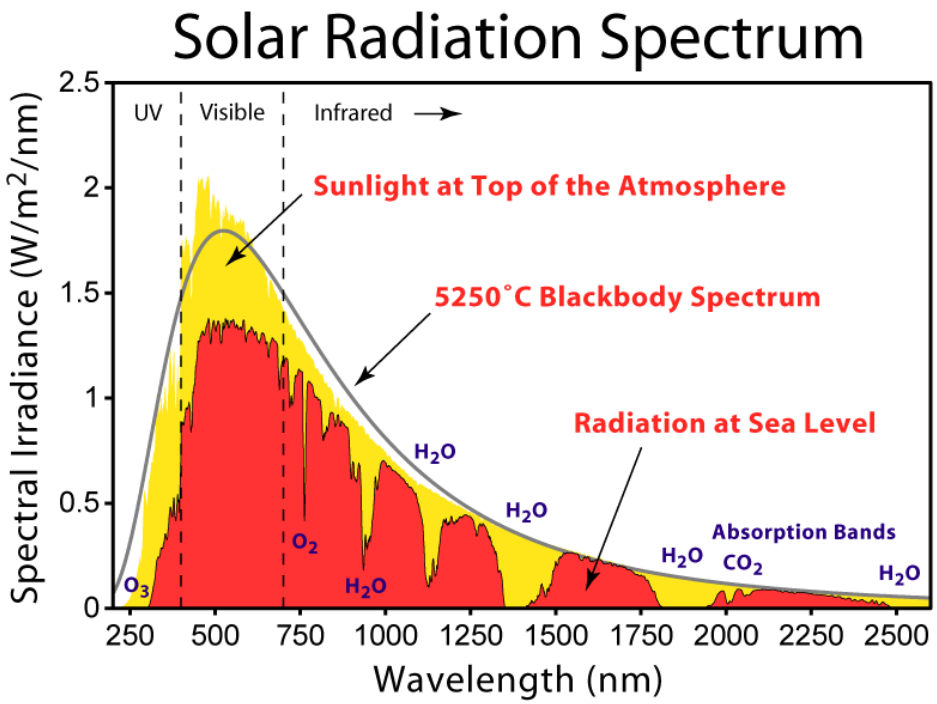


**Figure 1.2 Solar radiation spectrum: Top of the Earth's atmosphere and at sea level [7]**

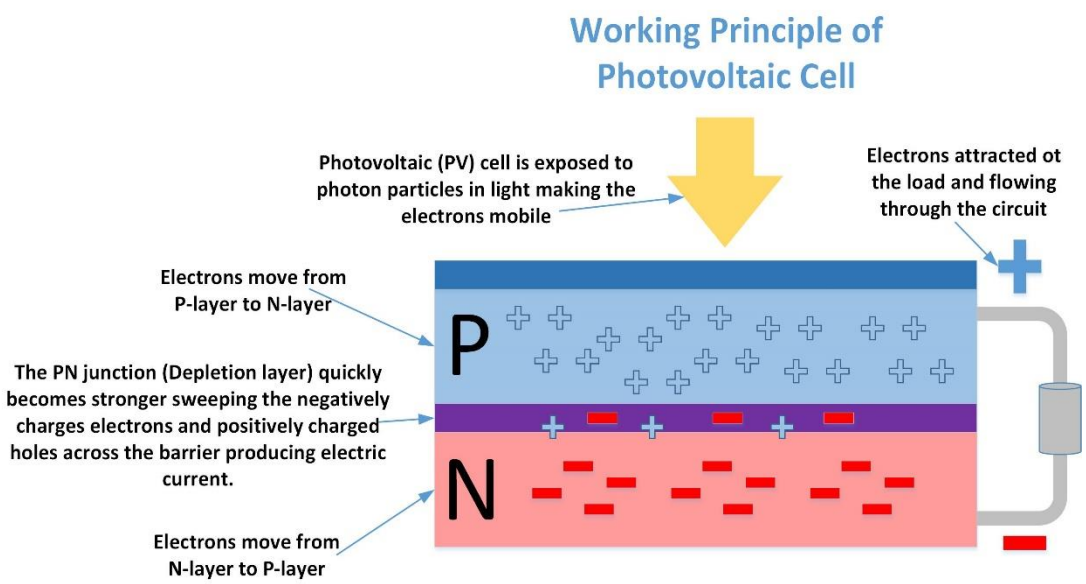


**Figure 1.3 Working Principle of Photovoltaic Cell**

| | Photovoltaic | Rectenna |
|---|---|---|
| **Efficiency** | Single cell produces 41%.<br><br>Multiple junctions give 87%. | Theoretical limit is around 85%.<br><br>Practically efficiency is more than 75%. |
| **Pros** | Well established and mature technology.<br><br>Less fabrication issues. | Basic knowledge of rectification.<br><br>Fabrication using standard dielectric substrates.<br><br>One time spending which is around 10 $. |
| **Cons** | Temperature dependent performance.<br>Costly for multiple junctions. | Polarization and spectral selectivity. |

**Table 1.2 Comparison between two technologies [11]**

## 1.3 Plasmonics and Surface Plasmons

Harvesting energy in the IR domain requires understanding of how the electrons will operate in the antenna designed at the nanoscale. With the advancements in nano technology fabrication, different theories and ideas are surfaced and new fields of study are created that explain these phenomena. One such field of study, which is a branch of nano-photonics, is Plasmonics [12]. Plasmonics deal with the interaction of light with free electrons at the surface of Noble metals. It explains the generation, manipulation and detection of surface plasmon polaritons (SPP), which are quasi particles, appearing due to coupling of light with surface plasmons on the surface of metal and insulator interaction. Simply put, the most common definition of a Plasmon is; *"A plasmon is a quantum of plasma oscillation"*. The requirement for a plasmon to get excitation is when an electron passes through a thin film or gets reflected from the surface of a metal. This excitation can be seen from figure 1.4 where an incident electron is interacting with a thin film generating scattered electrons from the thin films surface along with two or more plasmons with hypothetical energies as ;

Electron incident energy ~ 1-10 KeV

Plasmon energy: ~ 10 eV

Figure 1.4 shows a thin metal film where a beam of monochromatic light is projected onto to it with the help of a prism at certain angles of incidence i.e. between critical angle and $\theta c$ and $90$ degrees, where total internal reflection occurs. In this process, an evanescent waves (oscillating electric or magnetic field that tend to vanish exponentially and do not propagate far from the source) is produced. These evanescent waves tend to excite the electrons on the surface of the thin metal film that produces a phenomenon known as surface plasmon polaritons (SPP). With the mentioned angles on incidences, the wavelength of SPP's coincide with eh wavelength of

evanescent waves thus producing resonances at the boundary of the metal sheet. The SPP's produced are intensified with the energy received form the incident light source. To explain the working of the SPP's, an enlarged or zoomed view is shown in figure 1.4. When electron oscillations (white dots) happen on the surface of the thin metals film, interaction of photons from light waves interact with them causing production of plasmons. Also, electromagnetic field oscillation is induced near the surface in synchronization with the surface plasmons. The SPPs are quasiparticles resulting from coupling between surface plasmons and electromagnetic waves [13].

The first known application of this photon electron interaction was documented to the Roman Empire with the use of metal particles in colored glass. A practical example of this can be seen at the British museum in London where a glass is forged into a chalice in the fourth century. It describes story of the mythological King Lycurgus being trapped by a vine after he attacked the god; Dionysus (figure 1.5). The amazing thing about this cup which makes it unique than other utensils is the way it interacts with light waves. In natural ambience, the cup shines green/jade but when light is shine through it, it glows bright red. This remarkable feature exists due to the presence of small portions of silver and gold about 70 n min diameter embedded in the glass cup. At this scale, the interaction of light with these noble metals cause a change in color due to a phenomenon known as surface plasmons. Surface plasmons appear and cause a change in color when the photons in the light interact with the electrons available on the surface of the material [14]. Innovation in nanofabrication technology and modelling of near filed electromagnetics have introduced a pace in the research domain of Plasmonics. Last decade has seen an enormous growth in the field of plasmonic resonances where its applications can be utilized in the field of quantum electrodynamics and the interaction between metals and light particles for harvesting solar radiation energy.

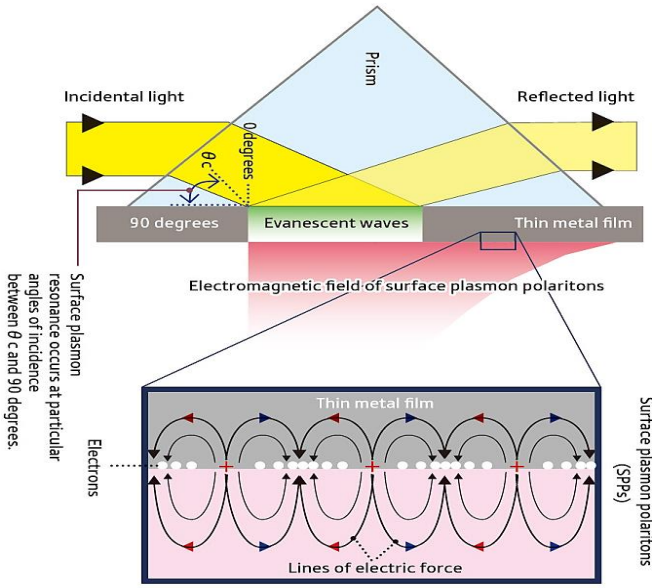


**Figure 1.4 Principle of surface plasmon resonance [13].**

**Figure 1.5 The Roman Lycurgus Cup: In normal daylight, the cup remains green in color but due to metal nanoparticles it turns red when light is shone through it.**

## 1.4 Context and motivation of the study

Recent years have witnessed an increased interest by the scientific community to acquire green and clean renewable sources of energy compared to traditional fossil fuels. One abundant source of renewable energy is the solar radiation which is applied currently for various applications [15]. There are generally two different ways in which solar energy is used – heat and electricity. The main motivation of this work is to utilize that abundant source of energy in producing a small fraction of output DC voltage. With the help of optical antennas and nano circuit elements, if technology permits, this could be possible. Also since optical antennas are nano scaled version of their microwave counterparts, they could furthermore be utilized in integration among various nano communication devices with better antenna performance [16].

Optical antennas are devices designed in the THz scale of the electromagnetic spectrum that convert ambient optical radiation into sub wavelength localized energy. This converted or captured energy can be manipulated in the nanometer sacle for various optical applications [17-18]. Many properties and parameters of optical antennas are similar to their radio wave and microwave counterparts, they have important differences resulting from their small size and the resonant properties of metal nanostructures. Optical antennas provide unprecedented means to tailor electromagnetic fields in all its aspects and applications. With the advent of nanotechnology, antennas operating at optical/near-infrared frequencies have become accessible, exceeding the energy localization capabilities of traditional optical elements such as mirrors and lenses [19-22]. Optical antennas are the subject of a growing number of scientific studies, and hold promise for enhancing the efficiency of photo detection, light emission sensing, heat transfer, energy harvesting and spectroscopy [23].

## 1.5 Objectives and research contributions

Keeping in view the motivation of energy harvesting, one of the main principle objectives of this research work is to design different kinds of optical antennas (nantennas) that can be considered as viable candidates for harvesting solar infrared energy. The selected spectrum for all the proposed nantennas to resonate will be in the infrared region. The proposed nantenna designs will capture solar energy in the THz range (180-200 THz) or one of the optical windows (1500-1600 nm). By studying, analyzing and understanding the theory behind electromagnetic waves at nano materials, mathematical investigations will be performed in the near field optical and far field radiation properties of the designed nantenna. Since the design will be at THz frequency, the other optional work as per technological availability will be to address some major challenges faced when harvesting solar energy.

**Objectives:**

1. Propose and design an energy harvesting rectenna working in the microwave bands i.e. GSM and WLAN.
2. Propose and study optical antenna designs based on dielectric resonators (DR).
3. Realization of a high gain Yagi-uda nantenna on available silicon materials in THz range.
4. Propose a lens array antenna design based on PDMS (Polydimethylsilicone) technology to confine the THz wave onto the nantenna.
5. Realization of thermopile optical antennas that will generate some output voltage.

**Contributions:**

*1. Energy harvesting rectenna for GSM and WLAN applications:* First step will be to present an energy harvesting rectenna for the GSM and WLAN bands. The design will have a monopole multiband antenna connected to a voltage multiplier. The electromagnetic signals received on the multiband antenna will be rectified via the rectifying circuit thus producing the output DC voltage. Lab experiments will be conducted to analyze and verify the results produced by simulations in terms of s-parameters, radiation patterns and output DC voltages.

*2. Propose optical antenna designs based on dielectric resonators (DR):* Since dielectric resonator based antennas have low radiation losses due to minimum surface waves, they are good candidates while designing antennas at very high frequencies (THz domain). Two different DR based antennas will be proposed. Their simulated results in terms of reflection coefficient and radiation patterns will be analyzed and studied to see how much suitable they are if realized for capturing solar energy. Near-field and far-field analysis will also be presented.

*3. Design and fabrication of Yagi –Uda nantenna:* Next task will be realization of a very directive antenna working at center frequency of 193.5 THz. An array of 100 x 100 elements will be fabricated using nano lithography technique. The materials used for

fabrication will be Noble metals as per availability in the fabrication lab. This designed nantenna will be then coupled to a commercially available optical diode in order to rectify the energy. Analysis will be presented on the interaction of the laser photons with the yagi-uda plasmonic nantenna fabricated on glass material.

*4. Lens array nantenna based on PDMS technology (Polydimethylsilicone):* Another nantenna design will be presented. It will be based upon a very flexible, transparent and transmissivity based material known as PDMS. Simulations of PDMS in form of a lens will be done to calculate the exact focal point. The idea will be to place the PDMS lens exactly on the optical diode that will produce certain output voltage when laser is passed through it. Realization of this task will be a challenge since it requires molding techniques and the dimensions might be very small for current fabrication tools to cope with.

*5. Realization of Thermopile optical antennas:* Finally, the third proposal for optical antennas would be to use the seebeck effect in nano design. Two different Noble metals will be used to fabricate the nantenna array. Upon receiving the laser light, the thermocouple metals will produce certain output voltages. Various designs will be explored based on the thermopiles.

The performance of implemented antenna configurations will be evaluated through simulations carried out in advance, using available electromagnetic problem solving software. An antenna prototype along with measured results will be presented based on availability of manufacturing and testing/measurement facilities.

## 1.6 Thesis structure

This thesis is divided into three main chapters.

The second chapter deals with the introduction of energy harvesting in the Radio Frequency (RF) domain. Various energy harvesting rectennas (antenna + rectifier) working at the lower frequency bands (less than 10 GHz) are presented. The detailed analysis of the working principle of rectifier and its integration to the antenna is also investigated. Impedance matching is also considered between two technologies. Finally a multiband antenna is presented that resonates at all commercially GSm and ISM bands. Also a wideband rectifier is presented. The whole rectenna system is experimentally verified producing output voltages at minimum input powers.

The third chapter discusses about the optical antennas and its comparison to microwave counterparts. Also dielectric resonators (DR) are introduced as an optimal nano antenna design because of their low radiation loss features at very high frequencies. Simulations based on these dielectric resonators shaped in hexagonal and triangular form are presented with results resonating at 193.5 THz which corresponds to 1550 nm wavelength.

The fourth chapter contains the main contribution of this research. It has all the portions needed to achieve the aforementioned objectives. Here, three different nanoantenna designs and strategies are discussed. The designs are such that they can be considered viable candidates for harvesting infrared radiation. Firstly, a high directive and wideband Yagi-uda nanoantenna is

realized at center frequency of 193.5 THz. The proposed yagi-uda nanoantenna is then coupled to one of the optical diodes in order to produce some output voltage. Second, a PDMS (Polydimethylsilicone) based flexible lens antenna is proposed. Again it is to be coupled with the optical diodes in order to achieve an output DC voltage. Third, a thermopile array is realized which gives output DC voltage in microvolts. This design is not coupled to any optical diode but rather is fabricated in a way that incident ways striking the antennas produce output voltages following the seebeck effect. All the realized designs are analyzed and explained thoroughly on this chapter.

This thesis ends with chapter five that presents general conclusion and future work associated with this research. The main points or achievements are summarized. Also the limitations in nano technology which halted some our long term objectives are listed. These limitations prevented my research but it will help and open many doors for researchers and students likewise, who are interested to work and find ways to efficiently harvest ambient infrared energy available in the Earth's surface.

# Bibliography


[1] The National Photovoltaics Program Plan 2000-2004, Photovoltaics–Energy for the New Millennium, DOE/GO-10099-940, Jan 2000.

[2] F. Yildiz, "Potential ambient energy-harvesting sources and techniques", *J. Technol. Studies*, vol. 35, no. 1, pp. 40-48, 2009.

[3] Harb, Adnan. "Energy harvesting: State-of-the-art." *Renewable Energy* 36.10, 2641-2654, 2011.

[4] M. Arrawatia, M.S. Baghini, and G. Kumar, "RF energy harvesting system at 2.67 and 5.8GHz," *IEEE Asia-Pacific Microwave Conference Proceedings,* Yokohama, pp. 900– 903, December 7–10, 2010.

[5] H.J. Visser, A.C.F. Reniers, and J.A.C. Theeuwes, "Ambient RF energy scavenging: GSM and WLAN power density measurements," *IEEE 38th European Microwave Conference*, Amsterdam, Netherlands. pp. 721–724, October 27–31, 2008.

[6] Hinrichs, Roger, and Merlin Kleinbach. *Energy: Its use and the environment*. Nelson Education, 2012.

[7] "File:Solar Spectrum.Png - Wikimedia Commons". *Commons.wikimedia.org.* N.p., 2017. Web. 16 Mar. 2017.

[8] Singh, Rajendra, Githin Francis Alapatt, and Akhlesh Lakhtakia. "Making Solar Cells A Reality In Every Home: Opportunities And Challenges For Photovoltaic Device Design". *IEEE Journal of the Electron Devices Society,* 2013.

[9] C. Balanis, Antenna Theory Analysis and Design, Wiley, 1997.

[10] Sika Shrestha, Sun-Kuk Noh, and Dong-You Choi, "Comparative Study of Antenna Designs for RF Energy Harvesting," *International Journal of Antennas and Propagation*, vol. 2013, Article ID 385260, 10 pages, 2013.

[11] Kauffman, Joanne, and Kun-Mo Lee. Handbook Of Sustainable Engineering. 1st ed. Dordrecht: *Springer*, 2013.

[12] Geddes, Chris D. Reviews In Plasmonics 2015. 1st ed.

[13] New Technique Lights Up The Creation Of Holograms". *Phys.org. N.p.*, 2017. Web.

[14] N. Savage, "Photonics: Trick of the light," *Nature*, vol. 495, no. 7440, 2013.

[15] D. Kotter, S. Novack, W. Slafer, and P. Pinhero, "Theory and manufacturing processes of solar nanoantenna electromagnetic collectors," *Journal of Solar Energy Engineering*, vol. 132, no. 1, p. 011014, 2010.

[16] P. Biagioni, J.-S. Huang, and B. Hecht, "Nanoantennas for visible and infrared radiation," Reports on *Progress in Physics*, vol. 75, no. 2, p. 024402, 2012.

[17] Bharadwaj, P., Deutsch, B. & Novotny, L. Optical antennas. Adv. *Opt. Photon*. 1, 438–483,2009.

[18] Giannini, Vincenzo, et al. "Plasmonic nanoantennas: fundamentals and their use in controlling the radiative properties of nanoemitters." *Chemical reviews 111*.6, 3888-3912, 2011.

[19] Greffet, Jean-Jacques. "Resonant optical antennas." *Antennas and Propagation (EuCAP),* 2014 8th European Conference on. IEEE, 2014.

[20] Taminiau, T. H. et al. Resonance of an optical monopole antenna probed by single molecule fluorescence. *Nano Lett*. 7, 28–33 (2007).

[21] Ghenuche, P.et.al, Spectroscopic mode mapping of resonant plasmon nanoantennas. *Phys. Rev. Lett*. 101, 116805,2008.

[22] Kinkhabwala, A. et al. Large single-molecule fluorescence enhancements produced by a bowtie nanoantenna. *Nature Photon.* 3, 654–657,2009.

[23] Schuller, J. A et.al.. Optical antenna thermal emitters. *Nature Photon*. 3, 658–661, 2009.

# Chapter 2
# Radio Frequency Energy Harvesting Rectenna

This chapter provides an overview of Radio Frequency (RF) energy harvesting. Background introduction and a review of state-of-the-art energy harvesting designs are presented. A hexaband monopole antenna is presented. Performance of the proposed hexaband antenna is discussed as per its realization. Also a multiband rectifier topology is proposed using the voltage doubler technique. Both technologies, i.e., the antenna and the rectifier, are combined together to work as a rectenna system at the GSM and WLAN bands at low input power levels.

## 2.1 Introduction to Radio Frequency (RF) Energy Harvesting

Environmental concerns, drastic decrease in existing energy sources from fossil fuels, and an increase in energy demand as per increase in technology, are the driving forces for considering alternative and renewable energy sources. Future demands of energy will not be fulfilled by existing sources such as oil, gas, and coal. Moreover, these sources are the main reason for carbon emissions and pollutants harming our atmosphere. Nuclear source is another option but it's costly in terms of establishing a plant and may cause some safety concerns to the local population during its operations. The energy from hydroelectric power plants are other options which are inexpensive but their lifetime in limited and restraints may occur due to socio-geographical locations and water availability. Therefore, we should look for other sources of energy that are environment friendly and last long to meet the energy needs.

A concept that captures the ambient energy in any form, stores it and utilizes it to provide energy or power to other small devices is called energy scavenging or energy harvesting. Sources for such energy includes both natural and artificial ones. Natural sources include solar, wind, thermal and water with artificial being generated by machines in the form of mechanical stress and vibrations. Environmental, geopolitical and economic constraints on the global energy conservation and fossil fuels being depleted forced the developed countries of the world to think outside the box and come up with alternate sources for harvesting various form of energies. To meet these challenges, technological advancements should be made to capture or harvest energy from various sources and converting them to useable electric energy. These developments have sparked interest in many communities such as science, engineering, and education to develop more energy harvesting applications and new curriculums for renewable energy and energy harvesting topics.

With the advancements in technology especially in the wireless systems, Radio Frequency (RF) energy harvesting has attracted widespread interest due to the increasing number of RF transmitting sources, which have created an abundance of ambient microwave energy available in the surrounding atmosphere [1-4]. Further motivation has been provided for RF energy harvesting

as more wireless power transmission (WPT) systems exist to meet the communication needs of the modern day. RF energy harvesting offers many advantages and has proven capabilities to provide power to remote of far flung areas and to charge batteries of various electronic devices [5-7]. Hence, RF energy harvesting can be a nominal and cost effective solution to provide energy to devices that work on batteries with extended battery lifetime while keeping the environment clean and healthy for coming generations.

The concept of energy harvesting has been around for decades, since the 1950's. A prominent advantage of RF energy scavenging is the ability to convert ambient energy into useable electrical power in any terrain, environment and at any given time. Figure 2.1 shows the generic RF energy harvesting scenario. The ambient energy is collected from various electromagnetic (EM) sources which then can later be rectified and be used as DC output voltages in charging or supplying small amount of power to devices in close vicinity. Moreover, RF scavenging has the advantage of capturing more energy as it can deal and receive multiple copies of signal occurring in the form of diffracting and penetration from buildings and materials. If we compare the solar energy harvesting from a photovoltaic (PV) solar cell to the RF rectenna, it is known that PV are a mature technology compared to the RF rectenna. But they lack in total solar energy conversion as only the light received during the day is converted while the infrared light existing during night time is wasted. Also the size of solar panel is huge and costly in order to make more converted energy. However the rectenna offers conversion in any time of the day i.e. 24 hours, with compact size and minimum installation and operational cost. Hence, RF energy harvesting is a promising solution to provide a sustainable energy source to meet future demands.

**Figure 2.1 Various RF energy sources with respective frequencies and power levels.**

## 2.2 Radio Frequency (RF) Energy Harvesting Principle

The basic working principle of a radio frequency (RF) energy harvesting rectenna consists of a receiving antenna, an input matching circuit, a rectifying schottky diode and a voltage elevator

load (resistance). The generic block diagram of the whole rectenna system is shown in figure 2.2. At the transmitter end, an electromagnetic source generates radiating waves. These waves are transferred into the free space via a high gain and directional antennas with mostly waveguides or horns been preferred as a source antenna. These free space propagating waves are then captured via a receiving antenna. The polarization of the receiving antenna will justify the received power on its surface. To receive the maximum power or energy from the waves, the antenna is connected to an input matching filter. The needed signals are filtered out and matched to the antenna connected to a rectifier. The input filter acts as a harmonic rejection device cancelling the unwanted waves and stopping the signals re-radiation back into free space. The matching circuit ensured that maximum signal reaches the antennas and is transferred completely to the rectification stage. Once the signals reaches the rectification stage, it is this area which is the core of the whole conversion process. The rectifier will convert the receive signal from alternating source (AC) to the desired output voltage (DC). The rectifier includes a rectification diode-capacitor combination. The diode is normally a fast switching schottky diode connected in specific orientation to the capacitors. Once the rectification is complete the signal may be passed through a low pass filter to clean the signals from any distortions and to get a nice and flat DC signal in the form of an output voltage. The load attached acts a voltage increase and is normally a resistor of some ohms value. The detail of main working elements in the presented block diagram are subsequently discussed in order to define specifications and limitations of the power conversion system.

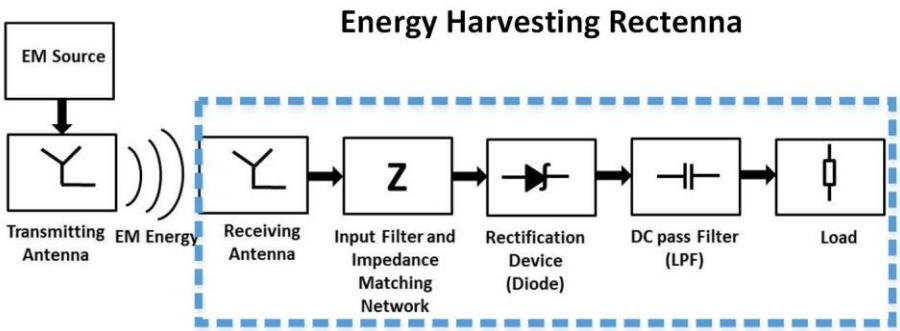


**Figure 2.2 Energy harvesting rectenna block diagram working principle [4].**

## 2.2.1 Antenna

Antenna is a vital part of any wireless communication system. Similarly for an efficient energy harvesting rectenna, an efficient receiving antenna is a major requirement. This antenna should be able to easily convert the received AC waves into DC output voltage that will power the remaining integrated circuit system. The antenna efficiency is another important parameter that relates directly to the frequency of operation. The designed antenna should capture more in terms of bandwidth in order to have more efficiency. The sources to capture RF energy are various for the antenna. The variety includes the broadcast TV signal (ultrahigh frequency (UHF)), mobile phones (900/1800 MHz), or Local Area Network (2.45 / 5.8 GHz).

In principle, it is known that the power harvested from RF signals is just enough to supply small and limited microelectronic devices [8]. However, to have more power received for large

circuits the design of the receiving antenna should follow an array pattern. Thus the received power will drastically rise [9-10]. Also the matching elements will be increased for array designs. Therefore in most cases the simplest way observed in the literature is to utilize the basic microstrip patch antennas integrated with rectifier elements on the same printed circuit board [11].

Figure 2.3 shows the equivalent electrical model of an antenna with an AC voltage source *($V_{ant}$)* with series impedance *($Z_{ant}$)*. Amplitude of the AC voltage source depends on the available power *($P_{AV}$)* and the real impedance ($R_{ant}$). The average power received *($P_{AV}$)* depends on the power density *(S)* and the antenna effective area *($A_e$)*, as expressed in Eq. (1);

$$P_{AV} = S.A \qquad (1)$$

The power received (or power density, *S)* can be calculated using the Friis transmission equation stated in Eq. (2). *S* is a function of several parameters: the transmitted power *($P_{TX}$)*, the transmitting antenna gain *($G_{TX}$)*, the received antenna gain *($G_{RX}$)*, the wavelength *(λ),* loss factor *($L_C$)*, and the distance between transmitter and antenna *(r);*

$$S = P_{TX}.G_{TX}.G_{RX}.L_c.\frac{\lambda}{4}.\pi.r \qquad (2)$$

Impedance of the antenna can be expressed by Eq. (3). The real component is presented by two resistances based on material loss *(Rloss)* and radiation loss *($R_s$)*. Whereas the imaginary component *($X_{ant}$)* depends on the antenna structure which is based in inductive (loop antenna) and capacitive (patch antenna) designs. Standard antenna impedance *($Z_{ant}$)* values are 50 Ω (wireless systems), 75 Ω (open dipole antenna), and 300 Ω (closed dipole antenna).

$$Z_{ant} = (R_{loss} + R_s) + jX_{ant} = R_{ant} + jX \qquad (3)$$

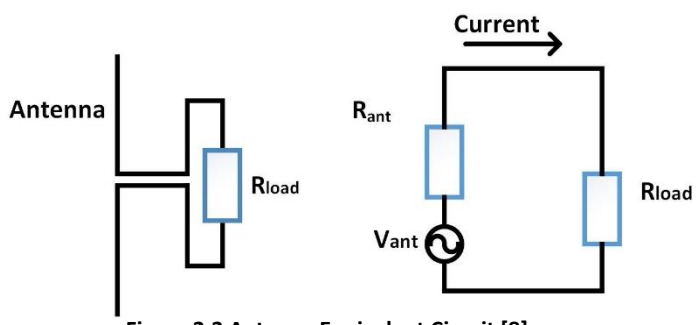


**Figure 2.3 Antenna Equivalent Circuit [8].**

## 2.2.2 Impedance matching circuit

Impedance matching circuits play an important role in any two elements or more systems that are meant to be integrated. For RF energy harvesting, matching circuits are used to match the impedance of the receiving antenna to the rectifier circuit element. Exact matching will provide maximum output DC voltage for the rectenna with minimum transmission losses. Literature provides various topologies for impedance matching circuits, however, the main configurations that have given substantial results LC network, the transformer and the series and parallel inductance coils as shown in figure 2.4.

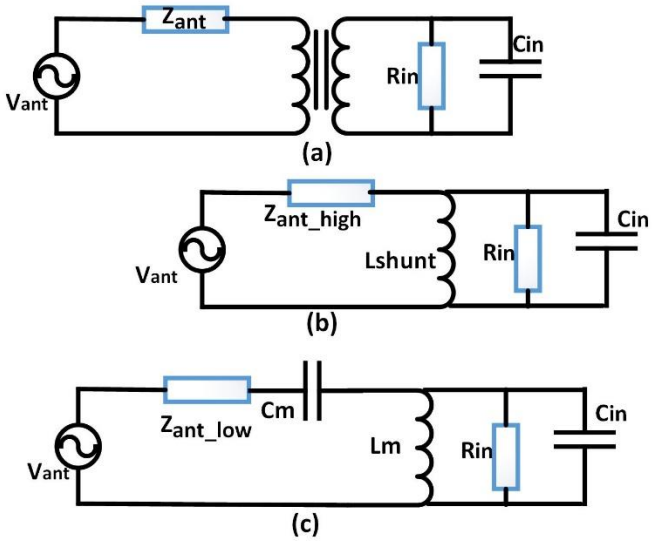


**Figure 2.4 Impedance Matching Configurations (a) Transformer (b) Shunt Inductor (c) LC Network [9].**

The impedance mismatch in the energy harvesting circuit can also be improved and replaced by a tuning circuit as in [12] in order to achieve maximum output voltage at multiple frequencies. Multiband antennas are another option for achieving higher output voltages but they are introduced with filters that increase the impedance matching complexity [13]. Stub utilization is another way of matching the antenna to the rectifier. The addition of the stub depends on the designed frequency that is either kept open circuit or short circuit to the ground plane. The current trend is to include antenna, impedance matching, and rectifier in a printed circuit board [14] that avoids cable, micro lumped components and transmission losses as with the design shown in figure 2.5.

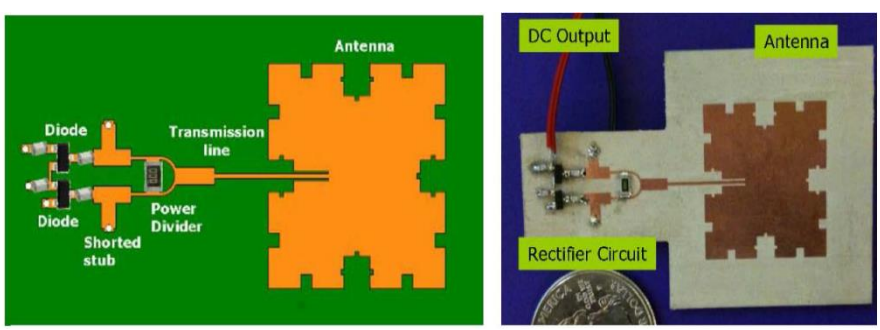


**Figure 2.5 Simulated and realized RF Energy Harvesting rectenna at 2.45 GHz [14].**

## 2.2.3 Rectifier

Rectifier is another important part of the rectenna system. The receiving antenna captures the electromagnetic waves in the form of alternating current (AC). In order to obtain an output DC voltage, rectifier comes into the play. The design and selection of rectifier topology should be such that it converts the AC into DC with maximum efficiency. The main parts in the rectifier are the lumped components, especially the capacitors and schottky diodes. The distance from the RF source also plays an important role in maximizing the output of the rectifier. In most cases the distance is more than a meter, then various amplification methods are used at the input of the rectifier. Some notable amplification methods are; 1) Dickson multiplier [15], which has the

function of rectifying the radio frequency signal and increases the DC voltage, 2) Complementary metal–oxide–semiconductor (CMOS) technology instead of diodes [16], 3) Greinacher circuit or voltage doubler [17], multiplier resonant [18] and boost converter [19].

Selection of multiplier depends on the resonant frequency and the output DC power required. The output DC can be increased with an increase in the number of stages in a multiplier, with each having a capacitor and diode combination. Increased number of stages will affect the output results in terms of number of diodes, impedance match losses and diode efficiency. The impact of rectifier stage number on the power received is presented in Figure 2.6 [20]. When the input power is low (Pin < 0 dBm), the output voltage *($V_{out}$)* is practically independent of the stage number, while efficiency remains acceptable for some stages. Maximum voltage is reached when power received is around 0 dBm and the number of stages is large, whereas efficiency decreases when ($V_{out}$) reaches its maximum. Therefore, it seems difficult to achieve a good design due to the received signal influence on the energy harvesting system.

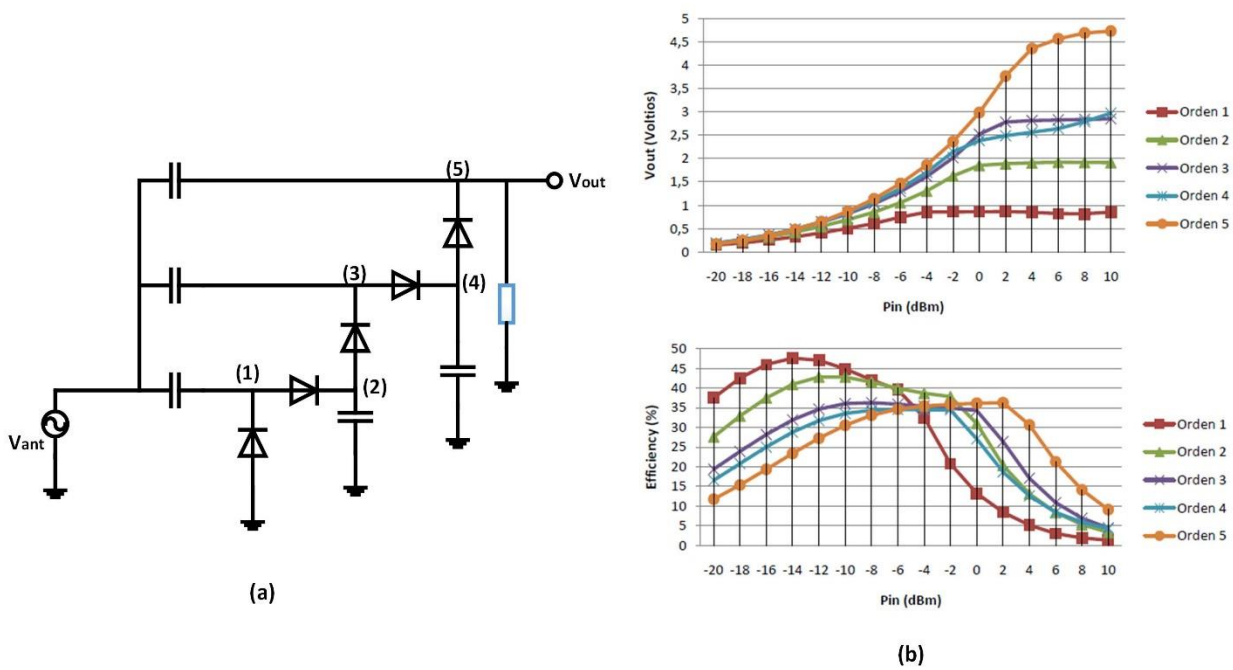


**Figure 2.6 (a) Multiple Voltage doubled stages (b) Output Voltage vs Efficiency for different diodes [20].**

Efficiency of the rectifier depends upon the input and output powers *($P_{in_rect}$ and $P_{out_rect}$)* as stated in Eq. (4). The efficiency *($\eta_{energy}$)* of the complete rectenna system depends on the total output power *($P_{out_dc}$)* generated in DC by the input received power *($P_{in_rf}$)* from the source as stated in Eq.(5);

$$\eta_{rect} = \frac{P_{out_{rect}}}{P_{in_{rect}}} \qquad (4)$$

$$\eta_{energy} = \frac{P_{out_{dc}}}{P_{in_{rf}}} \qquad (5)$$

Figure 2.7 represents the equivalent circuit for the multiplier. It is modeled by an input impedance in parallel to a capacitor with a current source depending on the input voltage, and a constant output resistor that presents the rectifier losses [21]. To achieve maximum output voltage, a number N of multiplier stages can be added with efficiency improvements based on various mathematical equations for the multiplier [21-23].

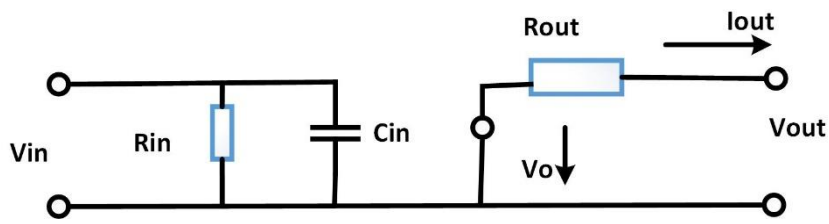


**Figure 2.7 Multiplier equivalent circuit [21].**

## 2.3 Literature Review: State-of-the-art Energy Harvesting Rectennas

In this section, state-of-the-art literature review on various energy harvesting configurations is presented. Some of the presented work focuses on achieving high efficiency design, other focus on multiband energy harvesting while some focus on the compactness of the proposed rectenna designs.

In [24], authors presented the design of a rectenna working at 2.45 GHz ISM band. The antenna was printed on FR4 substrate with thickness 1.6 mm using the simple microstrip patch design. The rectifier circuit was optimized using ADS simulator with its relevant capacitors and schottky diodes. The schottky diode used was from Avagos HSMS2860 series. As an experimental setup, horn antenna was used as an RF source to transmit power to the rectenna. Experimental results provided maximum output voltage of 50 mV at an input power of 10 dBm. Figure 2.8 and figure 2.9 show the fabricated prototype and DC output voltages of the rectenna.

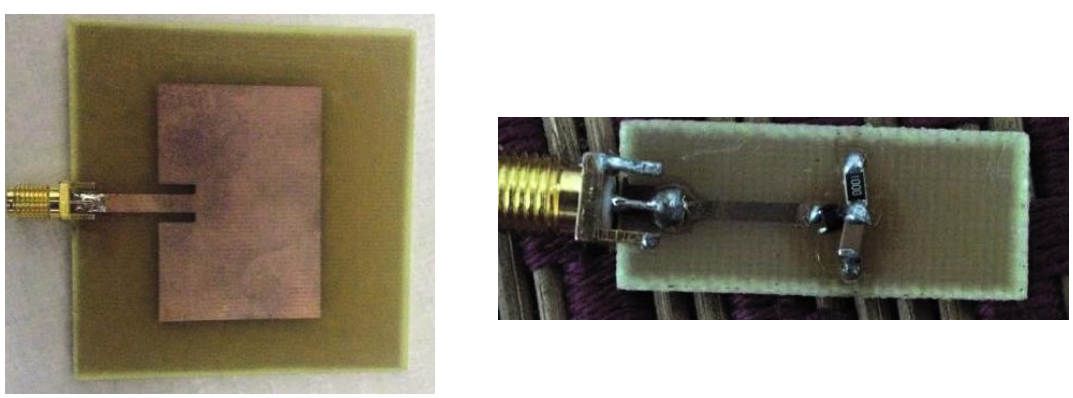

**Figure 2.8 realized patch antenna and Rectifier [24].**

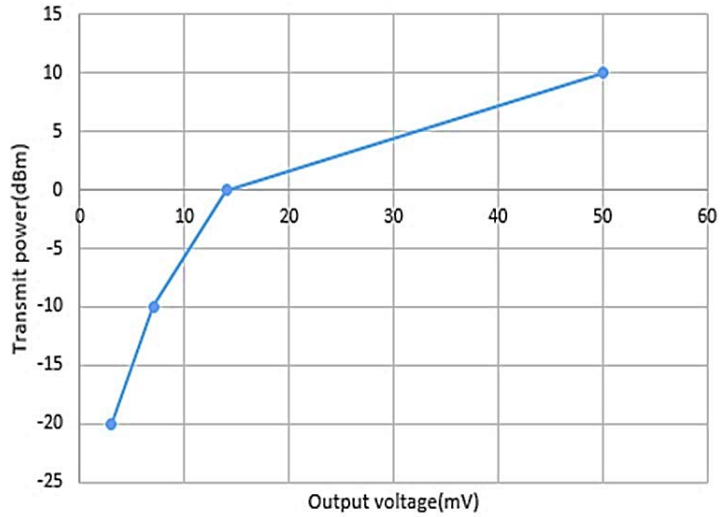


**Figure 2.9 DC Output voltage produces from the rectenna [24].**

Similarly in [25], authors proposed an ultra-compact low power rectenna working at 2.45 GHz but this time the technology used was paper based. The rectenna utilizes double layer technology where the antenna is on the back side with annular slot configuration while the remaining circuit components for the rectifier are on the other side of the substrate. The prototype was fabricated on a 230−µm thick paper sheet from Mitsubishi *($\epsilon r = 2.55$, $\tan\delta = 0.05$)* by means of the copper tape technology, which consists of the shaping of an adhesive copper tape by standard photolithography and the application of the Cu pattern on the hosting substrate by means of a sacrificial layer. The schottky diode used was HSMS2850 series. For the experimental setup, a 4 dBi gain log periodic antenna was used. The rectenna was placed at a distance of 20 cm from the source. The measured results showed that the rectenna achieved an efficiency of 40 % around −10 dBm, of 28 % around −15 dBm, and in the range 10 % around −20 dBm, corresponding to an output DC voltage in the order of 320, 240 and 60 mV respectively.

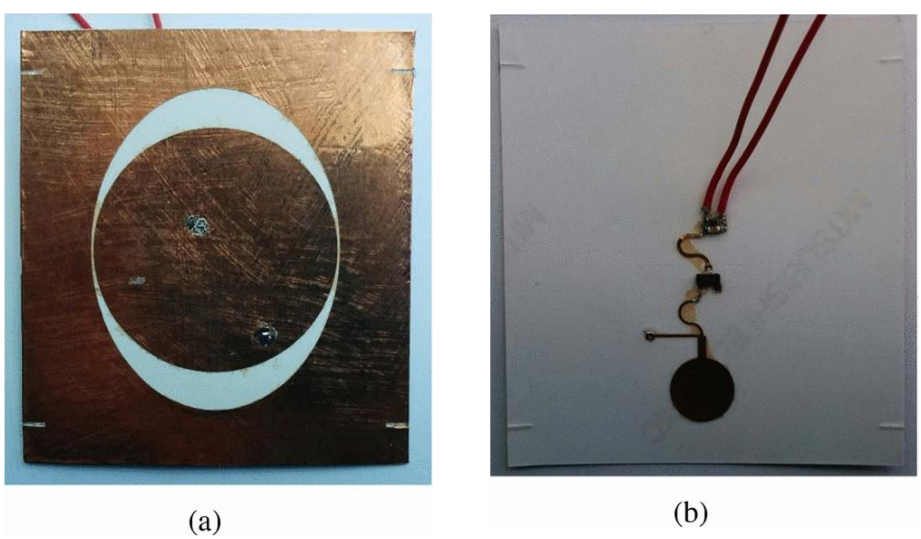


**Figure 2.10 (a) Paper based annular slot antenna (b) rectifier on the back side of the paper [25].**

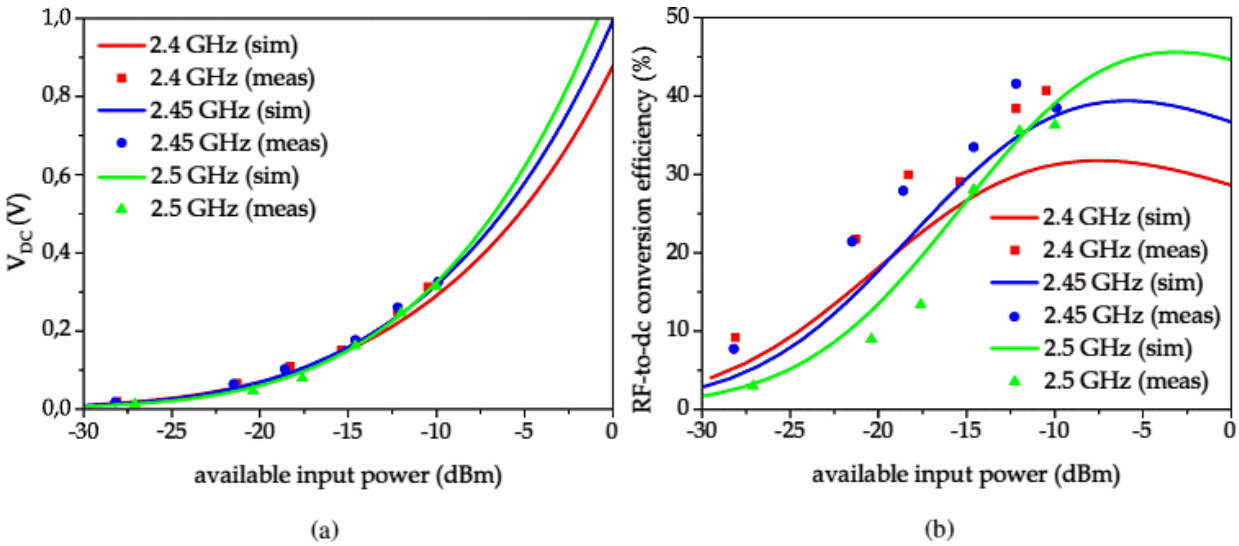


**Figure 2.11 Rectenna measurement: output DC voltage (a) and RF-to-dc efficiency (b) versus available power at the input of the rectifier in the band 2.4-2.5 GHz [25].**

A highly efficient UHF rectenna was presented in [26]. Authors implemented a novel idea with antenna design based on meander folded dipole technology having parasitic ground plane. The dimensions of the antenna was 41.3 mm x 17.5 mm at 915 MHz on a FR-4 based substrate. The rectifier circuit was based on a 5 stage charge pump having Cockroft-Walton voltage multipliers [17]. The conversion efficiency of the rectifier was 0.005% at a distance of 1.5 m realized on a FR4 board. Schottky diode, HSMS 285x and 286x, were used for its unique characteristics of very low signal compatibility feature (Pin <−20dB), and very low leakage current loss. A 3 V Zener diode was used to make it a ripple free DC voltage at 3 V and finally the output was measured across a 1.8 V distance. An UHF transmitter reader was to transmit microwave signals to the rectenna. The rectenna was able to harvest 200µW at an optimal distance of 1.5 m with the peak value of 647 µW at a distance of 0.5 m from the radiation source which was RFID based transmitter.

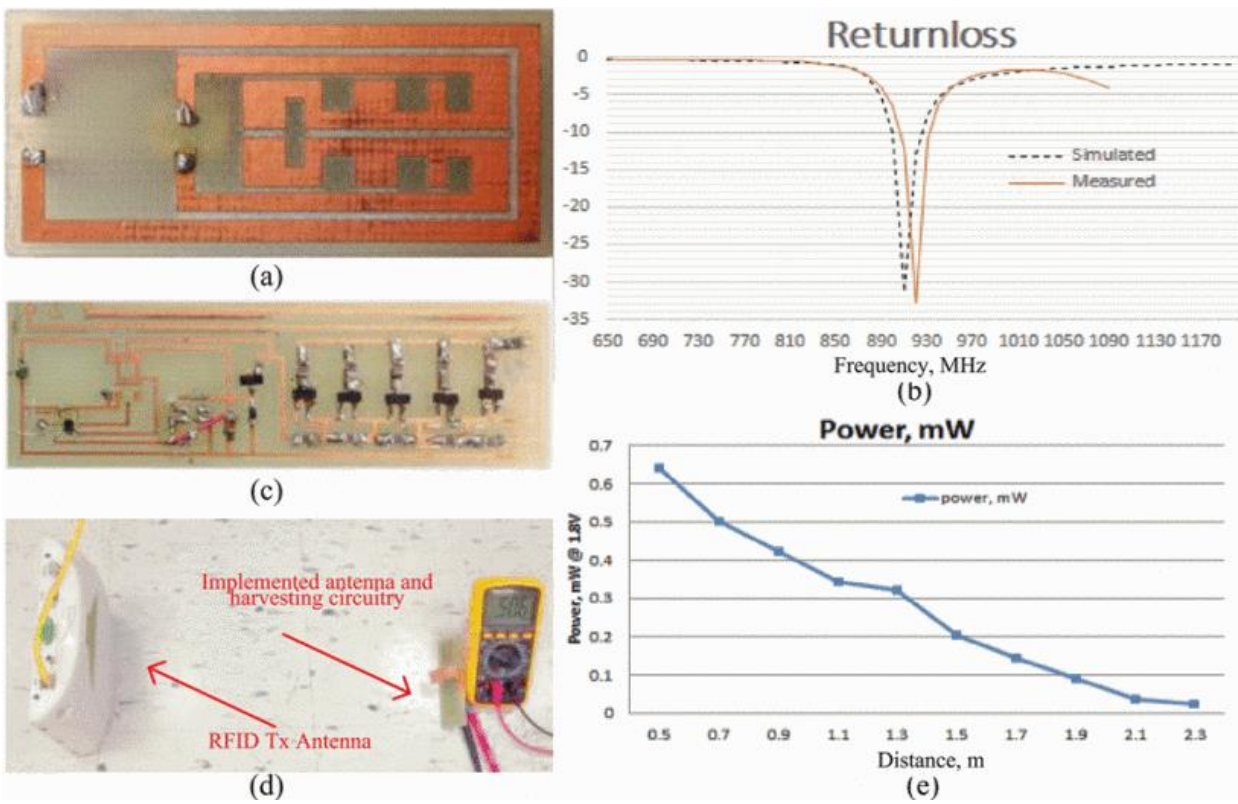


**Figure 2.12 (a) Implemented antenna; (b) simulated and measured return loss; (c) implemented cockcroft-walton charge pump; (d) snapshot of the test bench to measure harvested power; (e) harvested power vs distance curve [26].**

Another antenna at UHF for mobile telephony bands was presented in [27]. The rectenna system was based on a broadband annular slot antenna and a thin flexible substrate, weighed fewer than 15 g. Thanks to the proper design of the rectifier and the matching network, an excellent performance was verified over the whole band (400 MHz – 1 GHz), with a rectenna conversion efficiency of up to 60% and an efficient figure of merit (EFoM) equal to 37.6 dB for 2 µW/cm2 of incident power density. The antenna was designed on Taconic TLY-5-0100 substrate *(εr = 2.2, tanδ=0.0009, and h=0.254 mm).*

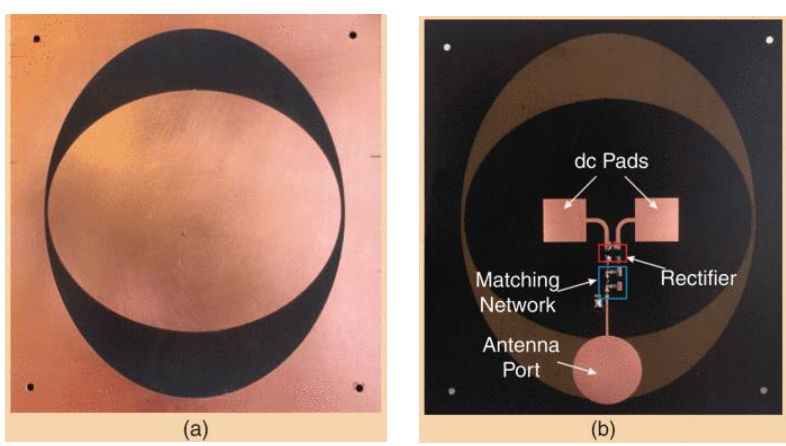


**Figure 2.13 Realized rectenna system: (a) Front side and (b) Back side [27].**

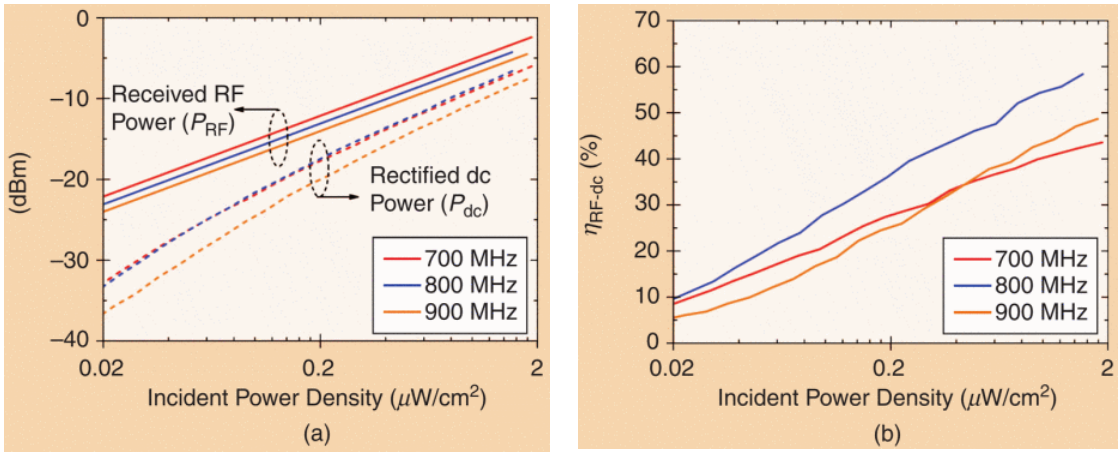


**Figure 2.14: The rectified voltage at the rectenna output over frequency for three different power levels at the transmitter side, which correspond to power densities of 1.92, 0.61, and 0.19 µW/cm2, respectively [27].**

In [28], authors proposed a dual band rectenna. This rectenna was working at the GSM bands (900/1800 MHz). Antenna was designed using meander lines on microstrip patch design which helped in reducing the size of the rectenna. Schottky diode SMS-7630 was used in the rectifier stage to convert the received signal into output voltage. Rectifier was optimized to receive signals as low as -20 dBm using harmonic rejection technique. The power conversion efficiency of 20% and 40.8% (in measurement) at the input power level of -20 dBm was achieved. The proposed rectenna had output voltage from 183-415 mV.

Similarly another dual band rectenna operating at 2.45 GHz and 5.8 GHz was presented in [29]. Square loop fed by a microstrip line technology was used to design the rectenna. Instead of exploiting multiband resonances from the square loop, for the first time according to the authors, half wavelength and full wavelength modes were generated from the design with the help of microstrip feed [29]. Impedance matching was achieved for the two resonances with the help of matching stub. The conversion efficiencies of 49% and 66% are achieved, respectively. The prototype rectenna measured only 13 mm × 24 mm or 0.106 $\lambda_0$ × 0.196 $\lambda_0$ at 2.45 GHz. Avago HSMS 2860 diode was used.

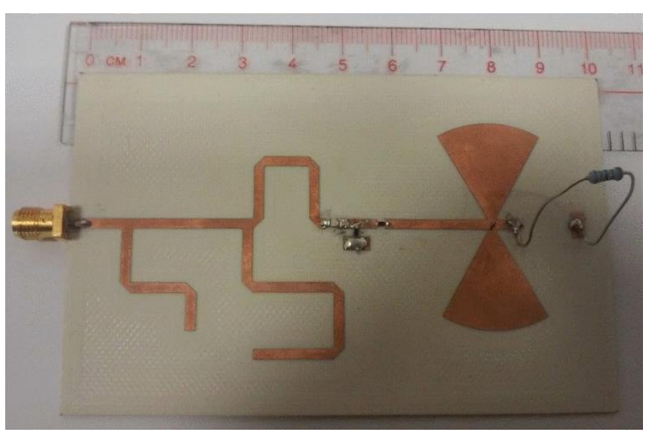

**Figure 2.15 Rectenna based on stubs [28].**

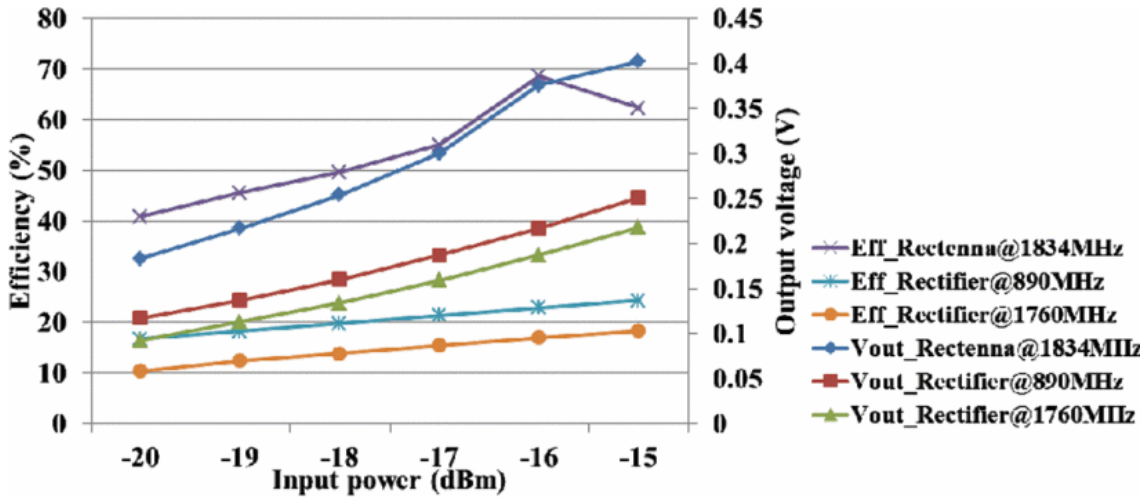


**Figure 2.16 Measured output voltage versus input power of only-rectifier and rectenna [28].**

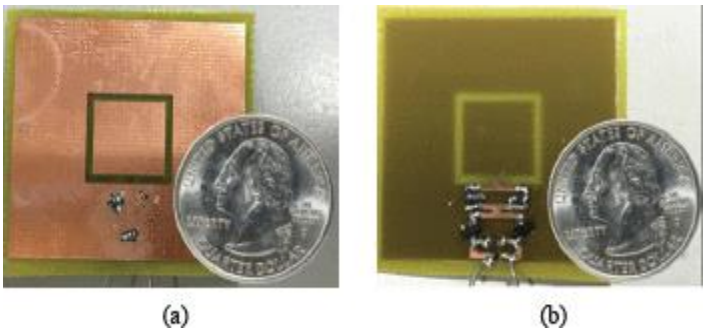


**Figure 2.17 Fabricated prototype of rectenna [29].**

**Figure 2.18 Experimental setup [29].**

In [30], a dual circular polarized energy harvesting rectenna based on six bands weas presented. Since diode in the rectifier stage is a non-linear device, its matching to get resonance at multiband is a challenge as varying input power or load can change its input impedance. In order to solve this, authors in [30] proposed an improved matching technique. They first realized a broadband antenna (550-2.5 GHz) with circular polarization and compact size. Compactness was acheinved using annular slots and novel feeding techniques. Then this wideband antenna was matched to a multiband rectifier with loads ranging from 10 to 75 kΩ. The measured results showed that the maximum harvested dc power of the rectenna in typical outdoor and indoor environments were 26 and 8 μW, respectively; it can therefore be applied to a range of low-power wireless applications.

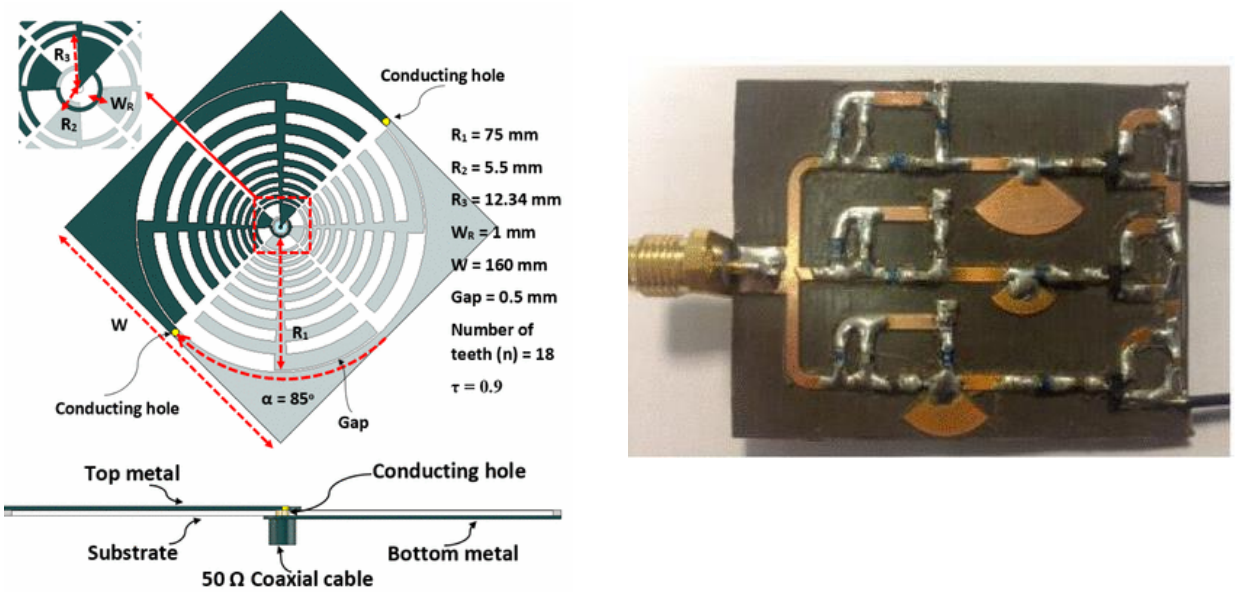


**Figure 2.19 Antenna and rectifier [30].**

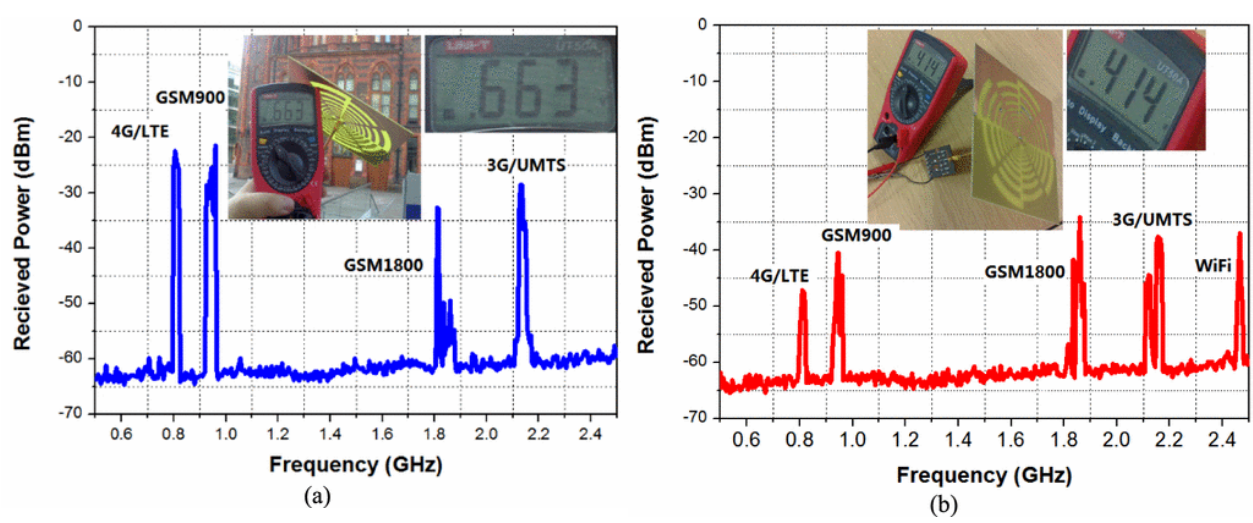


**Figure 2.20 Measured received power versus frequency and measured output voltage of the proposed rectenna in (a) outdoor ambient environment and (b) indoor ambient environment [30].**

A broadband rectenna array was presented in [31] having a triangular monopole antenna design. The antenna covered the electromagnetic spectrum from 800 MHz to 2.6 GHz. The gain was greater than 3.5 dBi from 900 MHz to 2.6 GHz and a maximum realized gain of 8.6 dBi was achieved at 2 GHz. Efficiency of 76% and 29% is obtained for a resistive load of 560 Ω at 900 and 1800 MHz, respectively. A voltage of 6.95 V for a load of 4.3 kQ was obtained close to a cell phone making a call.

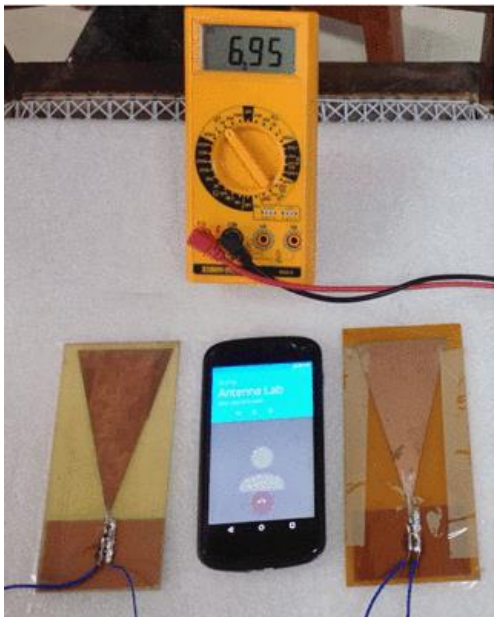


**Figure 2.21 Experimental setup to measure RF energy harvested from the cell phone using 2 element array for a load of 4.3kΩ [31].**

| Distance of Cell Phone from Rectenna (cm) | Output voltage with 4.3K load (V) | Power received (mW) |
|---|---|---|
| 5 | 6.95 | 11.2 |
| 10 | 5.58 | 7.2 |
| 20 | 4.64 | 5 |
| 30 | 3.07 | 2.2 |
| 40 | 1.76 | 0.7 |

**Table 2.1 2-element array with output voltage when placed at a certain distance from source [31].**

Similarly another ultra-broadband rectenna was proposed in [32]. This time solar technology was used with amorphous silicon as a substrate. A 0.6-W Si panel of 10 solar cells arranged in a series of five pairs of parallel connected cells was used with Vivaldi antennas cutted ion to the panel. The 400-nm-thick a-Si layer of each cell was 71×18 $mm^2$ and separated from other cells by a 2-mm gap. Each cell had seven silver electrodes on the front contact. The electrodes are 0.5×16.5 $mm^2$ and separated by 9.5 mm. Rear contacts, 19.9×146 $mm^2$, provided parallel connections between cells and were isolated from adjacent contacts by a 0.1-mm gap. The low-cost flexible panels were manufactured for one of many different power configurations, and the layout enabled various antenna shapes. End edge contacts on the panel were made from tin-coated copper plate. The entire panel was encapsulated by flexible polyimide layer. The rectenna maintained a peak power at 4.25 V, which overcomed a need for lossy power management components. The wireless communications device yielded solar energy or function as a rectenna for dual-source energy harvesting. The solar Vivaldi performs with 0.5-2.8 dBi gain from 0.95-2.45 GHz, and in rectenna mode, it covered three bands for wireless energy scavenging.

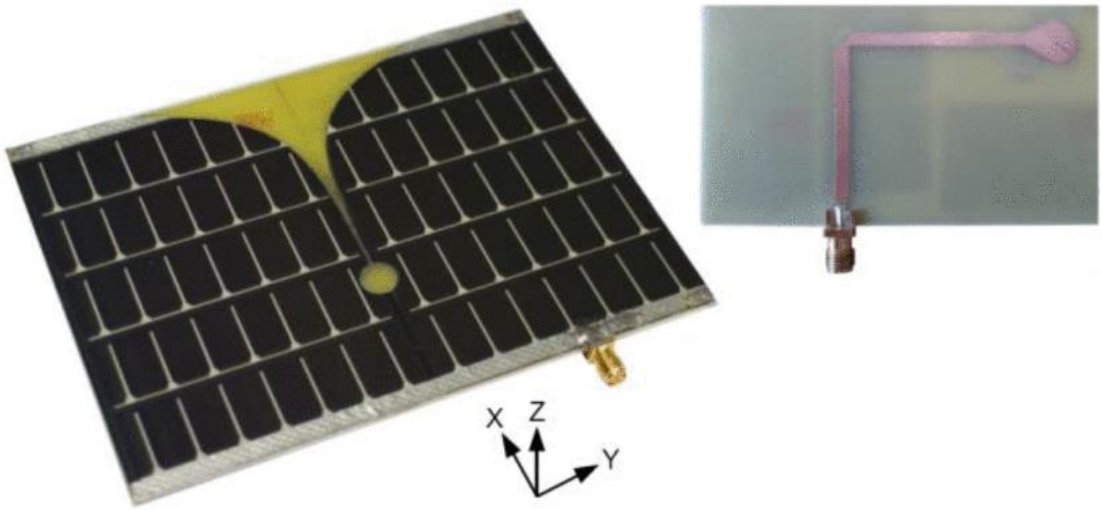


**Figure 2.22 Fabricated Solar panel Vivaldi antenna [32].**

| | -20 dBm | -15 dBm | -10 dBm |
|---|---|---|---|
| **Freq** | Voltage | Voltage | Voltage |
| 0.95 | 1.25 V | 3.25 V | 5.35 V |
| 1.87 | 1.22 V | 2.92 V | 4.78 V |
| 2.45 | 0.51 V | 1.27 V | 2.06 V |

**Table 2.2 Measured results for various input power levels [32].**

In [33], authors proposed a rectenna for a battery less thermal sensor operating at 2.45 GHz ISM band. The antenna was fabricated using microstrip technology and HSMS 2860 series schottky diodes were used for rectification. More than 80% efficiency was experimentally achieved at medium and low power densities. The circuit contained a symmetric and dual-access RF-to-dc rectifier and 2 patch antennas. The temperature sensor performs measurements every 10 seconds and required 1 V voltage and 30 μJ energy per period. It operated from low power densities of only 0.4μW/cm2 (E = 1.22 V/m).

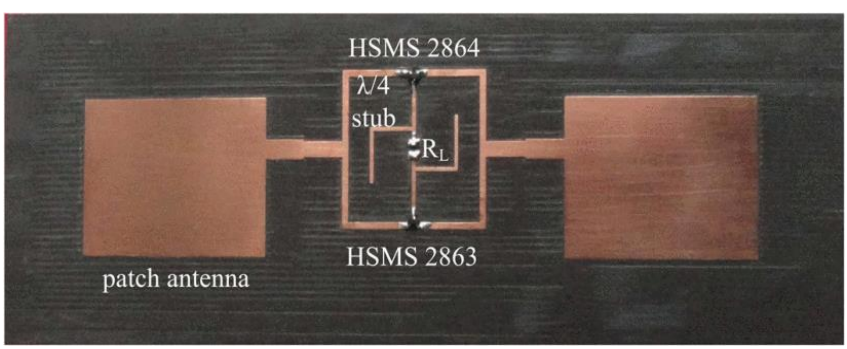


**Figure 2.23 Fabricated Rectenna [33].**

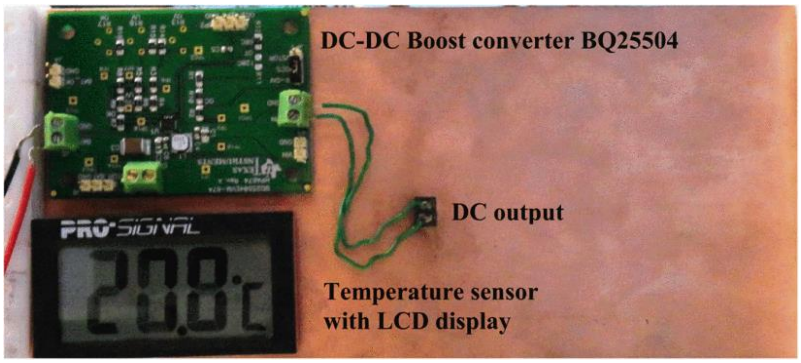


**Figure 2.24 Batteryless temperature-sensor prototype [33].**

| Reference | Topology | η RF to DC | Operating Level | Operating Frequency | Dimensions |
|---|---|---|---|---|---|
| **[24] Realized** | Microstrip Patch antenna, voltage doubler | 12.6 % | 50 mV @ 10 dBm | 2.45 GHz | 37.6 × 29.15 $mm^2$ |
| **[25] Realized** | Paper Based Annular slot antenna, Series Rectifier | 40 %<br>28 %<br>10% | 320 mV @ −10 dBm<br>240 mV @ −15 dBm<br>60 mV @ -20 dBm | 2.45 GHz | 49 × 54 × 0.23 $mm^3$ |
| **[26] Realized** | Meander Folded Dipole Design, Boost Converter | 0.005 % | 200µW @ 1.5 m distance<br>647µW @ 0.5 distance | 915 MHz | 41.3× 17.5 ×1.5 $mm^3$ |
| **[27] Realized** | Annular Slot Antenna, Multistage voltage doubler | 60 % | EFOM 37.6 dB for 2 µW/$cm^2$ of incident power density | 800 MHz | 83× 103 × 0.254 $mm^3$ |
| **[28] Realized** | Meander Stubs, voltage doubler | 20 %<br>40 % | 183 mV @- 20 dBm<br>415 mV @- 20 dBm | 900 / 1834 MHz | 42× 38 × 0.254 $mm^3$ |
| **[29] Realized** | Slot Loop Antenna, voltage doubler | 49 %<br>66 % | N/A | 2.4 / 5.8 GHz | 13 × 24 $mm^2$ |
| **[30] Realized** | Spiral Antenna, Cockroft-walton doubler | 67 % | 96 µW @ -15 dBm | 550 MHz - 2.5 GHz | 160 × 160 ×1.6 $mm^3$ |
| **[31] Realized** | Triangular Monopole array antenna, voltage doubler | 76 % @ 900 MHz.<br>29 % @ 1800 MHz | 6.95 V at 4.3KΩ Load in close vicinity | 800 MHz – 2.6 GHz | 158 × 57 $mm^2$ |
| **[32] Realized** | Vivaldi Antenna on Amorphous Si | -20 to -10 dBm | 1.25 V @ 0.97 GHz<br>1.22 V @ 18 GHz<br>0.151 @ 2.45 GHz | 0.97 GHz, 1.8 GHz, 2.4 GHz | 710 ×180 $mm^2$ |
| **[33] Realized** | Microstrip Patch Array, DC-DC boost conversion | 80 % | 0.3 V | 2.45 GHz | N/A |

**Table 2.3 Comparison among state-of-the-art presented in the literature review section.**

From the review that is presented in the above section, energy harvesting using RF source is still growing. Various design strategies and materials are being utilized in harvesting the maximum energies available in the atmosphere. Table 2.3 summarizes the state-of-the-art rectenna designs presented as literature review. It can be seen that most of the work is presented at 2.45 GHz, likely due to widespread usage. Limited work has been done in the multiband rectenna which shows more promise in terms of output voltage and efficiency. In the following sections, keeping with the harvesting spirit, a multiband antenna and a wideband rectifier is proposed. Both technologies are then combined and results are discussed in terms of efficiency and output DC voltage produced within a lab environment. The basic idea was to understand the working of the RF rectenna and present something to the research community as an alternate option for harvesting RF energy in the multiband spectrum.

## 2.4 Proposed Hexaband Antenna**

In this section, first part of the rectenna system, the receiving antenna is discussed. The proposed multiband antenna design is based on the monopole geometry which contains stubs or transmission lines of various lengths and widths. Using this technology will give us the required multi-bands that can be used for harvesting RF energy from various sources simultaneously. The details of the design and the results achieved are discussed in below sections.

### 2.4.1 Antenna Design

The geometry of the proposed hexaband antenna is shown in figure 2.25. The proposed antenna follows the principle of monopole antenna design where every printed monopole or stub length is $\lambda/4$ according to its relevant frequency. The antenna is fabricated on RT Duroid 5880 substrate with thickness of 1.57 mm, dielectric constant εr = 2.2 and loss tangent of 0.0009. The antenna is fed via a 50 Ω microstrip transmission line having a width and length of $W_f \times L_f$ = 2.8 mm x 87 mm. The overall antenna dimensions are $W_s \times L_s$ = 85 mm x 125 mm. The other side of the substrate has a finite ground plane with dimensions $W_g \times L_g$ = 54 mm x 60 mm and a rectangular slot with dimensions $W_{slot} \times L_{slot}$ = 0.7 mm x 7.6 mm. Each monopole antenna has been designed keeping in view its relevant frequency of operation. The capacitive coupling and parasitic looping of antenna elements also assists in achieving the required frequency resonance. The basic design consists of three monopole antennas with stubs introduced into the final design to achieve good bandwidth and resonances at bands of interest. Each monopole antenna element generates different resonant modes. The initial monopole, being the longest in length $(L_f + L_6)$, was designed to resonate at 900 MHz. The first monopole was loaded with a U-shaped stub to increase its electrical size, while maintaining its physical size and having a good resonance below -10 dB in terms of its reflection coefficient. The length of the inverted U-shaped stubs are $L_7$ and $L_8$ respectively with width represented by $W_2$. The second resonance was achieved at 1800 MHz band by a monopole placed in the center of the feed line having a form of inverted L-shape with dimensions $L_2$ and $L_3$. The third resonance (the smallest in dimensions) is at 2.45 GHz. The stub was placed below the inverted L-shape with dimensions $L_1$ and $W_1$. The final and fourth resonance was achieved at the higher frequency of interest at 5.8 GHz by introducing a slot within the finite ground plane on the backside of the substrate. In order to investigate the role of each monopole resonating at a specific


***Published in Microwave and Optical Letters Technology, Vol 59, 11, pp 2816-2822, Nov 2017.***

frequency band and its effect on overall antenna performance, extensive parametric studies have been carried out and best optimized values for the hexaband antenna are tabulated in Table 2.4.

| *Parameter* | ***L1*** | ***L2*** | ***L3*** | ***L4*** | ***L5*** |
|---|---|---|---|---|---|
| Value | 8 | 30 | 11.5 | 10.6 | 20 |
| | ***L6*** | ***L7*** | ***L8*** | ***W1*** | ***W2*** |
| | 24.6 | 80 | 15 | 2.8 | 4 |

**Table 2.4 Optimized hexaband antenna parameters (MM).**

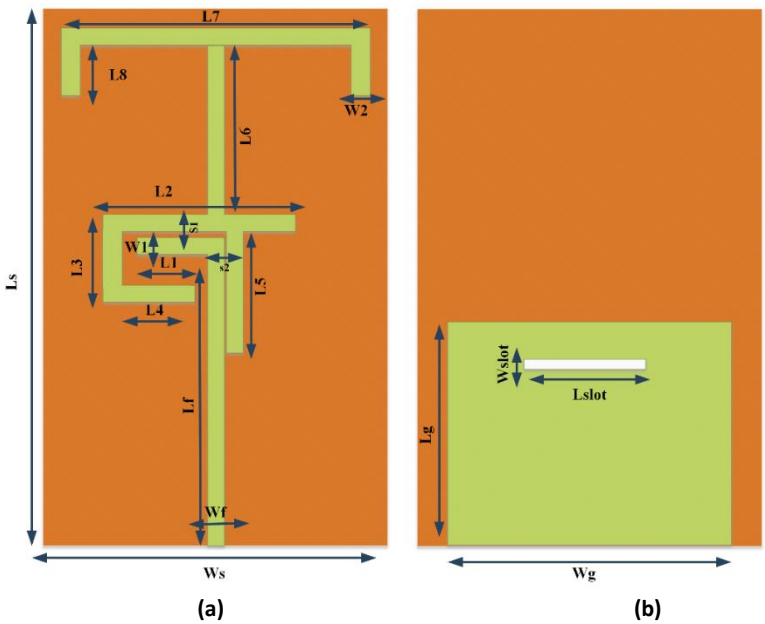


**Figure 2.25 Geometry of the proposed Hexaband Antenna (a) Front view (b) Back View.**

## 2.4.2 Antenna Simulation and Experimental Results

Proposed hexaband antenna simulations were carried out using a commercial electromagnetic time domain finite integration technique (FIT) simulator known as Computer Simulation Technology Microwave Studio CST MWS [34]. Antenna characteristics such as return loss, radiation pattern and gain were calculated. The simulated antenna was realized using LPKF Protomat S100 machine and the fabricated prototype is shown in figure 2.26. The measurements of the prototype were done using Agilent PNA-X Network analyzer (N5245A). Simulated and measured return loss $|S_{11}|$ of the optimized antenna is shown in figure 2.27. The resonances at the required bands are well matched and useable for applications listed in Table 2.5, while the minor difference observed between the two results are due to fabrication losses and substrate permittivity tolerances.

To understand the working part of each monopole on antenna performance, the surface current distributions at the specific frequencies of interest i.e. 900 MHz, 1.8 GHz, 2.45 GHz and 5.8 GHz are shown in figure 2.28. It is observed that the longest monopole radiates for the lowest frequency of interest while the slot in the ground plane is responsible for resonance at the highest frequency. The 3D simulated radiation patterns of the proposed hexaband antenna are shown in

figure 2.29, while the measured radiation polar plots of both the E-field and H-field components are shown in figure 2.30 for the above mentioned frequencies of interest. The maximum measured gain achieved at the 900 MHz, 1.8 GHz, 2.45 GHz and 5.8 GHz are 1.83 dB, 3.17 dB, 3.23 dB and 5.82 dB respectively. The radiation patterns reveal the antenna to be an omni-directional or donut shaped at the lower frequency bands i.e. GSM band however as the frequency tends to increase the gain also increases, hence becoming more directional for the higher frequency bands i.e. WLAN.

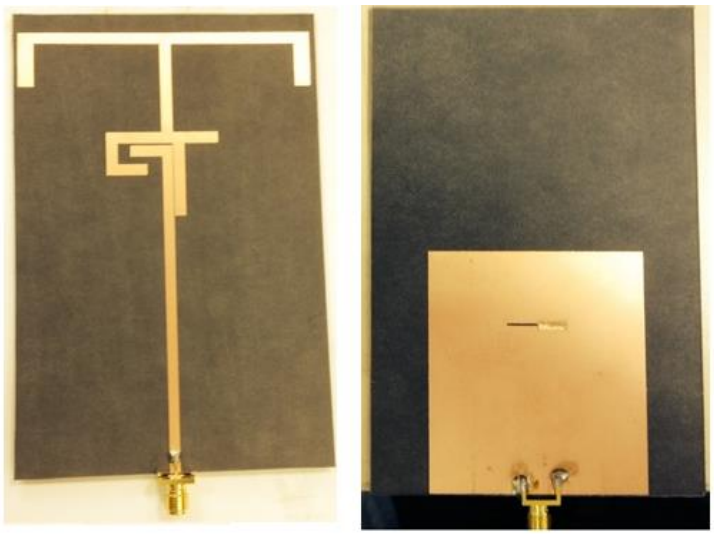

**Figure 2.26 Photograph of fabricated hexaband antenna.**

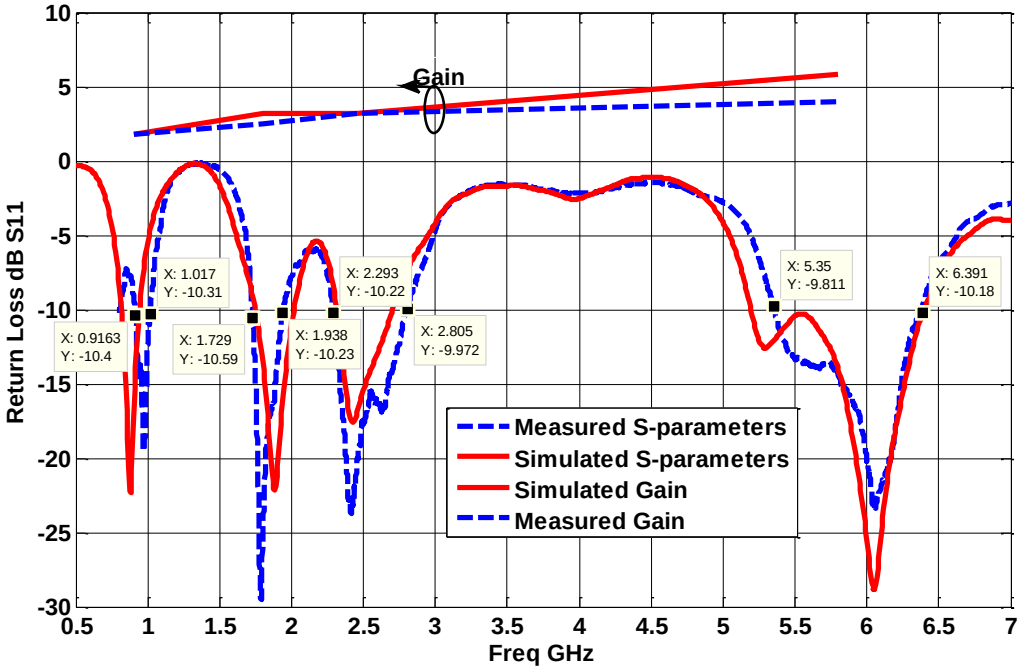


**Figure 2.27 Measured and Simulated $|S_{11}|$ of the proposed hexaband antenna.**

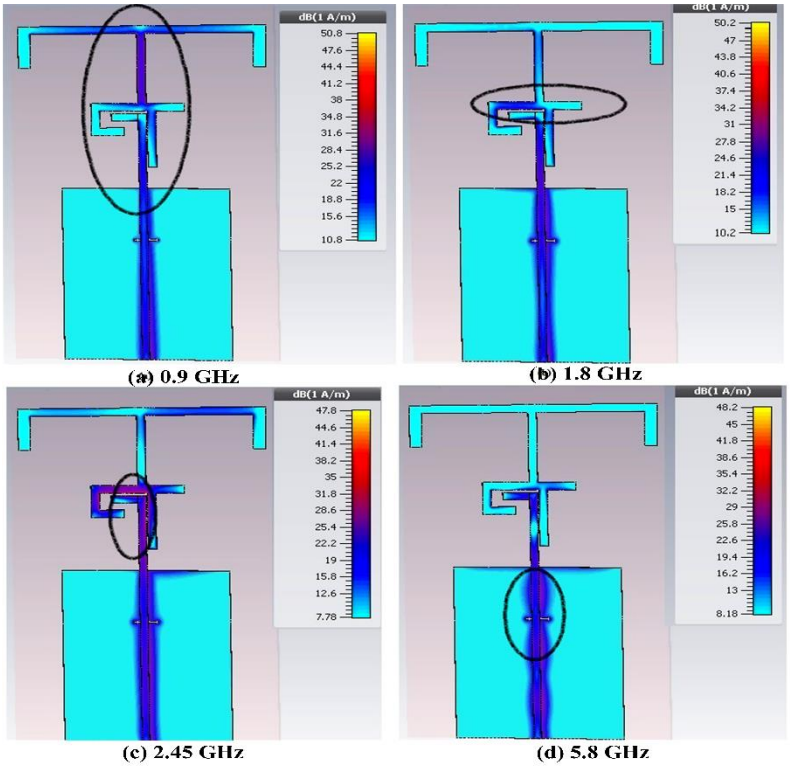


**Figure 2.28 Surface current distributions for the proposed hexaband antenna.**

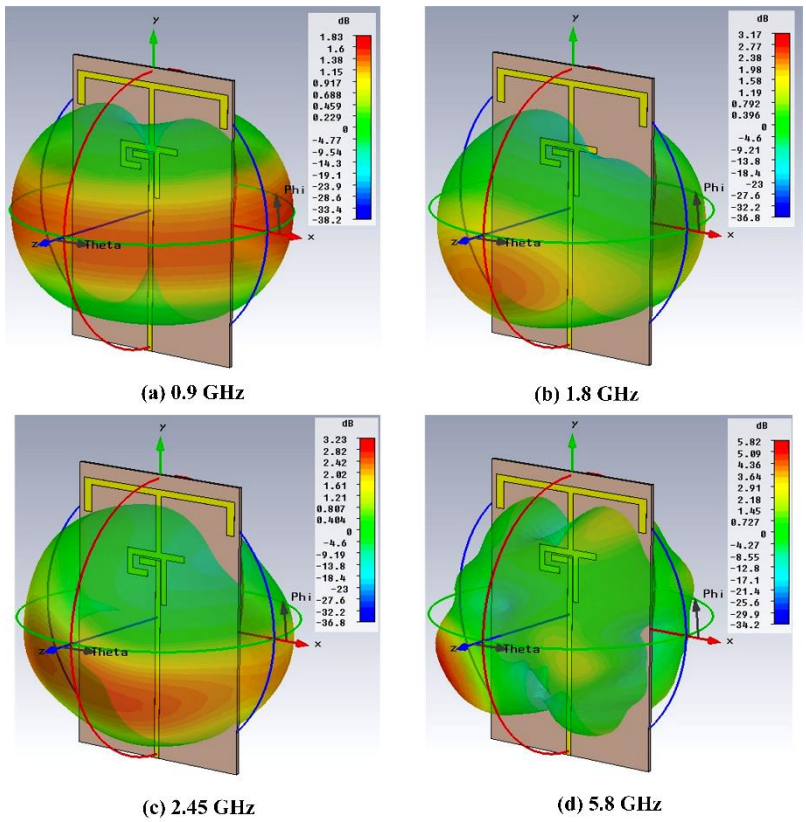


**Figure 2.29 3D gain patterns of proposed hexaband antenna.**

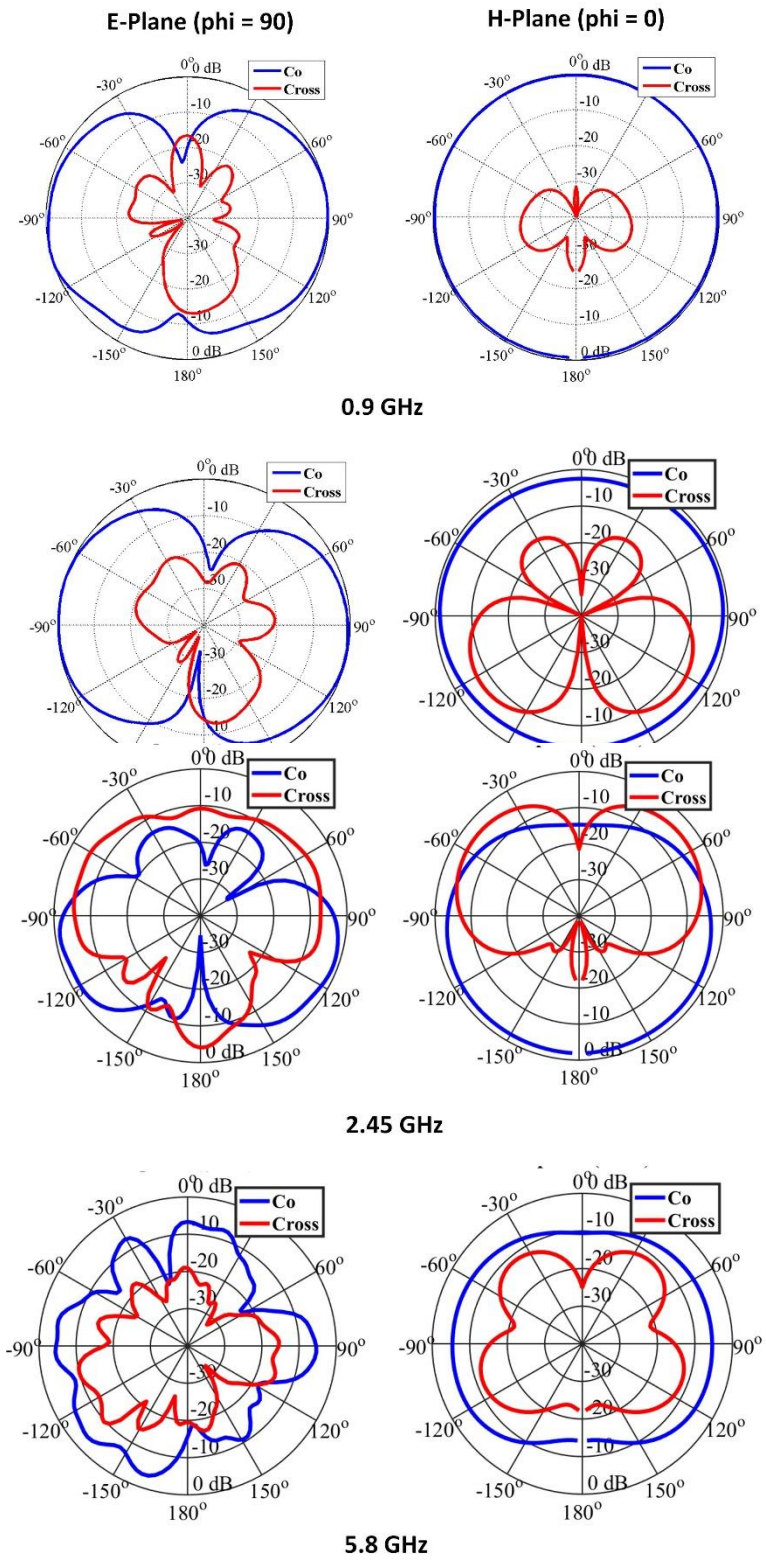


**Figure 2.30 Measured E-Plane and H-Plane radiation patterns of proposed hexaband antenna.**

| Frequency (MHz) | Wireless Applications |
|---|---|
| **870 – 900** | GSM 850 (824-894 MHz) |
| **900-1000** | GSM 900 (880-960 MHz) |
| **1722 – 1880** | DCS (1710-1880 MHz) |
| **1850-1900** | PCS (1850-1900 MHz) |
| **2287 - 2837** | WLAN (2400-2480 MHz) |
| **5713 – 6386** | WLAN (5470-5725 MHz) |

**Table 2.5 Frequency bands supported by hexaband antenna.**

## 2.5 Proposed Multiband Rectifier

In this section a multiband rectifier is presented. The selection of the multiband rectifier is such that it complements the earlier presented hexaband antenna. Rectifier circuit is one of the main components in the energy harvesting rectenna system that converts the available energy into useable output DC voltage. A rectifier must be sensitive to power detection, have good power handling capabilities and consumes low operational power [35]. A conventional single series diode rectifying circuit is shown in figure 2.31 (a). It consists of an impedance matching network for transferring maximum power from the antenna to diode, a rectifying element (schottky diode) to achieve RF-to-DC conversion, a DC filter for smoothing the output DC voltage followed by a load resistor. The antenna receives the RF power which gets attenuated while passing through the impedance matching circuit and the schottky diode. The remaining power is converted into the dc power. The capacitor $C_L$ works as an energy storing device and also acting as a high-pass filter. The single series configuration of figure 2.31 (a) allows only the positive half cycle of the signal to get rectified while the negative half cycle is rejected by the diode. This configuration is not an efficient one because the ambient RF energy received on the antenna has very low power that is not enough to meet the biasing requirements of the schottky diode in order to initiate the rectifying process of the circuit. In addition, the breakdown voltage of the single diode rectifier is limited, which could affect the power handling capability of the circuit. An improved version, which was selected for the presented rectenna design, is called the Cockroft-Walton voltage doubler or Grainacher single stage doubler [36]. Figure 2.31 (b) shows the proposed voltage doubler design. The circuit receives the signal from the antenna, after passing through the matching network with appropriate attenuation. Diode $D_1$ receives the positive half of the signal and stores in capacitor $C_1$ while the negative half of the signal gets rectified by diode $D_2$ with storage happening in capacitor $C_2$. To get maximum or twice the output voltage, the energy stored in capacitor $C_2$ can be transferred to capacitor $C_1$ thus generating twice the output voltage across capacitor $C_1$ at the load with a series configuration. This increases the breakdown voltage of the rectifier; hence the theoretical maximum conversion efficiency of the rectifier is also improved.

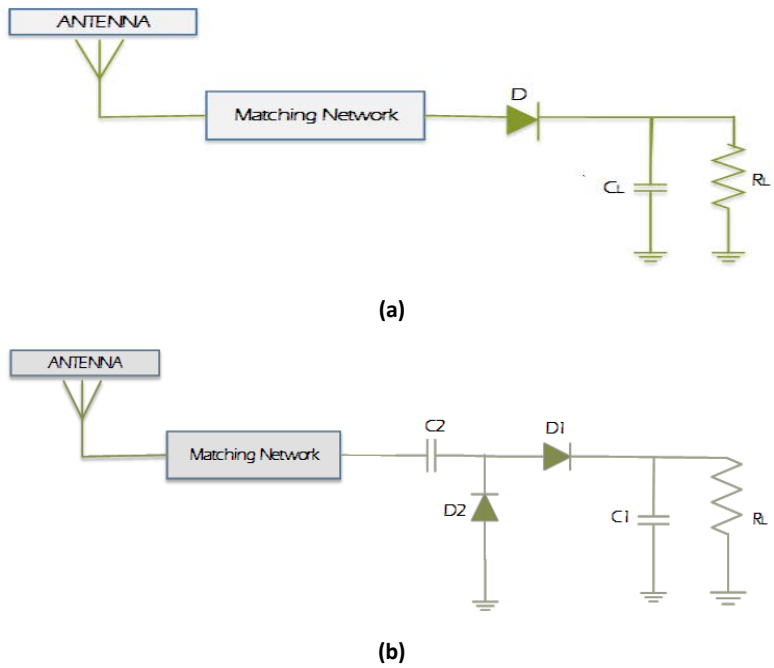


**Figure 2.31 Rectifier circuit configurations : (a) Conventional Single Series setting, (b) Voltage Doubler setting.**

## 2.5.1 Schottky Diode Selection

In a rectifier circuit, the selection of the diode determines the overall performance of the circuit which leads to a better RF-to DC conversion efficiency. A zero biased schottky diode is normally used for rectifier designs that provides better sensitivity at low input power levels (-50 dBm to 0 dBm). Different kinds of schottky diodes have been proposed in literature [36-38] with their efficient rectifier circuit designs but the one that was suited to this research work for multiband resonance was purchased from Avago's HSMS 2860 series schottky diode [39]. This dide belongs to the family of DC biased detector diodes designed to operate well in the frequency range of 915 MHz to 5.8 GHz. The applications it can support vary from RFID tag applications, signal modulation and demodulation, RF to DC conversion and voltage multiplication. The diode comes in various sizes and packages as per need of the application in terms of cost effectiveness and durability. Agilent's manufacturing techniques assure the highest degree of match between two or more diodes when mounted on a surface package. The three important parameters that determine the power conversion efficiency of the diode are: breakdown voltage $(V_{br})$, which limits the power handling capability of the rectifier circuit, the series resistance $(R_s)$, which limits the efficiency; and zero-bias junction capacitance $(C_{j0})$, that affects how harmonic currents oscillate through the diode. Considering these specifications, our selected schottky diode HSMS 286B had the values of $R_s$ =6 Ω, low value of $C_{j0}$ = 0.18 pF and $V_{br}$ = 7 V and a forward biasing voltage of $V_f$ = 250 mV. This diode also has fast switching characteristics necessary for high frequency input signals and a low-cutoff voltage to operate at a low RF input power.

### 2.5.2 Impedance Matching

Another important section in the rectifier design is the impedance matching between the antenna and the rectifier (Schottky diode) element as shown in figure 2.31. The non-linearity property of schottky diode makes it difficult to perfectly match the impedance among the elements. The schottky diode will have different input impedance as it varies with the varying frequency, input power levels and loads. In order to evaluate the diode characteristics in terms of impedance matching, Advanced Design System (ADS) 2014 from Agilent Technologies is utilized. The equivalent model of the diode, considering parasitic and packaging effects is constructed from the respective PSPICE values in the data sheet [39]. The Smith Chart tool provided in ADS is a good starting point in matching the circuit elements with the nonlinear diodes. Techniques on practical measurements were also studied in determining the input impedance of the schottky diode at various power levels centered on our frequency of interest [40].

### 2.5.3 Complete Rectifier in ADS Simulator

In order to design a multiband rectifier, that can be impedance matched and connected to the proposed multiband antenna, an Advanced Design System (ADS) simulation at input power level of 0 dBm was initiated to find out the input impedance of voltage doubler at various frequencies. Initially a voltage doubler rectifier, having two single pair schottky diodes (HSMS 286B) with a load of 5 KΩ, was analyzed in terms of its input impedance for various frequencies of interest i.e. (0.9 GHz, 1.8 GHz, 2.45 GHz and 5.8 GHz) by generating multiple tones. Figure 2.32 shows the voltage doubler design with multiple tones generation port. The circuit design also has various controllers such as harmonic balance controller *(HB)*, large scale S-parameters *(LSSP)*, input impedance at input port *($Z_{in}$)* and finally S-parameters controller to define the frequency range. The Harmonic balance *(HB)* is a frequency-domain analysis technique for simulating distortion in nonlinear circuits and systems specially the components used in RF and microwave domain of the electromagnetic spectrum. HB simulation works by excitation and enabling the multiple tones available among circuits for frequency conversion and avoids inter signal interference among harmonics generated by the circuit, the original signal and its copies. Straight forward frequency domain analysis is done with HB simulations on any given circuit. The current flows in the circuit as it passes from one node to the other node and nonlinear components. This analysis is done in the time domain that is conversion into the frequency domain for HB analysis using Fourier transform. Another parameter associated with the HB is the LSSP simulation controller available in the simulation-LSSP palette of the advanced design system (ADS) simulator. It computes S-parameters for nonlinear circuits across various frequencies by working in coherence with the HB simulations.

From figure 2.33 the input impedance of voltage doubler circuit for various frequencies of interest was noted. Table 2.6 list the input impedance for all the frequencies. The next step was to match the input impedance of the voltage doubler with the impedance of relevant frequencies of interest generated by the multiband antenna. Smith chart tool utility provided in ADS was used to achieve the matching. The impedance matching circuit for the rectifier is designed on the basics

of L-C matching network [41] to match the rectifier to antennas 50 Ω impedance for the specific frequency of interests. The L-C network acts as a filter blocking the rest of the hexaband frequencies. The values of C and L in the matching circuit for each frequency is shown in figures presented in following four cases. The voltage doubler circuit is placed after the matching network for each frequency with capacitor values being 120 pF and load resistor of 5 KΩ.

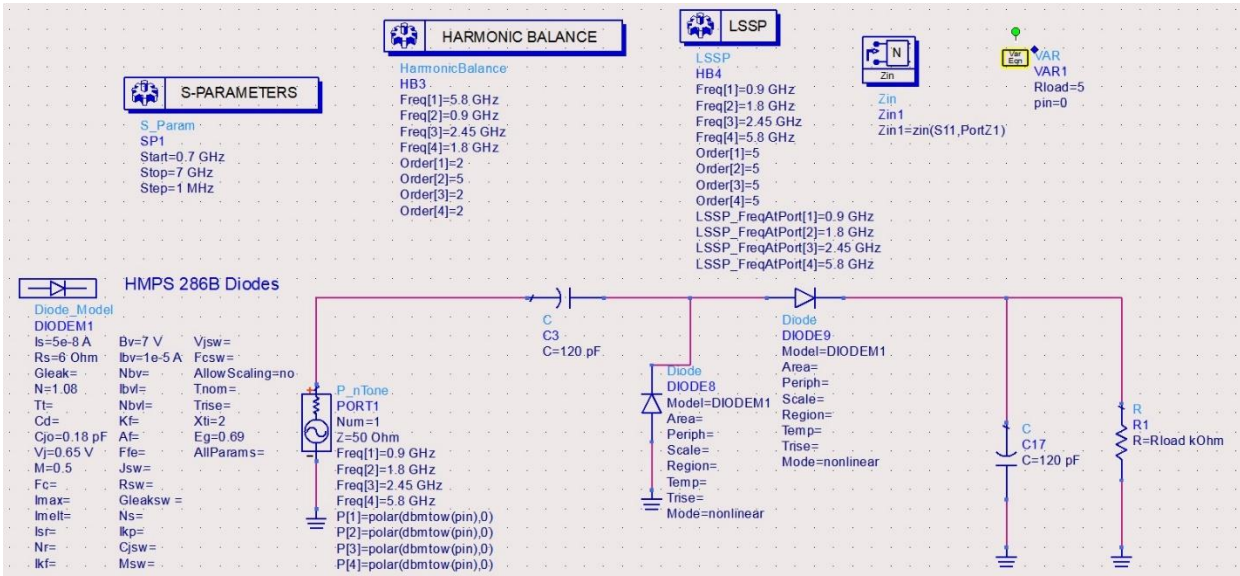


**Figure 2.32 Voltage doubler design with multiple tones**

| Frequency (GHz) | Input Impedance of Voltage Doubler ($Z_{in}$) |
|---|---|
| 0.9 | 3.874- j458 Ω |
| 1.8 | 3.217- j246 Ω |
| 2.45 | 3.117- j177 Ω |
| 5.8 | 3.021- j76 Ω |

**Table 2.6 Input impedance of voltage doubler at various frequencies.**

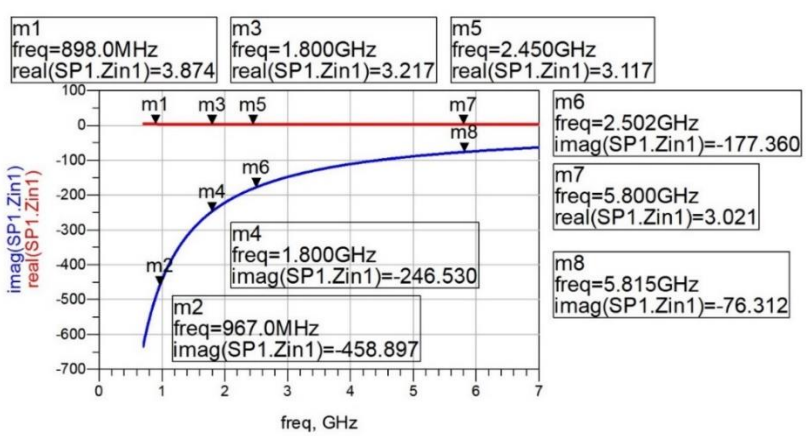


**Figure 2.33 Input impedance of voltage doubler for various frequencies**

**Case-1:** Matching design and results at 0.9 GHz band.

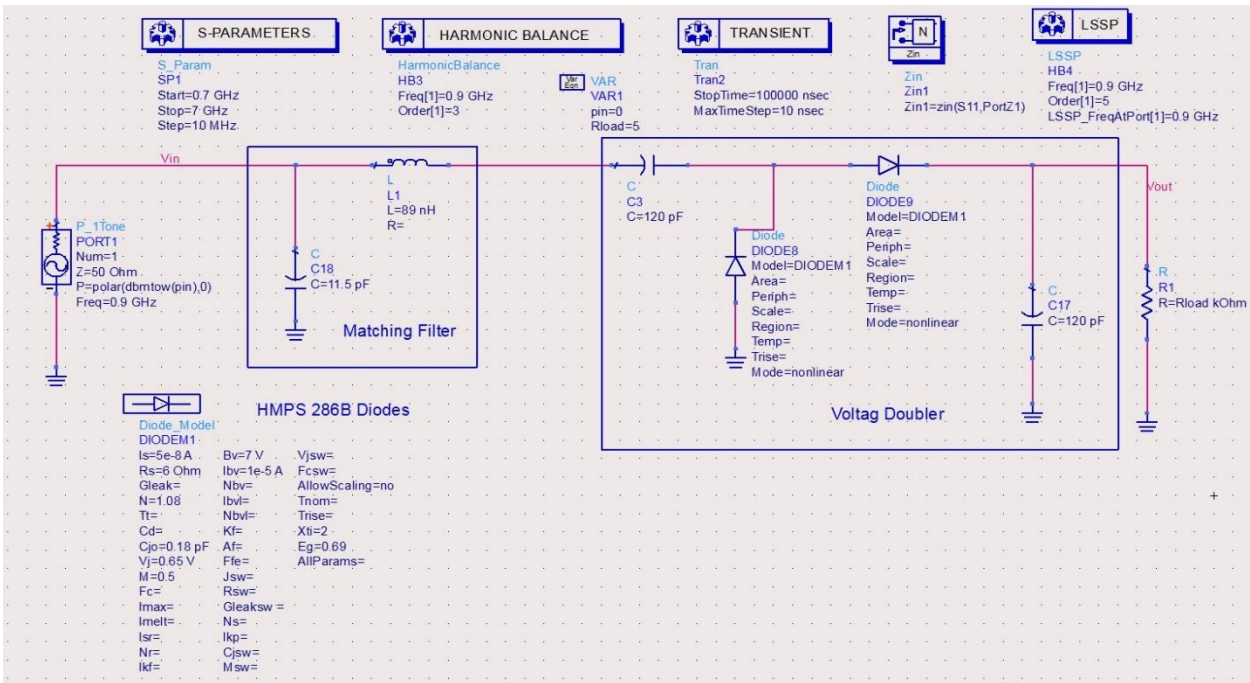


**Figure 2.34 (a) Matching circuit at 0.9 GHz frequency.**

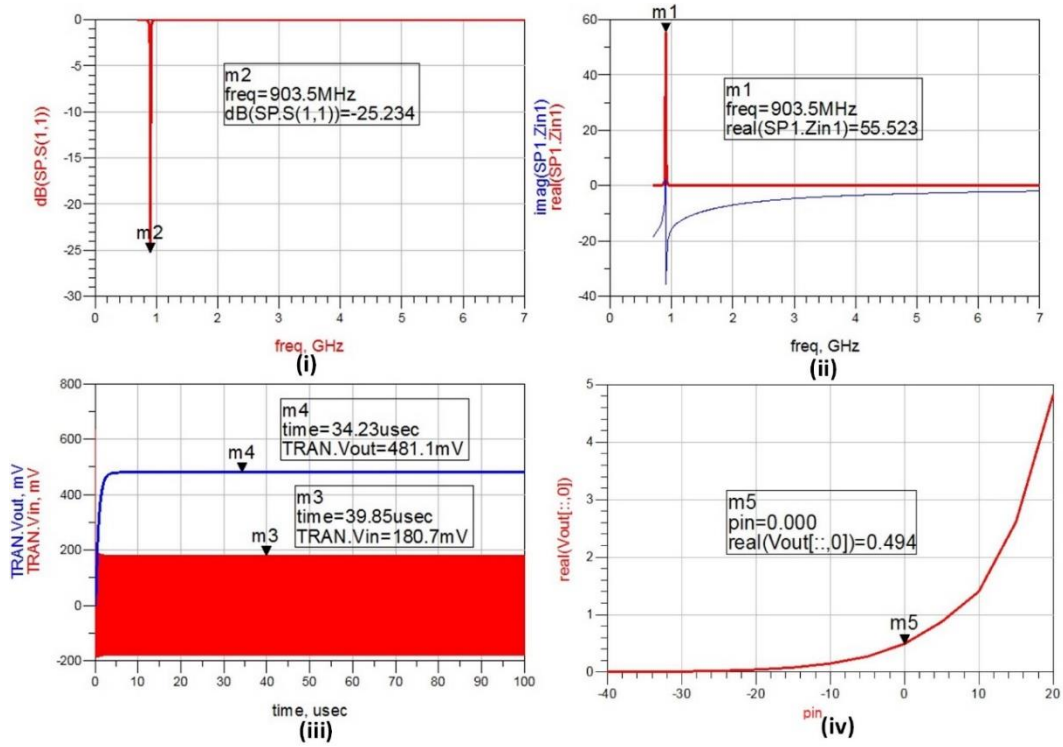


**Figure 2.34 (b) Results at 0.9 GHz frequency; i) resonance at 0.9 GHz, ii) Impedance matched around 50 Ω, iii) Voltage doubled at the output of the circuit, iv) DC output voltage at input power levels.**

**Case-2:** Matching design and results at 1.8 GHz band.

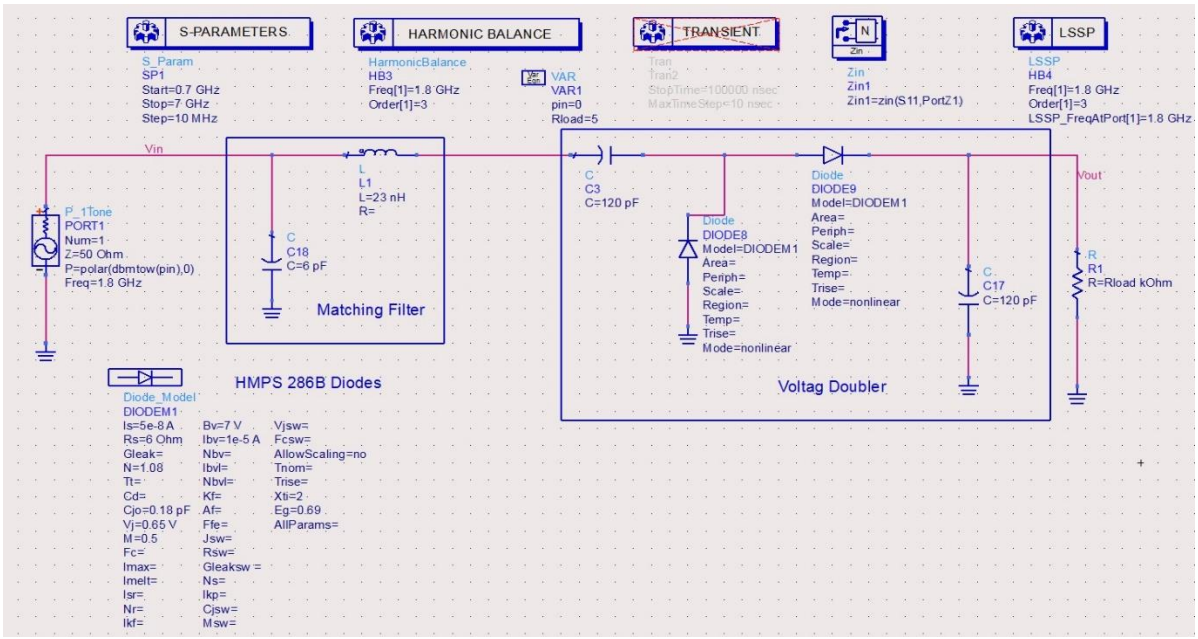


**Figure 2.35 (a) Matching circuit at 1.8 GHz frequency.**

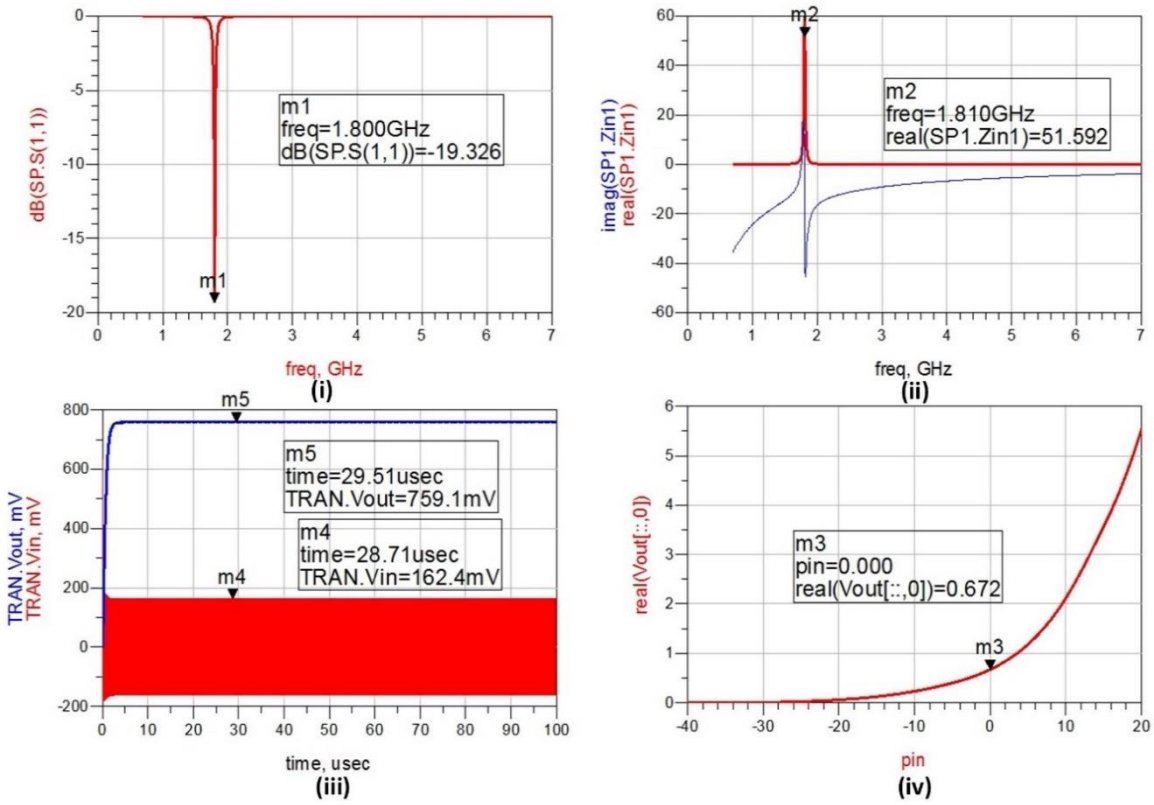


**Figure 2.35 (b) Results at 1.8 GHz frequency; i) resonance at 1.8 GHz, ii) Impedance matched around 50 Ω, iii) Voltage doubled at the output of the circuit, iv) DC output voltage at input power levels.**

**Case-3:** Matching design and results at 2.45 GHz band.

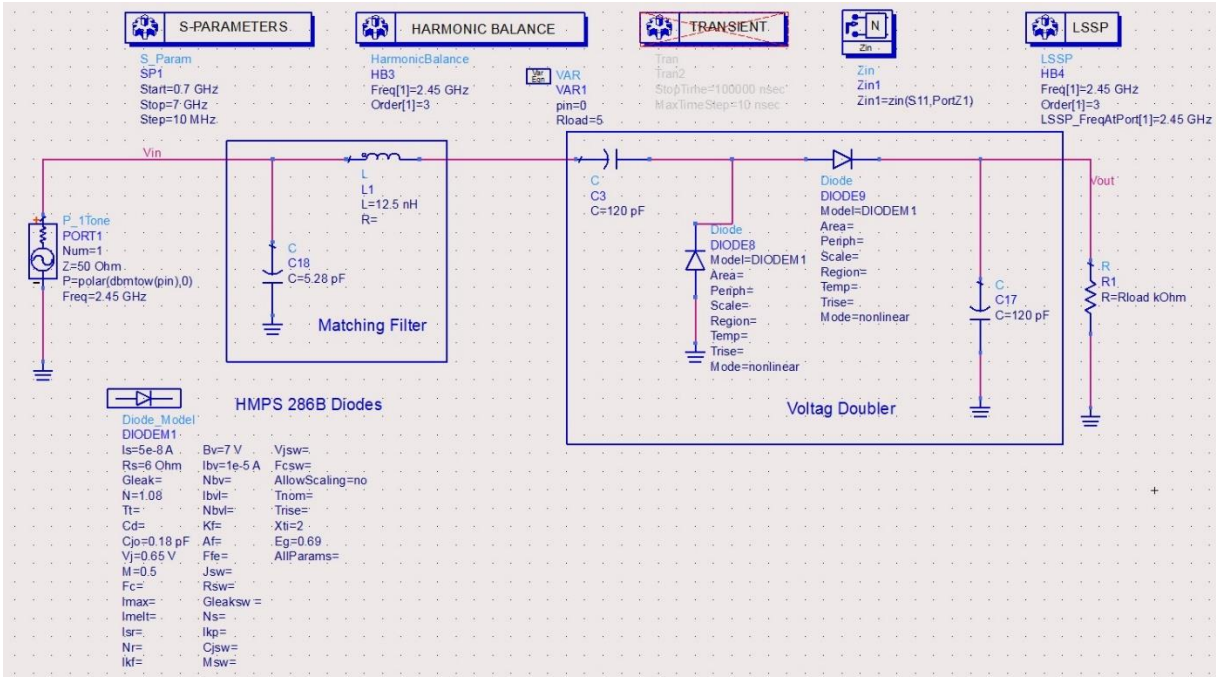


**Figure 2.36 (a) Matching circuit at 2.45 GHz frequency.**

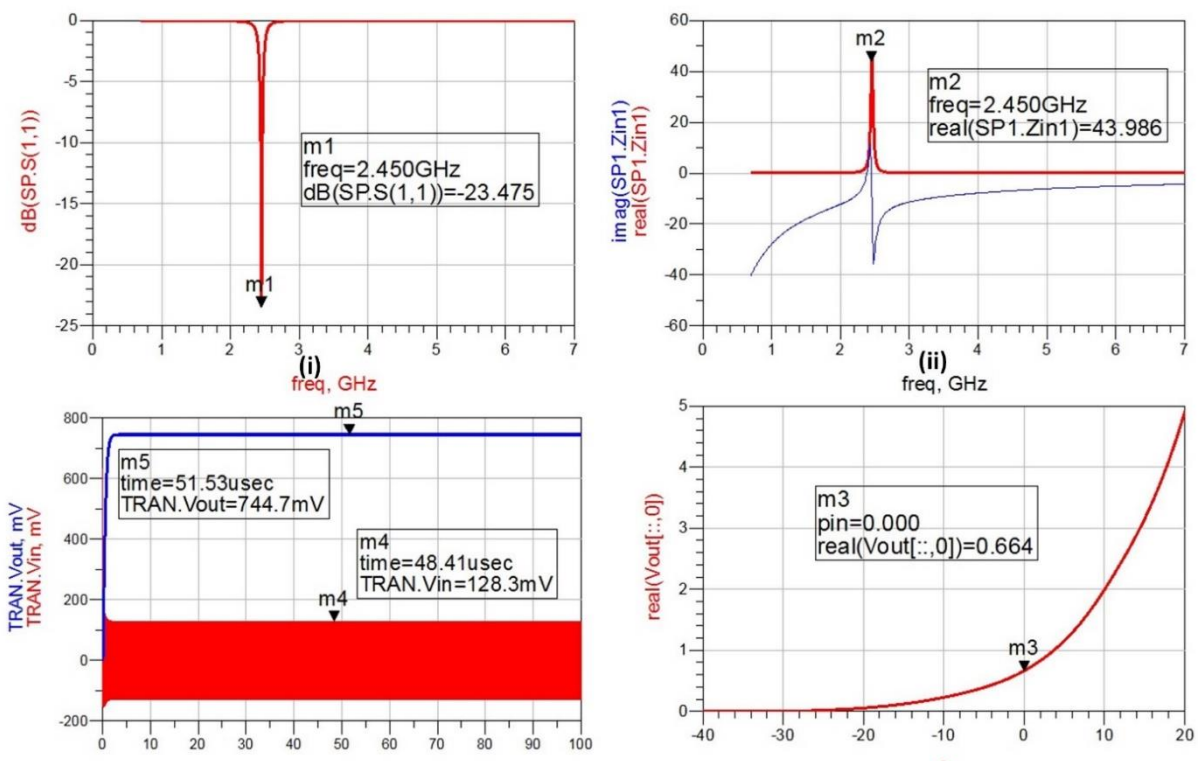


**Figure 2.36 (b) Results at 2.45 GHz frequency; i) resonance at 2.45 GHz, ii) Impedance matched around 50 Ω, iii) Voltage doubled at the output of the circuit, iv) DC output voltage at input power levels.**

**Case-4:** Matching design and results at 5.8 GHz band.

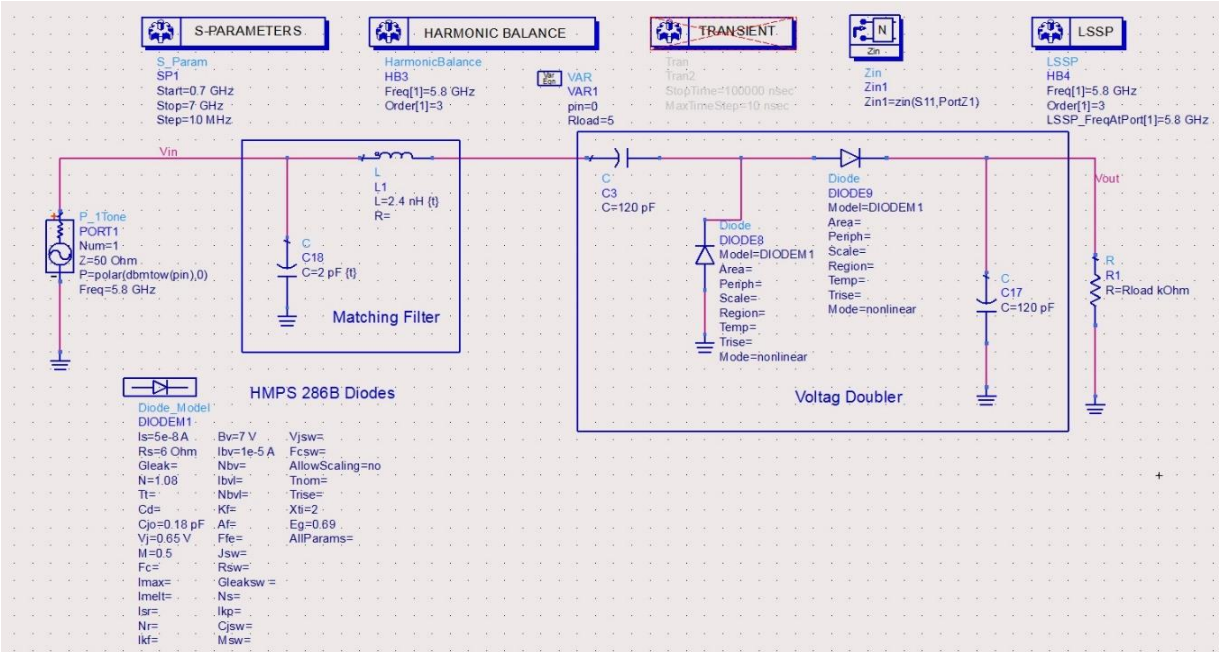


**Figure 2.37 (a) Matching circuit at 5.8 GHz frequency.**

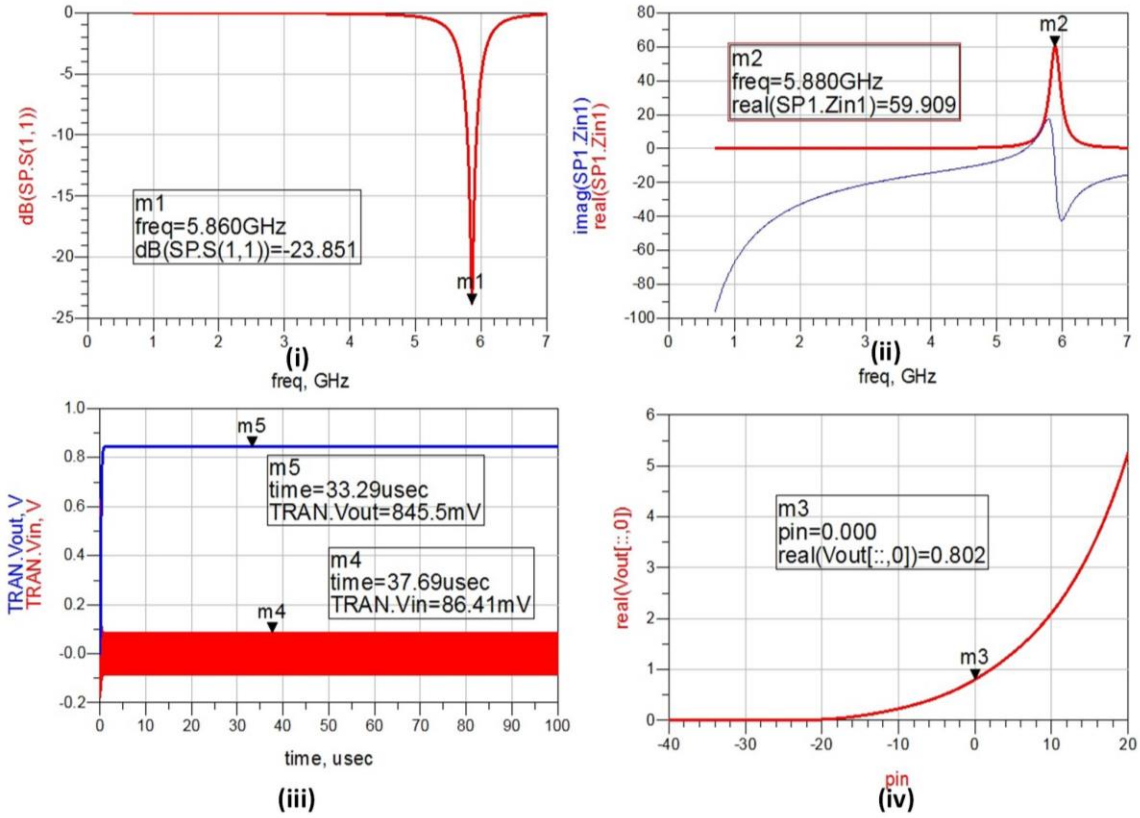


**Figure 2.37 (b) Results at 5.8 GHz frequency; i) resonance at 5.8 GHz, ii) Impedance matched around 50 Ω, iii) Voltage doubled at the output of the circuit, iv) DC output voltage at input power levels.**

All of the four cases (figure 2.34-2.37) were then merged into a single design to work as a multiband rectifier. The value of the load resistor also improves the output voltage for these individual matched rectifier designs. Figure 2.38 (a-d) shows linear relationship between the load resistor and the DC output voltage at all the frequencies. Figure 2.39 shows the whole rectifier design based on lumped components and voltage doubler with LC values listed in Table 2.7. The design is matched with the voltage doubler at all the relevant frequencies. Figure 2.40 shows the simulated matched results. Next, the multiband rectifier was to be realized on a printed circuit board. Since lumped components introduce losses into the circuit, the design was converted from lumped based into distribute microstrip based topology. Figure 2.41 shows the distributed components design with optimized values for transmission lines width and lengths. Computer simulation tool (CST-MWS) was used to design the 3D design of the distributed multiband rectifier. The design geometry is shown in figure 2.42 with the voltage doubler components and schottky diodes. Printed circuit boards (PCB) of the multiband rectifier was designed on Rogers substrate RT-5880 with permitivity 2.2, loss tangent of 0.0009 at 10 GHz and thickness of 1.6 mm. Realized multiband rectifier is shown in figure 2.43 with measured results comparison with simulation in figure 2.44. The multiband rectifier is resonating in the bands of interest as per taken from the results of the proposed hexaband antenna in the previous section.

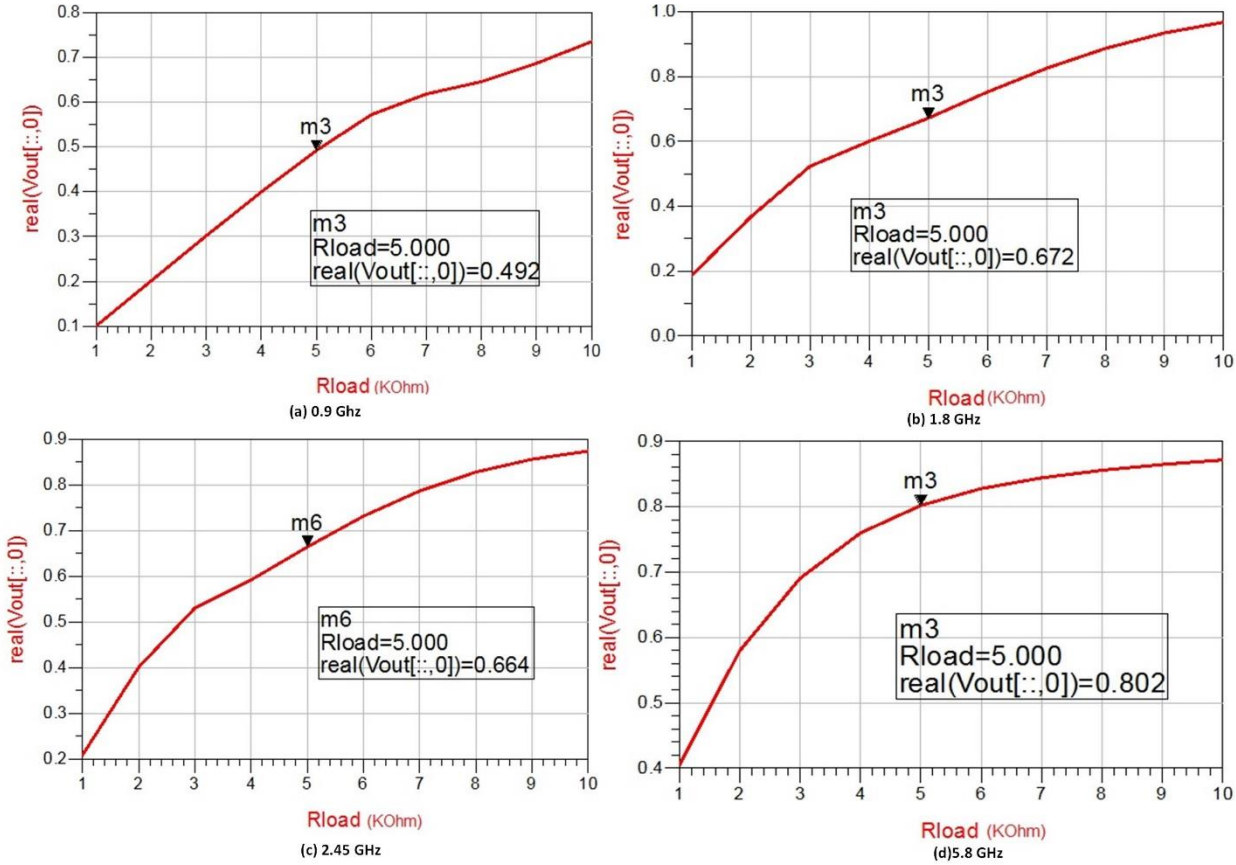


**Figure 2.38 $R_{load}$ vs DC output voltages at different center frequencies.**

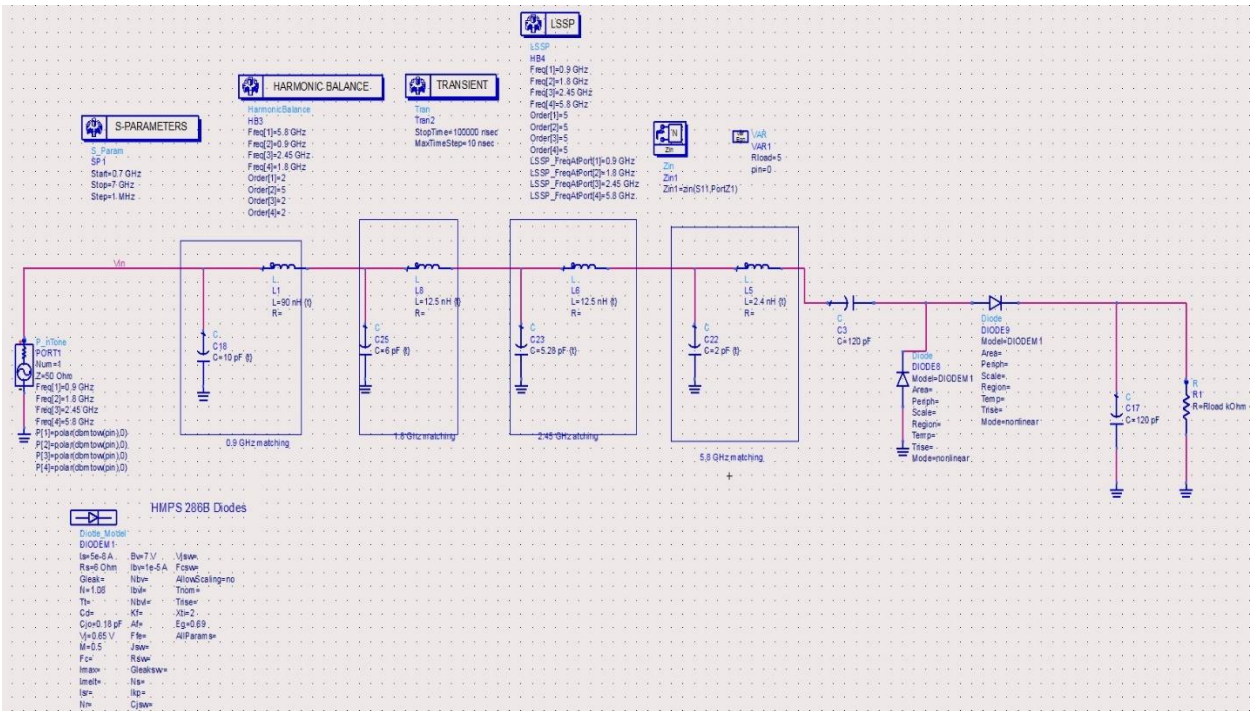


**Figure 2.39 Multiband rectifier based on lumped components LC network.**

| Frequency (GHz) | Inductor (nH) | Capacitor (pF) |
|---|---|---|
| 0.9 | 90 | 10 |
| 1.8 | 12.5 | 6 |
| 2.45 | 12.5 | 5.28 |
| 5.8 | 2.4 | 2 |

**Table 2.7 LC values for matching network at various frequencies.**

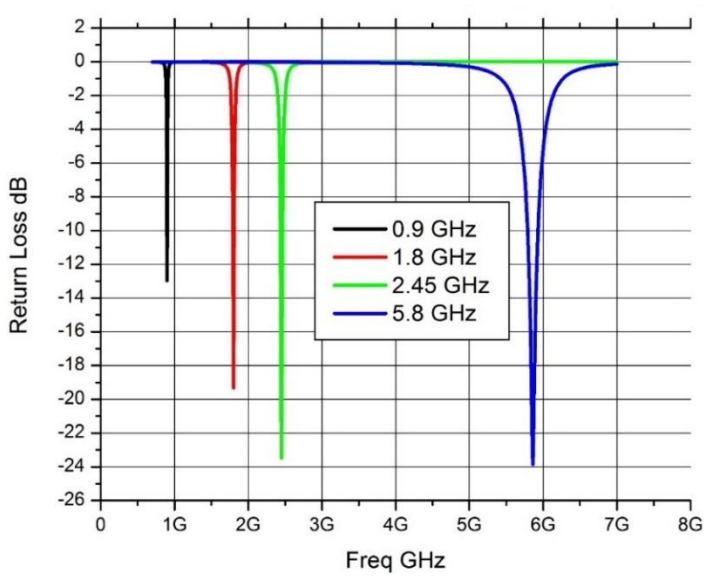


**Figure 2.40 Simulated matched results of multiband rectifier using lumped components.**

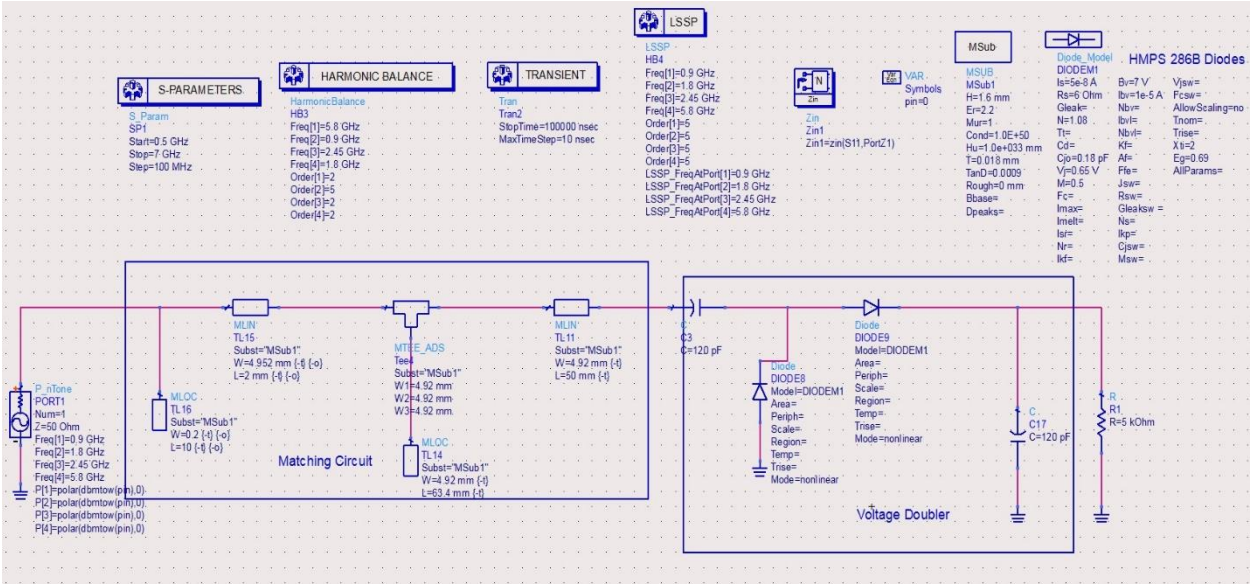


**Figure 2.41 Multiband rectifier based on distributed components.**

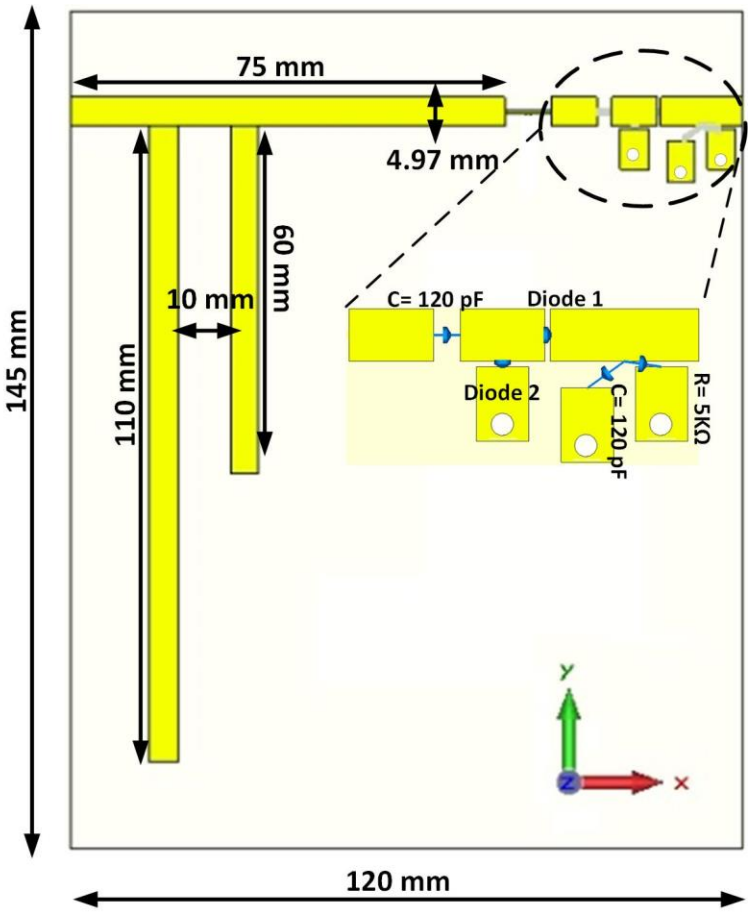


**Figure 2.42 Geometric design of multiband rectifier in CST-MWS with zoomed in circuit elements.**

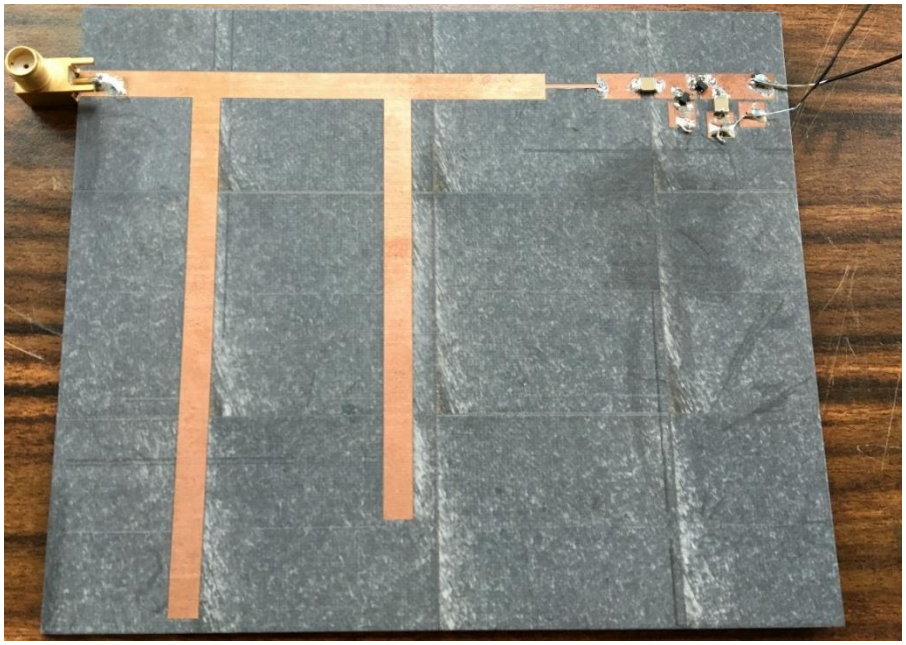

**Figure 2.43 Realized multiband rectifier on RT-5880 substrate.**

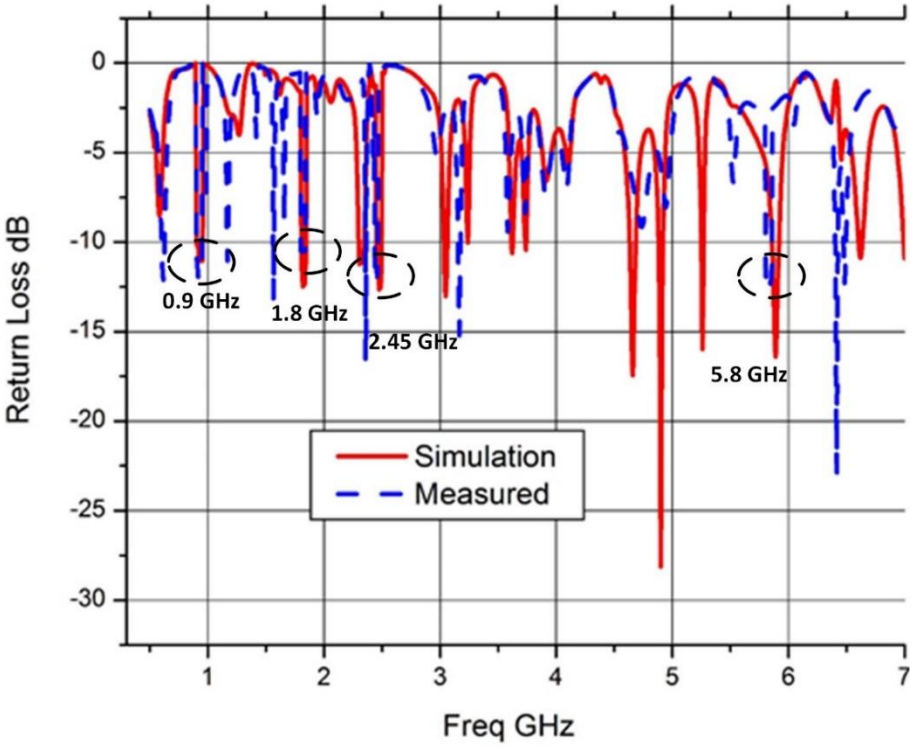


**Figure 2.44 Multiband rectifier measured s-parameters.**

For each four cases, the performance of the multiband rectifier in terms of output DC voltage and efficiency is shown in figure 2.45 (a-d). The RF source was taken from Rohde & Schwarz SMB 100A signal generator. The input power was varied from -20 to 20 dBm. The results were noted for all the frequencies at 0 dBm input power. At 0.9 GHz, the rectifier produced output voltage of 1.42 V with 42 % efficiency. At 1.8 GHz, the rectifier managed to produce output voltage of 1.5 V and efficiency of 45 %. At 2.45 GHz, the output voltage was 0.2 V with 2% efficiency and at 5.8 GHz, the output voltage was 0.5 V with efficiency of 0.3 %. It was observed that the output voltage increased with increasing input power and so did the efficiency. But the good thing was that the rectifier was even able to produce acceptable output voltages even when the power was below -10 dB, especially in the case of 0.9 GHz and 1.8 GHz frequency bands.

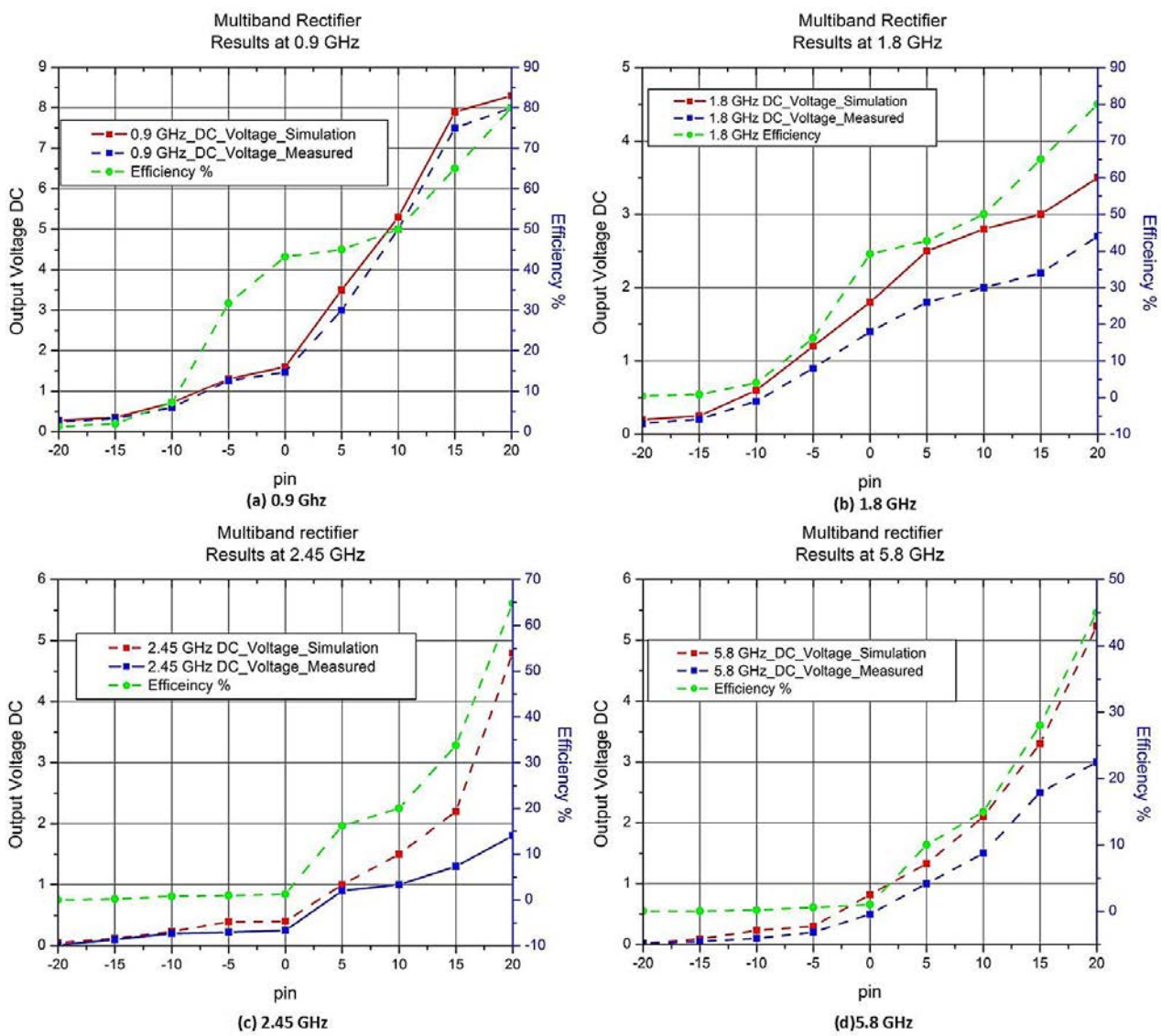


**Figure 2.45 Multiband Rectifier measured voltages and efficiency a) 0.9 GHz b) 1.8 GHz c) 2.45 GHz d) 5.8 GHz.**

## 2.6 Experimental Investigation of Rectenna System

In this section the hexaband antenna and the multiband rectifier are integrated together. The performance of the whole rectenna system is analyzed in terms of output DC voltage and efficiency at the input power level of 0 dBm.

A typical lab setup was adopted for the rectenna prototype measurement. Initially a spectrum analyzer was used to note down the received power levels from the ambient lab environment on the hexaband antenna at specific frequencies of interest i.e. 0.9 GHz, 1.8 GHz, 2.45 GHz and 5.8 GHz. Figure 2.46 shows the setup which consists of a Rhode & Schwarz RF signal generator, Anritsu vector network analyzer ZVA 67 working from 10 MHz to 67 GHz and a portable Anritsu MS2038C spectrum analyzer. The distance between the devices was kept at 1 meter. The source power from the generator was kept at 0 dBm. It was observed that the received power levels improved when the input power was increased from 0 dBm to 20 dBm. The power level received on the hexaband antenna are listed in Table 2.8.

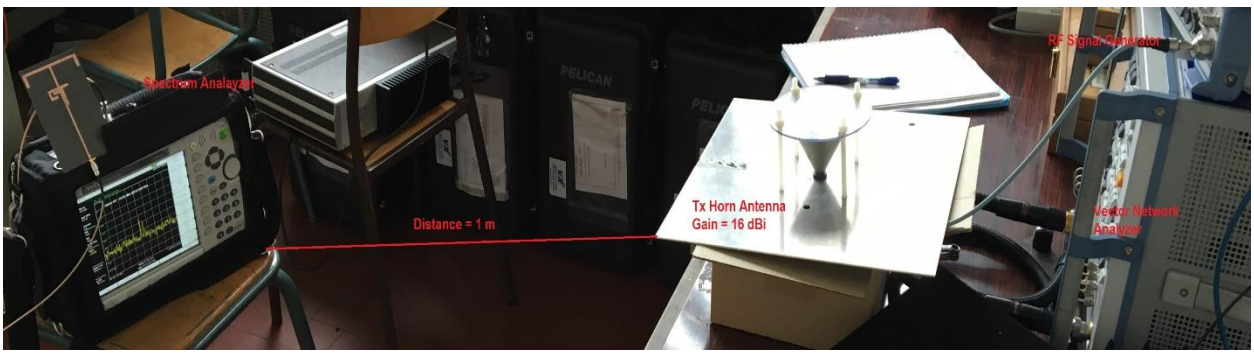


**Figure 2.46 Power levels received on the hexaband antenna measured via a spectrum analyzer.**

| Frequency GHz | Power Received dBm @ Pin = 0 dBm | Power Received dBm @ Pin = 10 dBm | Power Received dBm @ Pin = 20 dBm |
|---|---|---|---|
| **0.9** | -40 | -20 | -15 |
| **1.8** | -44 | -22 | -17 |
| **2.45** | -40 | -25 | -18 |
| **5.8** | -60 | -20 | -16 |

**Table 2.8 Power received on the hexaband antenna with various input power levels pin.**

Next, the hexaband antenna and the multiband rectifier were connected together to form a complete rectenna system. Figure 2.47 shows the integrated design while the experimental setup is shown in figure 2.48. The RF signal generator was used to provide power from 0 dBm to 20 dBm which was received by the hexaband antenna, connected to the multiband rectifier, at a distance of 1 meter from the source horn antenna (gain of 16 dBi). The output voltage (DC) was noted with the help of a digital multi-meter. Table 2.9 lists the output voltage produced at particular frequencies of interest with varying power levels. Figure 2.49 shows rectennas output voltage and efficiency at various power levels for different frequencies of interest.

**Figure 2.47 Hexaband Antenna and multiband rectifier connected together as a rectenna system.**

**Figure 2.48 Experimental setup of the rectenna system.**

| Frequency GHz | Pin (dBm) | Output Voltage (V) |
|---|---|---|
| **0.9** | 0 | 0.024 |
| | 10 | 0.13 |
| | 20 | 0.5 |
| **1.8** | 0 | 0.004 |
| | 10 | 0.15 |
| | 20 | 0.63 |
| **2.45** | 0 | 0.0003 |
| | 10 | 0.0004 |
| | 20 | 0.03 |
| **5.8** | 0 | 0.002 |
| | 10 | 0.0028 |
| | 20 | 0.03 |

**Table 2.9 Output voltage produced at various frequencies as per input power levels.**

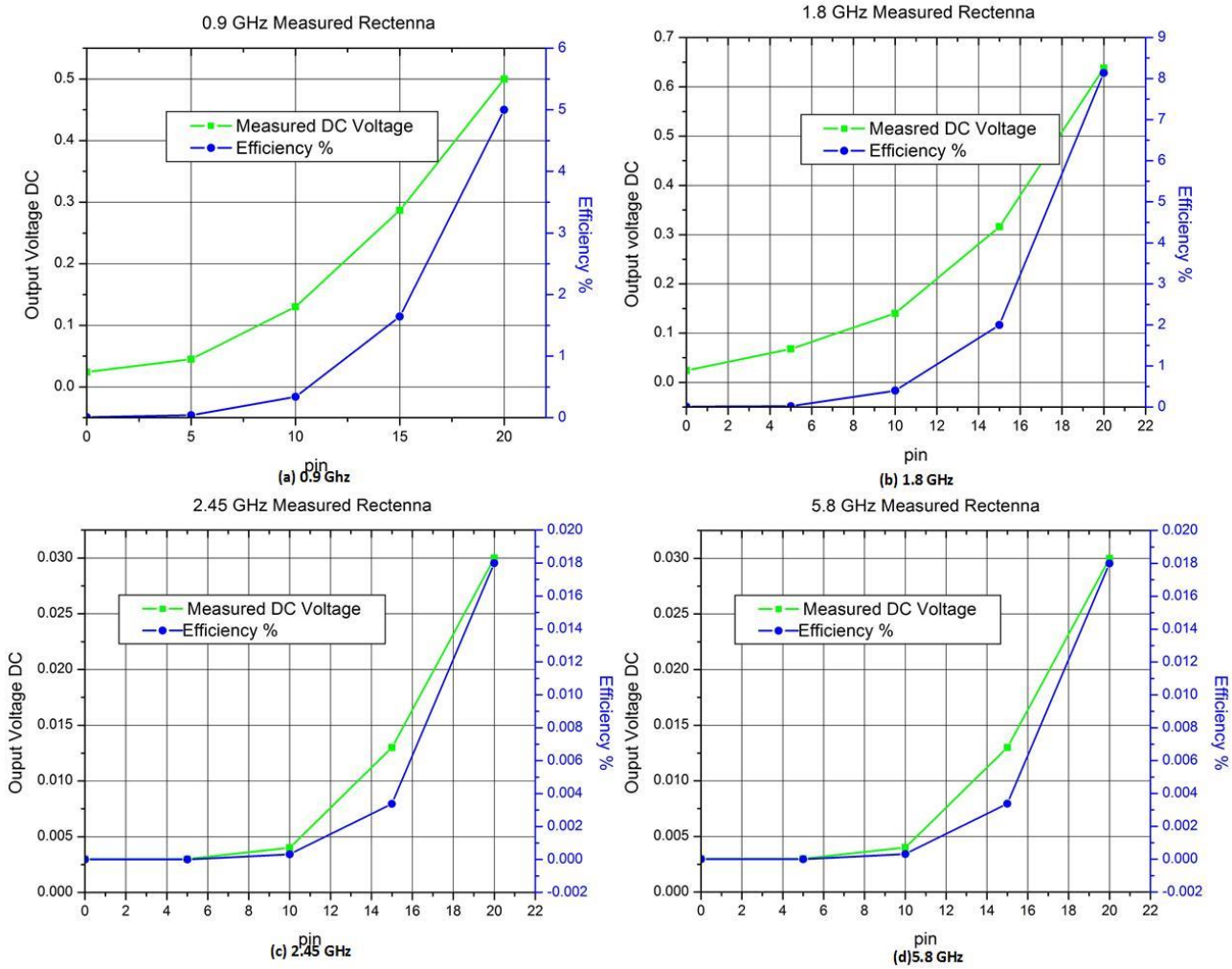


**Figure 2.49 Experimental results of output voltages and efficiency on rectenna at various frequencies.**

It was observed from the readings in Table 2.9 and figure 2.50 that when the power from the source was set at 0 dBm, minimum output voltages (0.003-0.024 V) were produced by the rectenna at the frequency bands of interest i.e. 0.9, 1.8, 2.45 and 5.8 GHz, and when the power source was at its maximum i.e. 20 dBm, the rectenna produced maximum output voltages ranging from (0.5-0.63 V) at desired frequency bands. It was expected that the power received on the rectenna was going to be in the -20 to -10 dBm range, the rectifier design is such that it is able to convert only a portion of this received power into output voltage, as it has been already verified by the independent multiband rectifier results in the previous section. In order to increase the output voltage, as per minimum power received, additional voltage doubler circuits can be added in cascade to the rectifier design. This will help improve the efficiency and output voltages of the proposed rectenna system.

## 2.7 Summary and Conclusion

In this chapter an energy harvesting rectenna was presented. The main objective was to get an understanding of how the RF energy harvesting technology works. In principle, a RF rectenna consists of a receiving antenna and a rectifier circuit made with schottky diodes. In this work, a hexaband antenna based on monopole microstrip technology was proposed and presented. The antenna was able to resonate in the GSM and WLAN bands also covering the LTE, CDMA and DCS bands. The gain of the antenna was omni directional in most of the bands while getting directional as the frequency increased i.e. at WLAN band. Measured results showed good agreement with the simulation. Next, a multiband rectifier was proposed. The rectifier was able to convert the received RF power into output voltage DC in the bands of interest i.e. GSM and WLAN. The rectifier alone produced output voltages as low as 0.2 V to a maximum of 8 V within the range of -20 to 20 dBm. Finally the whole rectenna system was observed in the lab environment. The rectenna produced an output voltages in the range of 0.024 V to 0.63 V when the input power was varied form 0 dBm to 20 dBm at a distance of 1 meter.

# Bibliography


[1] R. Vullers, R. van Schaijk, I. Doms, C. Van Hoof, and R. Mertens, "Micropower energy harvesting," *Solid State Electron.*, vol. 53, pp. 684-693, 2009.

[2] K. Sangkil, R. Vyas, J. Bito, K. Niotaki, A. Collado, A. Georgiadis, et al., "Ambient RF Energy-Harvesting Technologies for Self-Sustainable Standalone Wireless Sensor Platforms," *Proceedings of the IEEE*, vol. 102, pp. 1649-1666, 2014.

[3] Lu, Xiao, Ping Wang, Dusit Niyato, Dong In Kim, and Zhu Han. "Wireless charging technologies: Fundamentals, standards, and network applications." *IEEE Communications Surveys & Tutorials* vol.18, no. 2, pp.1413-1452, 2016.

[4] Bi, Suzhi, Chin Keong Ho, and Rui Zhang. "Wireless powered communication: Opportunities and challenges." *IEEE Communications Magazine, vol.* 53.4,pp. 117-125, 2015.

[5] Dinis, H., I. Colmiais, and P. M. Mendes. "A multiantenna approach to maximize wireless power transfered to implantable devices." *Applied Computational Electromagnetics Society Symposium-Italy (ACES),*pp.1-2*,* 2017.

[6] Assimonis, Stylianos D., Spyridon-Nektarios Daskalakis, and Aggelos Bletsas. "Sensitive and efficient RF harvesting supply for batteryless backscatter sensor networks." *IEEE Transactions on Microwave Theory and Techniques*, vol. 64.4, pp.1327-1338, 2016.

[7] Shariati, Negin, et al. "Multi-service highly sensitive rectifier for enhanced RF energy scavenging." *Scientific reports, vol*. 5, pp. 9655, 2015.

[8] Bai, J., Fan, M., Yang, J., Sun, Y., & Phillips, C. "Smart Energy Harvesting Routing Protocol for WSN based E-Health Systems", *In Proceedings of the 2015 Workshop on Pervasive Wireless Healthcare,* pp. 23-28, 2015.

[9] Muncuk, U, "Design optimization and implementation for RF energy harvesting circuits", (Doctoral dissertation, Northeastern University), 2012.

[10] Di Marco, P., et al. "Dual band harvester architecture for autonomous remote sensors." *Sensors and Actuators A: Physical*, vol. 247,pp. 598-603, 2016.

[11] Elsheakh, Dalia. "Microwave Antennas for Energy Harvesting Applications." *Microwave Systems and Applications,* InTech, 2017.

[12] M. Muramatsu, H. Koizumi, An Experimental Result using RF Energy Harvesting Circuit with Dickson Charge Pump, *IEEE Conference on Sustainable Energy Technologies (ICSET)*, Sri Lanka, 2010.

[13] Okba, Abderrahim et al. "Multiband Rectenna For Microwave Applications". *Comptes Rendus Physique* 18.2 (2017): 107-117.

[14] U. Olgun, C. C. Chen, J. L. Volakis, Investigation of Rectenna Array Configurations for Enhanced RF Power Harvesting, *IEEE Antennas and Wireless Propagation Letters*, Vol. 10, pp. 262-265, 2011.

[15] D. Michelon, E. Bergeret, A. Di Giacomo and P. Pannier, "Optimization of integrated dickson voltage-multipliers for RF energy harvesting," *2014 IEEE 12th International New Circuits and Systems Conference (NEWCAS)*, Trois-Rivieres, QC, 2014, pp. 448-451.

[16] W. W. Y. Lau and L. Siek, "A 2.45GHz CMOS rectifier for RF energy harvesting," *2016 IEEE Wireless Power Transfer Conference (WPTC),* Aveiro, 2016, pp. 1-3.

[17] Hakim Takhedmit, Zied Saddi, Armine Karami, Philippe Basset, Laurent Cirio, Electrostatic vibration energy harvester with 2.4-GHz Cockcroft–Walton rectenna start-up, *Comptes Rendus Physique*, Volume 18, Issue 2, Pages 98-106, February 2017.

[18] Kausar, ASM Zahid, et al. "Energizing wireless sensor networks by energy harvesting systems: Scopes, challenges and approaches." *Renewable and Sustainable Energy Reviews, vol.* 38, pp. 973-989, 2014.

[19] D. Seong, K. Jang, W. Hwang, H. Jeon and J. Choi, "Radio-frequency energy-harvesting IC with DC-DC converter," *2016 International SoC Design Conference (ISOCC),* Jeju, 2016, pp. 339-340.

[20] O. A. Escala, Study of the Efficiency of Rectifying Antenna Systems for Energy Har- vesting, Thesis for the degree of Engineer, UPC-Barcelona, Spain, 2010.

[21] J.P. Curty, N. Joehl, F. Krummeanacher, C. Dehollain, M.J. Declercq, A model for uPower Rectifier Analysis and Design, *IEEE Transactions on Circuits and systems I*, 2005.

[22] Elefsiniotis, A., et al. "A thermoelectric-based energy harvesting module with extended operational temperature range for powering autonomous wireless sensor nodes in aircraft." *Sensors and Actuators A: Physical* , vol.206 , pp.159-164, 2014.

[23] Hosain, Md Kamal, et al. "RF rectifiers for EM power harvesting in a Deep Brain Stimulating device." *Australasian physical & engineering sciences in medicine*, vol.38.1,pp. 157-172, 2015.

[24] N. Abdullah, A. M. Shire, E. Mohd and A. M. Shire, "Rectenna for RF energy harvesting," *2016 International Conference on Advances in Electrical, Electronic and Systems Engineering (ICAEES)*, Putrajaya, Malaysia, 2016, pp. 318-321.
[25] V. Palazzi et al., "Performance analysis of a ultra-compact low-power rectenna in paper substrate for RF energy harvesting," *2017 IEEE Topical Conference on Wireless Sensors and Sensor Networks (WiSNet),* Phoenix, AZ, USA, 2017, pp. 65-68.
[26] M. S. Khan and H. Deng, "Design and implementation of a highly efficient UHF energy harvesting antenna," *2016 IEEE International Symposium on Antennas and Propagation (APSURSI)*, Fajardo, 2016, pp. 611-612.
[27] V. Palazzi, M. Del Prete and M. Fantuzzi, "Scavenging for Energy: A Rectenna Design for Wireless Energy Harvesting in UHF Mobile Telephony Bands," in *IEEE Microwave Magazine*, vol. 18, no. 1, pp. 91-99, Jan.-Feb. 2017.
[28] D. K. Ho, I. Kharrat, V. D. Ngo, T. P. Vuong, Q. C. Nguyen and M. T. Le, "Dual-band rectenna for ambient RF energy harvesting at GSM 900 MHz and 1800 MHz," *2016 IEEE International Conference on Sustainable Energy Technologies (ICSET),* Hanoi, 2016, pp. 306-310.
[29] J. K. Huang and S. Y. Chen, "A compact slot loop rectenna for dual-band operation at 2.4- and 5.8-GHz bands," *2016 IEEE International Symposium on Antennas and Propagation (APSURSI)*, Fajardo, 2016, pp. 411-412.
[30] C. Song et al., "A Novel Six-Band Dual CP Rectenna Using Improved Impedance Matching Technique for Ambient RF Energy Harvesting," in *IEEE Transactions on Antennas and Propagation*, vol. 64, no. 7, pp. 3160-3171, July 2016.
[31] M. Arrawatia, M. S. Baghini and G. Kumar, "Broadband rectenna array for RF energy harvesting," 2016 IEEE *International Symposium on Antennas and Propagation (APSURSI)*, Fajardo, 2016, pp. 1869-1870.
[32] O. O'Conchubhair, K. Yang, P. McEvoy and M. J. Ammann, "Amorphous Silicon Solar Vivaldi Antenna," in *IEEE Antennas and Wireless Propagation Letters,* vol. 15, no. , pp. 893-896, 2016.
[33] H. Takhedmit, "Ambient RF power harvesting: Application to remote supply of a batteryless temperature sensor," *2016 IEEE International Smart Cities Conference (ISC2)*, Trento, 2016, pp. 1-4.
[34] Computer Simulation Technology CST MWS 2015.
[35] Hemour, S.; Yangping Zhao; Lorenz, C.H.P.; Houssameddine, D.; Yongsheng Gui; Can-Ming Hu; Ke Wu, "Towards Low-Power High-Efficiency RF and Microwave Energy Harvesting," in Microwave Theory and Techniques, *IEEE Transactions on* , vol.62, no.4, pp.965-976, April 2014
[36] C.L.Wadhwa, "High Voltage Engineering", New age Interantional Limited Publishers, 1994.
[37] Visser, H.J.; Vullers, R.J.M., "RF Energy Harvesting and Transport for Wireless Sensor Network Applications: Principles and Requirements," in *Proceedings of the IEEE* , vol.101, no.6, pp.1410-1423, June 2013
[38] Surface Mount Mixer and Detector Schottky Diodes, Data Sheet. Skyworks Solutions, Inc., Woburn, MA, USA, 2013.
[39] Hsms-286x, surface mount zero bias schottky diodes data sheet.
[40] Keyrouz, S.; Visser, H.J.; Tijhuis, A.G., "Rectifier analysis for Radio Frequency energy harvesting and Power Transport," in *Microwave Conference (EuMC), 2012 42nd European* , vol., no., pp.428-431, Oct. 29 2012-Nov. 1 2012.
[41] Nintanavongsa, P.; Muncuk, U.; Lewis, D.R.; Chowdhury, K.R., "Design Optimization and Implementation for RF Energy Harvesting Circuits," in Emerging and Selected Topics in Circuits and Systems, *IEEE Journal on* , vol.2, no.1, pp.24-33, March 2012.

# Chapter 3
# Optical Antennas based on Dielectric Resonators (DR)

This chapter provides an overview of optical antennas/nantennas and its comparison to radio frequency (RF) antennas. Basics and introduction of plasmonics is also discussed in this chapter. Background, importance and review of state-of-the-art optical antennas based on dielectric resonators (DR) is also presented. The last two sections contain the design of optical antennas that are based on DR technology. A hexagonal and a triangular DR based antenna is proposed. Various simulations are performed in getting the results at the desired frequency of interest i.e. 193.5 THz. At the end, an array synthesis and a technique to achieve tuneability for one of the DR nantennas is presented. Most of the discussion in this chapter is based on simulations and theoretical discussions. The designs and results presented in this chapter are also published in the form of reputed journals and book chapters.

## 3.1 Introduction to Optical Antennas/Nantennas

Over the last few years, with the introduction of various portable and wireless handheld devices, a surge in mobile and internet data traffic has been observed. This drastic increase is also effected by the way our society creates, shares, and consumes information on regular basis. This abundant data and information sharing also demands for increase in delivery time. High data rate communication with compact size of device is the new norm in technology. Researchers and industry are working at a fast pace to fulfill the consumer demands. It is estimated that wireless data rates are getting doubled every year and are quickly approaching the provided capacity of the wired communication systems [1-5]. Following this trend, systems working at higher data rates are needed. Although millimeter waves and 60 GHz radio [6-9] currently provide a solution and are being implemented in 5G applications, still researchers have to think ahead of time. The electromagnetic spectrum has a lot of bands to offer in terms of wide bandwidth. One section of the spectrum that has not been explored completely in the Terahertz (THz) band that can offer communication in the Terabit-per-second (Tbps) domain. These (Tbps) links can be realized over the next ten years. Terahertz Band communication [10-14] is intended as a key wireless technology to satisfy this growing demand of bandwidth hungry devices with requirements of higher data rates. Since THz band is in the early exploring phase, a lot of revisions and new standards have to be designed for the systems operating at these higher bands of the electromagnetic spectrum (Ultra violet band - Infrared band). Special considerations have to be made in the design of transmission and receiving portion of the THz system [15]. Figure 3.1 displays the electromagnetic spectrum with THz waves window between the radio waves and optical light wave applications.

Antenna is an important component of any wireless system. For the antenna to be designed at this higher end of the spectrum (THz band), special tools are needed from its realization to characterization. The antennas designed at this spectrum are also termed as optical antennas or nantennas [16]. Optical nantennas work on the operating principle that the electromagnetic wave or the light wave received can be controlled or placed into localized energy spots pertaining to the design of the nantenna. This property of the optical nantennas have gained immense interest from the research point of view as it can be applied to various fields of applications such as: spectroscopy, sensing, photo-detection, meta-surfaces, medicine, photovoltaics, and energy-harvesting applications [17-20]. With the advancements in nano technology fabrication, the nantennas designed at THz band can be realized. Nanotechnology is a fast growing research area that makes use of machines that can fabricate nano components. It is considered as an enabling technology for a set of applications in biomedical, environmental, and military fields as shown in Figure 3.2. To enable more complex applications such as intra-body drug delivery or cooperative environment sensing, the exchange of information and commands between networking entities and/or external controller is required. The need for coordination and information sharing naturally leads towards the concept of nanonetworks. One promising way to enable networking capabilities is to use wireless communications between nano-machines [21] made possible with optical nantennas fabricated on these machines.

Optical antennas or nantennas present some similarities with their radio frequency (RF) counterparts, yet, there still exists some major difference. For any wireless communication system, antennas generally operate at the transmitter and reception side, as is the case with nantennas. A schematically description is shown in figure 3.3. It can be seen from figure 3.3a that the nantenna is places near a quantum emitter which converts the near field resonances into a far field propagation meaning the optical antenna now works as a transmitter nantenna. Similarly on the reception side as shown in figure 3.3.c, the nantenna receives the signal and strongly confines it into a near field propagation. Figure 3.3b shows this scenario in the microwave term where the signals reach the antenna via waveguides before getting transmitted into the free space. For the nantennas case, due to their significantly small size, the waveguides have plasmonic modes in them as depicted in figure 3.3b. The principle of reciprocity is also applicable for nantennas as shown in figure 3.3.d, were the transmitted signal from a plasmonic waveguide can also act as a receiving section.

The main challenges associated with nantennas arise from their fabrication tolerances at the nano scale. As the metals behavior change at optical frequencies, the fabrication of these metals are introduced with material losses that arises from Plasmonics losses from the metal conductors [22]. This is usually described as the well-known dispersive plasmonic effects, and results in a significant decrease of radiation efficiency caused by conduction losses. These losses can be theoretically explained via different models at specific frequencies with mostly known models such as Drude and Lorrentz model [23-24]. One solution, that is proposed in this chapter, to cope

with these metallic losses at high frequencies and to fully utilize the properties of metallic nano structures is to design resonators or absorbers made with dielectric based materials such as ceramics.

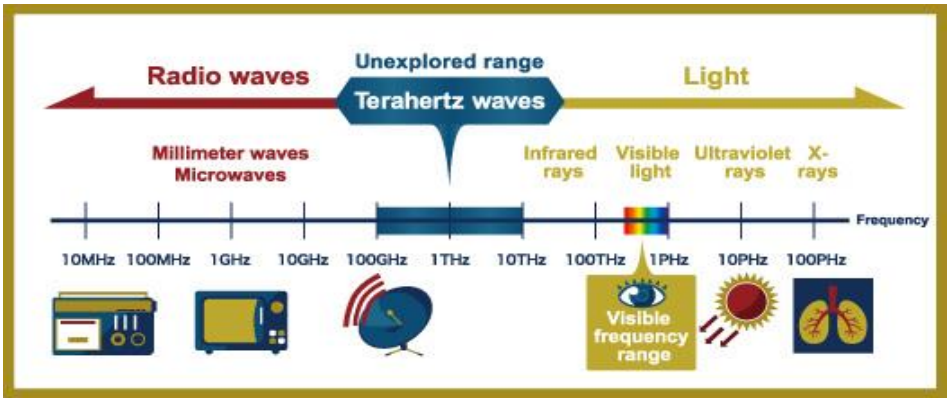


**Figure 3.1 Electromagnetic spectrum with THz range [10]**

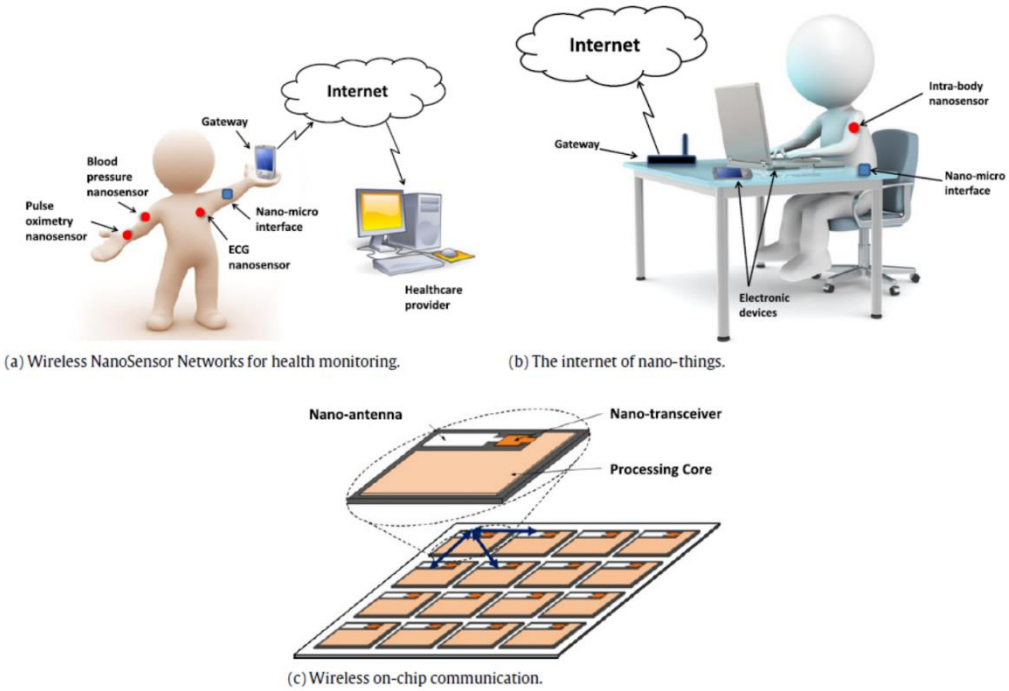


**Figure 3.2 Applications for Terahertz Band (Nano scale antennas) [15].**

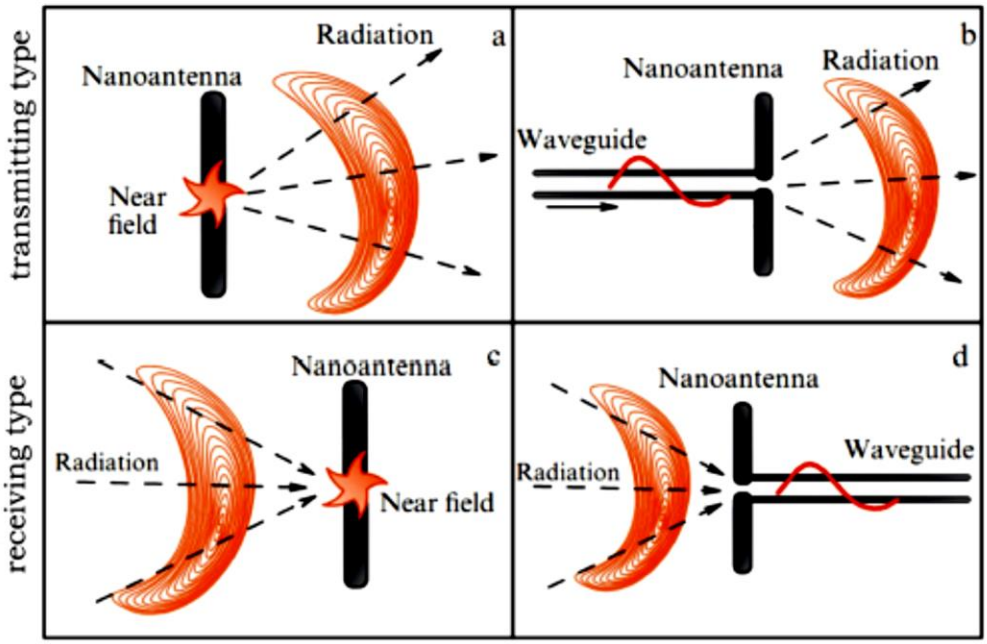


**Figure 3.3 Nantennas working principle excited via a dipole nano emitter, (a) Near field to far-field transmission (b) or waveguide mode transmission (c) reception from far-field to near field propagation ( d) waveguide reception [25].**

## 3.2 Electromagnetic interaction with metals and Maxwell equations

Maxwell equations describe the basics of electric and magnetic fields and their properties. Their combination gives the basics of electromagnetic (EM) waves. The interaction of these EM waves with metals can easily be understood by the classical approach based on the famous Maxwell equations. Even if the size of the metals are in the nanoscale domain, their properties can be described with Maxwell equations rather exploring into quantum mechanics. From our daily life experiences, we know that the metals are highly reflective for the frequencies up to the certain visible range [26] and they do not allow the EM waves to penetrate as the electric field inside the metal conductor is zero. Traditional microwave and far-infra red frequencies employ the metals as hard cladding layers to be used for the construction of waveguides and resonators. Metals start to behave like lossy dielectric near the infra-red and far infra-red region. Thus allowing the light to penetrate the metals making it transparent. In a metal EM wave or light will interact with both the electrons in the conduction band and with the valance electrons of the metal lattice. If the frequency is above the so-called plasma frequency the conduction band electrons can be considered free (very few collisions between oscillations). The electrons simply re-emit the light which makes the metal transparent. However, at lower frequencies like in the visible range the conduction band electrons will collide with the lattice much faster than the period of the wave and will absorb the energy without being able to re-emit energy. Basically, due to the lattice collisions the electrons cannot follow the incoming light. This absorption prevents the light to penetrate the metal. The effect of strong absorption somewhat counter intuitively leads to reflection. Because the waves do not penetrate deeply not many of the conduction electrons see the incoming wave and not that much overall energy is absorbed. Most of the energy is reflected by the first few layers of metal atoms

in the lattice with a spectrum that depends on the scattering properties of these particular metals atoms. Sodium as an alkali metal have almost free electron response and presents an ultraviolet transparency. On the other hand noble metals like silver and gold exhibit strong electronic-valence band transitions that lead to strong absorptions in this regime.

Metallic properties when they interact with optical wave will be discussed in later sections, but here the discussion will start with basic interaction of EM wave with metals at eh macroscopic level using known Maxwell equations [27-29]. As a starting point Maxwell's equations at macroscopic level for electromagnetism in the following form is given as:

$$\boldsymbol{\nabla . D = \rho v} \qquad (\mathbf{3.1})$$

$$\boldsymbol{\nabla . B = 0} \qquad (\mathbf{3.2})$$

$$\boldsymbol{\nabla \times E = -\frac{\partial B}{\partial t}} \qquad (\mathbf{3.3})$$

$$\boldsymbol{\nabla \times H = J + \frac{\partial D}{\partial t}} \qquad (\mathbf{3.4})$$

where D (the dielectric displacement), E (the electric field), H (the magnetic field), and B (the magnetic induction or magnetic flux density) with the charge and current densities $\rho v$ and *J*. Eq. (3.1) is the famous Gauss Law which simply describes that charged particles are enclosed in any volumetric surface will diverge with their fields i.e inwards for negative charge and outward for positive charges. Eq. (3.2) is the Gauss magnetization law which explains that there are no monotonic magnetized poles and the charred bodies have zero effect as the magnetic field lines originate from one side (North) and come back to the other side (South). The other equations are curled based meaning they produce electric and magnetic fields in a loop, eq. (3.3), Faradays law, when time varying magnetic field is produced and in eq (3.4), Ampere's Law, when time varying electric displacement with current density happens.

The magnetizing fields *H* and the displacement field *D* are defined by;

$$\boldsymbol{D = \varepsilon_o E + P} \qquad (\mathbf{3.5})$$

$$\boldsymbol{H = \frac{1}{\mu_o} B - M} \qquad (\mathbf{3.6})$$

where $\varepsilon_o$ is the electric permittivity and $\mu_0$ is the magnetic permeability of the vacuum, *M* is the magnetization and *P* is the electric polarization. From standard electromagnetism it is known that the electric polarization *P* is linked to the internal charges by the relation $\boldsymbol{\nabla . P = \rho_{int}}$.

The conservation of charge $\boldsymbol{\nabla . J_{int} = -\frac{\partial \rho_{int}}{\partial t}}$ links the electric polarization and the internal current density as;

$$\boldsymbol{J_{int} = \frac{\partial P}{\partial t}} \qquad (\mathbf{3.7})$$

and by the definition of conductivity, the internal current density $J_{int}$ and the electric field $E$ are connected by the relation:

$$\boldsymbol{J_{int} = \varepsilon_o E} \qquad (\mathbf{3.8})$$

For a linear, isotropic medium the relations between the fields can be written as:

$$\boldsymbol{D = \varepsilon\varepsilon_o E} \qquad (\mathbf{3.9})$$

$$\boldsymbol{B = \mu\mu_o H} \qquad (\mathbf{3.10})$$

where $\mu = 1$ for non-magnetic media. It is understood that equations (3.8) and (3.9) are valid only for temporally and spatially non dispersive media (i.e. not for metals, since their response is strongly dependent on the frequency). In the general case the expressions are:

$$\boldsymbol{D(r,t) = \varepsilon_o \int dt'dr'\varepsilon\,(r'-r,t'-t)E\,(r-t')} \qquad (\mathbf{3.11})$$

$$\boldsymbol{J_{int}(r,t) = \varepsilon_o \int dt'dr'\sigma\,(r'-r,t'-t)E\,(r-t')} \qquad (\mathbf{3.12})$$

where $\varepsilon_o$, $\varepsilon$ and $\sigma$ therefore describe the impulse response of the respective linear relationship. In case of a local response $\boldsymbol{\varepsilon(r,t) = \varepsilon\delta\text{^}(4)(r,t)}$, it is possible to obtain again eq. (3.9) by taking the Fourier transform $\int \boldsymbol{dtdre^{i(Kr-wt)}}$ and turning the convolution into a multiplication, eq. 3.11 simplifies to:

$$\boldsymbol{D(K,w) = \varepsilon_o\varepsilon(K,w)E(K,\omega)} \qquad \mathbf{3.13}$$

$$\boldsymbol{J_{int}(K,w) = \sigma(K,w)E(K,\omega)} \qquad \mathbf{3.14}$$

Using equations (3.5), (3.7) and (3.11) and recognizing that in the Fourier domain $\boldsymbol{\partial/\partial t \rightarrow -i\omega}$, the fundamental relationship between the relative permittivity and the conductivity is gives as;

$$\boldsymbol{\varepsilon(K,\omega) = 1 + \frac{i\sigma(K,\omega)}{\varepsilon_o\omega}} \qquad \mathbf{3.15}$$

This derivation does not take into account the existence of the magnetic field since the additional term due to the magnetic field B is suppressed by a factor $v/c$ compared to the term with the electric field $E$. In typical conditions this factor is around $10^{-10}$ therefore, it can reasonably be neglected [30]. The interaction of electromagnetic waves with metals can be simplified in the limit of spatially local interaction. This condition is met when the wavelength $\lambda$ is large compared to any characteristic length of the medium such as the size of the unit cell and the mean free path of the electrons. This situation is generally satisfied up to the ultraviolet frequencies for metals, i.e. for wavelength larger than $10^{-7}$ m, and it implies that $\boldsymbol{\varepsilon(K=0,\omega) = \varepsilon(\omega)}$ . When this condition is not satisfied one has to resort to more complicated non local theories [31].

At low frequencies, $\varepsilon$ is usually describes bound charges and is used to present the electric field while $\sigma$ describes the current flow of free charges. However, at optical frequencies, the difference between bound and free charges is unclear. In the optical domain, $\varepsilon$ can be experimentally determined by taking the reflective studies where the complex refractive index $\boldsymbol{n(\omega) = n(\omega) + i\kappa(\omega)}$ of the medium, defined as $\boldsymbol{n} = \sqrt{\boldsymbol{\varepsilon}}$. Explicitly, this yields;

$$\boldsymbol{\varepsilon_1 = n^2 - k^2} \qquad (3.16)$$

$$\boldsymbol{\varepsilon_2 = 2nk} \qquad (3.17)$$

$$\boldsymbol{n^2 = \frac{\varepsilon_1}{2} + \frac{1}{2}\sqrt{\varepsilon_{1^2} + \varepsilon_{2^2}}} \qquad (3.18)$$

$$\boldsymbol{k = \varepsilon_2/2n} \qquad (3.19)$$

wherer $k$ is called the extinction coefficient and determines the optical absorption of electromagnetic waves propagating through the medium and is also linked to the absorption coefficient $\alpha$ of Beer's law (describing the exponential attenuation of the intensity of a beam propagating through the medium via $I(x) = I_0 e^{-\alpha x}$ by the relation;

$$\boldsymbol{\alpha(\omega) = \frac{2k(\omega)\omega}{c}} \qquad (3.20)$$

Therefore, from equation.3.19, the imaginary part $\varepsilon_2$ of the dielectric function determines the amount of absorption inside the medium. For $|\varepsilon_1| >> |\varepsilon_2|$, the real part n of the refractive index, quantifying the lowering of the phase velocity of the propagating waves due to polarization of the material, is mainly determined by $\varepsilon_1$. Examination of equation (3.15) thus reveals that the real part of σ determines the extent of absorption, while the imaginary part determines the amount of polarization.

### 3.2.1 Optical Properties of Metals (Drude Model)

Light is a form of electromagnetic waves having different wavelengths between radio waves ($10^{10}$ m) to gamma rays ($10^{-12}$m) as depicted in figure 3.4. Wavelengths that can be viewed by the naked eye lies in the range of 400-700 nm (< 800 nm gender dependent) corresponding to colors from violet to red respectively. Interaction of light with materials happens due to reflections, refractions, absorptions and scattering. All these are perceived by the human eye in the form of color representing the material being viewed [27].

Optical properties of metal is defined by the interaction light waves with the motion of electrons on the surface of metals. To study this effect Drude Model has been vastly used [32]. It shows the behavior of electrons in the metal as a form of classical gas molecules. It considers that the metal has positive ions and electrons in the form of a lattice structure. The positive ions are constant while the electrons are moving freely without colliding with each other. The electrons only get excited by external electromagnetic fields. The interactions between electrons is not taken into account apart from introducing a damping constant γ defined as $\gamma = 1/\tau$ where $\tau$ is the

relaxation time of the electron, i.e. a parameter that means the mean time the electrons travel freely before colliding with some positive ions that randomize their velocities.

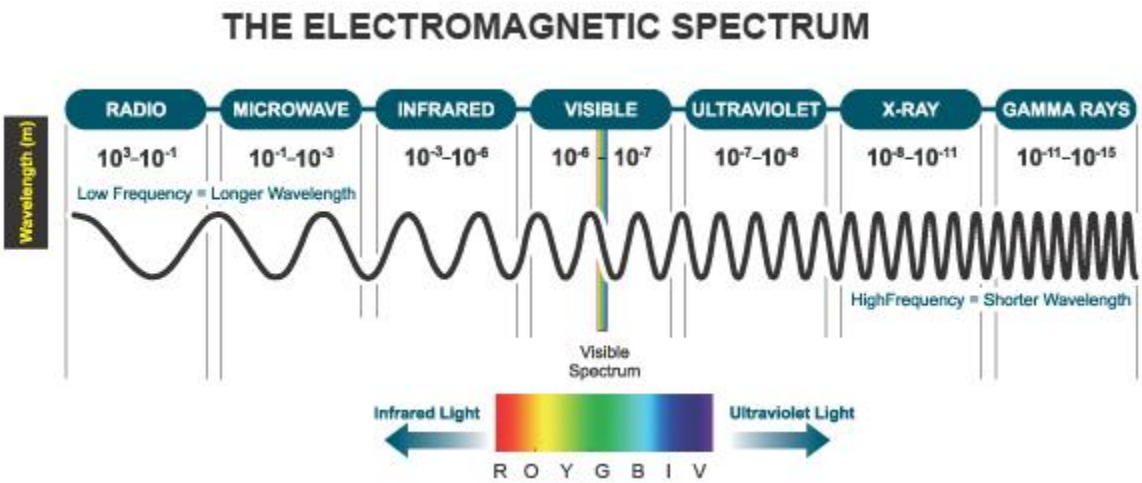


**Figure 3.4 The electromagnetic spectrum with focus on visible light region [20]**

It is possible to write a simple equation of motion for an electron that interacts with an external electric field $E$ as;

$$m\frac{d^2x}{dt^2} + \frac{m\,dx}{\tau\,dt} = -eE \qquad (3.21)$$

The second term on the left-hand-size corresponds to an averaging effect of the scattering to slow down the electrons. Assuming a harmonic time dependence of the driving field $\boldsymbol{E} = \boldsymbol{E_o}\, e^{-i\omega t}$ the steady state solution of the motion of the electrons is of the form $\boldsymbol{x} = \boldsymbol{x_o}\, e^{-i\omega t}$. Substituting into eq. (3.21) one can obtain:

$$x_o = \frac{e}{m(\omega^2 + i\gamma\omega)} E_o \qquad (3.22)$$

The polarization is the dipole moment induced by the electron movement in unit volume, thus:

$$P = -nex_o = -\frac{ne^2}{m(\omega^2 + i\gamma\omega)} E_o \qquad (3.23)$$

By inserting eq.3.23 into eq (3.5) and using it with eq. (3.9), the permitivity and refractive index of free electrons is;

$$\varepsilon(\omega) = 1 + \frac{P(\omega)}{\varepsilon_o E(\omega)} = 1 - \frac{ne^2}{\varepsilon_o m(\omega^2 + i\gamma\omega)} \qquad (3.24)$$

$$n = \sqrt{\varepsilon(\omega)} = \sqrt{1 - \frac{ne^2}{\varepsilon_o m(\omega^2 + i\gamma\omega)}}$$

$$= \sqrt{1 - \frac{\omega_p^2}{\omega^2 + i\gamma\omega}} \qquad (3.25)$$

where the plasma frequency, $\omega_p$ is defined as $\omega_p{}^2 = \frac{ne^2}{\varepsilon_o m}$. This property just depends on the mass, *m,* the electric charge *e* and density of the electrons, *n*. For normal metal $\omega_p$ is about $10^{15}$-$10^{16}$ Hz and $\tau$ is around $10^{-14}$ s at room temperature. This means that around plasma frequency the electron is oscillating much faster than the collision. If the operating optical frequency is lower than the plasma frequency $\omega_p$, the permittivity is negative and index of refraction becomes purely imaginary. In this case the electric field will just penetrate in to the material without forming oscillations. All the incoming wave will get reflected if the material is thick enough. It is this reason that the surface of metals look shiny and colorless. Now, if the optical frequency is higher than the plasma frequency $\omega_p$, the index of refraction becomes real, which means the material becomes transparent to the optical wave. For normal metals this usually happens at ultra-violet frequency range. It is interesting that at this frequency range the index of refraction is smaller than 1. This means the phase velocity of light within the material is larger than the speed of light in vacuum. This leads to many interesting phenomenon and applications. If the polarization effect in the ion core for electrons is taken into account, eq. (3.24) can be written as;

$$\varepsilon(\omega) = \varepsilon_\infty - \frac{\omega_p^2}{\omega^2 + i\gamma\omega} \qquad (3.26)$$

Table 3.1, as an example, shows the coefficient for gold and silver used for the calculation of the dielectric function using the Drude model.

| **Nobel Metal** | $\varepsilon_\infty$ | $\omega_p$ **[Hz]** | $\gamma$ **[Hz]** |
|---|---|---|---|
| **Gold (Au)** | 10.7 | $1.37 \times 10^{16}$ | $1.17 \times 10^{14}$ |
| **Silver (Ag)** | 5 | $1.36 \times 10^{16}$ | $27.3 \times 10^{12}$ |

**Table 3.1 Coefficients of the Drude model used in eq. (3.26) for gold (Au) and silver (Ag) [24].**

## 3.3 Brief Introduction to Surface Plasmons Polaritons (SPP) and Local Surface Polaritons (LSP)

As discussed in chapter 1, Plasmons is the branch of nanophotonics that deals with the interaction of light with free electrons at the surface of Noble metals. It explains the generation, manipulation and detection of surface plasmon polaritons (SPP), which are quasi particles, appearing due to coupling of light with surface plasmons on the surface of metal and insulator interaction. Simply put, the most common definition of a Plasmon is; *"A plasmon is a quantum of plasma oscillation"*. The excitation of a Plasmon requires the interaction of an electron passing through a thin metal or by reflecting an electron or a photon from the metallic film. On the other hand, surface plasmon Polaritons (SPP) are electromagnetic excitations whose propagating at exists at the interface between a dielectric and a conductor. These electromagnetic surface waves arise via the coupling of the electromagnetic fields to oscillations of the conductor's electron plasma. The most simple geometry in which they arise is the interface of two materials with opposite signs of the real part of their dielectric permittivity, i.e. between conductors and insulators, and they are able to concentrate light in subwavelength dimensions, leading to an electric field enhancement. SPPs arise in planar, ideally infinite, structures, whereas localized SPPs are produced in confined structures, e.g., spheres. The derivation of the SPPs solution starts from Maxwell's equations, from which it is possible to obtain the wave equation [27];

$$\nabla^2 E - \frac{\varepsilon}{c^2}\frac{\partial^2 E}{\partial t^2} = 0 \qquad (3.27)$$

By solving eq. (3.27) for field with a time harmonic dependence $E(r,t) = E(r)e^{-i\omega t}$ the Helmholtz equation is obtained;

$$\nabla^2 E + K^2 E\varepsilon = 0 \qquad (3.28)$$

where $k = \omega/c$ is the wave vector of the wave propagating in vacuum. THe Helmholtz equation can be solved, as an example, in a one dimensional problem, i.e. with $\varepsilon(z)$ varying only in the spatial coordinate $z$, with the wave propagating in the x direction and the coordinate z = 0 corresponding to the interface between the conductor and the insulator. The propagating wave is described by the formula $E(x, y, z) = E(z)e^{ikSP\,x}$ , where the complex number $k_{SP} = kx$ , also called the propagation constant, corresponds to the component of the wave vector of the SPP in the direction of propagation.

The interaction of the conduction electrons with the electromagnetic waves causes the wave vector $k_{SP}$ of the SPP to be larger than that of a photon of the same frequency $\omega = 2\pi\nu$ and wave vector, propagating in the free space. By obtaining the solutions of eq. (3.28) for the two materials at the interface and by imposing the continuity of the fields, as dictated by Maxwell's equation, it is possible to derive the dispersion relationship of the SPPs as;

$$k_{sp} = k_o \sqrt{\frac{\varepsilon_d \varepsilon_m}{\varepsilon_d + \varepsilon_m}} \qquad (3.29)$$

where $\varepsilon_d$ and $\varepsilon_m$ are the dielectric constant of the dielectric and the metal respectively. Eq. (3.29) is valid either for real or complex values of the dielectric constant, i.e. for metals with and without attenuation. From the analysis of the boundary conditions it is possible to demonstrate that SPPs exist only with TM polarization. Figure 3.5 shows the combined electromagnetic wave and polarization charges for an SPP at the interface between a metal and a dielectric and the the SPPs dispersion relation. In order to avoid any confusion, for TE polarization (p-polarization), the electromagnetic wave has the electric field vector parallel to the plane defined by the direction of propagation of the wave and normal to the incident plane (when incidence is not orthogonal), and orthogonal for TE (s-polarization).

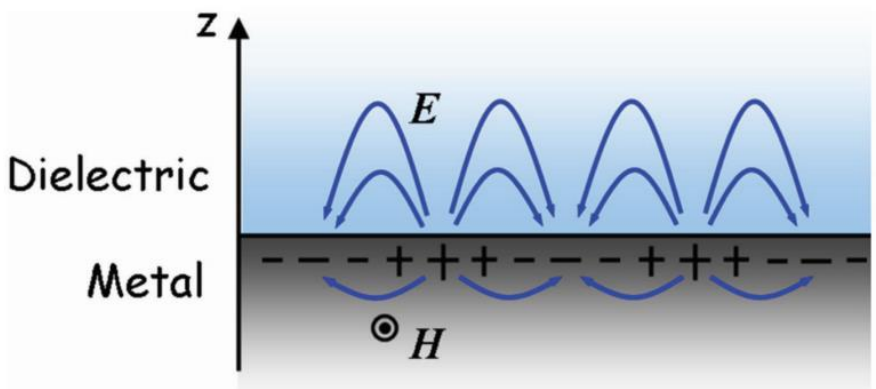


**Figure 3.5 SPP propagating at the interface of a metal and dielectric that has high strengths at the interface and exponentially decays when away from the interface [33].**

### 3.3.1 Localized Surface Plasmons (LSP)

SPPs are propagating electromagnetic waves on a conductor/ dielectric interface coupled to the electron plasma. Localized surface plasmons (LSPs) instead are non-propagating excitations of the electron plasma of metal nanostructures coupled with the electromagnetic field and can be excited by direct light illumination. The dynamics of the electrons in small curved structures are changed by the effective force that arises at the interface between the metal and the dielectric, leading to the formation of natural resonant frequencies and field enhancement both inside and outside the particle. The resonant frequencies depend on the particle shape and size and, apart for some particular shapes, e.g., spheres, rigorous analytical solutions do not exist. In general, to describe the electromagnetic behavior of these structures, one has to resort to computational methods. The electromagnetic interaction between particles in ensembles leads to a further complication of the problem since it causes a modification, sometimes dramatic, of the resonances.

## 3.4 Literature Review: Dielectric Resonator (DR) Based Nantennas

In this section, some state-of-the-art literature review on various nantennas designs will be presented. Although most of the work has been published for metallic nano antennas but with the introduction of dielectric resonators (DR), the research trend is shifting. DR offers better antenna characteristics at the nano scale dimensions as the material is less lossy due to its ceramic nature compared to metallic nano antennas [34-35].

In [36], authors presented the numerical simulation of a dual band compact nano plasmonic antenna that can control the emission released form a nano source i.e. the dipole emitter antenna. A multilayer metal−dielectric nantenna consisting of three identical gold strips were used as separation between two dielectric spacers. It was shown that the local dipole source efficiently excited various plasmonic modes including one electric dipole (ED) and one magnetic dipole (MD). The combination of these two dipoles (ED and MD) lead to the creation of unidirectional emission in opposite direction from the source at various wavelengths. The exact emission direction was determined with the relative phase difference between the resonating modes. It was possible to control the emission between the forward and backward emissions by control the spacing thickness between the metal and dielectric medium. The directionality achieved for the forward and backward radiation was -20 and -21 dB with MD mostly controlling the emission strength. The simulation analyses presented by the authors suggested that the proposed design can be useful n designing dual band unidirectional optical nantennas that can control eh emission form the radiating source.

Authors in [37] introduced a novel concept where they introduced super directive nano antennas. This task was achieved by creating highly induced magnetic multipoles. The all dielectric based nano antennas were designed by making use of small spheres excited by a local source. Experimental verifications were done by realizing the antenna at a lower microwave frequency of 16 GHz. For the nano antenna, small semiconductor material was used which produced maximum directivity without the need of arrays or using metamaterials. The maximum size of the sphere was between 0.4 λ - 0.5 λ. The laser source was operating between 440-460 nm. The super directive nature of the nano antenna was compared to that of all yagi-uda based nantenna [38], where the current proposed design achieved experimental directivity of 5.9 and 8.4 dB in both the E-plane and H-Plane.

In [39] spectroscopic analysis were done on the dielectric plasmonic nantenna by placing a nonlinear dielectric nanoparticle in a hot spot that provided field enhancement provided and nonlinear optical susceptibility of dielectric nanoparticles. The idea was tested by combining a gold gapped nantenna with a centered zinc sulfide nano particle. Second harmonic spectroscopy analysis were done on the hybrid plasmonic dielectric antenna. The paper findings revealed that the bare gold nano particles produced several orders of magnitude of strong second harmonics compared to the hybrid plasmonic dielectric nantenna i.e. combination of gold nano antenna with zinc sulfide sphere.

A nano dielectric reflect array was presented in [40]. It was designed for THz applications working at 633 nm. Various metals such as copper, aluminum, gold and silver were analyzed to be used as a ground plane for the nano dielectric reflect array. A 21 x21 unit cell array was designed. Analysis of the metals showed that gold produced the worst results to be used as a reflector ground plane while silver was among the nest materials for reflect array. Following table shows the results produces in terms of various parameters for the array;

| **Material** | **Sliver** | **Copper** | **Aluminum** |
|---|---|---|---|
| **Gain dBi** | 25.8 | 27.2 | 25.4 |
| **1-dB BW** | 30 THz | 35 THz | 40 THz |
| **SLL (dB)** | -17.9 | -19.4 | -12.51 |
| **HPBW (degree)** | 4.5 | 4.5 | 4.3 |

**Table 3.2 Different material response as per characterization of reflect array [40]**

In [41], authors realized the properties of nano dielectric materials to scatter visible light. Electron beam deposition was used to realize the nano rods antenna that consisted of amorphous alloys of C and O with a width of 180 nm on average and a length of 4.5 μ m. Measurements showed that the transverse electric and transverse magnetic modes covered the full visible range of electromagnetic spectrum with the height of the nano rod varying from 90 to 280 nm. The experimental results prove the usefulness of the proposed nano dielectric material as an analysis tool for near field nantennas.

Authors in [42] drew inspiration from low frequency DRA designs and present an up-scaled nano version of the dielectric antenna. The proposed nantenna was excited with a laser of 633 nm (He-Ne laser red light, 1.96 eV). The structure had $TiO_2$ cylindrical arrays (126 x 126 elements) with a height of each being 50 nm and diameter of 162 nm was placed on a 380 um thick silicon slab. 200 nm silver coating was used on the silicon which holds the array elements. All the structure was realized using electron beam lithography (EBL). The excitation of array nantennas showed beam deflections at various angles. These observations opened new paradigms compared to alternate metallic nantennas. Ultrafast computations, short range optical communication and molecular sensing can be achieved using these types DRA designs based on nano photonics.

## 3.5 Proposed Equilateral Triangular Dielectric Resonator Nantenna [ETDRN]**

In this section and the later ones, nantenna designs based on dielectric resonators (DR) are presented. The designs are based mere on simulations as this accounts for my first trials with simulations on nantenna designs. Most to the work presented here is a re-print of my work published in international peer reviewed journals.

### 3.5.1 Introduction to Dielectric Resonator antenna (DRA)

The idea of using antennas based on dielectric resonators (DR) was first proposed in 183 by Long et al [43] where the DRAs performance was based on its unique characteristics of minimum radiation loss, high permitivity values ($5 < \varepsilon r < 100$) and utilization it as a resonator or a storage device for various microwave circuits and filters. Over the years various aspects of DR antennas have been published and designs patented [44-45]. Most notable publications are seen at the antennas operating as filters and circuits integrators at the microwave regime due to their compact size and high resistibility to losses. One striking feature of DR resonators is that they are immune to ohmic losses, which drastically appear at higher frequencies (bands above millimeter waves till far infrared), making them suitable candidates for optical nantennas. DRs' are very efficient radiators compared to metallic antennas even at higher frequencies [46]. In this context, the work presented in the coming sections will focus on integrating the resilient DR with metallic nano elements for operating at THz band. The losses incurred due to appearing of plasmonics inside the metal elements are subsided with the integration of various DR shaped resonating elements. The results presented in the later sections validate the selection of DR as a suitable candidate and replacement to traditional metallic resonators working at higher THz band.

### 3.5.2 ETDRN Design Geometry

Figure 3.6 shows the configuration (cross sectional and front view) of the proposed equilateral triangular dielectric resonator nantenna (ETDRN). The nantenna is designed to operate as a receiving antenna that can capture energy from the free space. The operating band of interest lies in the standard optical communication band at a wavelength of 1550 nm which corresponds to central frequency of 193.5 THz. From the geometric configuration presented in Figure 3.6, the design follows a basic multilayer substrate approach. A silicon substrate *(Si)* having an oxide layer *($O_2$)* is sandwiched between two conducting materials layers. The $SiO_2$ substrate has properties of thickness of $h_1$ = 0.150 μm, $\varepsilon_r$ = 2.09 and loss tangent $tan\ \delta$ = 0 [47]. The partial conducting material below the substrate acts as a ground plane. Its dimensions and thickness are $W_g \times L_g$ having a thickness of $t$ = 0.010 μm. The nanoantenna is fed via a feed line placed on the top side of the substrate. It has geometric dimensions and thickness of thickness $W_f$ x $L_f$; $h_2$ = 0.025 μm. The ground and the nanostrip are made up of Nobel metal silver *(Ag)*. The dimensions of the substrate are taken as $W$ x $L$ = 5 x 5 μm$^2$. The resonator, made from *(Si)*, placed on top of the feed line is made from dielectric material. It has the shape of an equilateral triangle with properties as $\varepsilon_r$ = 11.9 and estimated loss tangent $tan\ \delta$= 0.003 at 100 THz [48]. The nantenna is excited and matched considering 50 Ω impedance source. In order to control the matching at the central frequency of



***Published in Advances in Low-Profile Antennas in Wireless Communications, International Journal of Antennas and Propagation, May 2015.***

193.5 THz and to achieve a wide bandwidth with acceptable radiation patterns the same *($SiO_2$)* substrate material with thickness $h_3$ = 0.015 μm has been introduced between the equilateral triangle and the nanostrip. The dimensions of the equilateral triangular dielectric are calculated from equation (3.30) [49-50].

$$f_{mnl} = \frac{c}{2\sqrt{\varepsilon_r}}\left[\sqrt{\left(\frac{4}{3a}\right)^2 + \left(\frac{p}{h}\right)^2}\right]^{1/2} \qquad (3.30)$$

where '*a*' is the side length of the equilateral triangular DRA, $\varepsilon_r$ is the dielectric constant of the DRA, *'h'* is two times the height of the triangular DRA to account for the image effect of the ground plane and p = 1 for the fundamental mode [50]. For a low-profile triangular DRA, we have $a >> h$, and therefore equation (3.31) demonstrates that the frequency is predominantly determined by the height of the DRA;

$$fr = \frac{c}{4h\sqrt{\varepsilon_r}} \qquad (3.31)$$

where $h$ and $\varepsilon_r$ are the height and dielectric constant of triangular DRA.

Metals working in the optical regime are faced with another loss. This loss appears as negative permitivity therefore complex permittivity $\varepsilon_{Ag}$ of the metals, in our case silver *(Ag)*, is calculated from equation (3.32) explained by the Drude model which is based upon kinetic theory of electron gas in solids [51];

$$\varepsilon_{Ag} = \varepsilon_o\left\{\varepsilon_\propto - \frac{f_{p^2}}{[f(f+i\gamma)]}\right\}$$

$$= -129.17 + j3.28 \qquad (3.32)$$

where $\varepsilon_o$ = 8.85x10$^{-12}$[F/m], $\varepsilon_\propto = 5$, plasmonic frequency $f_p$ = 1.41e$^{16}$ rad/s, $f$ = central frequency and collision frequency $\gamma$ = 2.98e$^{13}$. The plasmonic frequency, which appears after the photon and free electron gas collision, defines the collective motion of the electrons and can be expressed as follows;

$$f_p = \sqrt{ne^2/\varepsilon_0 m} \qquad (3.33)$$

where $n$ is electron concentration, $e$ is the free electron charge (1.6 × 10−19 C), $\varepsilon_0$ is the free space (vacuum) permittivity (8.854 × 10−12 F/m), and $m$ is the electron effective mass. From equation (3.33) the behavior of arriving EM wave to the metal can be deduced. For $f < f_p$ corresponds to and exponential decay field, EM wave will be reflected backs and will not propagate through the metal. On the other hand if $f > f_p$, the EM wave will behave as a travelling wave and it will pass through the metals. Similarly, the collision or damping factor describes the losses within the metal and can be expressed;

$$\gamma = \frac{e}{\mu m} \qquad (3.34)$$

where μ is mobility of free carriers. The proposed model has taken into account the conductive and dielectric losses and has been simulated in commercially available EM simulator CST MWS 2016 based on FIT numerical technique using optical template.

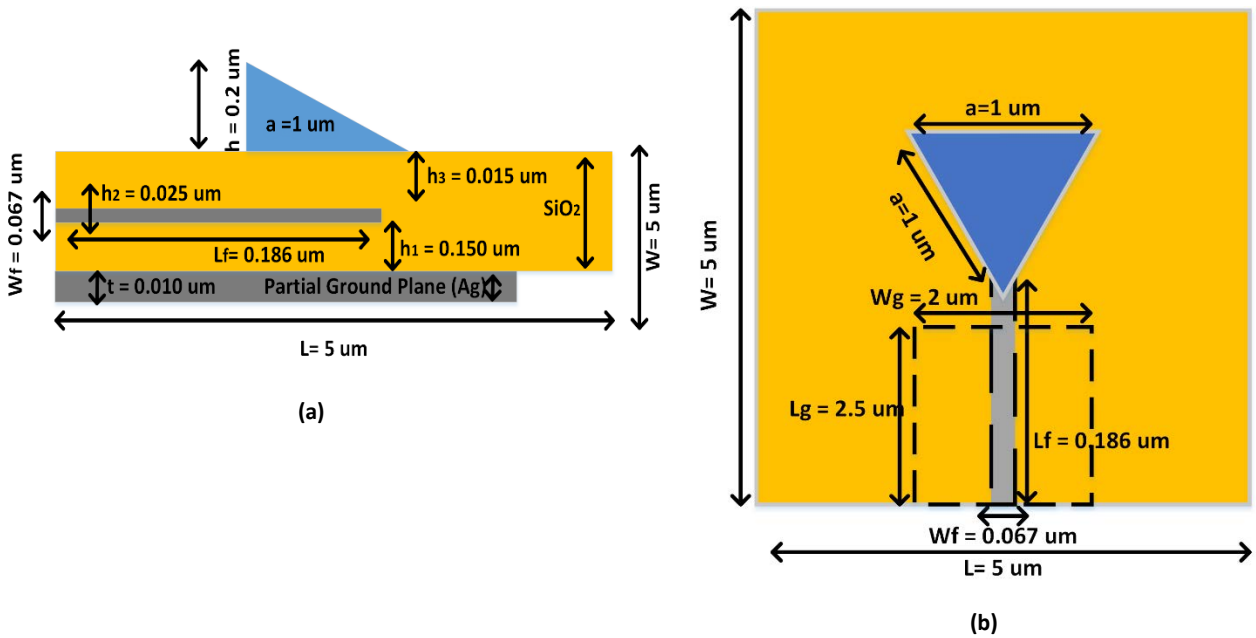


**Figurere 3.6 Antenna Geometry of proposed nantenna design based on Equilateral Triangular DR (ETDRNA) (a) Cross sectional view (b) Front View.**

## 3.5.3 Antenna Simulation and Experimental Results

To get an understanding on the working principle of the proposed ETDRN, various parameters of the nantenna were extensively optimized. In order to study the effects on the antenna performance in terms of bandwidth and directivity, the following parameters were observed and analyzed were made;

**a. Nanostrip Feed:** The nano strip feed line placed on top of the $SiO_2$ substrate was optimized in terms of its length and width. The traditional empirical formulas [52] were used as a starting point for the nanostrip design. The nanostrip acts like a coupling resonator that excites the triangular dielectric place on an upper $SiO_2$ substrate with height $h_3$.Traditionally at RF frequencies the length of the transmission lines are characterized to the wavelengths (λ) of incoming and outgoing radiations. However working at the optical frequencies the incident waves reflect less and penetrate more in to the substrate passing through the metal atoms. This phenomena is known as plasmonic affect and it gives rise to free plasmonic gaseous atoms. To deal with this new phenomena at optical frequencies, we use shorter effective wavelength ($\lambda_{eff}$) compared to traditional wavelengths (λ) which depends on material characteristics given by the following equation for length of a transmission line [53];

$$\frac{m\lambda_{eff}}{2} = L(\lambda o) \qquad (3.35)$$

where eq.(3.35) shows the relationship between the free space wavelength *($\lambda_o$)* and the effective wavelength *($\lambda_{eff}$)* and the order of resonance (*m*). Here effective wavelength is given by;

$$\boldsymbol{\lambda_{eff} = \frac{\lambda_o}{n_{eff}}} \qquad (\mathbf{3.36})$$

Typical values of $n_{eff}$ has been measured to be in the range of 1.5 - 3 [54]. In our case for the silver nanostrip feed line, we use $n_{eff} = 2.8$ which resulted the minimum resonating length of to be 0.27 um. The length $L_f$ of the nanostrip was optimized from 0.1 um - 0.27 um with the best optimized value producing required resonance at 193.5 THz was at $L_f = 0.186$ *um* as shown in Figure 3.7a. The effect of the width *'$W_f$'* of the nanostrip was also examined by extensive parametric studies. Initial values were taken from the empirical formulas [52] and optimization was done from 0.02 um - 0.28 um. Figure 3.7b shows the best optimized value achieved at resonance of -22 dB with $W_f$ = 0.067 um.

b. **Partial Ground Plane:** The ground plane plays an important role in controlling the bandwidth and radiation characteristics of any designed antenna. At the nanoscale geometry, we simulated and observed its parameters effect on our nantennas resonance behavior. We started off initially with a finite ground plane that achieved a good radiation pattern with an acceptable bandwidth. The ground plane was then optimized and a partial section of it was used with optimized dimensions $L_g$ *x* $W_g$ = 0.5 um x 2 um. Figure 3.8a and Figure 3.8b show the effects of varying the ground plane in terms of its length and width. The optimized results produces a wide impedance bandwidth of 2.5 % (192.3 THz - 197.3 THz) at a center frequency of 193.5 THz. This makes our proposed nantenna cover all of the standard optical transmission widow (C-band), with a directivity of 8.6 dB.

**c. Height of Triangular DR:** Since the height of the triangular DR predominately determines the resonance frequency as according to equation (3.36), the height *h* of the DR was optimized from 0.1 um - 0.5 um. Figure 3.9 shows the best optimized value of $h = 0.3$ *um* having a resonance at -23 dB.

d. **Rotation of Triangular DR:** In order to study the effects of bandwidth, frequency shift and directivity of the nano antenna design, the proposed silicon based triangular DR was rotated on its axis. The rotation was from $0^0 – 360^0$ with an angular spacing of $40^0$. Figure 3.10 shows the angular rotation of the triangular DR. The tip of the triangle was initially aligned at $0^0$ shown in green color. The DR was then rotated along the counterclockwise direction with varying angles. It was observed that with the rotation of the DR, the bandwidth remained the same at 2.5 % but the resonant frequency shifted to other bands (200 THz - 205 THz) in the frequency range from (180 THz - 220 THz) as shown in Figure 3.11a. Since the triangle is an equilateral one, the angular rotation produces the same shifts at other angles i.e. the shift will be the same at (0=120=240=360 degree) as shown in Figure 3.11b. The directivity was also affected with the rotation of the triangle as shown in Figure 3.11b. It is clear that the effect of the rotation of the triangular DR lowers the directivity to nearly 3 dBi.

After extensive optimization of stated parameters above and analyzing the results achieved from these optimizations, the best geometric parameters that achieve an impedance bandwidth of

2.5 % (192.3 THz - 197.3 THz) and a directivity of 8.6 dB, are listed in Table 3.3. It is also observed that the simple ETDRN structure can act as a tunable resonator when rotated around its axis resulting in usage of applications that work in the wavelengths in the range of (1463 nm -1500 nm). The proposed design, if facility exists, can be fabricated via the known techniques involved in nanofabrication technology i.e. e-beam lithography, photolithography and chemical vapor deposition. In this case, the fabrication will follow a bottom-up approach where the $SiO_2$ substrate will have silver deposited on its surface.

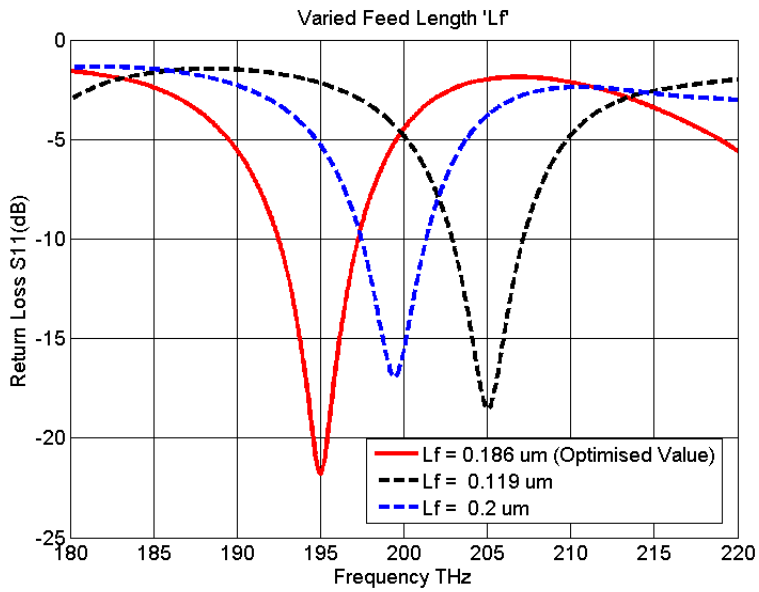


**(a)**

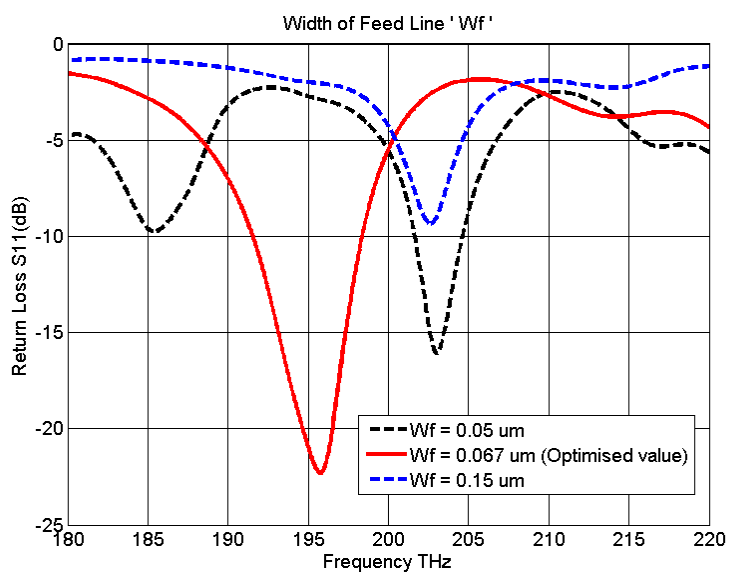


**(b)**

**Figure 3.7 Optimized Parameters: (a) Length of Feed Line (b) Width of Feed Line**

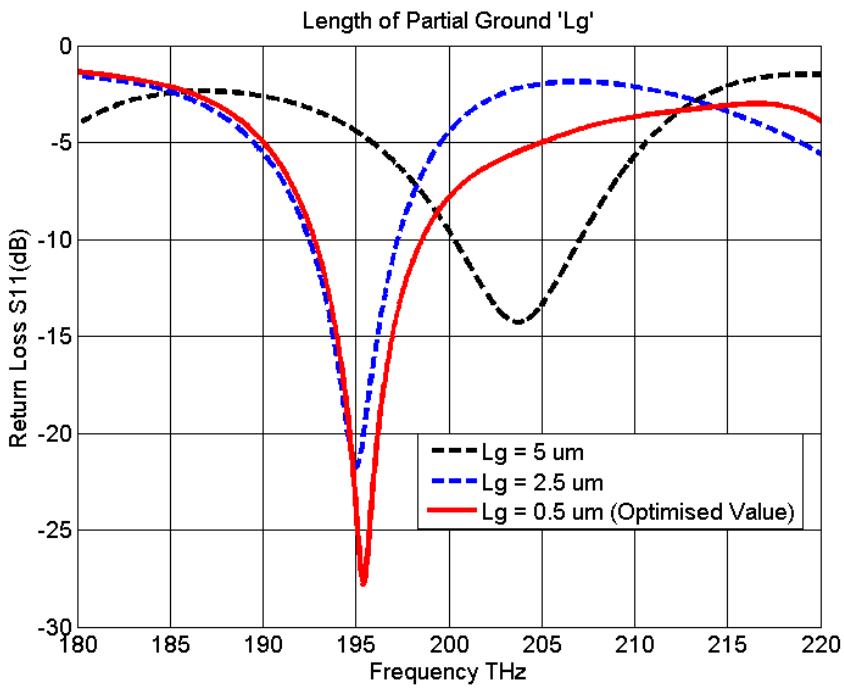


**(a)**

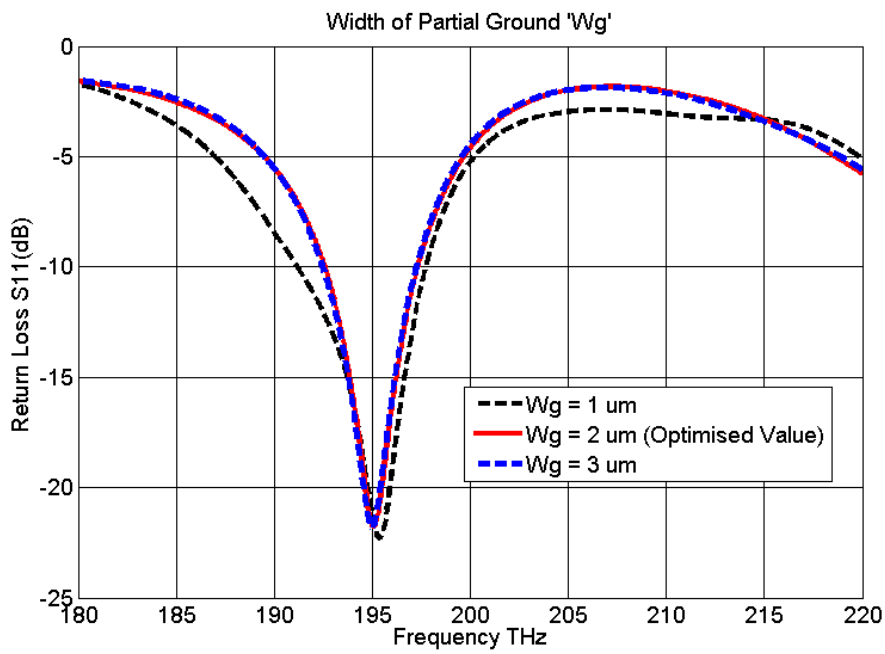


**(b)**

**Figure 3.8 Optimized Parameters: (a) Length of Ground Plane (b) Width of Ground Plane**

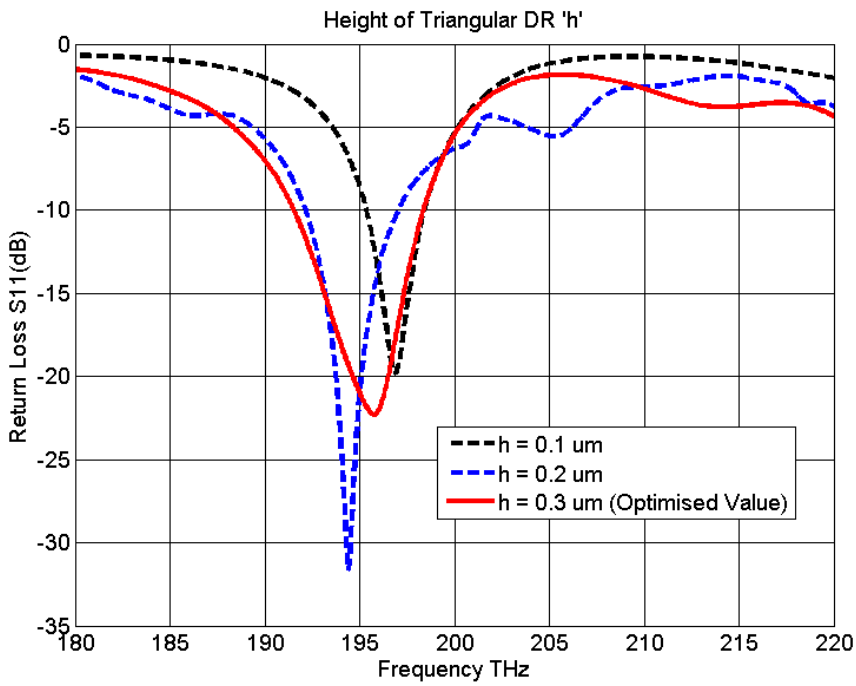


**Figure 3.9 Height of the ETDRN antenna**

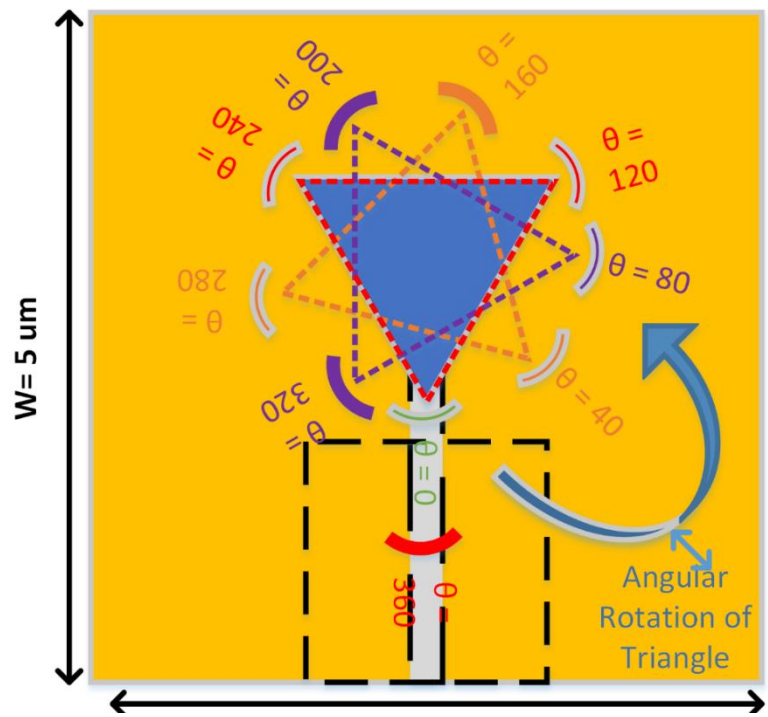


**Figure 3.10 Angular Rotation of Triangular DR**

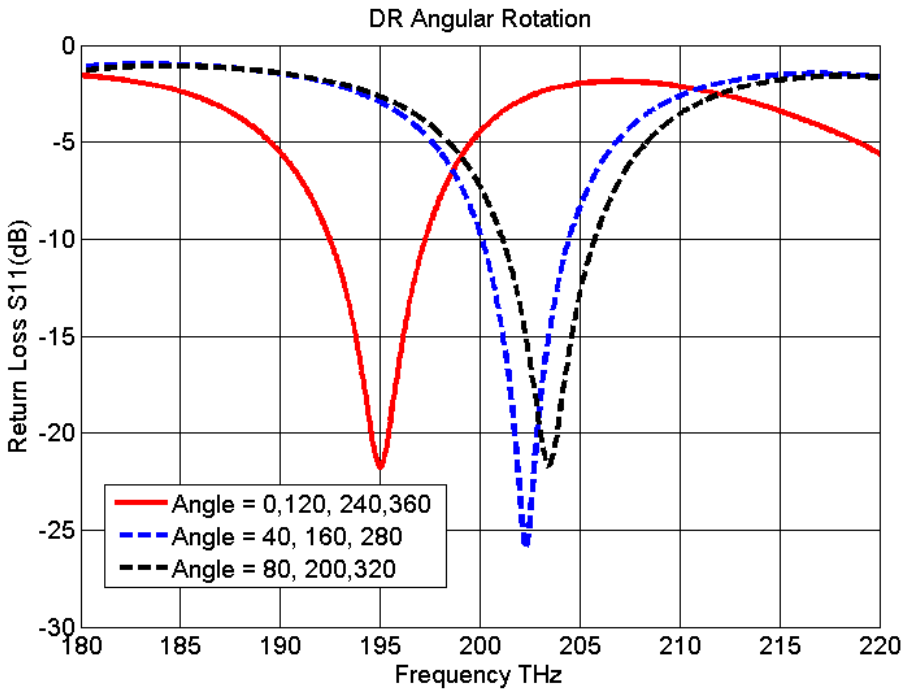


**(a)**

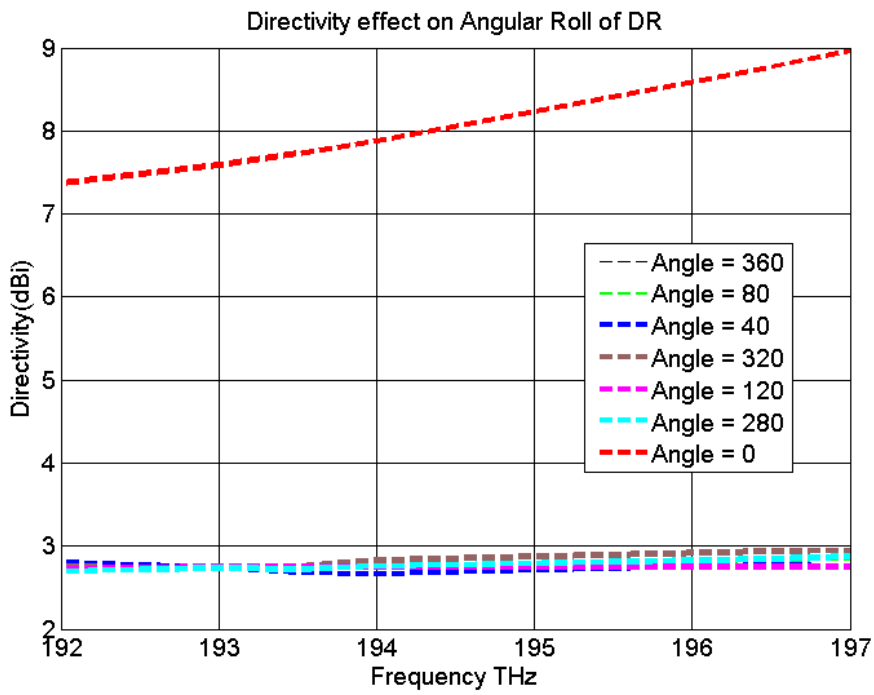


**(b)**

**Figure 3.11 Optimized Parameters: (a) Effect of Angular Rotation of Resonant Frequency (b) Effect of Angular Rotation on Directivity**

| PARAMETERS | VALUE (um) |
|---|---|
| **Feed Length $L_f$** | 0.186 |
| **Feed Width $W_f$** | 0.067 |
| **Ground Length $L_g$** | 2.5 |
| **Ground Width $W_g$** | 2 |
| **Height of Triangular DR $h$** | 0.2 |
| **Area of Triangular side $a$** | 1 |
| **Rotation Angle $\Theta$** | $0^0$ |

**Table 3.3 Optimized parameters of the proposed ETDRN**

## 3.5.4 Results and Discussion

This section presents the simulation results of the proposed ETDRN. Figure 3.12 shows the return loss *($S_{11}$)* and directivity of the proposed ETDRN. The 3D radiation patterns of the nano antenna at 192 THz, 193.5 THz and 197 THz are shown in Figure 3.13 (a-c). The maximum dip of -22 dB is achieved from the resonance of the nantenna at the central frequency of 1936.5 THz. The nantenna covers some part of the S-band while most part is covered for the C-band optical communication window. 3-D radiation patterns provides the proof of the ETDRN radiating in end-fire pattern. At present, the nano fabrication technology is limited and the proposed design is a theoretical one, yet we believe that our contribution in the fast growing field of nantennas, with the proposed ETDRN design will prove itself to be a promising candidate for next generation energy harvesting and green sustainable solution applications based on nano technology designs.

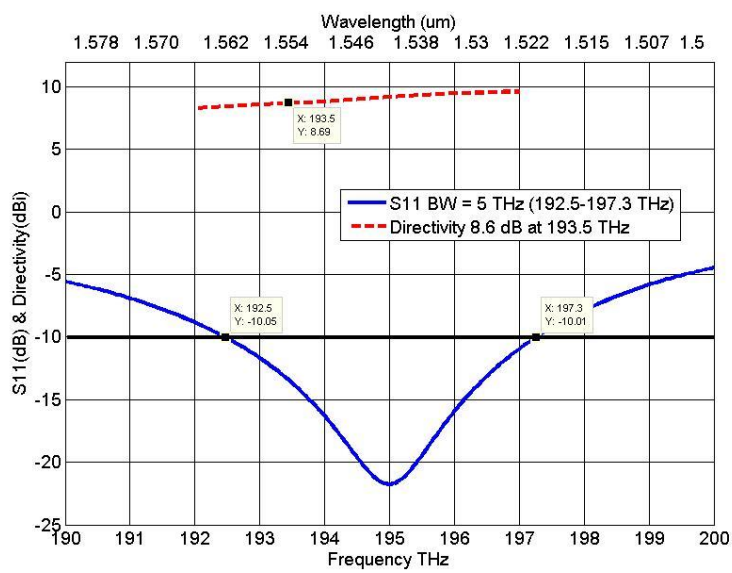


**Figure 3.12 Simulated Return Loss and Directivity of ETDRNA**

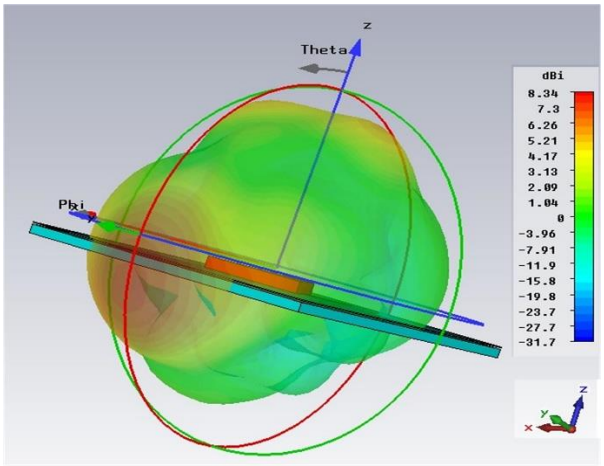


**(a)**

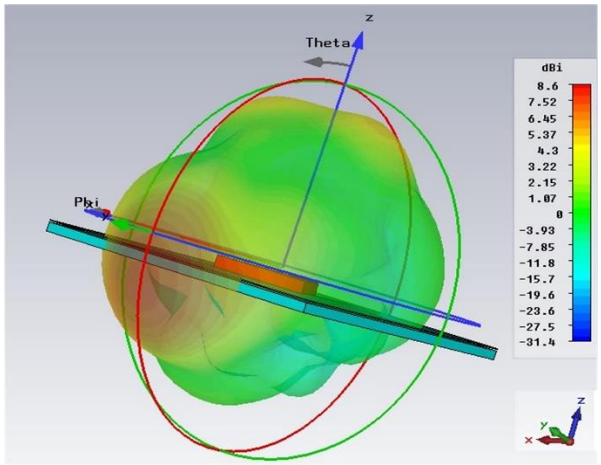


**(b)**

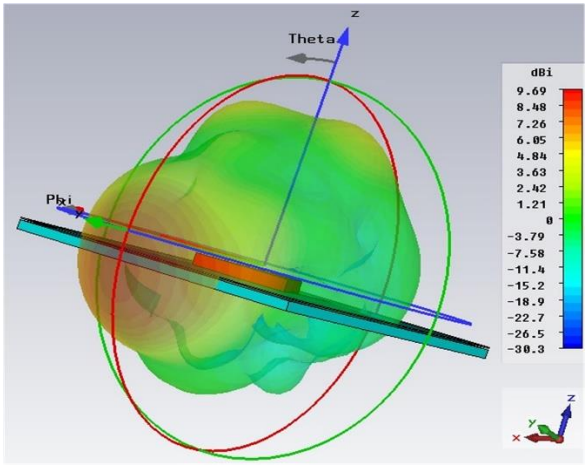


**(c)**

**Figure 3.13 3D end-fire Radiation Pattern at a) 192 THz (b) 193.5 THz (c) 197 THz**

## 3.6 Proposed Hexagonal Dielectric Resonator Nantenna [HDRN]**

In this section another nantenna design based on dielectric resonator material is presented. The shape of this DR is in hexagonal form with material chosen as silicon *(Si)*. The proposed design works as a loading element. The structure is again in multilayer form having *($SiO_2$)* sandwiched between two silver *(Ag)* sheets. The radiating element is an equal sided hexagonal shaped *(Si)* dielectric loaded material. The whole nantenna structure is excited via a nano strip transmission line made from a Noble silver metal *(Ag)* whose conductive properties are calculated via the Drude model. The antenna achieves an impedance bandwidth of 3.7% (190.9 THz – 198.1 THz) with a directivity of 8.6 dBi at the frequency of interest. The obtained results make the proposed nantenna a possible solution for future nano photonics and nano scale communication devices.

### 3.6.1 HDRN Design Geometry

The proposed nantenna is in the shape of a hexagon utilizes the loading properties of ceramic dielectric silicon and is termed as Hexagonal dielectric Loaded Nantenna (HDLN). It is also designed to operate at the central frequency of 193.5 THz which corresponds to wavelength of 1550 nm. The cross sectional and front view of the proposed HDLN is in Figure 3.14 (a) and (b). The design is based on a multilayer structure with *($SiO_2$)* substrate sandwiched between two Noble metals each made form silver *(Ag)*. The properties of substrate are; thickness of $h_1$ = 0.150 µm, $\varepsilon_r$ = 2.1 and loss tangent *tan* $\delta$ = 0.003 at $f = 100$ *THz* [47]. The ground layer, made from silver, below the substrate has partial form with properties as thickness of $t$ = 0.010 µm and dimensions $L_g$ x $W_g$ = 1.95 x 2 µm. The feeding line is a nano silver strip on top of the substrate with parameters; thickness $h_2$ = 0.025 µm, $W_f$ = 0.067 µm and $L_f$ = 0.186 µm. The substrate dimensions are taken as $W_s$ x $L_s$ = 5 x 5 µm$^2$. The hexagonal dielectric is made of *(Si)*, with $\varepsilon_r$ = 11.9 and estimated loss tangent, *tan* $\delta$= 0.0025. To achieve a further increase in the bandwidth with minimum resonance losses, a small substrate with thickness $h_3$ = 0.015 µm made from *($SiO_2$)* has been introduced between the hexagon and the nanostrip. The dimensions of hexagonal dielectric are calculated from equation (3.37) [52] by inscribing the hexagon inside a circle and equating the areas of both designs, thus giving an optimized equal side lengths of hexagon as $s$ = 1 µm and thickness ( $\lambda_g/4 < h < \lambda_g/2$ ) $h$ = 0.377µm;

$$\pi a_e^2 = \frac{3\sqrt{3}}{2} s^2 \quad (3.37)$$

where $a_e$= area of the circle and s = side of the hexagon. Since at optical frequencies metals appear with a negative permittivity therefore complex permittivity '$\varepsilon_{Ag}$' of silver (Ag) was calculated from equation (3.38) explained by the Drude model;

$$\varepsilon_{Ag} = \varepsilon_o \left\{ \varepsilon_\propto - \frac{f_{p^2}}{[f(f + i\gamma)]} \right\} = -128 + j3.28 \quad (3.38)$$



**This section has been published in International Journals of antenna and propagation Hindawi, July 2016.

where $\varepsilon_o$ = 8.85x10$^{-12}$[F/m], $\varepsilon_\propto = 5$, plasmonic frequency $f_p$ = 2175 THz, $f$ = central frequency and collision frequency $\gamma = 4.35$ THz. Figure 3.14 (b) illustrates the antenna operating in the transmitting (Tx) mode by means of propagation vector orientation *(k)*.The magnetic and electric field distributions of the hexagonal dielectric and nanostrip waveguide, along with the wave propagation in the y-axis, is also shown. Optical nantennas can be excited with a few known techniques; (1) coupling of light using the so called nanotapers since nano antennas cannot handle much power because of their small footprints, this makes them ideal candidates for being excited by micro lasers such as micro disks and photonic crystal lasers and (2) by reducing the reflection induced power loss by using slot dielectric waveguides [55].

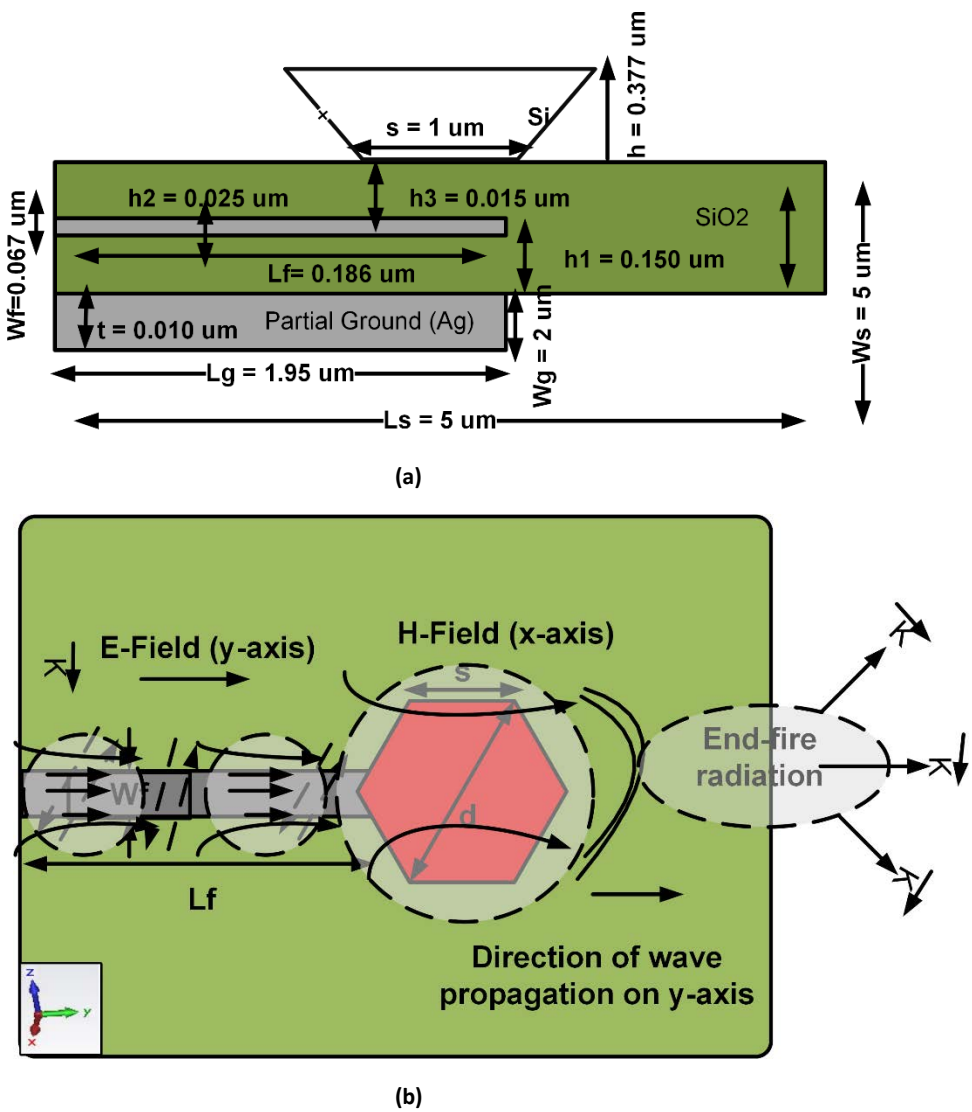


**Figure 3.14 Geometry of Hexagonal Dielectric Loaded Nantenna (HDLN) (a) cross sectional view (b) Front View with field vectors**

### 3.6.2 Design Simulation and Optimisation

In this section, the use of the optimization techniques available through the simulator are used. Investigation on the performance of each parameter involved in the design geometry of the proposed nantenna as shown in Figure 3.14 is one. In order to study the impact on the antenna performance in terms of bandwidth, the following parameters have been studied and analyzed;

a. **Nanostrip Feed:** Properties of conducting materials change when working at optical frequencies. The silver nano strip line used to feed the nantenna was analyzed in terms of Drude model. The nanostrip acts like a coupling resonator, that excites the hexagonal dielectric, placed on an upper $SiO_2$ substrate with height $h_3$. Traditionally at RF frequencies the length of the transmission lines are characterized to the wavelengths *(λ)* of incoming and outgoing radiations. However working at the optical frequencies most of the incident light is transparent through the metals. This gives rise to plasmonic free electrons thus the feed line is analyzed considering shorter effective wavelength $(\lambda_{eff})$ which depends on the material properties [53], refractive indexes and equations as listed above in equations (3.35) and (3.36). In simulations, the optimized dimensions of the feed line produced values of length $L_f$ to be 0.27 µm. The length $L_f$ of the nanostrip stub was optimized from 0.1 µm - 0.27 µm with the best optimized value producing required resonance at 193.5 THz was at $L_f$ = 0.186 µm as shown in Figure 3.15 (a). Similarly the width *'Wf'* of the nanostrip was also examined and optimization was done from 0.02 µm - 0.28 µm. Figure 3.15 (b) shows the best optimized value achieved at resonance of -22 dB with $W_f = 0.067\ \mu m$.

**b. Partial Ground Plane:** The effect of the ground plane was studied and its optimization gave dimensions of $L_g \times W_g$ = 1.95 µm x 2 µm. Figure 3.16 (a) and Figure 3.16 (b) show the effects of varying the partial ground plane in terms of its length and width. The optimized results produces a wide impedance bandwidth of 3.7 % (190.9 THz - 198.1 THz) at a center frequency of 193.5 THz, covering all of the standard optical transmission widow (C-band).

**c. Height of Hexagonal DR:** The wide impedance bandwidth achieved is also affected by the height of the hexagonal DR. The height h of the DR was optimized within the range ($\lambda g/4 < h < \lambda g/2$). Figure 3.17 shows the best optimized value of h = 0.37 µm having a resonance at -23 dB.

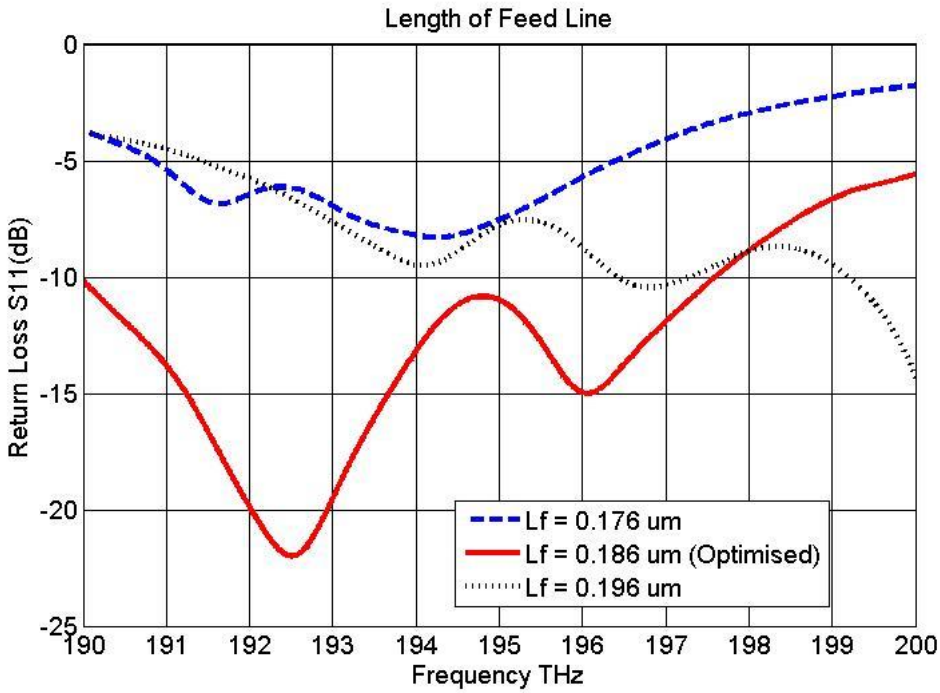


**(a)**

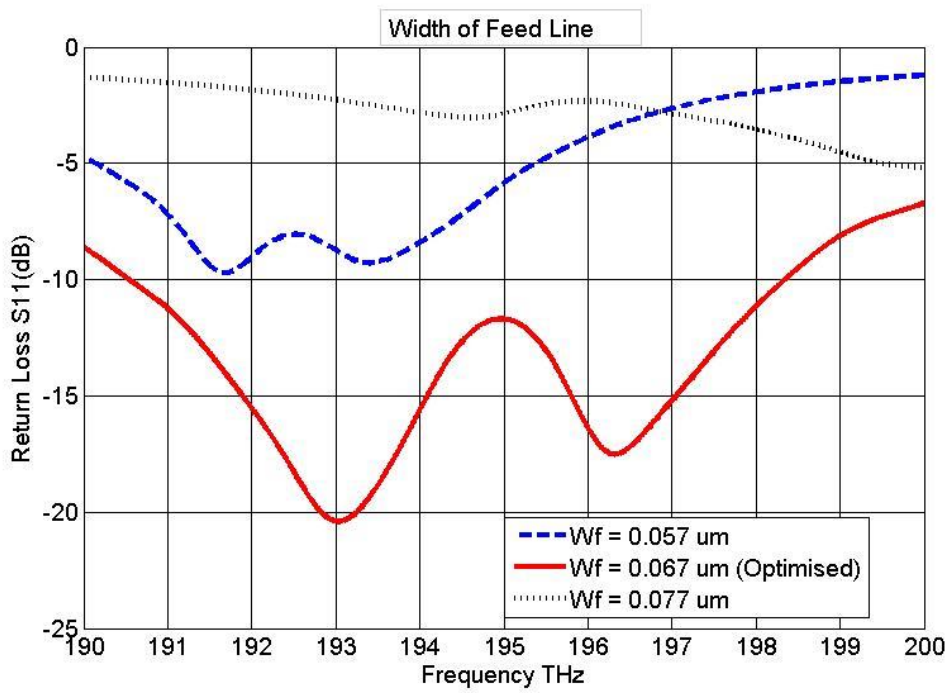


**(b)**

**Figure 3.15 Optimized Parameters: (a) Length of Feed Line (b) Width of Feed Line**

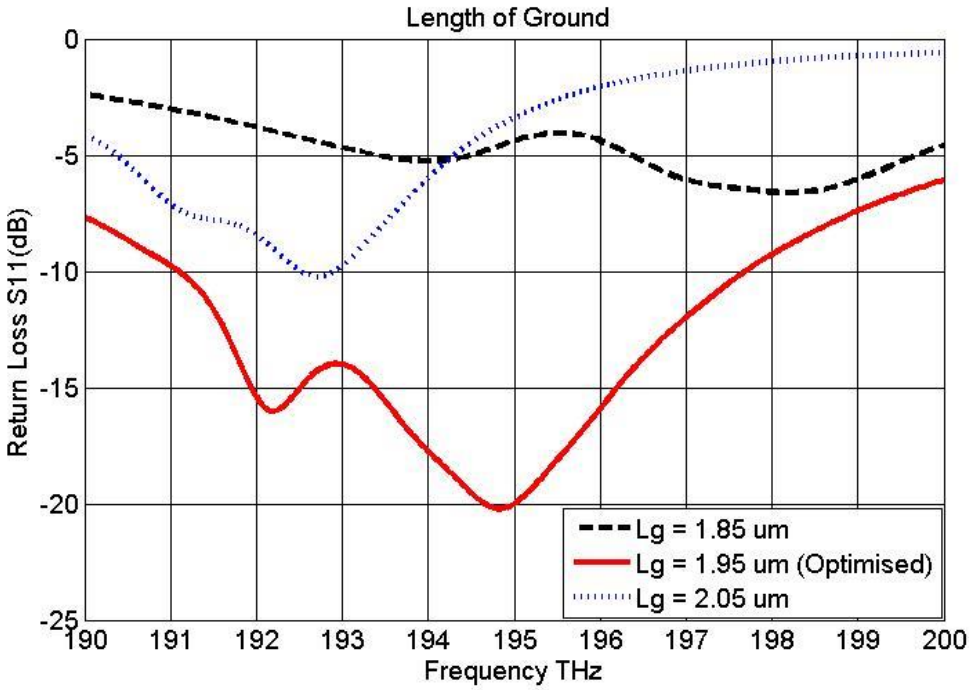


**(a)**

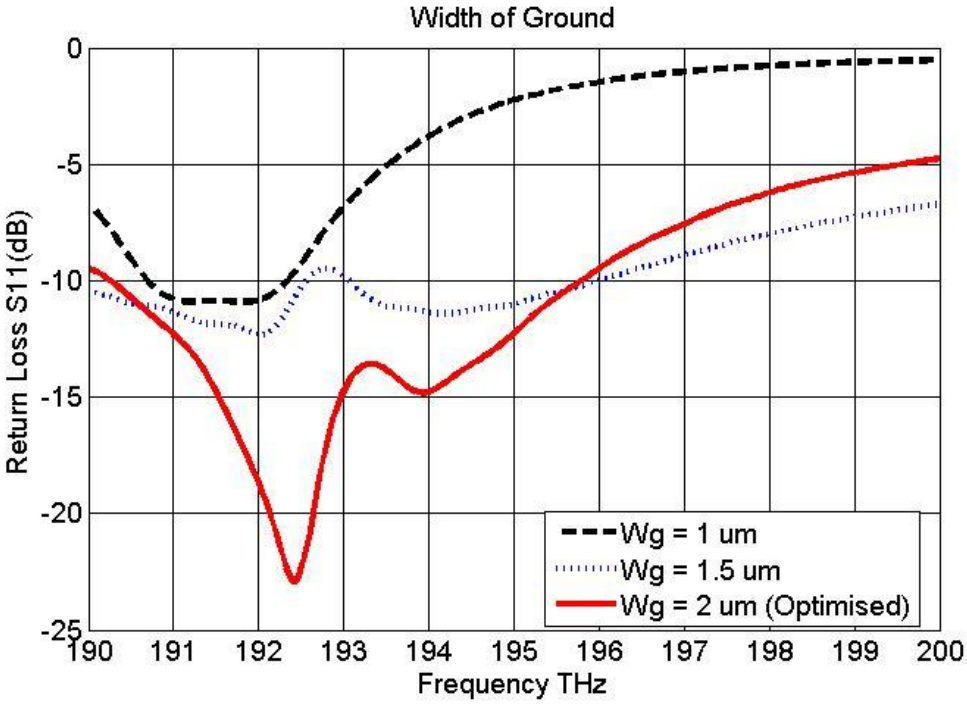


**(b)**

**Figure 3.16 Optimized Parameters: (a) Length of Ground Plane (b) Width of Ground Plane**

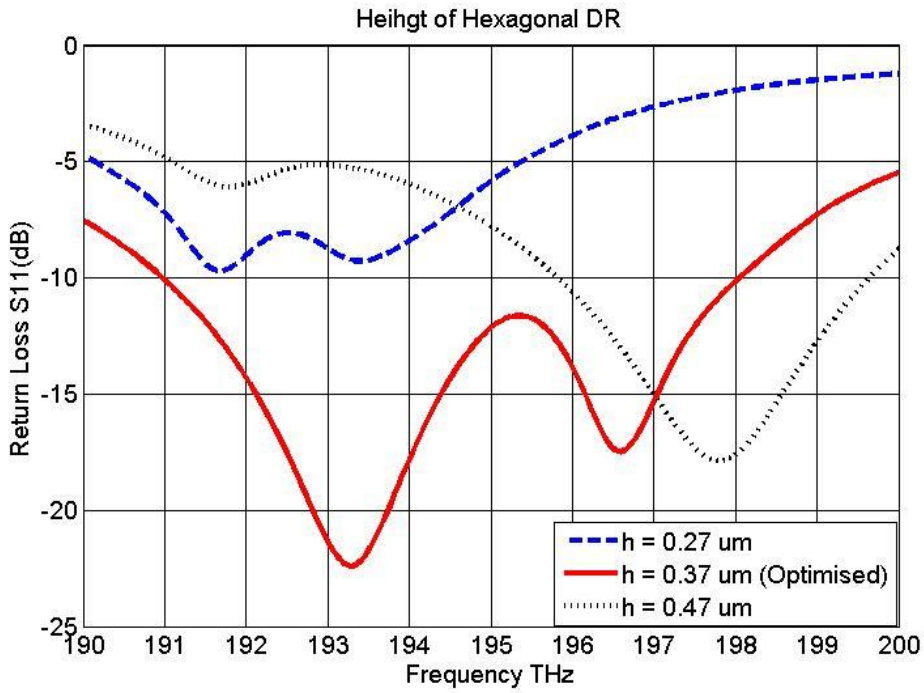


**Figure 3.17 Optimized Parameters: Height of Hexagonal DR**

## 3.6.3 Results and Discussion

To compare the properties and results of the proposed HDLN nantenna, I first simulated a hexagonal dielectric resonator antenna at the lower frequency band [49]. Observations were made in terms of plane wave propagation in the transmission lines to the radiating structures of the two antennas with results shown in Figure 3.18 (a) and Figure 3.18 (b) respectively. From Figure 3.18 (a) it can be observed that the E-field propagation or the power propagation in the transmission line is following the fringing effects in order to radiate the hexagonal structure operating in the microwave domain. Whereas the proposed nantenna structure depicted in Figure 3.18 (b), shows the E-field propagation in the nano transmission line follows a travelling wave effect. It is also observed that the hexagonal DR elements for both the cases exhibit different properties. At the microwave domain the hexagonal DR as shown in Figure 3.18 (a) works as a resonator while the DR at the nanoscale structure shown in Figure 3.18 (b) exhibits loading properties which benefits the nantenna to operate as a lens and thus achieve more directivity.

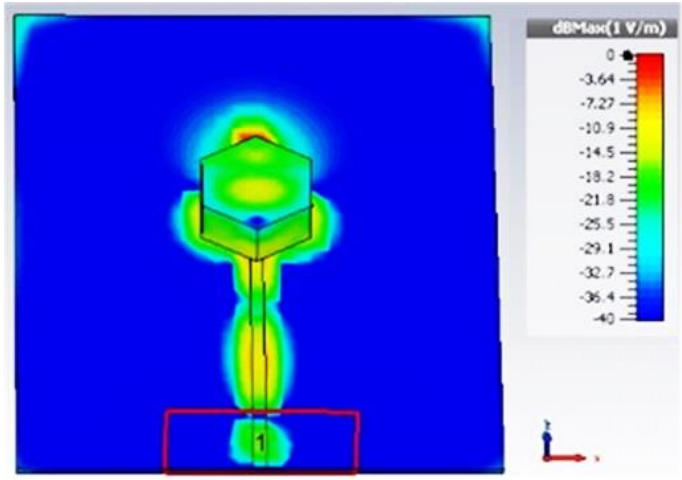


**(a)**

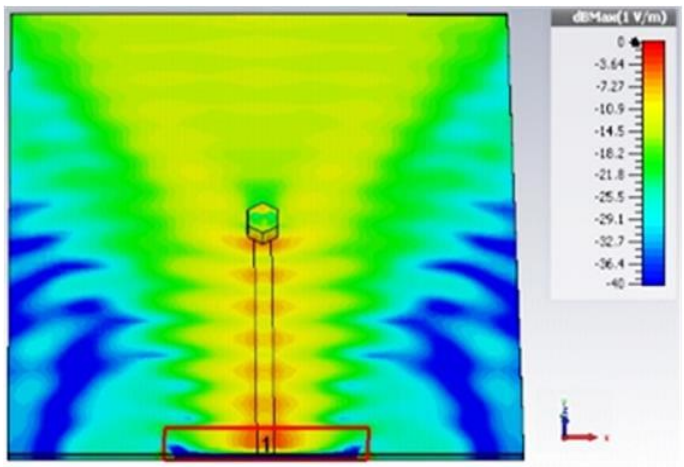


**(b)**

**Figure 3.18 E-Field Propagation: (a) Fringing effects at lower frequency (b) Travelling wave effect at THz spectrum**

The return loss ($S_{11}$) and directivity of the proposed HDLN with respective wavelength and directivity axis is shown in Figure 3.19. After extensive optimization, the nantenna achieves an impedance bandwidth of 3.7% (190.9 THz – 198.1 THz) with a directivity of 8.6 dBi, making it useful for nanoscale fabrication due to its robustness against fabrication tolerances.

Typically, the modes of hexagonal DR [56] are derived from the cylindrical dielectric resonator, which has three distinct types: TE (TE to z), TM (TM to z) and hybrid modes. The TE and TM modes are asymmetrical and have no azimuthal variation. On the other hand, fields produced by hybrid modes are azimuthally dependent. Hybrid mode is further divided into two subgroups of: HE and EH. The modes generated by the hexagonal dielectric nantenna is represented in terms of magnitude of electric field distribution on its surface as shown in Figure 3.20, at the center frequency of 193.5 THz. The mode analysis was done via EM simulator CST MWS.

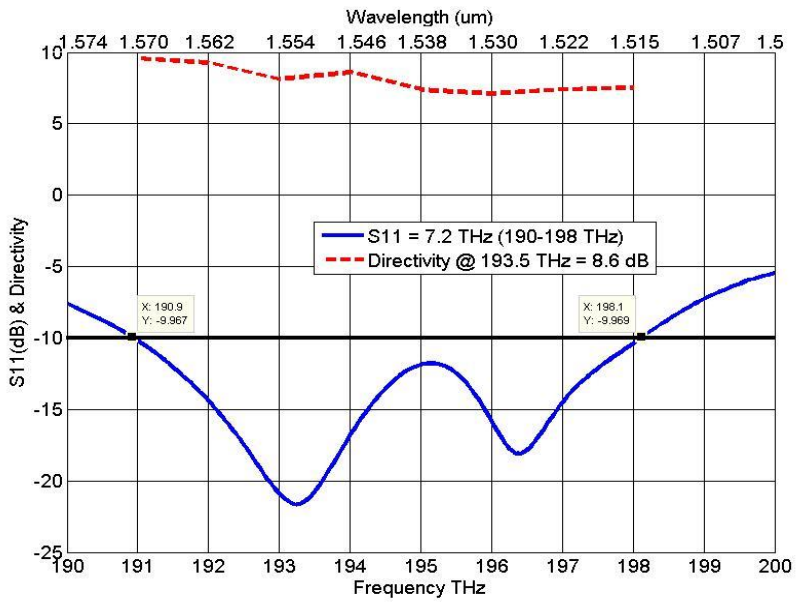


**Figure 3.19 Simulated return loss and Directivity of proposed HDLN**

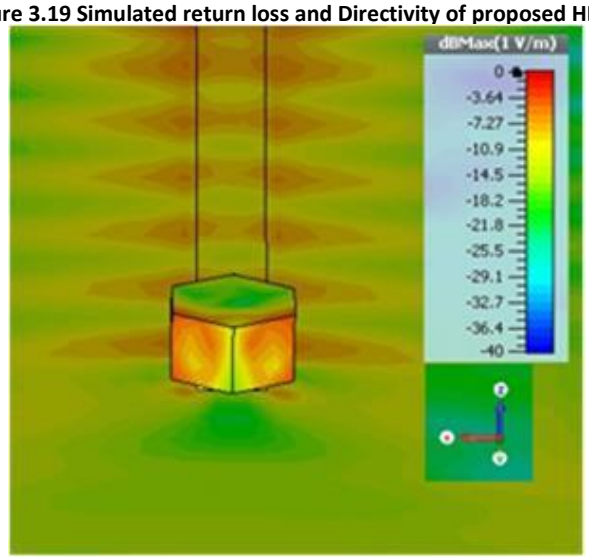


**Figure 3.20 E-field distribution as shown via the magnitude at 193.5 THz with HE20δ mode.**

From the infinite modes available [57], in the simulations as shown in Figure 3.20, it was observed that the nano hexagonal dielectric antenna producing $HE_{20\delta}$ mode between the achieved wide impedance band. The subscript in the modes represent the variation of fields along azimuthal, radial and z-direction of the cylindrical axis. It was observed from the figure that the magnitude of electric field variation is produced on the azimuthal direction with no variation in the radial direction thus giving a mode excited at $HE_{20\delta.}$ Also the intensity is highest at the azimuthal plane resulting in a radiation pattern towards the end-fire direction. The 3D radiation patterns of the nano antenna at 191 THz, 193.5 THz and 198 THz are shown in Figure 3.21 (a-c). The directivity of the antenna at the center frequency is 8.6 dBi. Keeping in mind the state-of-the -art nantenna designs and limited availability of nano fabrication equipment and facilities worldwide, we believe our

proposed theoretical HDLN design will prove itself to be a promising communication device for applications based on nano technology.

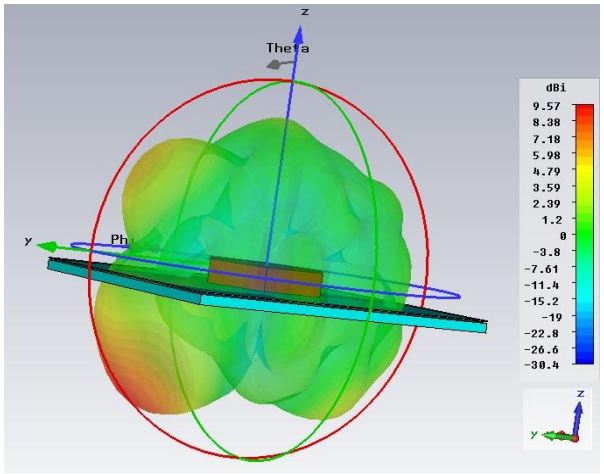


**(a)**

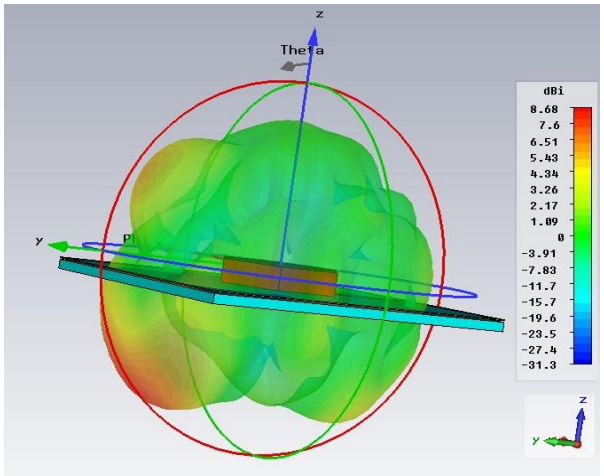


**(b)**

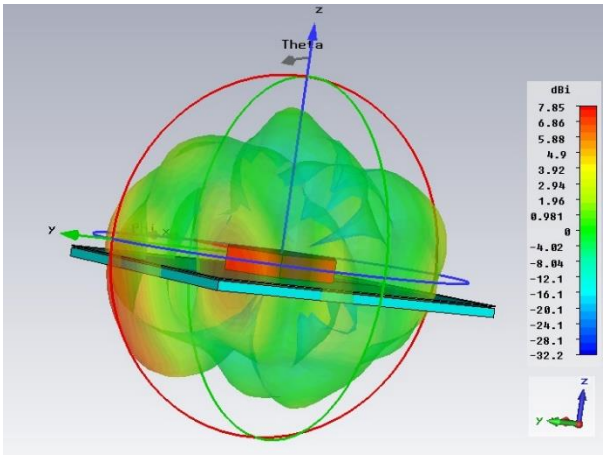


**(c)**

**Figure 3.21 3D radiation pattern: (a) 191 THz (b) 193.5 THz (c) 198 THz**

## 3.7 Array Synthesis**

This section presents the array synthesis done on one of the two proposed nantenna designs based on DR element. The ETDRN was opted for array optimisation. The ETDRN was fed via a 1 × 2 corporate feed network working at optical C-band (1.55 µm). Numerical results prove that the proposed nantenna exhibits a directivity of 9.57 dB with an impedance bandwidth of 2.58% (189–194 THz) covering the standard optical C-band transmission window. Furthermore, by selecting the appropriate orientation of the triangular dielectric resonators, the proposed nantenna structure can be tuned to operate at the higher or lower optical bands offering a threshold value of directivity and bandwidth $\Delta f$. By tuning the nantenna they achieve an increase in bandwidth of 4.96% (185.1–194.7 THz) and directivity also improves to 9.7 dB. The wideband and directive properties make the proposed nantenna attractive for a wide range of applications including broadband nanophotonics, optical sensing, optical imaging and energy harvesting applications.

### 3.7.1 Antenna Array Design Geometry

An array of 1x2 configuration for the ETDRN is presented. The front and side view is shown in Figure 3.22. The geometry of the proposed nantenna utilized the same parameters as the proposed ETRDN in the previous section. The gap between the elements to counter mutual coupling is around $(\lambda_{eff}/2)$ at the central frequency of 193.5 THz .The dimensions of the single element equilateral triangle dielectric based on frequency dependence can be calculated from equations (3.30) and (3.31) previously presented.

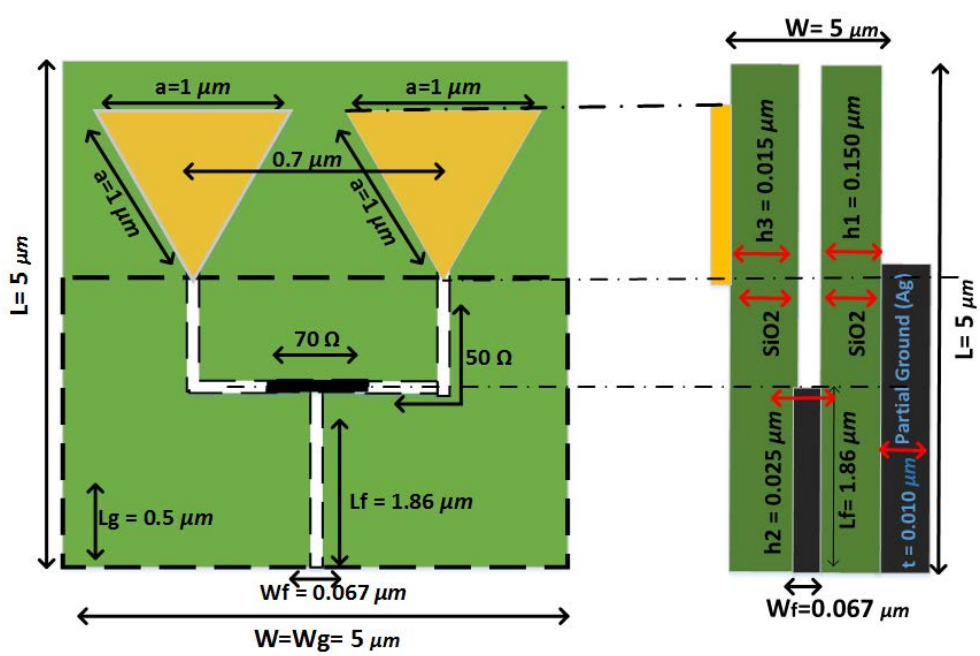


**Figure 3.22 Geometry of proposed 1x2 Array: (a) Front View (b) Side View**



***This section has been published in IET Micro & Nano Letters, Aug 2016.*

In order to increase the directivity of the proposed nantenna, arrays with a corporate feed network has been utilized for best power transfer from the source to the radiating ETDRN. Figure 3.22 shows the corporate feed network along with appropriate feed line (50 Ω and 70 Ω) markings. The optimized width of the 70 Ω feed line is 0.045 μm while the length is 0.76 μm. For the 50 Ω feed line, the width and length are $W_f$ and $L_f$ respectively. The shaded region in black shows the partial ground and feed lines to be on the back side of the substrate. The optimum distance between the triangular plasmonic resonators achieve minimal mutual coupling at 0.7 μm center to center. The properties of the Noble metals are explained as per Drude Model used throughout the sections for the proposed nantenna designs.

### 3.7.2 Results and Discussion

In this section investigation of the proposed nanoantenna arrays resulted in terms of two important feature; 1) directivity improvement and 2) tuneability. Directivity is very important because it measures the power density the antenna radiates in the direction of its strongest emission, versus the power density radiated by an ideal isotropic radiator (which emits uniformly in all directions) radiating the same total power and on the other hand tuneability is an attractive feature as it makes antenna operational in various frequency bands simultaneously as well as resonating at its center frequency. In fact, during our performance analysis we learned the importance of the angle of rotation between the triangular structure and the feed line direction. In the following paragraph and the next section the performance study is addressed when this angle is zero and then investigate the importance when different angles are introduced.

The simulated return loss ($S_{11}$) and directivity of the proposed 1x2 nantenna array is presented in Figure 3.23. The proposed nantenna achieves an impedance bandwidth of 2.58 % with $S_{11}$ < -10 dB (189 THz – 194 THz) at a center frequency of 193.5 THz (1550 nm) with a dip at -15 dB. The antenna covers all the portion of the standard C-band transmission window in optical domain and can be used for relevant optical applications in nano networks and high speed optical data transfer. The 3D radiation plot of the nantenna resonating at 193.5 THz is shown in Figure 3.24. The directivity of the nantenna is 9.57 dBi, 0.97 dB improvement compared to the single element ETDRNA discussed in section three. CST MWS studio has been used to acquire the optimize results with verification done by another EM simulator HFSS. Examining the plot in Figure 3.24 reveals the E-field component having main lobe direction at 45°, side lobe levels at -4.1 dB and beam width of 20.1°. Similarly the H-field component in Figure 3.24 has main lobe direction of 180°, side lobe levels of -1.5 dB and beam width of $127.2^0$. Although the nantenna achieved a directive nature, the losses associated with high side lobe levels are to be expected due to substrate selection and working at higher THz frequencies.

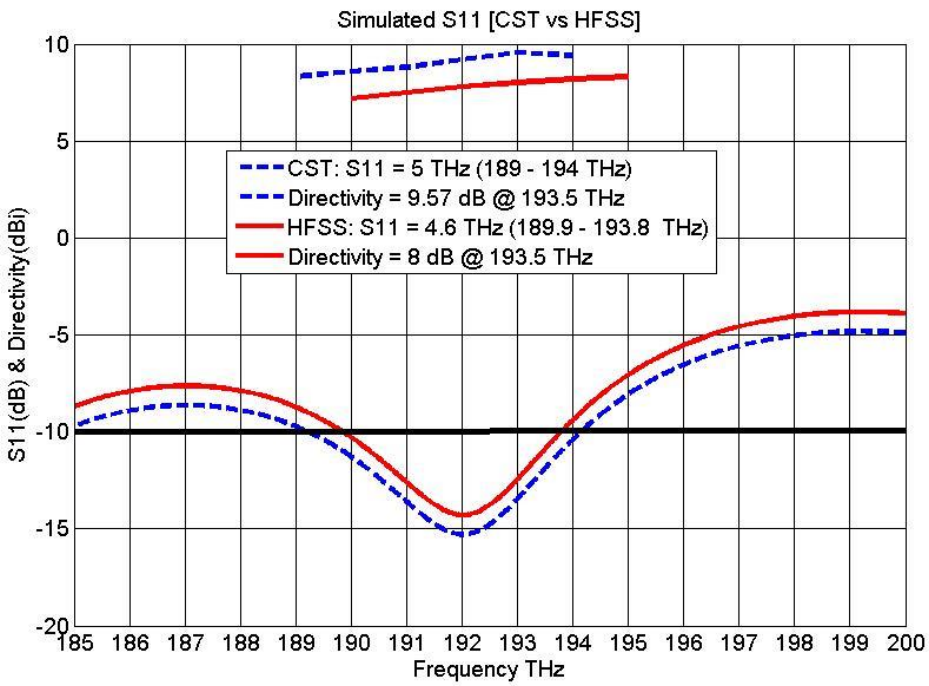


**Figure 3.23 Return Loss and Directivity of 1x2 ETDRN Array**

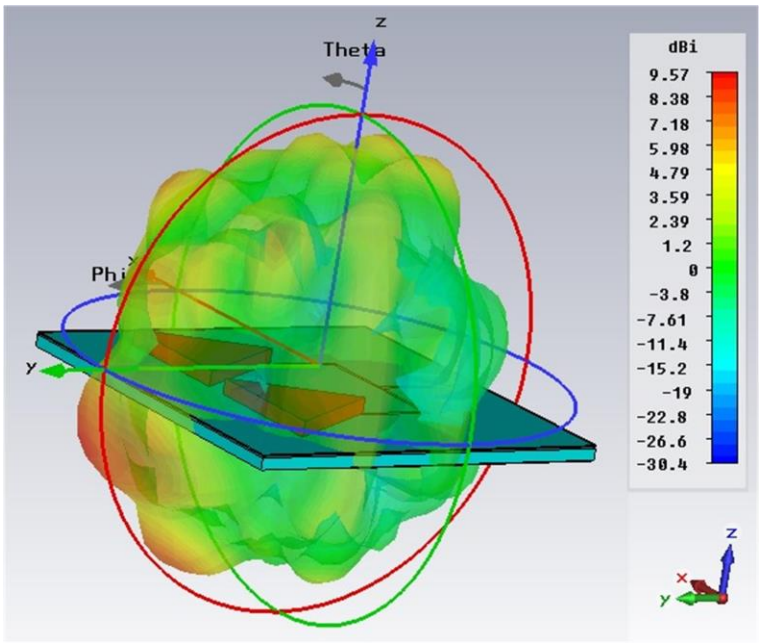


**Figure 3.24 3D radiation pattern at 193.5 THz**

### 3.7.3 Tuneability of proposed 1x2 ETDRNA Array

Achieving an antenna design for a specific frequency band (wide, notch or filter) with tuneable (or changeable) center frequency is an important challenge task. The proposed nantenna array structure achieves this task and offers a large flexibility to the antenna in terms of operating frequency for a wide range of applications. Various parameters and design strategies such as loading slots, lumped components, switches, diodes and capacitors are introduced in order to achieve this feature. Although the utilized design has a corporate feed network and the antenna geometry is based on nano scale dimensions, which means more parametric study, but the simple and featured equilateral shape of the DR elements enables to make natural yet simple tuneability. Figure 3.25 shows the rotation angles of the two equilateral triangular DR elements (T1 and T2). Since it is an equilateral triangle, the rotation angles were swept from (-180º to 180º) with a step size of 10º. The rotation angle is defined as counterclockwise movement from the bottom tip of the triangle. Three scenarios of rotations were applied: (i) rotate T1 while T2 is fixed (Figure 3.25a), (ii) Fix T1 and rotate T2 (Figure 3.25b), and (iii) simultaneously rotate T1 and T2 in the same counterclockwise direction (Figure 3.25c). In all the three scenarios, as shown in Figure 3.25, the simulation of rotation was done for the whole 360 º but only five rotating angles have been shown i.e. (0 º, +60 º, +90 º,-60 º,-90º) for purpose of simplicity. For this case of center frequency at 193.5 THz, the best resonance with improved bandwidth of 4.96 % (185.1 THz – 194.7 THz) and a directivity (9.7 dBi) is achieved when we opted to select the angles of T1 and T2 to be -90º and 90º respectively. Figure 3.26 displays the results in terms of s-parameters and directivity for rotation of triangles T1 and T2.

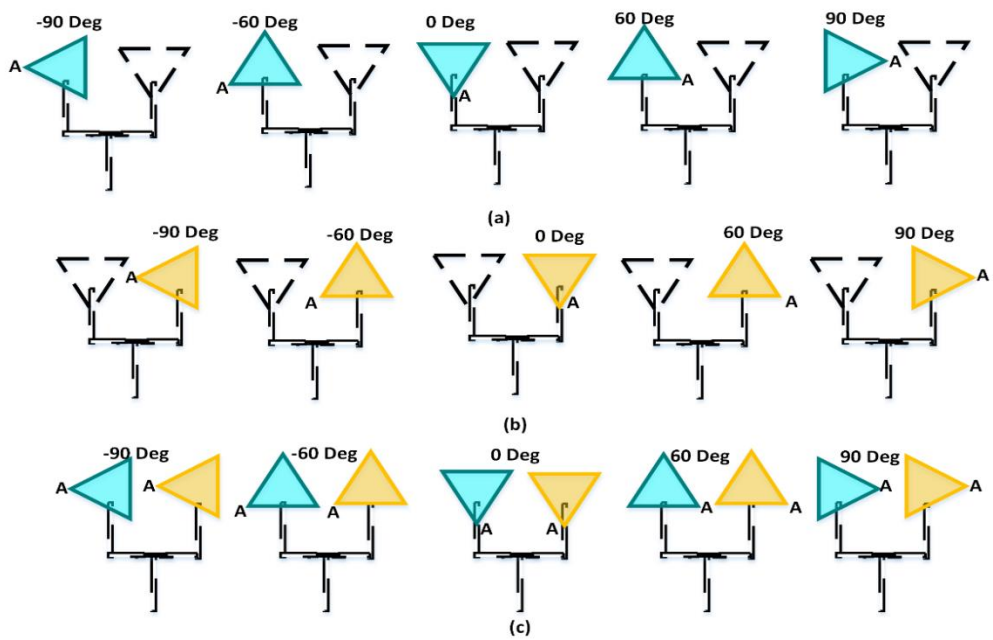


**Figure 3.25 Rotation scenario of triangular DR's for spectral shifts (a) Rotate Triangle T1 (Left) (b) Rotate Triangle T2 (Right) (c) Rotate both T1 and T2 simultaneously +/- 90o**

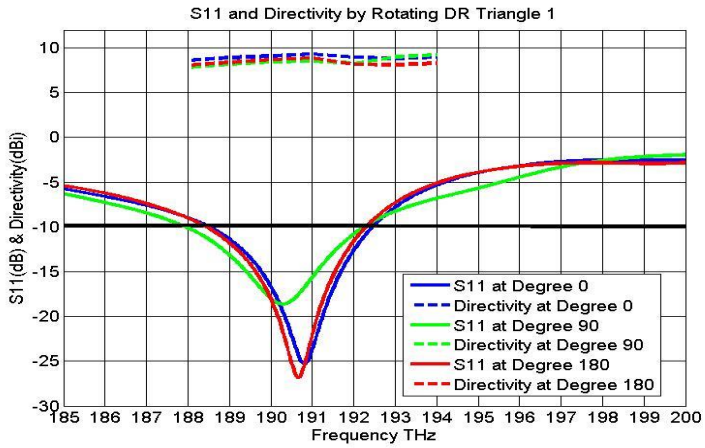


**(a)**

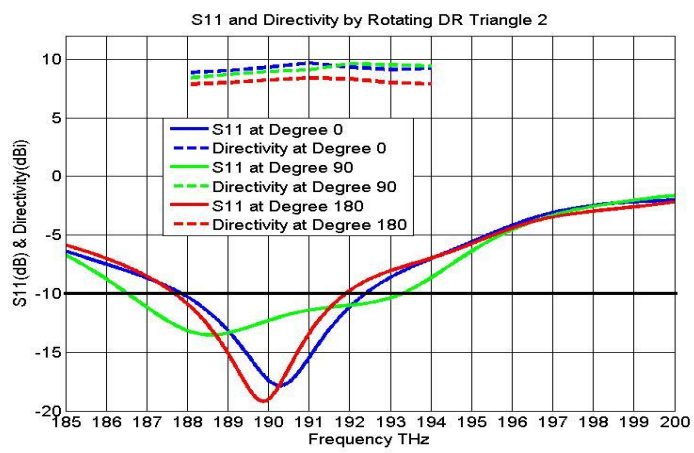


**(b)**

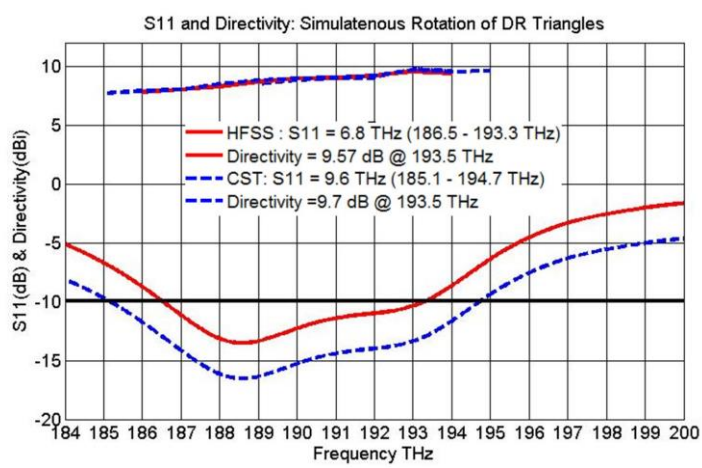


**(c)**

**Figure 3.26 Return Loss and Directivity as per Rotation (a) T1 Rotated (b) T2 Rotated (c) Both T1 and T2 simultaneously rotated**

Figure 3.27, details of the E-field (yz-axis) shows main lobe at a direction of 45 °, side lobe levels of -4.5 dB and beam width of 19°, whereas the H-field (xz-axis) has a main lobe direction of 115 °, side lobe levels of -2.6 dB and beam width of 99.8° with a lot of losses in terms of high side lobe levels at a higher frequency. Figure 3.27 shows the tuneability effects of simulataneous rotation of triangular DRs' in terms of the minimum and maximum values achieved for directivity and also the bandwidth difference $\Delta f$ at -10 dB resonance in the frequency band (185 THz–195 THz). The minimum directivity achieved is 7.15 dB and the maximum achieved is 9.71 dB when the triangles are tuned. Similary the difference of bandwidth $\Delta f$ ranges from a minimum to maximum of 4 THz to 9 THz respectively.

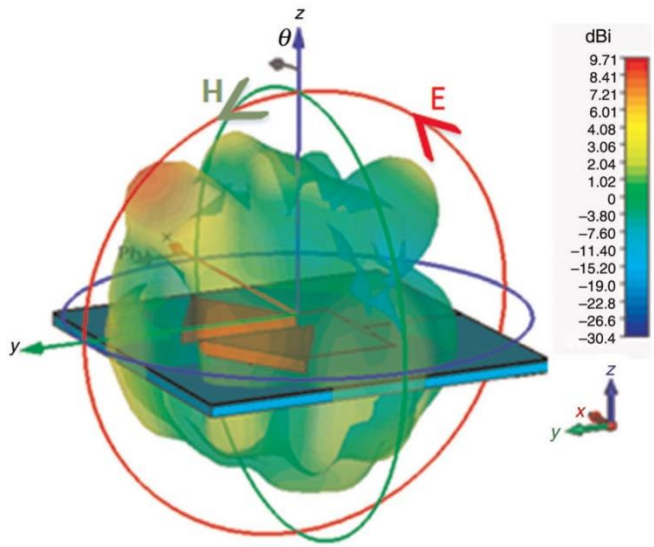


**Figure 3.27 3D radiation pattern of directivity at 193.5 THz after appropriate**

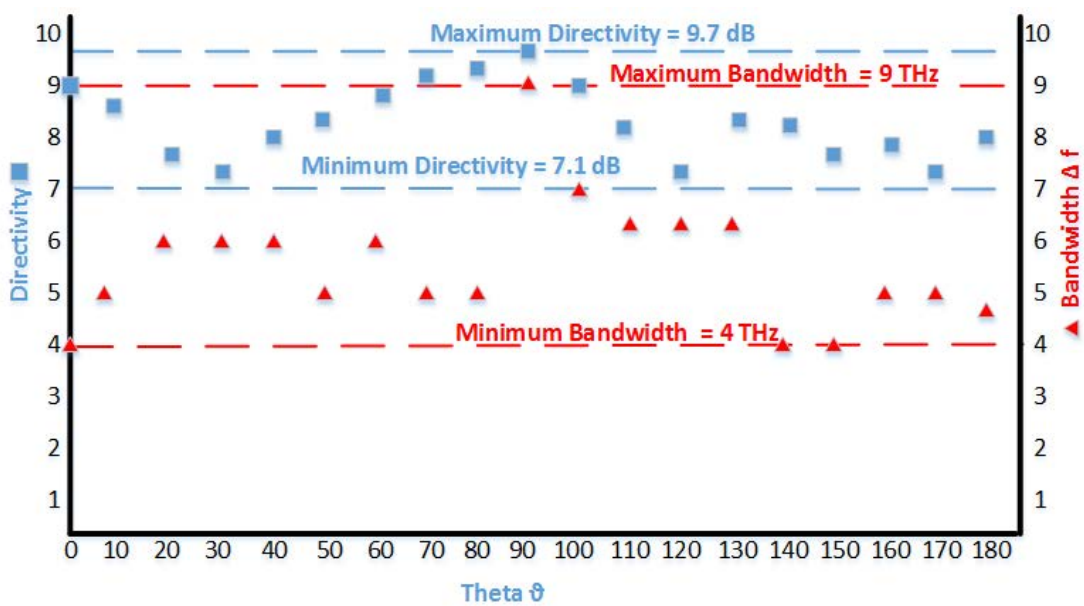


**Figure 3.28 Effect of Tuneability on Directivity and fractional bandwidth**

## 3.8 Summary and Conclusion

In this chapter, two new optical nantenna designs working at center frequency of 193.5 THz (1550 nm wavelength) were presented. Dielectric resonators, which are ceramic based having very high dielectric permitivity, were used to assist the metallic designs mostly utilized in making plasmonic nanaoantennas. Keeping with the offered characteristics of DR, suggestions were made on two nantenna designs with triangular and hexagonal shaped DR material. Both the designs are based on multilayer technology where the ground and transmission lines are made from Noble metal silver. The properties of silver at optical domain are discussed and defined on the basis of Drude Model. The first deign ETDRN achieved an impedance bandwidth of 2.58 % (192.3 THz - 197.3 THz), whereas the second nantenna design with hexagonal shaped DR, HDLN, offered and an impedance bandwidth of 3.7% (190.9 THz – 198.1 THz). Both the nantennas achieved high directivity of 8.6 dBi with end-fire radiation pattern. Array synthesis was also performed, in order to compare and observe how much improvement is possible. The 1x2 ETDRN achieved an improvement of 0.97 dB compared to the original directivity. Also the array antenna offers tuneability in simple manner, compared to other methods discussed, making the proposed nantenna adaptable to many other optical frequency bands of interest for various optical communications.

# Bibliography


[1] S. Cherry, Edholm's law of bandwidth, IEEE Spectr. 41 (7) (2004) 58–60.

[2] Q. C. Li, H. Niu, A. T. Papathanassiou and G. Wu, "5G Network Capacity: Key Elements and Technologies," in *IEEE Vehicular Technology Magazine*, vol. 9, no. 1, pp. 71-78, March 2014.

[3] J. Stephan, M. Brau, Y. Corre and Y. Lostanlen, "On the Effect of Realistic Traffic Demand Rise on LTE-A HetNet Performance," *2014 IEEE 80th Vehicular Technology Conference (VTC2014-Fall),* Vancouver, BC, 2014, pp. 1-5.

[4] M. Gregori, J. Gómez-Vilardebó, J. Matamoros and D. Gündüz, "Wireless Content Caching for Small Cell and D2D Networks," in *IEEE Journal on Selected Areas in Communications*, vol. 34, no. 5, pp. 1222-1234, May 2016.

[5] Ben Mustafa, Ibrahim, Mostafa Uddin, and Tamer Nadeem. "Understanding The Intermittent Traffic Pattern Of HTTP Video Streaming Over Wireless Networks". *2016 14th International Symposium on Modeling and Optimization in Mobile, Ad Hoc, and Wireless Networks (WiOpt) (2016):* n. pag. Web. 6 Mar. 2017.

[6] TU/e to develop 5G technology with European grant, https:// www.tue.nl/en/university/news-and-press/news/13-05-2016tueto- develop-5g-technology-with-european-grant/.

[7] Valdes-Garcia, Alberto, Su-Khiong Yong, and Pengfei Xia. 60Ghz Technology For Gbps Wlan And Wpan. 1st ed. Hoboken, N.J.: Wiley, 2013.

[8] Chester, Edward. "4.6Gbps Wi-Fi: How 60Ghz Wireless Works—And Should You Use It?", Ars Technica. N.p., 2017. Web. 6 Mar. 2017.

[9] Researchers Demonstrate World's First 5G, 100 To 200 Meter Communication Link Up To 2 Gbps". *Phys.org*. N.p., 2017. Web. 6 Mar. 2017.

[10] T. Kürner, S. Priebe, Towards THz communications-status in research, standardization and regulation, *J. Infrared Millim. Terahertz Waves* 35 (1) (2014) 53–62.

[11] Nagatsuma, Tadao, Guillaume Ducournau, and Cyril C. Renaud. "Advances In Terahertz Communications Accelerated By Photonics". *Nature Photonics* 10.6 (2016): 371-379.

[12] V. Petrov, A. Pyattaev, D. Moltchanov and Y. Koucheryavy, "Terahertz band communications: Applications, research challenges, and standardization activities," *2016 8th International Congress on Ultra Modern Telecommunications and Control Systems and Workshops (ICUMT*), Lisbon, 2016, pp. 183-190.

[13] Lukasz Lopacinski, Marcin Brzozowski, and Rolf Kraemer, "Data Link Layer Considerations for Future 100 Gbps Terahertz Band Transceivers," *Wireless Communications and Mobile Computing*, vol. 2017, Article ID 3560521, 11 pages, 2017.

[14] Yilmaz, Turker and Ozgur B. Akan. "On The Use Of Low Terahertz Band For 5G Indoor Mobile Networks". Computers & Electrical Engineering 48 (2015): 164-173.

[15] Akyildiz, I. F., Jornet, J. M. & Han, C. Terahertz band: Next frontier for wireless communications. *Phys. Commun*. 12, 16–32, 10.1016/j.phycom.2014.01.006 (2014).

[16] S. Obayya, N. F. F. Areed, M. F. O. Hameed, and M. Hussein, "Optical nano-antennas for energy harvesting," in *Innovative Materials and Systems for Energy Harvesting Applications*, Hershey, PA, USA: IGI Global, 2015, ch. 2, p. 26.

[17] Y. Yang, Q. Li, and M. Qiu, "Broadband nanophotonic wireless links and networks using on-chip integrated plasmonic antennas," *Sci. Rep.*, vol. 6, 2016.

[18] L. Yousefi and A. C. Foster, "Waveguide-fed optical hybrid plasmonic patch nano-antenna," *Opt. Express* 20(16), 18326–18335 (2012).

[19] Hong, SoonGweon et al. "Bioinspired Optical Antennas: Gold Plant Viruses". *Light: Science & Applications* 4 (2015).

[20] Horiuchi, Noriaki. "Optical Antennas: Reconfigurable Resonance". *Nature Photonics* 10.5 (2016).

[21] J.M. Jornet, I.F. Akyildiz Channel modeling and capacity analysis for electromagnetic wireless nanonetworks in the terahertz band *IEEE Trans. Wireless Commun*., 10 (10) (2011), pp. 3211–3221.

[22] L. Novotny and N. van Hulst, "Antennas for light," *Nat. Photon*. 5, 83–90 (2011).

[23] E.D. Palik, Handbook of Optical Constants of Solids, Academic Press, New York, 1998.

[24] P.B. Johnson and R.W. Christy, *Phys. Rev*. B 9 (1974) p.5056–5070.10.1103/PhysRevB.9.5056.

[25] A.E. Krasnok, I.S. Maksymov, A.I. Denisyuk, P.A. Belov, A.E. Miroshnichenko, C.R. Simovski, and Yu.S. Kivshar. Optical nanoantennas. *Phys.-Usp*., 56:539, 2013.

[26] N. Vaso, "Interaction of normally incident polarized light with strained layered structure “dielectric-metal”," 2013 XVIIIth International Seminar/Workshop on Direct and Inverse Problems of Electromagnetic and Acoustic Wave Theory (DIPED), Lviv, 2013, pp. 59-62.
[27] Born, Max, and Emil Wolf. Principles of optics: electromagnetic theory of propagation, interference and diffraction of light. *Elsevier*, 1980.
[28] Jackson, John David, and Ronald F. Fox. "Classical electrodynamics." *American Journal of Physics* 67.9 (1999): 841-842.
[29] Fleisch, Daniel. A student's guide to Maxwell's equations. Cambridge University Press, 2008.
[30] N.W. Ashcro and N.D. Mermin, “*Solid state physics*. Holt, Rinehart and Winston.
[31] A. I. Fernández-Domínguez; A. Wiener; F. J. García-Vidal; S. A. Maier; and J. B. Pendry,” Transformation-optics description of nonlocal effects in plasmonic nanostructures. In Phys. *Rev. Lett.,* vol. 108, 2012.
[32] Markovic, Mihailo I., and Aleksandar D. Rakic. "Determination of the reflection coefficients of laser light of wavelengths λ∈(0.22 μm, 200 μm) from the surface of aluminum using the Lorentz-Drude model." *Applied optics* 29.24 (1990): 3479-3483.
[33] S. Mokkapati and K. R. Catchpole, “Nanophotonic light trapping in solar cells. *In Journal of Applied Physics*, vol. 110, no.10, 2012.
[34] Patel, Shobhit K., and Christos Argyropoulos. "Plasmonic nanoantennas: enhancing light-matter interactions at the nanoscale." (2015).
[35] Dobson, Peter J. "Nanoantenna Plasmon-Enhanced Spectroscopies for Biotechnological Applications, edited by Marc Lamy de la Chapelle and Annemarie Pucci." *Contemporary Physics* 56 (2015): 506-506.
[36] Zhang, Xiaoming, et al. "Dual-Band Unidirectional Emission in a Multilayered Metal–Dielectric Nanoantenna." *ACS Omega* 2.3 (2017): 774-783.
[37] Belov, Pavel A., et al. "Superdirective all-dielectric nanoantennas: theory and experiment." IOP Conference Series: *Materials Science and Engineering*. Vol. 67. No. 1. IOP Publishing, 2014.
[38] D. S. Filonov, A. E. Krasnok, A. P. Slobozhanyuk, P. V. Kapitanova, E. A. Nenasheva, Yu. S. Kivshar, P. A. Belov, *Appl. Phys. Lett.,* vol. 100, 201113, 2012.
[39] Linnenbank, Heiko, et al. "Second harmonic generation spectroscopy on hybrid plasmonic/dielectric nanoantennas." *Light: Science & Applications* 5.1 (2016).
[40] Malhat, Hend A., et al. "Reflectarray Nano-Dielectric Resonator Antenna Using Different Metals." *Applied Computational Electromagnetics Society Journal* 30.9 (2015).
[41] Lee, Eun-Khwang, et al. "Resonant light scattering from a single dielectric nano-antenna formed by electron beam-induced deposition." *Scientific reports* 5 (2015).
[42] Zou, Longfang, et al. "Dielectric resonator nanoantennas at visible frequencies." *Optics express* 21.1 (2013): 1344-1352.
[43] A. Petosa and A. Ittipiboon, “Dielectric resonator antennas: A historical review and the current state of the art,” *IEEE Antennas Propag. Mag.,* vol. 52, pp. 91–116, 2010.
[44] K. M. Luk and K.W. Leung (eds.), Dielectric Resonator Antennas, Baldock, England, Research Studies Press, 2003.
[45] A. Petosa, Dielectric Resonator Antenna Handbook, Norwood, MA, Artech House, 2007.
[46] Keyrouz and D. Caratelli, “Dielectric Resonator Antennas: Basic Concepts, Design Guidelines, and Recent Developments at Millimeter-Wave Frequencies,” *International Journal of Antennas and Propagation*, vol.10,pp 0-20, 2016.
[47] P. B. Johnson and R.W. Christy, “Optical constants of the noble metals,” *Physical Review B*, vol. 6, no. 12, pp. 4370–4379, 1972.
[48] R. Sinha, M. Karabiyik, C. Al-Amin, P. K. Vabbina,D. ¨ O.G¨uney, and N. Pala, “Tunable room temperature THz sources based on nonlinear mixing in a hybrid optical and THz micro-ring resonator,” *Scientific Reports*, vol. 5, article 9422, 2015.
[49] H.Y.Lo, K.W. Leung, K.M. Luk, andE.K.N.Yung, “Lowprofile equilateral-triangular dielectric resonator antenna of very high permittivity,” *Electronics Letters*, vol. 35, no. 25, pp. 2164–2166, 1999.
[50] A. A. Kishk, “A triangular dielectric resonator antenna excited by a coaxial probe,” Microwave and Optical Technology Letters, vol. 30, no. 5, pp. 340–341, 2001.
[51] Z. Li, H. T. Hattori, L. Fu,H.H. Tan, and C. Jagadish, “Merging photonic wire lasers and nanoantennas,” *Journal of Lightwave Technology*, vol. 29, no. 18, Article ID 5892863, pp. 2690–2697, 2011.
[52] C. Balanis, AntennaTheory: Analysis andDesign, JohnWiley& Sons, New York, NY,USA, 2005.
[53] R. L. Olmon and M. B. Raschke, “Antenna-load interactions at optical frequencies: impedance matching to quantum systems,” *Nanotechnology*, vol. 23, no. 44, Article ID 444001, 2012.

[54] F. Neubrech, D. Weber, R. Lovrincic et al., "Resonances of individual lithographic gold nanowires in the infrared," *Applied Physics Letters*, vol. 93, no. 16, Article ID 163105, 2008.
[55] H. T. Hattori, Z. Li, and D. Liu, "Driving plasmonic nanoantennas with triangular lasers and slot waveguides," *Applied Optics*, vol. 50, no. 16, pp. 2391–2400, 2011.
[56] V.Hamsakutty and K. T.Mathew,Hexagonal dielectric resonator antenna—a novel DR antenna forwireless communication [Ph.D. thesis], Department of Electronics, Cochin University of Science and Technology, Dyuhti , India, 2007.
[57] R. K. Mongia and P. Bhartia, "Dielectric resonator antennas—a review and general design relations for resonant frequency and bandwidth," *International Journal of Microwave and Millimeter- Wave Computer-Aided Engineering*, vol. 4, no. 3, pp. 230–247, 1994.

# Chapter 4
# Proposed Optical Antennas for Harvesting Infrared Energy

This chapter will present the simulated designs and experimental realization of the proposed optical antennas. Three antenna design techniques have been investigated that can focus the received THz waves or optical light and later convert it into output voltage by passing through the optical photodetectors. Some brief introduction to optical photodetectors will be presented with state-of-the-art detectors being used in two categories i.e. as thermal and electric detectors. Both of the categories will be analyzed with the three proposed optical designs. First technique uses Yagi-uda nantennas for capturing the light and then passing it to fermionics electric photodiode. The second technique, based again on electric photodetector, is polymer based where the PDMS lens shape is used for capturing and focusing the light. The final technique is based on thermal optical detection and conversion of light into electrical output. All the antennas presented in this chapter are viable candidates for harvesting infrared energy that is abundantly available from natural and artificial sources.

## 4.1 Introduction to Optical Photodetectors (PD)

Photodetectors (PD) hold an important position in optoelectronic integrated circuits as they convert light signals into electric signals. They are semiconductor based devices that work over a large spectrum of optical wavelengths with design guidelines based on geometric size and applications. The way in which PD work is based on the principle of photoelectric effect proposed in 1905 by Albert Einstein [1]. In its basic term, photoelectric effect is the process by which electrons lying on the surface of metals gets launched or emitted into free space via interaction with photons present in the incident light waves. Figure 4.1 shows the working principle of the photoelectric effect. It can be seen from figure 4.1(b-d) that when the light waves shine on the metal surface, the energy of photons must be large enough to excite the emission of electrons from the surface of metals. This energy is relative to a threshold frequency called the work function (∅). If the photon energy is equal to that of the threshold frequency, the electrons get emitted from their nucleus core leaving a vacant hole, but are unable to propagate for long distance in free space and thus remain on the metals surface. Finally, if the photon energy is higher than the threshold frequency, the electrons get emitted and the remaining photon energy gets translated into electrons kinetic energy.

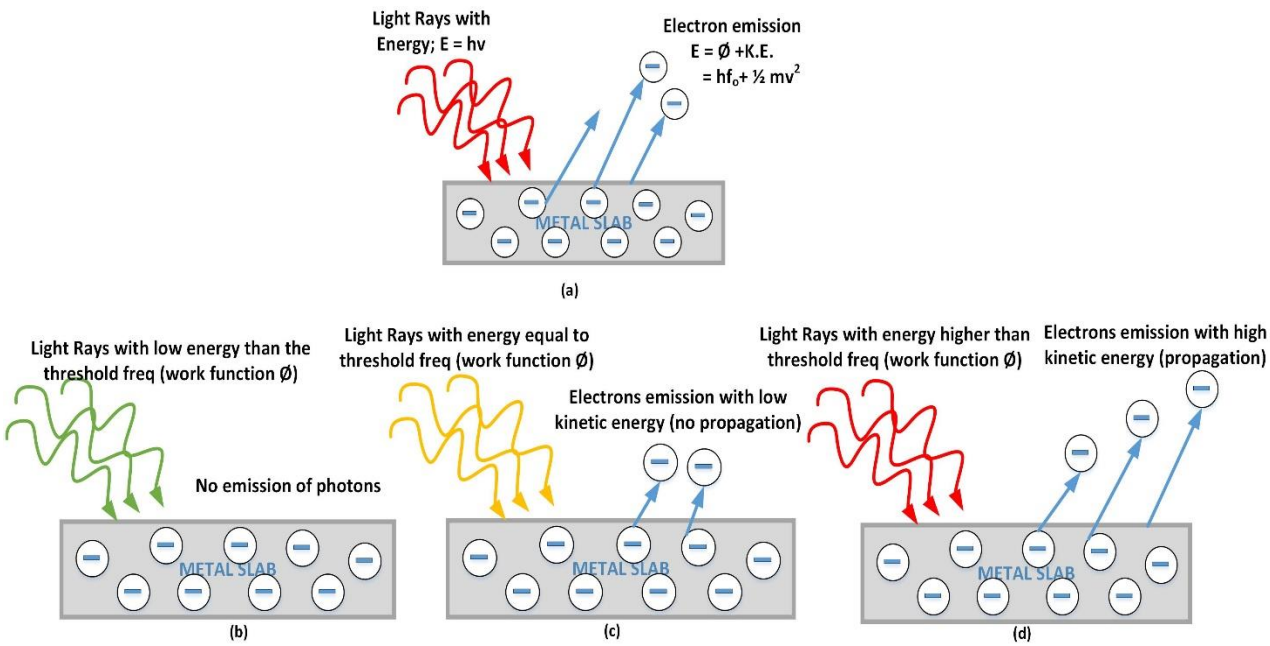


**Figure 4.1 (a) The photoelectric effect, (b) Light energy less than threshold frequency, (c) Light energy equal to threshold frequency and (d) Light energy higher than the threshold frequency**

The energy gained by the electron which is called the work function must be sufficient to make the electron cross the barrier height between the metal contact and the semiconductor with kinetic energy *(Ee).* The kinetic energy can be given as [1];

$$\boldsymbol{E_e = \frac{h_c}{\lambda} - \emptyset_m} \qquad (\mathbf{4.1})$$

where $c$ is the light velocity, $\emptyset m$ is the metal work function and $\lambda$ is the incident wavelength. Since the photoelectric effect is based on the photon energy $hv$, the wavelength of interest is related to energy transition $\Delta E$ in the device operation, with the following relationship:

$$\boldsymbol{\lambda = \frac{h_c}{\Delta E} = \frac{1.24}{\Delta E(eV)}\ \mu m} \qquad (\mathbf{4.2})$$

where $\Delta E$ is the transition of energy levels. Because the photon energy $hv > \Delta E$ can also cause excitation, Eq. 4.2 is often the minimum wavelength limit for detection. The transition energy $\Delta E$, in most cases, is the energy gap of the semiconductor. It depends on the type of photodetector, and it can be the barrier height as in a metal-semiconductor (MS) photodiode. [2]. In general, following performance parameters are observed when opting for an optical PD [3];

1. <u>Responsivity:</u> It is the sensitivity of the device which is defined as the ratio of output voltage signal per input power.
2. <u>Quantum efficiency (n %):</u> It is the ratio of electron generation rate to the incident photo rate.
3. <u>Detectivity:</u> It is the inverse of noise equivalent power received by the optical detector.

4. Response time: It defines the sudden change in response to a received signal. It shows how fast the detector process the rise and decay of a received signal.
5. Spectral response: It defines the changes in output signals as a functional change in input wavelength signal.

## 4.2 Optical Photodetectors for THz detection

Most of optical communications is based on the transmission wavelengths from 1300-1600 nm because this window offers less losses for most of the optical fiber technologies. Keeping this standard in mind, the photonic devices proposed and designed are made to work with this range of wavelengths. These photonics devices can be easily connected to external optical devices without a need for change and modifications [4-5]. Similarly, among these devices, optical photodetector (PD) is one such device that is designed and can be easily integrated at the end of these optical paths that can convert the light signal impinging on it into electrical signals. The PD can be categorized as per their applications at the THz domain. Most of them can be divided into two classes, i.e., 1) Thermal detectors and 2) photon semiconductor detectors. Following paragraphs will detail some of the state-of-the-art optical photodetectors been used for both cases.

1) Thermal detectors are fabricated with materials that show a strong change in their characteristics when the temperature is varied across their surface. The radiating thermal source affects the detecting material by the amount of absorbed energy, e.g., a change in their electrical conductivity or the expansion of gas molecules. The radiation is generally absorbed in a black surface coating giving a broad and uniform spectral response. However, the sensitivity of thermal detectors is low which means a huge amount of heat needs to be generated to acquire some higher output electrical signal in the form of voltage or current. Few examples of thermal and semiconductor based detectors are mentioned below with comparison in achieved literature results are presented in Table 4.1;

   a. **Bolometers:** A highly sensitive thermal detection device [6-7]. It detects the incident electromagnetic/heat radiation falling onto it and shows the output results as a change in temperature/resistance comparted to the initial reservoirs temperature to which it is connected via a thermal link.
   b. **Thermopiles:** They are the oldest thermal detection technique mostly used for infra-red detection [8-9]. They are formed when many thermocouples are connected either in series or parallel configuration. They operate on the combined principle of three effects (known as Seebeck, Peltier and Thomson effect) which states that when two dissimilar conducting metals are joined together at two different junctions, an electromotive force (emf) is produced a the two junctions due to varying temperature among the conductors. This varied temperature produces a change in voltage at their junction. This generated voltage is very small and often measured in microvolts (μV).

c. **Pyroelectrics:** Pyroelectric effect is observed in polar materials or crystals. Pyroelectric effect [10], is a less known property of certain materials in which changing temperature of a material homogeneously with for instance an incident radiation, it can generate a temporary voltage or a current flow across the material.

2) Semiconductor Detectors or photon materials on the other hand offer better sensitivity. It is due to the excitation and displacement of electrons, within the materials, that cause the bandgap, or charge space area, to expand, thus collecting more light into the device. The method of observing this output signal identifies two distinct categories of photon detectors, the photo-emissive device and the solid state sensors. In the former, the excited electrons are emitted from the photosensitive electrode into the surrounding medium, which may be either a vacuum or a gas. Whereas for solid state detector the photons cause a change in the electronic energy distribution within the material.

a. **Schottky diodes:** The Schottky detector is one of the basic and promising devices among THz detectors due to their fast response time and ability to operate both ambient and cryogenic temperatures. The fundamental principle of Schottky diodes depends on the physical mechanism of the Schottky barrier which is known to be a potential energy barrier formed when a metal and semiconductor are brought into contact as a junction. A substantial characteristic of the Schottky barrier is to have rectifying process which is a key property for functionality of diodes.

b. **MIM/MIIM diodes:** A very attractive and promising candidate for energy harvesting at infrared spectrum are the metal-insulator-metal (MIM) diodes. There high speed characteristics and compatibility with integrated circuits (IC's) makes MIM diodes good choice for infrared (IR) regime of the electromagnetic spectrum. Moreover, it is possible to obtain large volume of devices in same unit area due to smaller active area required for MIM diodes [11].

c. **Carbon nanotubes:** With the advancements in nano fabricating technology, the next generation of photodetectors will be low dimensional materials. One such example is of carbon nanotubes (CNT) [12] based optical photodetectors. CNT are 1D structures with diameters of a few nanometers and lengths that be scaled up to centimeters. By controlling the arrangement of the carbon atom structure with respect to their axis (e.g. indices (n, m)), CNTs could be direct band gap semiconductors, or even metals with nearly ballistic conduction. The band gap of the CNT is inversely proportional to its diameter (the band gap ranges from 0.2 to 1.5 eV for CNT diameter from 0.8 to 3 nm), which allows CNT photodetection from ultraviolet to infrared [13].

| | Thermal Detectors | | | Semiconductor Detectors | | |
|---|---|---|---|---|---|---|
| | **Bolometers** | **Thermopiles** | **Pyroelectric** | **Schottky** | **MIM** | **CNT** |
| **Reference** | [14] | [15] | [16] | [17] | [18] | [19] |
| **Application** | THz imaging | Polarimetry imaging | Examining THz radaitions | Spectrometer | Infrared rectification | Optical rectenna |
| **Design** | Skirt antenna, dual polarization | Gold nano rods | Commercial pyroelectric sensor MG33 coupled with inhouse PP-absorber | Patch antenna integrated with coplanar waveguide | Various materials for diode implementation | 10 nm nano antenna rods array |
| **Output** | Responsivity at 600 mA/W | Responsivity at 43 mV/W | 4V for just 2.3 ms | 0.01 V at -10 dBm power | Responsivity 15 A/W | Responsivity at 0.4 A/W |
| **Fabrication technology** | 0.18 um SOI-CMOS micromachine using MOFSET bolometer | E-beam and PECVD | Photolithography | On chip antenna | E-beam lithography | Multiwalled CNT using LPCVD |
| **Dimensions** | 19 x 19 pixel each with 250 x 250 $um^2$ | 24 x 24 $um^2$ | 2.47 x 2.3 $mm^2$ | 400 x 545 $um^2$ | Silicon Wafer | Silicon Wafer |
| **Frequency** | 0.6-1.2 THz | 40 THz | 0.14 THz | 0.1-1.5 THz | 193 THz | 193 THz |
| **Journal** | IEEE Transaction | Nature | Nature | IEEE MTTS | Optics SPIE | Nature |
| **Year** | Nov 2015 | Oct 2016 | Feb 2016 | 2016 | 2016 | Oct 2015 |

**Table 4.1 Comparison among the state-of-the-art in thermal and semiconductor optical detectors**

The presented PD in the above section are capable of working in the THz domain of the electromagnetic spectrum. Some of them are able to detect the whole range while others are application specific. Two types of PD have been explained. One of them is based on thermal detection that detects and converts thermal energy into electrical voltage. The other is based upon traditional electron movement from the conduction band to valence bands. Both of them have their pros and cons. For this research work, it was seen from the state-of-the-art that there still is window to explore optical antenna designs integrated with optical photodectors in both the domains i.e. thermal and semiconductor based. Therefore in the following sections, various optical antennas will be presented, they will be realized, integrated with photodetectors from both the domains i.e. thermal and semiconductor based and experimented via excitation form a laser source operating at 1550 nm wavelength.

## 4.3 Optical Antenna Design I: Yagi-uda Antenna with Fermionics Photodiode

In this section, the first design technique for the optical antennas will be presented. The objective of this design was to have an antenna that can capture infrared radiation and also have good gain and directivity. The intended frequency band or wavelength of the antenna will lie in the 193.5 THz frequency or its equivalent 1550 nm optical communication window. Simulation designs will be followed by realization of the proposed antenna. The materials for the proposed antennas were selected as per availability in the nano fabrication labs at Rennes University. Antenna designs with various materials will be tested and realized on silicon substrate followed by voltage detection by integrating the optical antennas with fermionics photodiode. Figure 4.2 shows the general depiction of the experimental setup of the proposed first technique of energy harvesting.

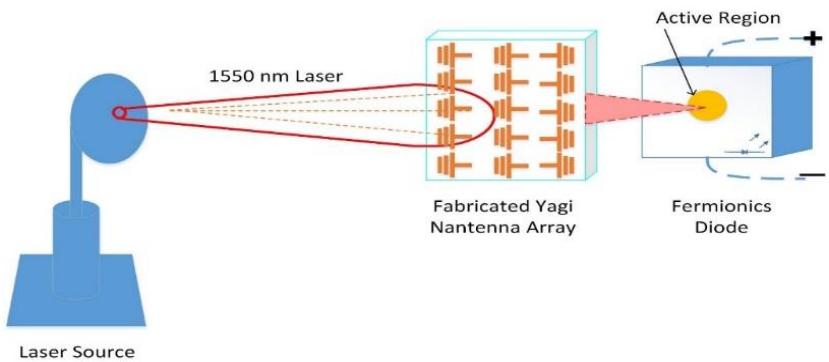


**Figure 4.2 Proposed experimental setup for the first technique for harvesting energy.**

### 4.3.1 Molybdenum based Yagi-uda Antenna Design

In order to meet the requirements of the optical antenna that can harvest infrared energy, Yagi-uda design was selected. The generic design for the Yagi-uda, shown in Figure 4.3, consists of a main driven or a feeding element in the center with a large reflector on its back and some directors on its front. The antenna is excited via the feeding element while the rest of the elements are working on the principle of parasitic or coupling properties of the antenna [20]. The spacing between the elements define the bandwidth and directivity of the Yagi-Uda antenna. In the RF and Microwave domain, the dimensions of the Yagi-Uda antenna are dependent on the length of the main feeding or the driven elements wavelength i.e. half wavelength ($\lambda/2$) for the case of a simple or a folded dipole. The dimensions for the feed are in the range of ($0.45\ \lambda - 0.48\ \lambda$), resonating at the desired center frequency, while the lengths of the reflector and the directors are selected to be off resonating, in order to have maximum phase addition in the forward direction and cancellation in the reverse direction. The length of the reflector is normally $0.5\ \lambda$ while that of directors is ($0.15\ \lambda - 0.3\ \lambda$). The spacing between the elements vary from ($0.1\ \lambda$ - $0.3\ \lambda$).

For the optical Yagi-uda antenna, the choice of optimum length for the feeding element is different compared to the RF domain due to the metals interaction with light waves. The electrons in the metals collide and tightly bound together due to the phenomenon of Plasmons. The wavelength for the feeding element is reduced from traditional (λ) to more effective wavelength called the plasmonic effective wavelength ($\lambda_{eff}$). The relationship between the incident wave and the reduced effective wavelength seen by the nano-antenna is given by the following relation;

$$\boldsymbol{\lambda_{eff} = n_1 + n_2(\lambda/\lambda_p)} \qquad (\mathbf{4.3})$$

where ($n_1$)and ($n_2$) are arbitrary coefficients depending on the lengths defined by the antenna geometry and material properties, *($\lambda_p$ )* is the plasma wavelength [21]. According to this wavelength scaling eq. 4.3, the optical Yagi-uda antennas dimensions are defined in terms of the effective wavelengths for the relevant elements. The optimized parameters, with front and side view, of the proposed Yagi-uda antenna are shown in Figure 4.4 (a-b). Since the commercial available silicon slab is at *380 um* in thickness, high frequency THz design with nano scale dimensions will always create the problem of big mesh cells (> 100 million cells) during simulation. In order to deal with this problem and to have the results produced in efficient time, an interesting technique was adopted. The proposed Yagi-uda antenna was first simulated with just the Si slab of *1 um* thickness sandwiched between the ground plane and the Noble metals (radiators). When the optimization produced the required resonance at 193.5 THz, the commercial available Si slab of thickness *380 um* was introduced into the simulation as shown in Figure 4.4 (b), producing the same results, thus saving precious time.

Metals interaction with the light source at the optical frequency vary from that of RF and Microwave domain. The Noble metals that are deposited or sputtered onto the substrate are defined in terms of their refraction and extinction coefficients (n, k) values. Table 4.2 shows the (n, k) values [22-23] derived for the substrate *(Si)* and Molybdenum ground *(Mo)* and radiators used in the proposed Yagi-uda design. These parameters are derived through the known theory of Drude Model [24] that describes the interaction of photons colliding with the clustered electrons present within the metals and the intra-band movement among electrons. Metals at optical frequency appear with negative complex permittivity which is described by following equation given by Drude Model as;

$$\boldsymbol{\varepsilon_{metal} = \varepsilon_o \left\{ \varepsilon_\propto - \frac{f_{p^2}}{[f(f + i\gamma)]} \right\}} \qquad (\mathbf{4.4})$$

$$\boldsymbol{\varepsilon_{Mo} = -54.468 + j\,24.303} \qquad (\mathbf{4.5})$$

where, $\varepsilon_o$ = = *8.85x10*$^{-12}$*[F/m],* $\varepsilon_\alpha$ is the permittivity for infinity frequency, $f_p$is the plasma frequency, γ and is the collision frequency or damping factor. Eq. 4.5 describes the negative complex permitivity for the Noble meals used in the proposed nantenna design at the center frequency of 193.5 THz corresponding to central wavelength of 1550 nm. The proposed model has taken into account the conductive and dielectric losses during simulation based on FIT numerical technique using optical template.

| Material | N | K | εr |
|---|---|---|---|
| Molybdenum (Mo) | 1.6 | 7.55 | 2.56 |
| Silicon (Si) | 3.47 | 0 | 12 |

**Table 4.2** N K VALUES FOR NOBLE METALS AND SI SUBSTRATE [3-4].

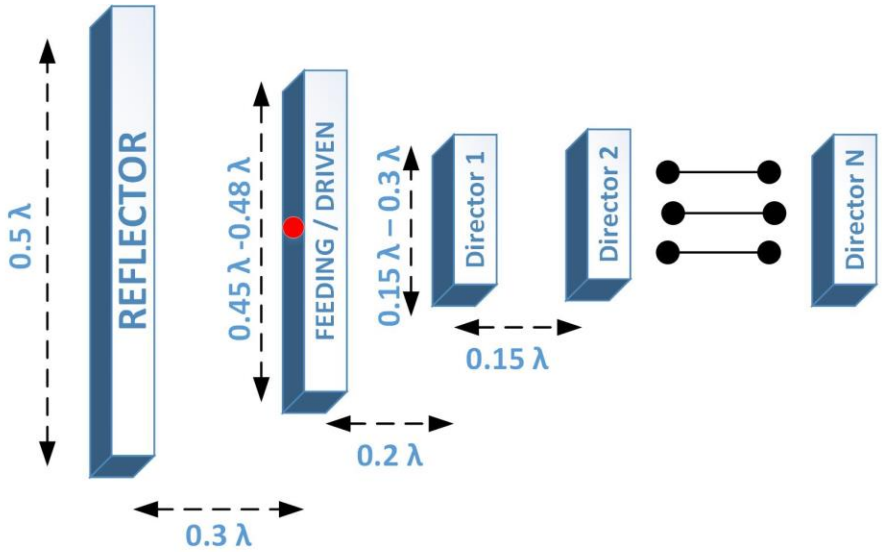


**Figure 4.3 Generic dimensions and layout of a Yagi-uda antenna [1]**

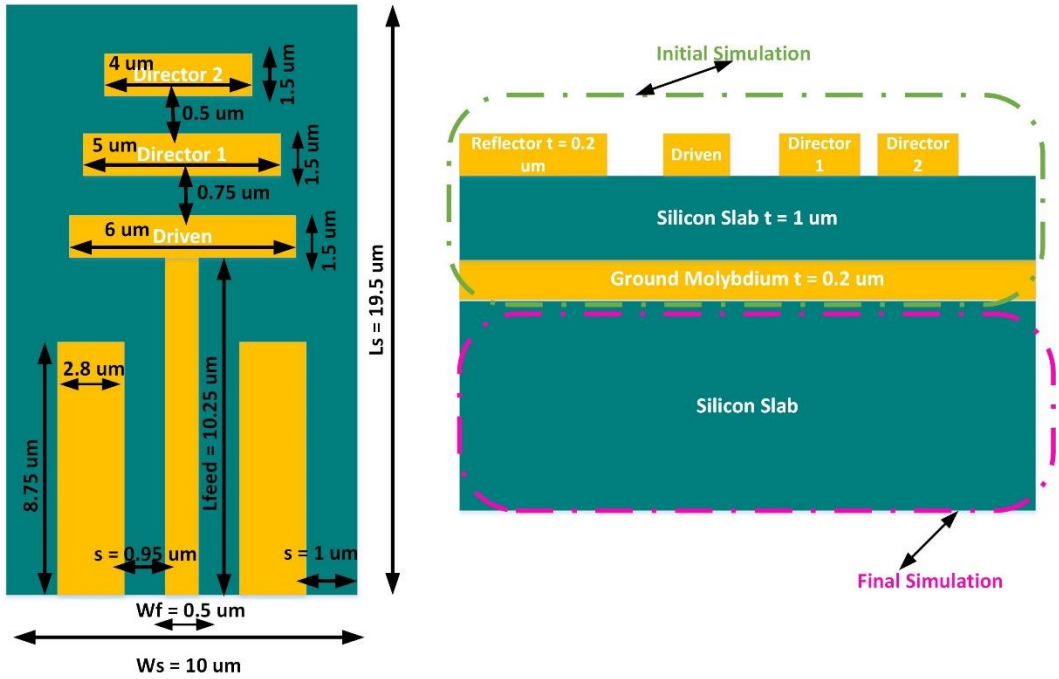


(a) (b)

**Figure 4.4 Geometry and dimensions of Yagi-uda optical antenna (a) Front Side (b) Cross sectional view.**

### 4.3.2 Simulation Results and Fabrication Method of the proposed Yagi-uda optical antenna

The simulated s-parameters of the proposed nantenna is shown in Figure 4.5. The Yagi-uda nantenna achieves a bandwidth of 0.3 THz (193.37 THz to 193.71 THz). Thus covering the intended band of interest at the optical C-window i.e. 193.5 THz or its equivalent 1550 nm wavelength. The near-field and far-field results are also shown in Figure 4.6 and Figure 4.7 respectively. The radiation pattern is end-fire with acceptable side lobe levels of -13.2 dB. For the near-field study, the concentration of received energy or EM waves is more towards the E-plane compared to the H-Plane as shown in Figure 4.6 (a-b). This concentration of energy on the nantenna can be useful in connecting or integrating additional nano-sensors or nano scale electronics in producing output voltages as for one application of energy harvesting. The nantenna also achieves a high gain and directivity of 12.9 dB and 16.6 dB respectively as shown in Figure 4.7 (a,b), thus making a viable candidate for high directional spectroscopic applications as well.

The fabrication of planar nantennas can be achieved using known method of Electron Beam Lithography (EBL) which is followed by liftoff procedure and metal evaporation [25]. Figure 4.8 shows the fabricated Yagi-uda nantenna. The nano antenna was fabricated on silicon wafer (Si) that was covered with 300 nm of silicon dioxide ($SiO_2$). Before the metal deposition, the wafer was cleaned in buffered hydro-flouridric acid and then in de-ionized water in order to remove the native oxides. A 200 nm Molybdenum film was deposited on this wafer using e-beam evaporation. Poly-Si films were deposited after using LPCVD Tempress Omega Junior. These sample were prepared at 625 °C, 40 Pa sccm of silane (SiH4), with a thickness of 1000 Å. This structure was covered by two layers of resist. The first layer was a copolymer methyl methacrylate-methacrylic acid (MMA-MAA) based with thickness of 350 nm baked on a hot plate for 10 min at 1800 $^0$C while the second was olymethyl methacrylate (PMMA) again baked at 1800 $^0$C with thickness 150 nm for 10 min. The Electron-beam lithography using an electron microscope (SEM) was used to design the structure of our nantenna. Raith Elphy Quantum software was used to manipulate the electron beam. The bilayer of resist was exposed in a 100 µm×100 µm write field at an area dose of 300 µC/cm$^2$ and 1 µs of dwell time and developed for 30 seconds in a 1:3 mixture of methylisobutylketone:isopropanol (MIBK: IPA). At the end, a 200 nm thick film of Molybdenum (Mo) was deposited using DC sputtering at 150 W of power at a chamber base pressure of 1.98 x $10^{-6}$ Torr and Argon (Ar) pressure of 3 mTorr. The fabricated structure shown in Figure 4.8 is taken as a scanning electron microscope (SEM) image. This was the first success with many trials in terms of fabrication of the optical antenna that encompasses a size of 100 x 100 µm$^2$.

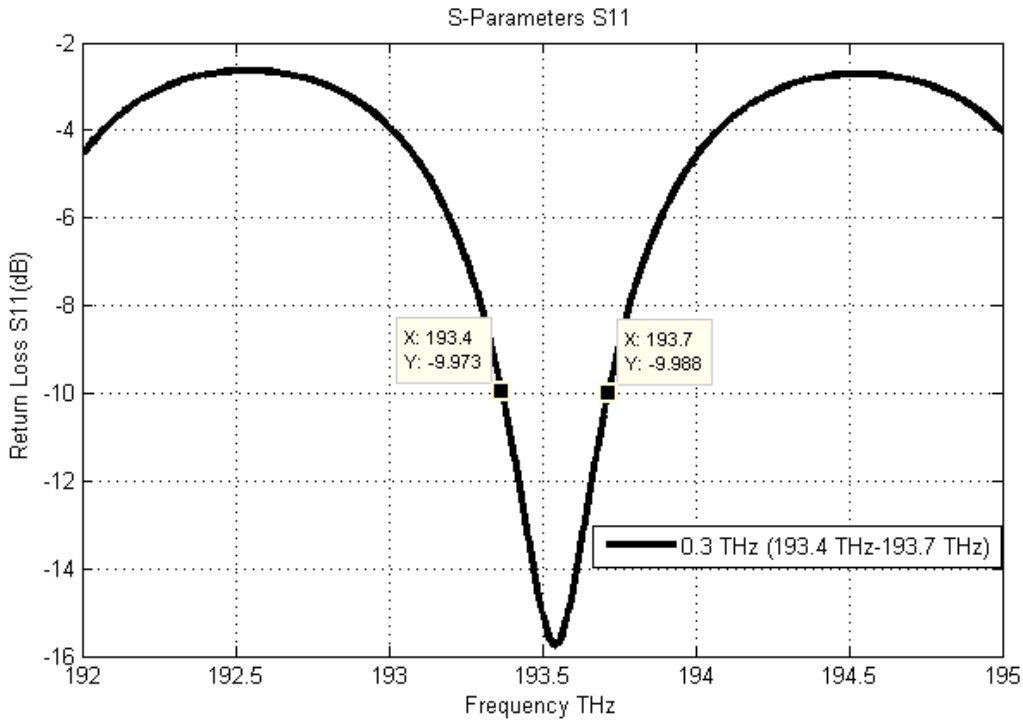


**Figure 4.5 Simulated s-parameters of proposed Yagi-uda nantenna.**

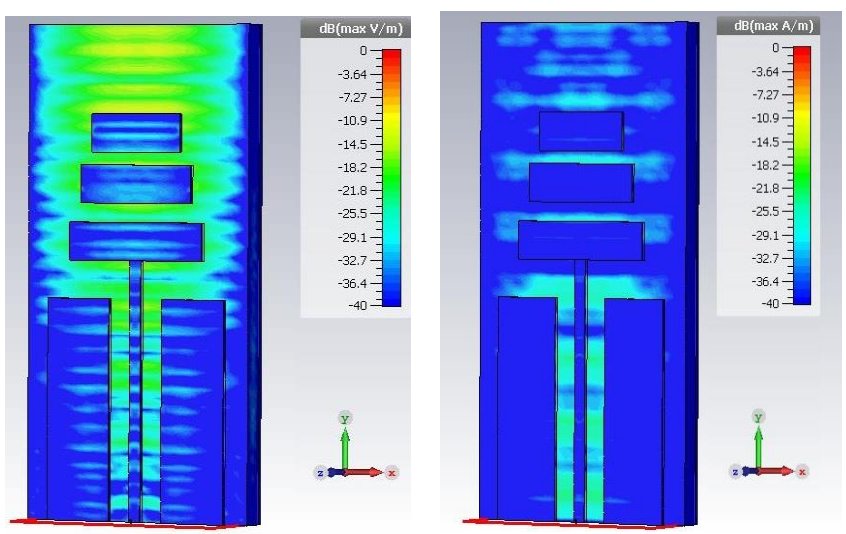


**(a)** **(b)**

**Figure 4.6 Near Field Current Distributions**

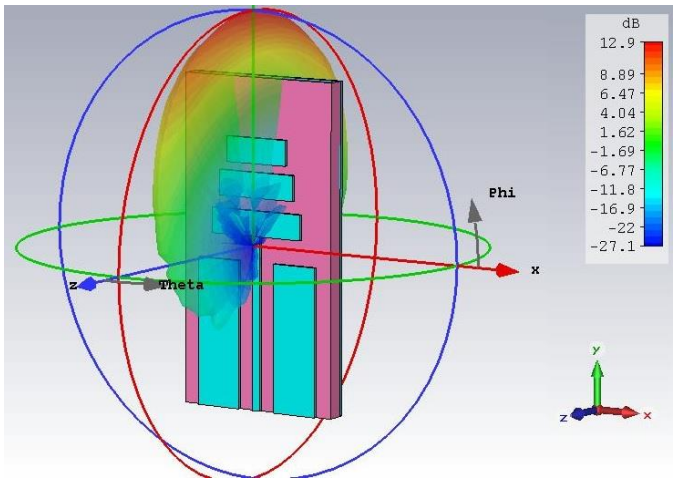


**(a) Gain**

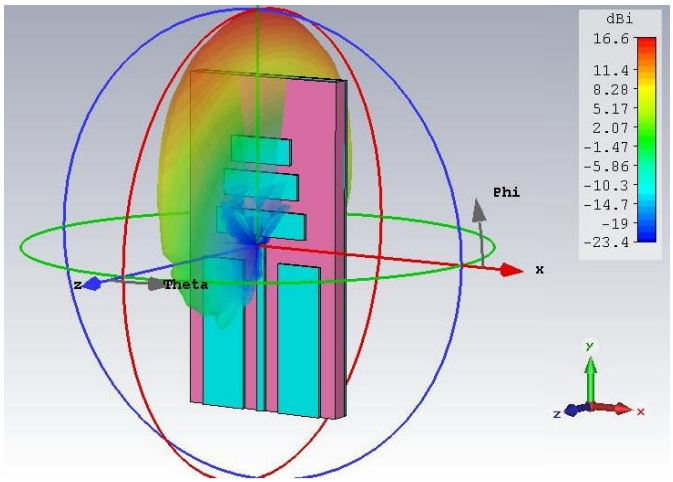


**(b) Directivity**

**Figure 4.7 Gain and Directivity at 193.5 THz (a) 12.9 dB Gain; (b) 16.6 dB Directivity.**

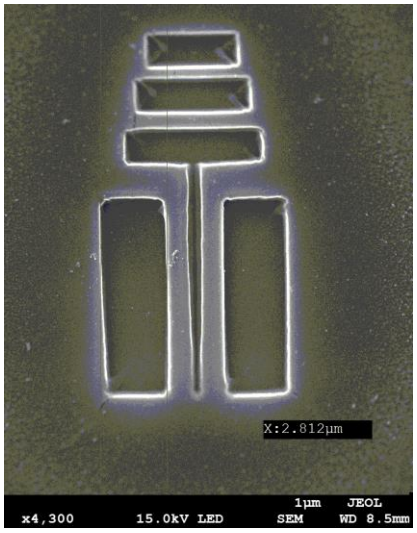


**Figure 4.8 Fabricated Yagi-uda nantenna using Chemical Vapor Deposition [CVD] technology: SEM image.**

### 4.3.3 Aluminium based Yagi-uda Antenna Designs

Previously proposed and realized Yagi-uda nantenna was based on Molybdenum material. It came to our understanding that using Molybndenum (Mo) material required temperatures higher than 2400 $^0$C which means depositing it on silicon substrate it was a bit challenging since most atomic particles combines to each other rather than being separated. To overcome this problem, we decided to use less adhesive conductor to temperature and the most easily available, Aluminium (Al). Aluminium like other metals i.e. Cu, Ag and Au can easily be melted or sputtered onto silicon substrates around 600 $^o$C temperature [26]. In the coming sections (Al) will be used in all the antennas based on Yagi-uda design. First a simple (Al) based antenna will be presented, next a slot will be introduced that will represent fermionics photodiode and in the end an array will be presented with maximum elements on it as per allowed and processed by the electromagnetic simulator CST MWS. The final realization will be on the silicon substrate with array elements deposited on it using conventional chemical vapour deposition [CVD] methods.

**(a) Antenna Design with Aluminium Material**

As previously demonstrated in section 4.3.1, a Yagi-uda nantenna was designed and simulated. This time the metal used was Aluminum (Al) rather than Molybdenum. The design of the antenna is shown in Figure 4.9. It is a basic structure having (Al) on bottom and top side with (Si) sandwiched between them. The thickness of metal and silicon substrate is ($t_m$) and ($t_s$) respectively. The feed width is 0.12 um with equal space between the directors and driven elements of 0.1 um. The dimensions and material properties are calculated from equations mentioned above i.e. eq. 4.4 and 4.5. For (Al), the material permitivity is given as follows with (n, k) values as (1.5, 15.2);

$$\boldsymbol{\varepsilon_{Al} = -229.78 + j\,46.3119} \qquad (4.6)$$

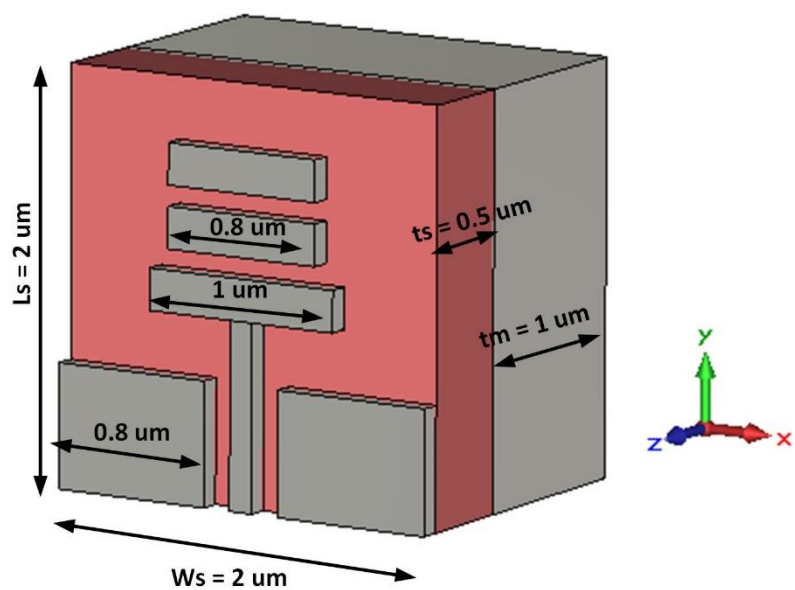


**Figure 4.9 Geometry and dimensions (Al) based of Yagi-uda nantenna.**

The simulated return loss and gain of the proposed yagi-uda nantenna are shown in Figure 4.10 and Figure 4.11 respectively. It can be seen that the nantenna resonates at the desired frequency of 193.5 THz with the gain of 8.26 dB. The radiation patterns suggests that most of the power transmitted or received will be in the end-fire direction.

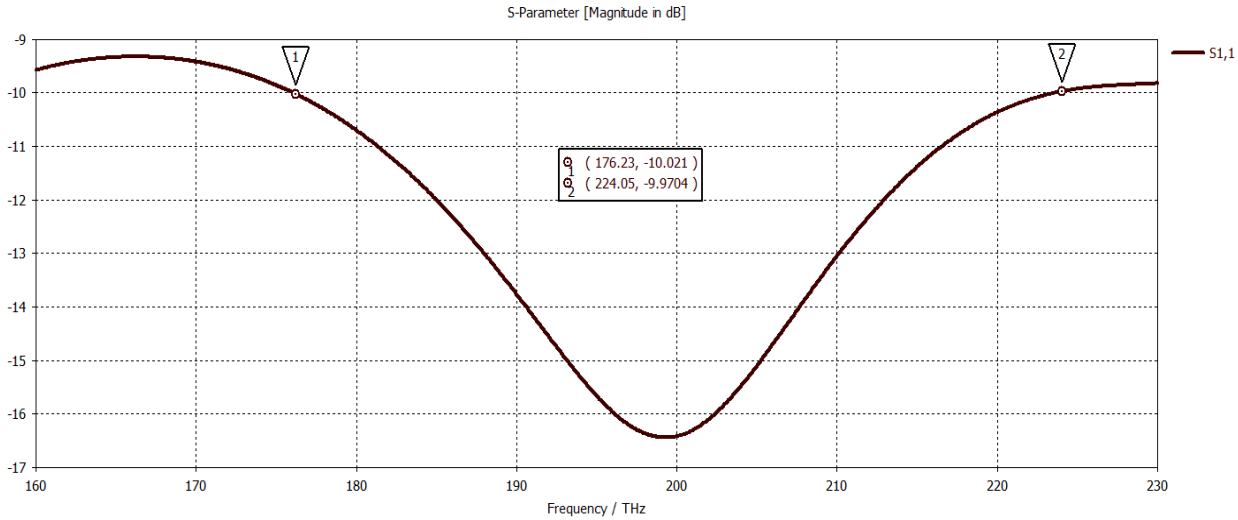


**Figure 4.10 Simulated return loss of proposed Yagi-uda nantenna.**

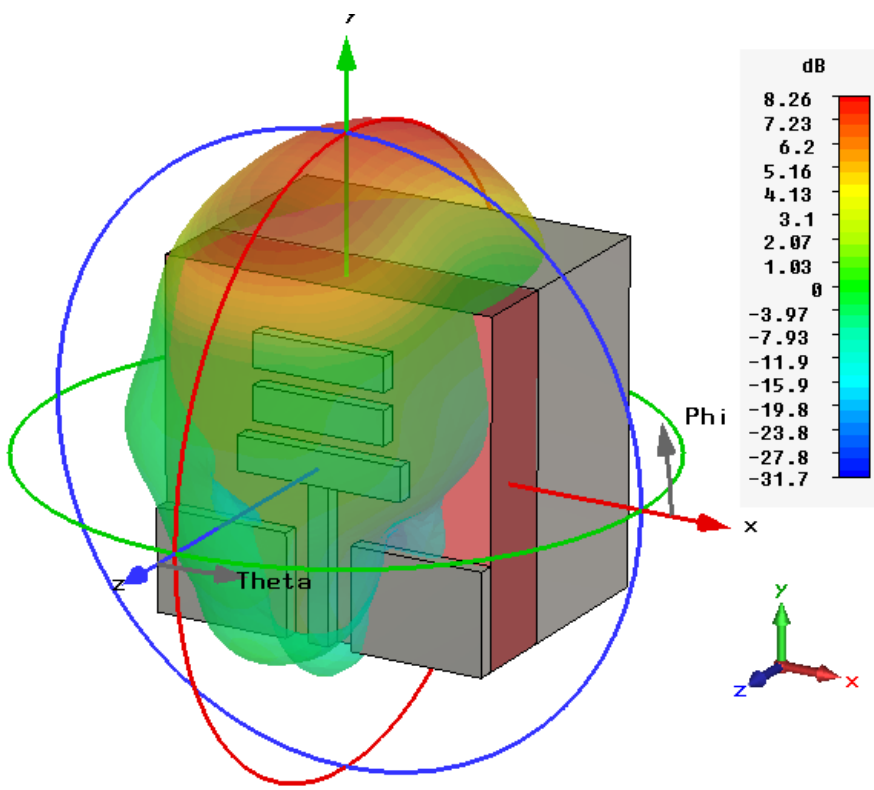


**Figure 4.11 Simulated gain of proposed Yagi-uda nantenna.**

The next step in the designing phase of the nantenna was to introduce a concentrating area in the antenna design where the electromagnetic energy received is collected. This area in simulation will be the point where the fermionics photodiode will be connected with a bonding wire. Fermionics diode (FD100L) is produced by Fermioncs-Opt Technology since 1991 California, USA [27]. They are InGAs based light detecting diodes that are high-speed, have low dark current and low capacitance photodiode for high speed communication systems, LANs, and FDDI applications. The photosensitive area of the diode is 100 microns in diameter. For the application of photodetection with the proposed Yagi-uda antenna, the FD100L was utilized with a flat lens cap on the top as shown in Figure 4.12. The electrical and optical properties of the photodiode are shown in Table 4.3. The Yagi-uda antenna design is modified with an introduction of a small square area that represents the dimensions of the photodiode. The geometry and dimensions of the new design are shown in Figure 4.13. The thickness of the substrate (Si) and ground (Al) is the same as in earlier design i.e. ts and tm, while the remaining dissensions are mentioned in the Figure 4.9, with spacing between directors and radiators being 0.2 um.

| Parameter | Symbol | Test Condition | Value | Units |
|---|---|---|---|---|
| **Responsivity** | R | λ= 1330 nm<br>λ = 1330 nm | 0.8<br>0.85 | A/W |
| **Dark Current** | $I_d$ | 5 V | 3 | nA |
| **Rise/Fall Time** | tr/tf | 5 V | 0.7 | ns |
| **Capacitance** | C | 5 V | 1.5 | pF |
| **Forward Current** | Ic | -- | 5 | mA |
| **Reverse Current** | Ir | -- | 0.5 | mA |
| **Reverse Voltage** | Vr | -- | 30 | V |

**Table 4.3 Optical and Electrical parameters of Photodiode FD100L [27].**

**Figure 4.12 Fermionics Photodiode FD100L with lens cap [27].**

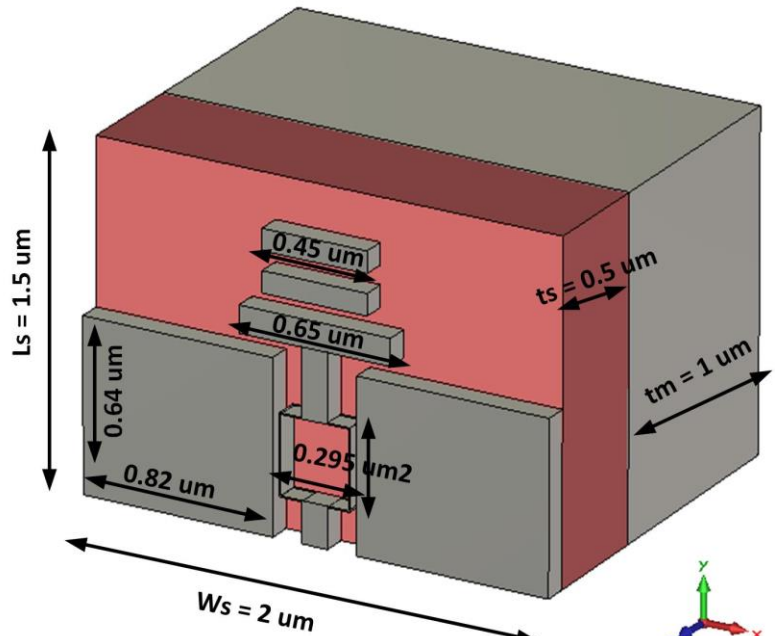


**Figure 4.13 Geometry and dimensions of Yagi-uda nantenna with slot for fermionic diode.**

The simulated s-parameters and gain of the nantenna are shown in Figure 4.14 and Figure 4.15 respectively. It can be seen from the s-parameters results that the antenna resonates slightly above the -10 dB reference line at 193.5 THz while the gain of the nantenna is 7.72 dB. The reduction in gain is observed which is due to the reduction in length of the nantenna and the directors' dimensions. To confirm the energy been received and concentrated at the center of the slot, Figure 4.16 shows the current distribution of the Yagi-uda nantenna. The energy received is making its way to the center of the slot which makes it appropriate for connection with photodiode.

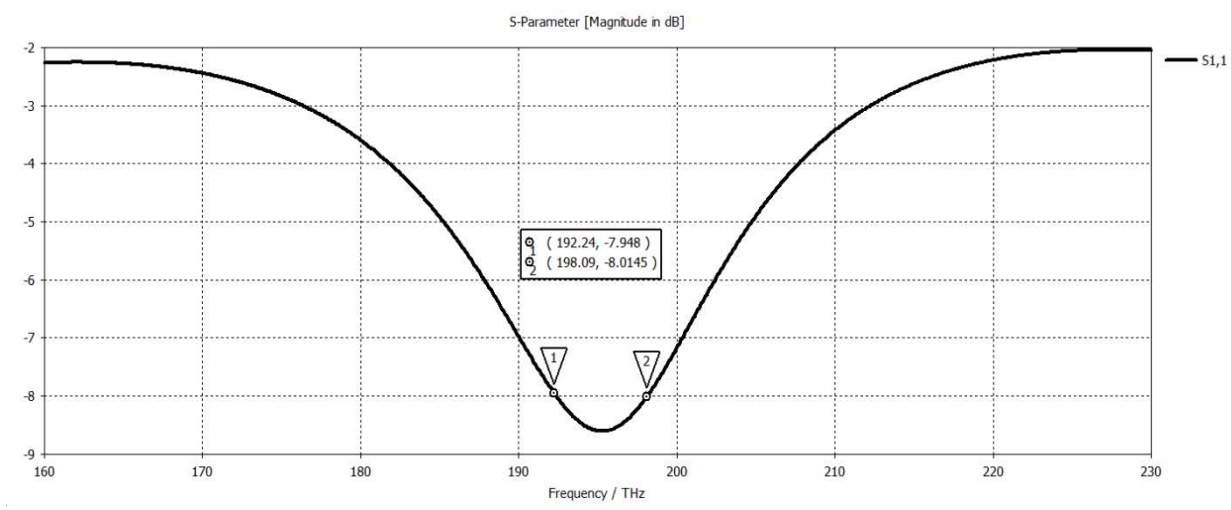


**Figure 4.14 Simulated return loss of proposed Yagi-uda nantenna with slot for fermionic diode.**

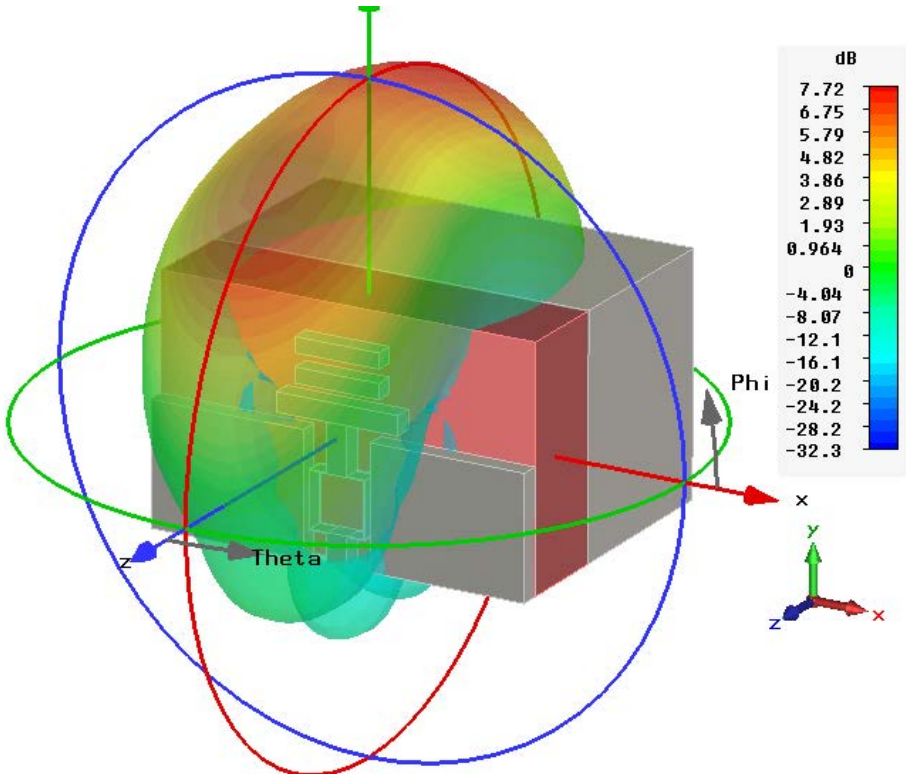


**Figure 4.15 Simulated gain of proposed Yagi-uda nantenna with slot for fermionics diode.**

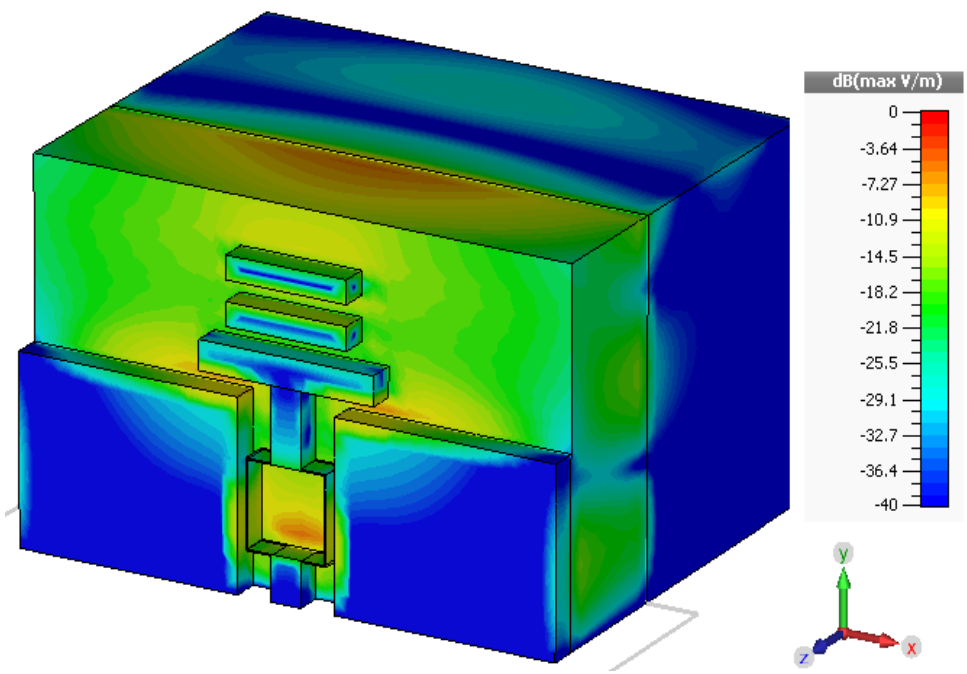


**Figure 4.16 Current Distribution of Yagi-uda with slot for photodiode.**

### (b) Array Design with Aluminium Material

The basic function of an array design is to increase the gain of any antenna along with widening the bandwidth to some extent [28]. Various array designs have been simulated that follow the

Yagi-uda design with slot for fermionics diode. Initially 1x2 array and then 1x4 array designs have been simulated and excited with plane wave to get the resonance at desired frequency band of 193.5 THz along with current distribution at the slot end. Finally a large array of 8x20 elements have been designed but not simulated as it's the maximum the software and hardware resources can cope with and limits us from further processing. The large array is then realized on silicon substrate which will be discussed in next section. Figure 4.17 shows the geometric design of 1x2 array with its simulated s-parameters, gain and current distribution shown in Figure 4.18, Figure 4.19 and Figure 4.20 respectively. From the results the nantenna resonated in the required 193.5 THz band with gain of 5.21 dB.

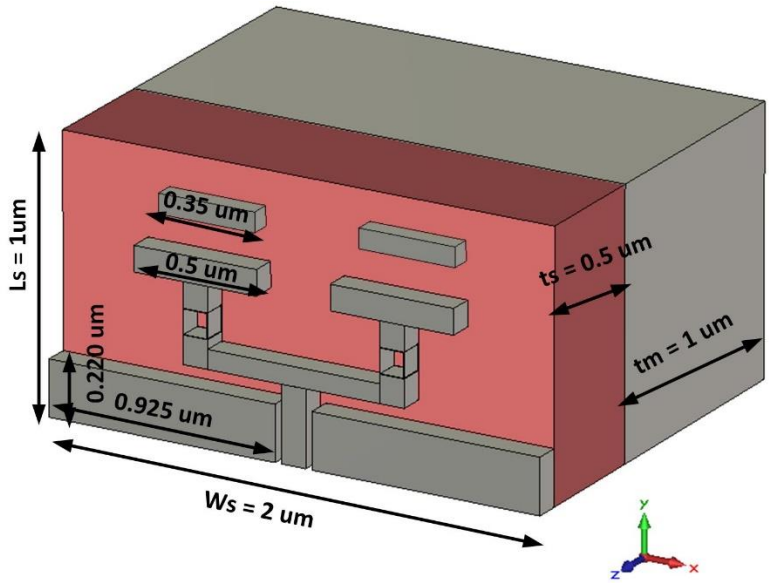


**Figure 4.17 Geometry and dimensions of Yagi-uda nantenna 1x2 array with slot for fermionic diode**

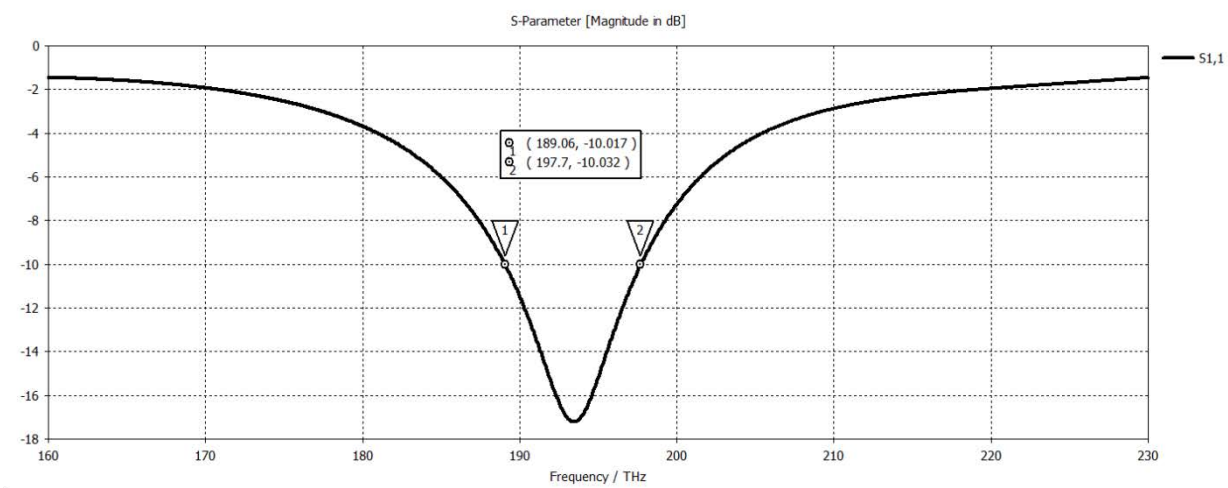


**Figure 4.18 Simulated return loss of proposed 1x2 Yagi-uda nantenna with slot for fermionic diode**

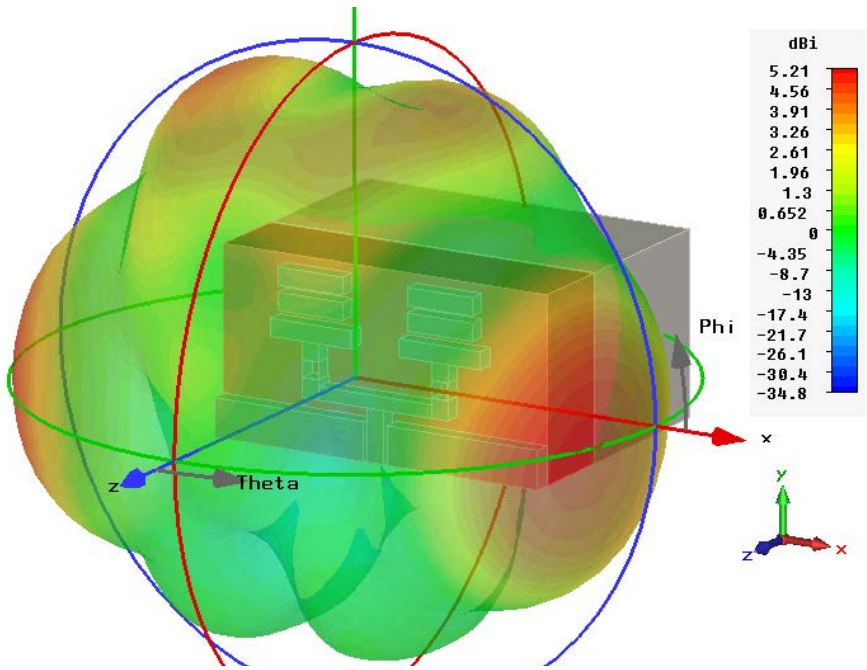


**Figure 4.19 Simulated gain of proposed 1x2 Yagi-uda nantenna with slot for fermionics diode**

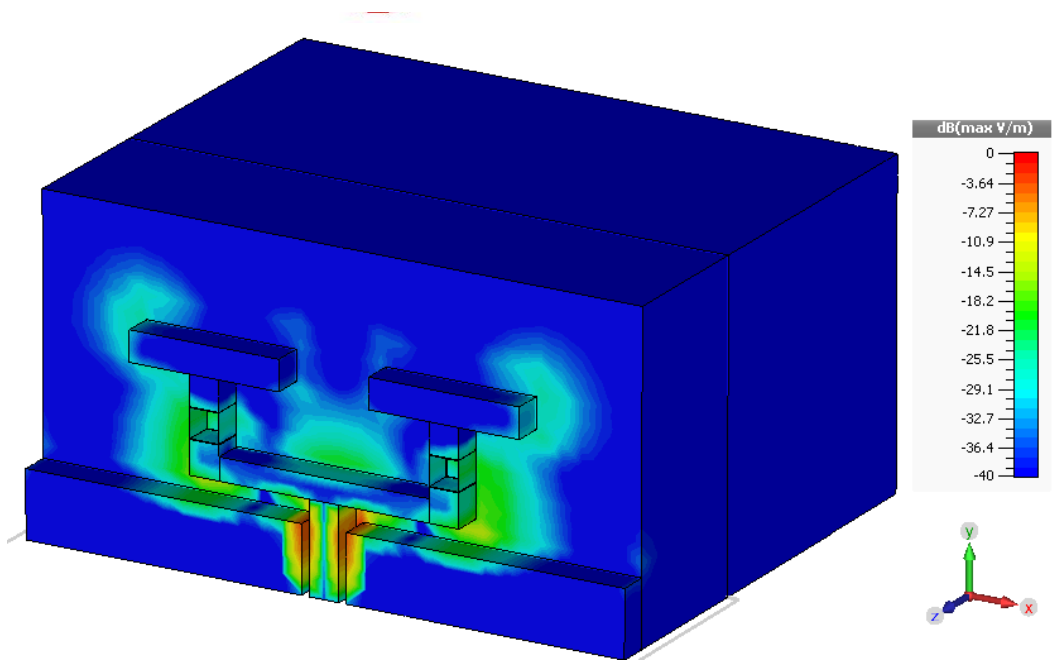


**Figure 4.20 Current distributions of 1x2 Yagi-uda array with slot for fermionics diode**

To see the effects of radiation on the nantenna, 1x4 array was simulated. The dimensions of the nantenna are shown in Figure 4.21. All the dimensions are kept same as for 1x2 array with distances between the radiating elements as 0.5 um. Again the nantennas was excited with a plane wave and its response was observed in terms of s-parameters, gain and current distribution, as shown in the Figures (4.22-4.44). From the s-parameters, it can be seen that nantennas resonates in the required band of interest i.e., 193.5 THz and the coupling among the ports is also below -20

dB. The gain of the nantennas at both ports is 7.76 dB and 8.94 dB, an improvement to the 1x2 array.

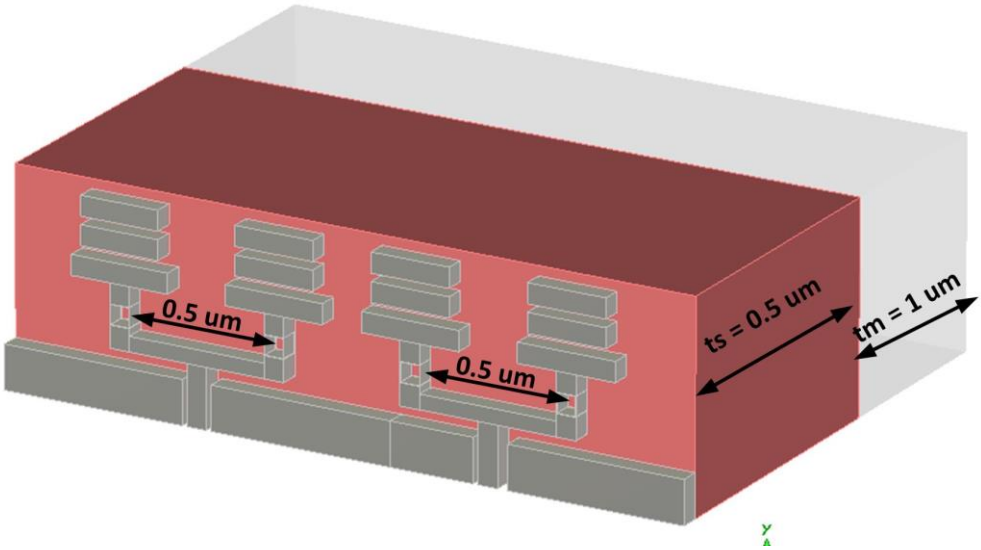


**Figure 4.21 Geometry of 1x4 Yagi-uda nantennas array**

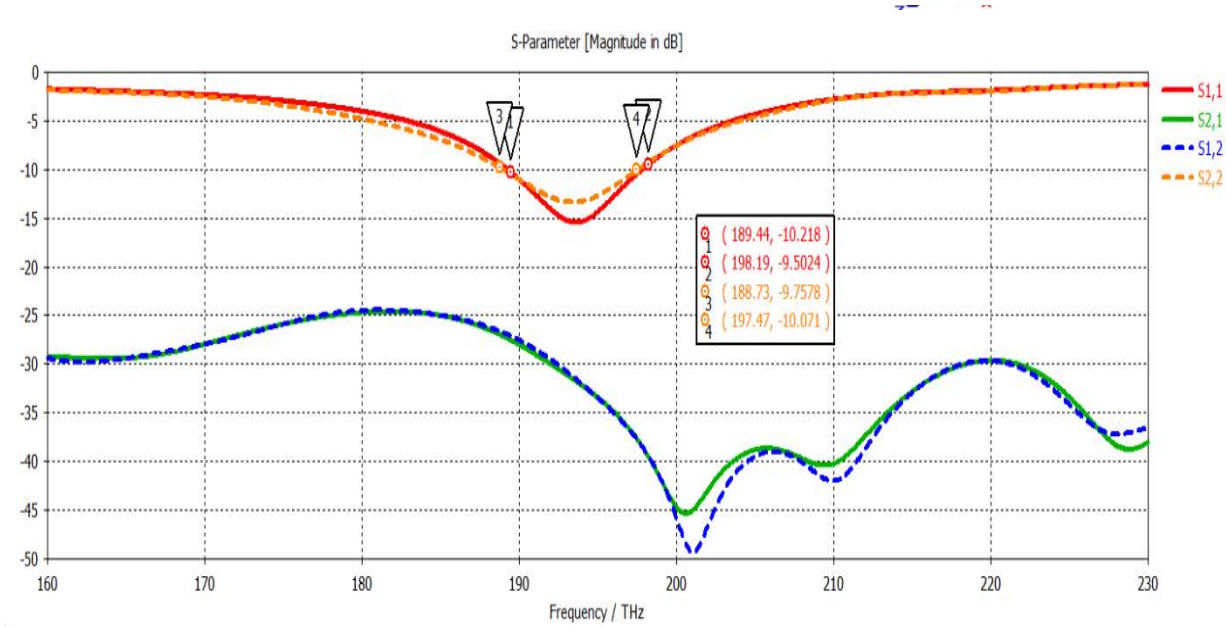


**Figure 4.22 Simulated return loss of proposed 1x4 Yagi-uda nantenna with slot for fermionic diode.**

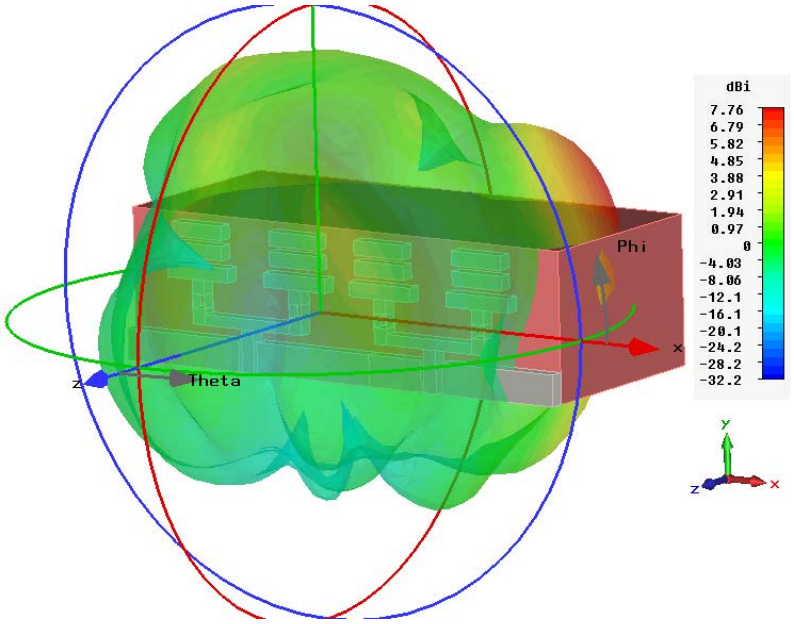


**(a) Gain at Port-1**

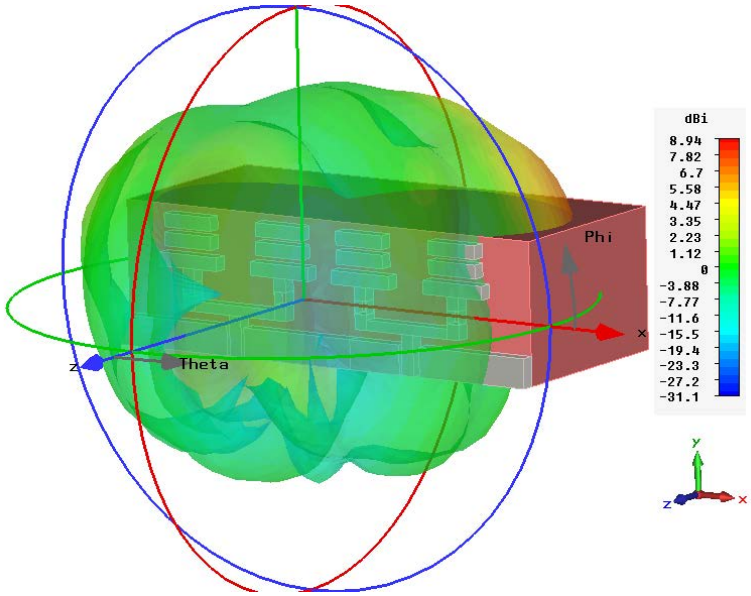


**(b) Gain at Port-2**

**Figure 4.23 Simulated gain of proposed 1x4 Yagi-uda nantenna with slot for fermionics diode.**

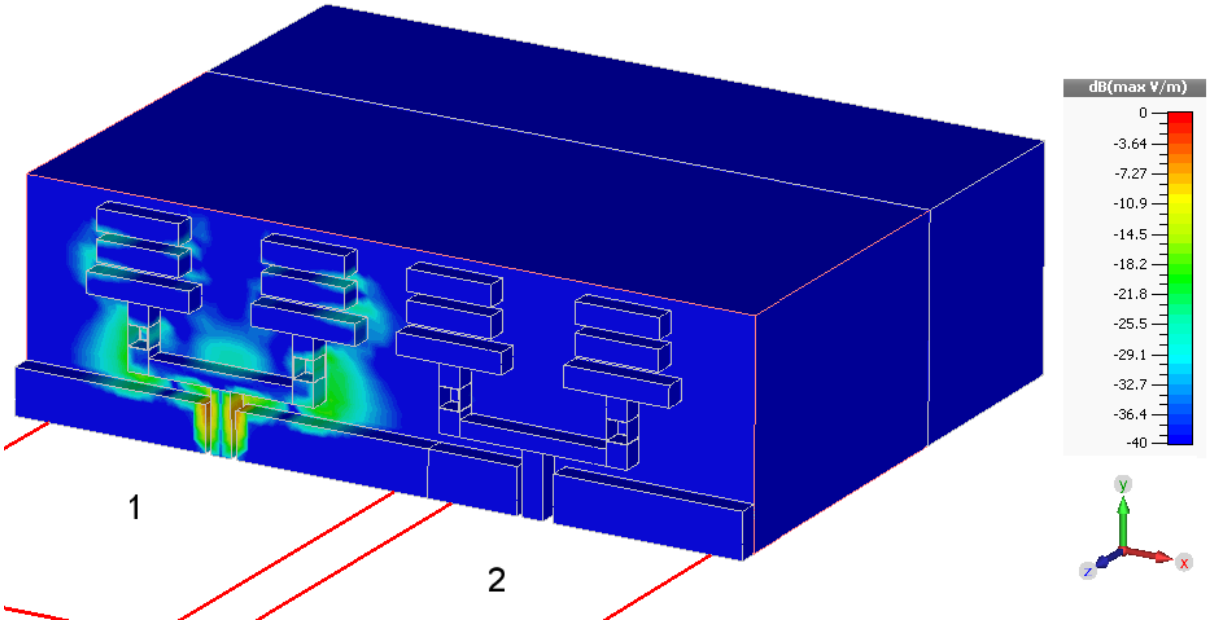


**(a)**

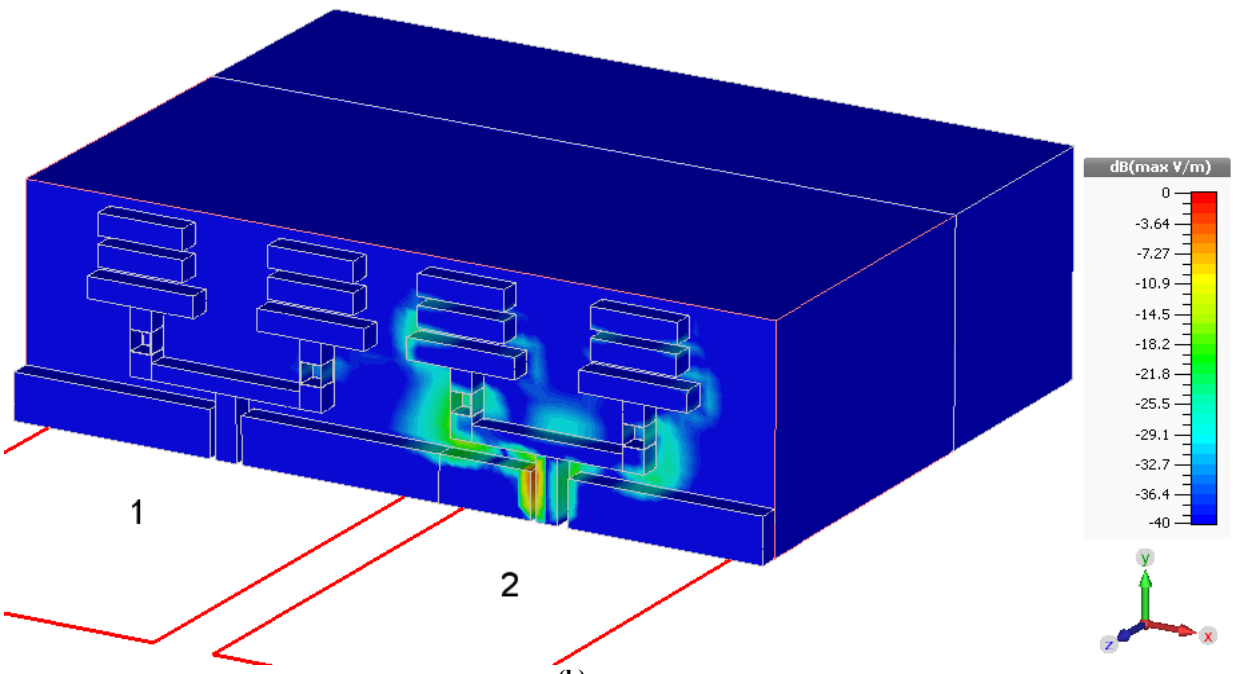


**(b)**

**Figure 4.24 Current distributions at 193.5 THz of 1x4 Yagi-uda nantenna with slot for fermionics diode (a) Port-1, (b) Port-2**

Finally a large array of Yagi-uda antennas were designed. It was not simulated as the machine hardware resources were not capable enough to process more than 1 billion mesh cells. The idea was to put the elements on a substrate before it is realized on silicon base. Figure 4.25 shows the large array of 8x20 elements placed on a silicon substrate before fabrication.

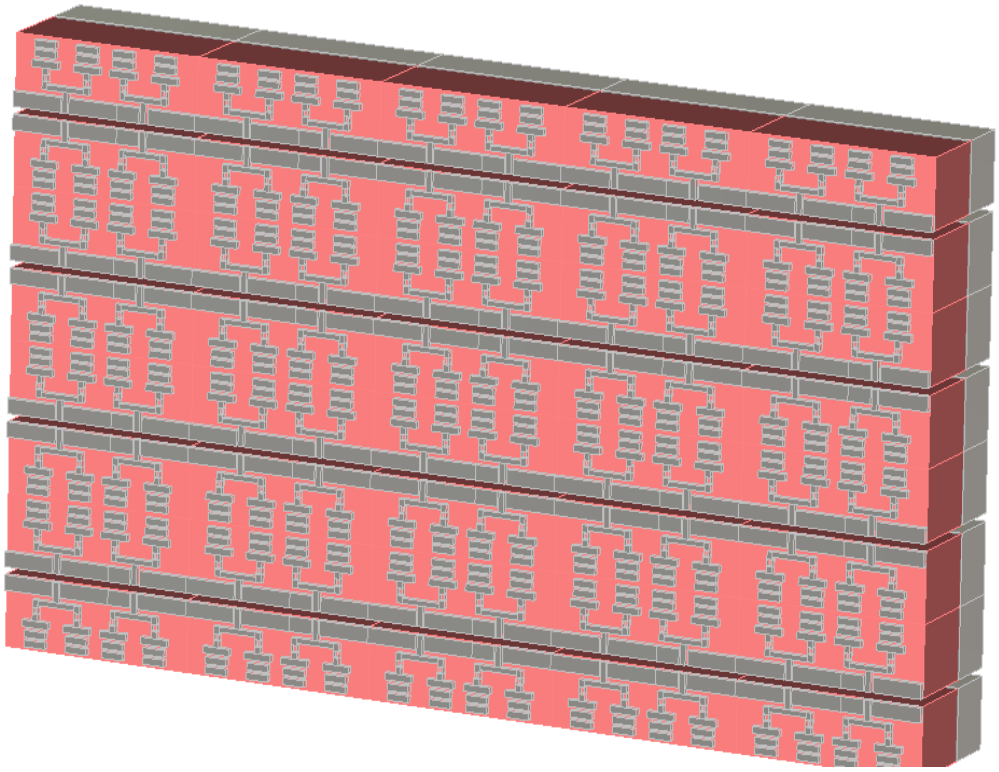

**Figure 4.25 Large array of 8x20 elements of Yagi-uda design with slots for fermionics diode**

### (c) Experimental realization of Yagi-uda Nantenna Array having Aluminium Material

In order to test the proposed Yagi-uda nantenna simulation designs, an array of the simulated structure was selected i.e. the largest possible array fabricated on the substrate. The fabrication process was done on a silicon wafer which was cut into a square later on as per machine placement limitation. The final substrate size was 2 x 2 $mm^2$ on which the Yagi-uda arrays were realized. The fabrication process was done using the electronic beam lithography [EBL] and chemical vapour deposition process [CVD]. E-beam lithography is the process of creating specific customized patterns on nay surface using an electron beam across a resist layer [29]. The designs, as small as 20 nm can be etched or produced, which is often used to create nano scale electronic and microwave components. Two types of EBL techniques can be used. The first and most economical is the scanning electron microscope controlled via a beam software while the other expensive e-beam method uses a direct beam to make patterns on the resist layers. The economical EBL process can make extremely fine patterns but is suitable for single layer designs as the process is slow and not suited for multi-layer designs. The process is as follows and depicted in Figure 4.26;

i. First of all the silicon wafer is cleaned with acetone, isopropanol and ionized water to remove any excess residue or dust that it may have collected as per packaging and transporting from its container.
ii. Once cleaned, the wafer is dried off with dry nitrogen to harden and remove the water droplets.

iii. The wafer is then placed in a spin coating machine where a positive or negative photoresist is applied in a the form of droplets of 1-3 ml. Positive photoresist is applied when the trace needs to be removed upon irradiation from the e-beam electrons while negative photoresists keeps the trace pattern in the unexposed regions from the e-beam blanker. The photoresists is applied by spinning the machine around 3000-4500 rpm. The thickness of the photoresist is controlled via the viscosity and rotation of the spinning. The thickness achieved can also be confirmed via the change in colour of the wafer e.g. green colour of the wafer suggest a thickness of 300 nm for the photoresist.

iv. The photoresists that is commonly used is Polymethyl methacrylic [PMMA].

v. The spin coating takes about 30-60 sec. Once done, the wafer is put on a hot plate for about a minute to solidify and equally distribute the PMMA and remove excess photoresist.

vi. Next, the wafer is cut according to the placement board in the scanning electronic machine [2 x 2 $cm^2$] where the e-bean scanner scans the wafer area. The circuit design file [Yagi-uda array] is uploaded in the SEM software. The e-beam will trace the circuit onto the photoresist by projecting electrons onto the positive surface of photoresist. The areas exposed to the e-beam will penetrate and break the positive ions on the photoresist thus making the circuit [Yagi-uda array] on the resist.

vii. The wafer will be taken out of the machine and sent for developing. During the developing stage, the wafer will be dipped in a solvent solution normally iso-propylene to remove the photoresists beneath the circuit trace area.

viii. The wafer is next placed into the sputtering machine. The sputter will deposit/sputter metal in this case Aluminium (Al) all over the wafer area.

ix. Finally the wafer is placed in the lift off stage where it is dipped in acetone to remove or lift off the remaining photoresist and the metals on top of it. Thus leaving only the circuit trace intact on the substrate surface.

x. Final circuit as an SEM image is shown in Figure 4.26 (f). It is covering an area of 2x2 $mm^2$ with 100 x 100 elements on a 303 um thick substrate.

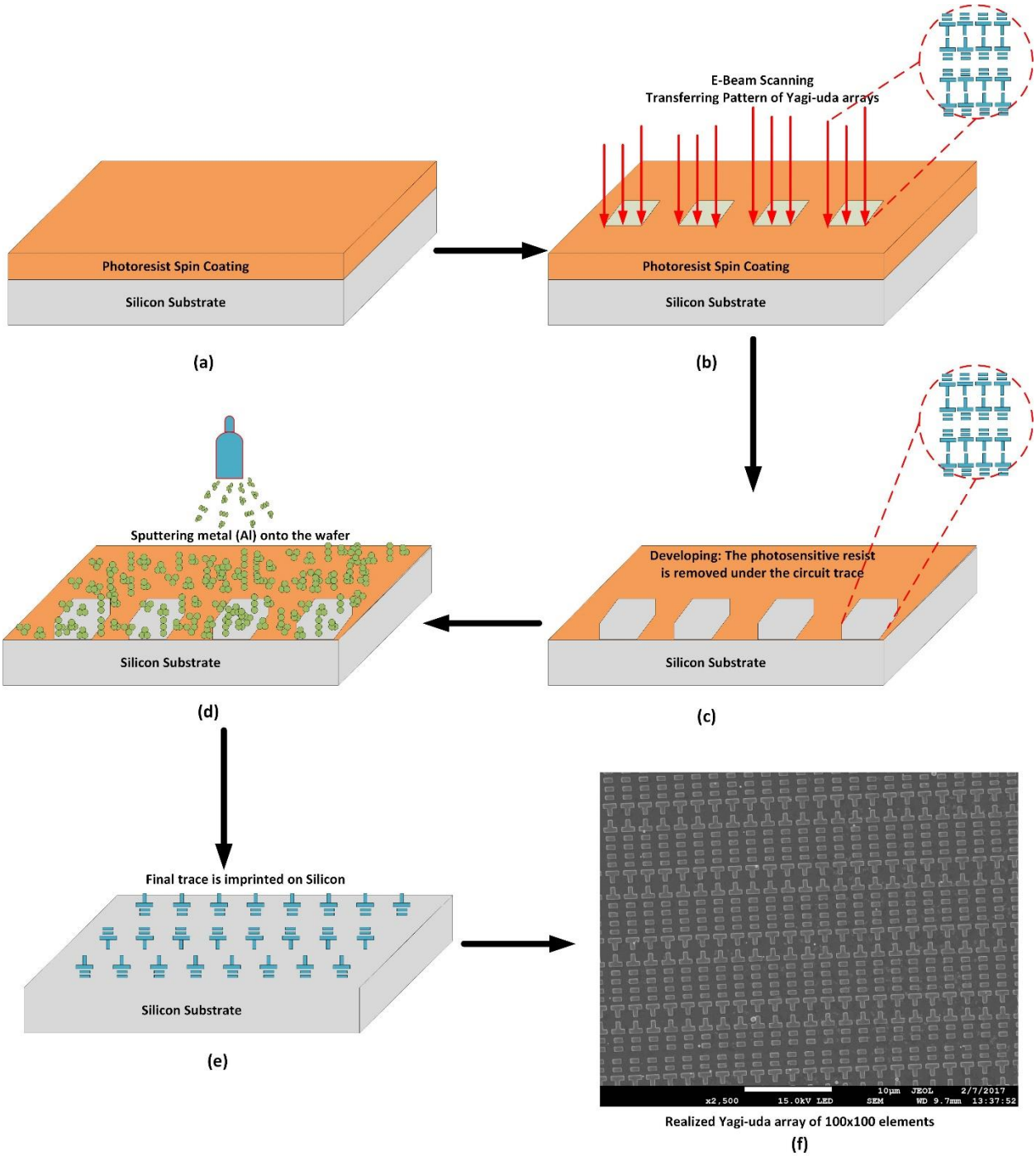


**Figure 4.26 E-beam lithography process of realized yagi-uda nantenna array**
**(a) Photoresist deposited on silicon substrate; (b) E-beam imprinting yagi-uda designs on the photoresists; (c) Developing stage where photoresists under the yagi-uda circuit is removed; (d) Noble metal Al is sputtered onto the whole silicon substrate (e) Final design is put into a solvent to remove the remaining photoresist leaving just the yagi-uda arrays in silicon (f) Realized Yagi-uda array**

Figure 4.27 shows the realized and zoomed scanned electron microscopic (SEM) image of the nantenna on the substrate. The next task was to characterize the realized nantenna array. First the nantenna was placed under a visible light of a microscope to see the effect it will have on the fermionic diode in terms of producing the output voltage. The nantenna was carefully bonded with a thin metallic wire to the fermionic diode as shown in Figure 4.28. The process was so challenging that a part of the substrate broke during the experiment but it didn't affect the results. It was found during the test that visible light passed through the silicon substrate but was reflected back via the Aluminum reflectors. When the nantenna array was totally covered by the metal no voltage was produced as the visible light was reflected back. When the nantenna array was illuminated with visible light, few portions of the light passed through the transparent silicon which gave an output voltage of 0.15 V. The output produced was not very satisfying, as the diode can produce more if the spot is direct on it. In order to see how much the diode can produced, a second experiment was conducted. This time an infra-red laser operating at 1550 nm was used.

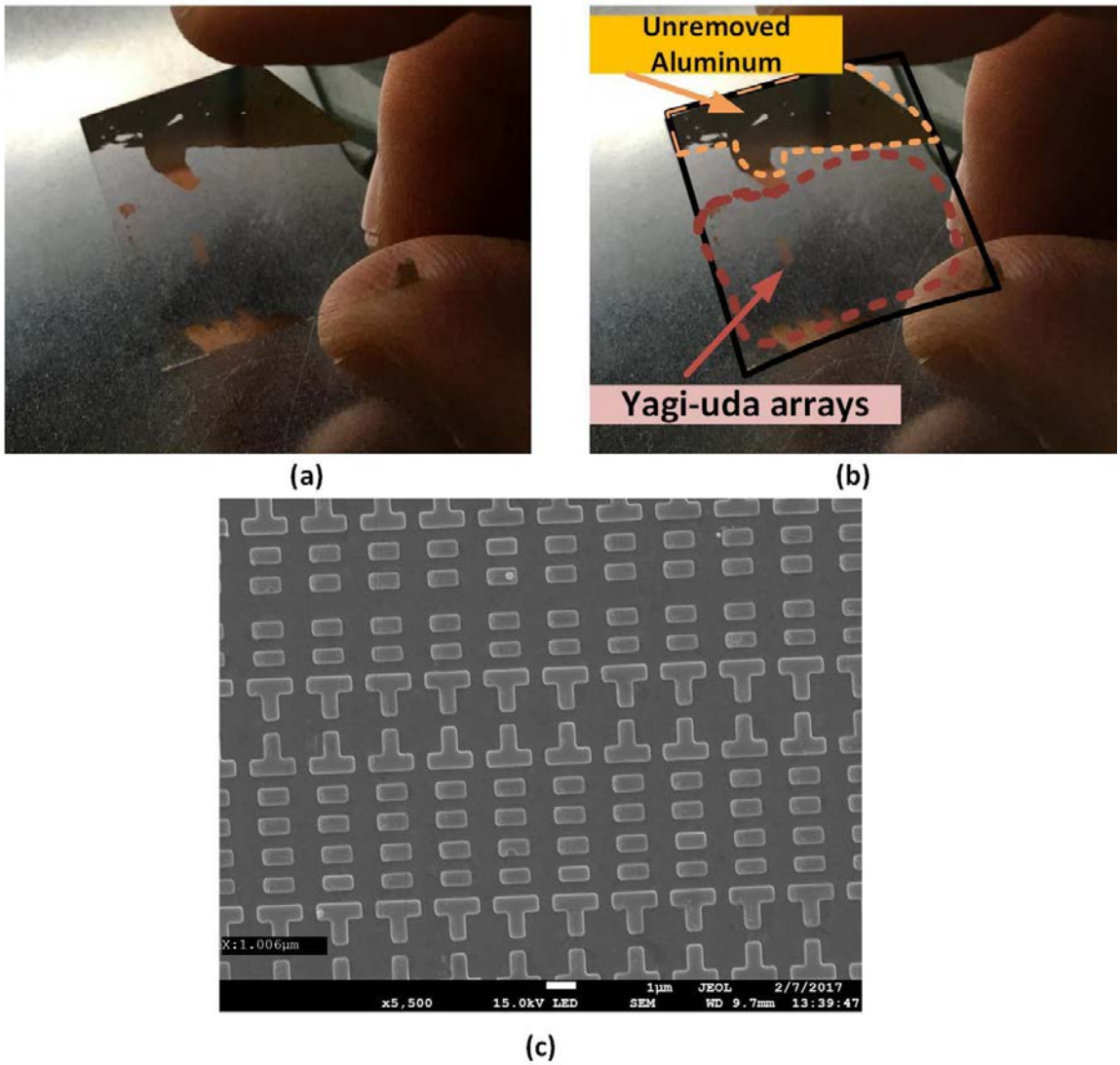


**Figure 4.27 (a) Realized Yagi-uda nantenna array (b) Highlighting the borders (c) Zoomed SEM image**

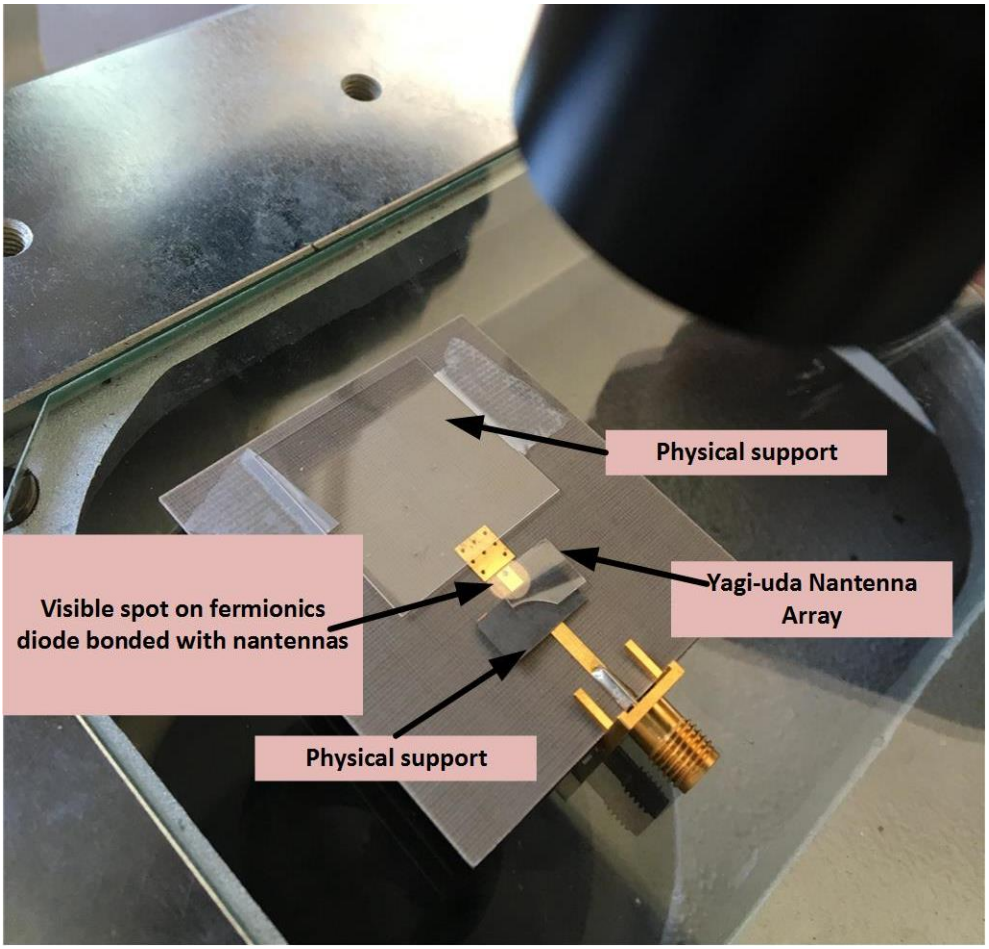


**Figure 4.28 Yagi-uda nantenna array under test with visible light from microscope producing 0.15 V output voltage**

Figure 4.29 shows the experimental setup of the nantenna placed in front of an infra-red laser operating at 1550 nm wavelength. Figure 4.29 (a) shows the nantenna being mounted on a support to firmly hold the design. The experimental setup is shown in Figure 4.29 (b) where the laser source is placed at a certain distance of 5 cm so that the maximum power and spot size is focused on the nantenna and specially the fermionic diode. Once the spot size is centrally located with correct power level, the output voltage is measured. The observations noted in this experiment reveals that the infra-red light passes through the metal and substrate equally thus producing maximum output voltage of 0.52 V as shown in Figure 4.29 (c). In conclusion, it was identified that the nantennas bonded with the fermionic diode produces the desired output voltage but extreme care needs to be taken when bonding the wire such that the nantenna might break. Also the infra-red spot size has to be controlled and placed such that it covers all the area of the nantenna array, which was a challenging and time consuming task. Therefore it was decided that although the results produced were satisfactory some other methods should also be explored that can resolve the issue of focusing the laser onto the nantenna with minimum bonding or integration to avoid damaging the nantenna prototype.

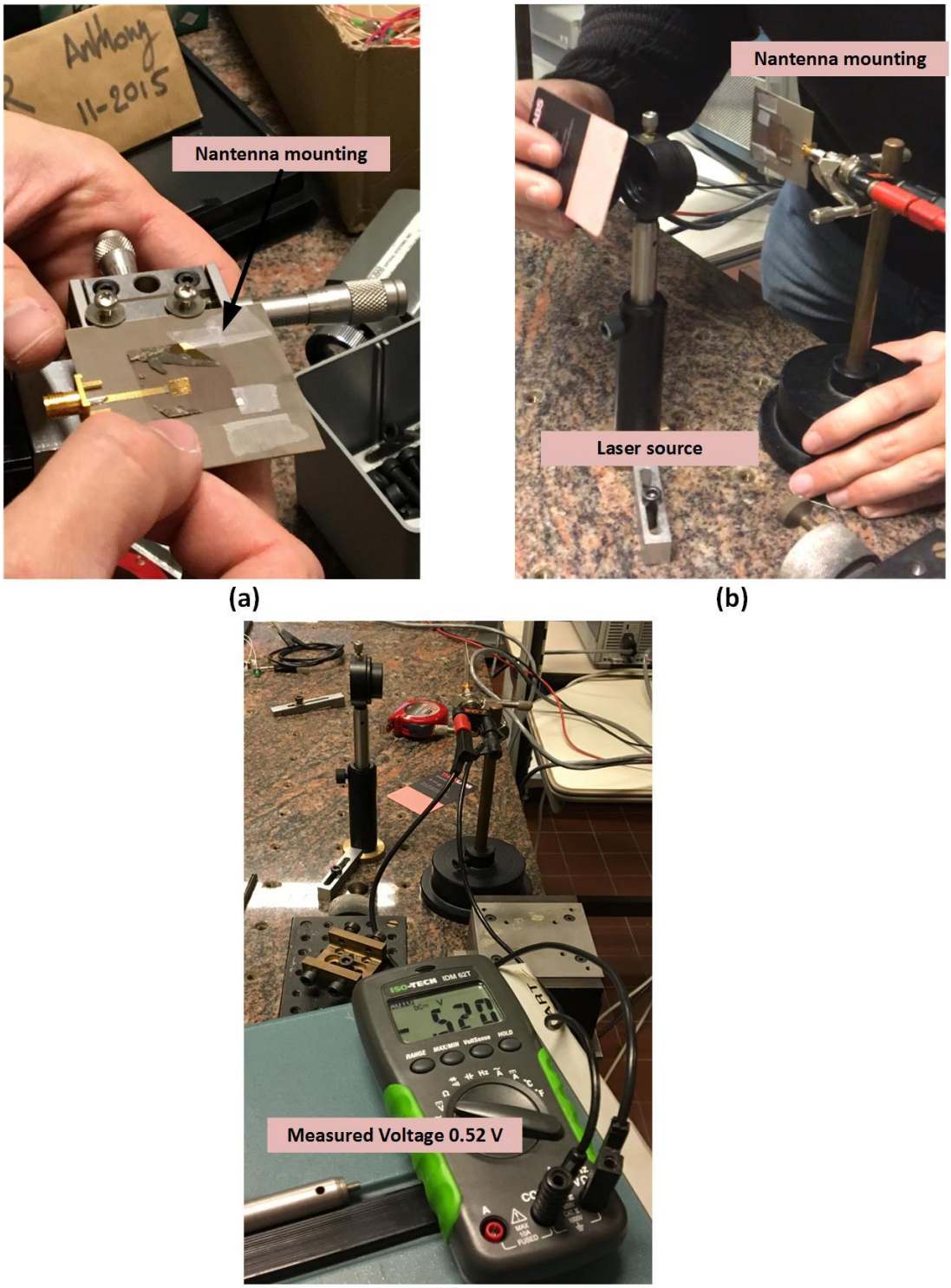


**Figure 4.29 Experimental setup of nantenna with infra-red laser (a) Nantenna mounting; (b) Setup with laser placed at a certain distance; (c) Measured output voltage of 0.52 V**

## 4.4 Optical Antenna Design II: Polydimethylsiloxane [PDMS] Lens Antennas

In this section, the second design technique for the optical antennas will be presented. The objective of this design was to concentrate the optical energy, mostly the infrared wave, onto a lens shape based made from dielectric material and then pass it through to the fermionics diode. Lens antennas offer many advantages compare to other high gain (i.e. parabolic reflectors and horn waveguides) antennas such as high gain, narrow beamwidths, low noise temperature and compact size. Lens antennas are quite popular and advantageous at millimeter and sub-millimeter waves due to their low loss characteristics and quasi optical nature. Lens being a dielectric material offer much easier beam shaping capabilities as the shape can be controlled via the diameter of the lens and are easily produced in a large scale, compared to other reflector antennas, for many niche directive applications. The material used for this lens antenna was based on a highly transparent polymer called polydimethylsiloxane [PDMS]. Figure 4.30 shows the general depiction of the experimental setup of the proposed second technique concentrating infra-red energy onto the photodiode.

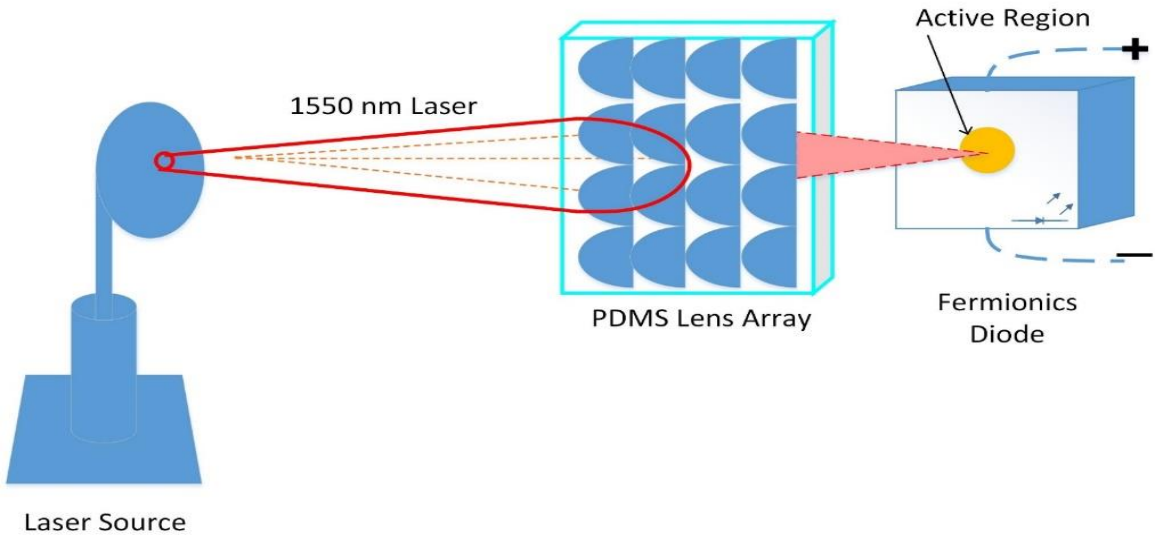


**Figure 4.30 Proposed experimental setup for the second technique for harvesting energy based on PDMS lenses.**

### 4.4.1 PDMS based Lens Antenna Design

**(a) PDMS Polymer:** Last decade has seen a lot of attention from researchers in the field of polymers. Polymers offer flexibility and good mechanical characteristics in terms of low cost, low material losses and good absorption which makes them suitable for many photonics applications [29]. For the polymer infused devices, literature review is quite limited. Kerbage et al. reported the tuning of a fiber optic based on polymer material. This tuneability was achieved by varying the refractive index of the material which produced guiding properties for light waves inside the fiber [30]. However, tapering was required after the completion of the process to produce

interactions of evanescent fields with the infused polymer which caused high losses. In addition, polymers can exhibit shrinkage during polymerization and create stress and often cracks [31]. Therefore, selection of a polymer is quite crucial when designing flexible and tunable micro-optical devices. A well-known polymer used in the domain of micro-optical fluid is the polydimethylsiloxane (PDMS). It has been used as stamp resin in the procedure of soft lithography and has very good optical and mechanical properties as well as low shrinkage with ease of fabrication [29]. Its refractive index at the infra-red spectrum is around 1.96 with loss tangent of 0.001 [32-33] and it is highly transparent to a wide range of wavelengths [34]. The combination of these properties make PDMS a viable material for usage in low frequency applications [35-36] and especially in the millimeter and terahertz applications [37-38].

**(b) Lens Antenna Design Simulations:** Figure 4.31 shows the design geometry of the semi-spherical or hemispherical lens antenna based on transparent polymer PDMS material. The material properties of PDMS at 1550 nm infra-red is given as permitivity = 1.96 and loss tangent = 0.001. The incident rays will hit the lens from the spherical side while the concentration of its energy will be observed in the vacuum box. The antenna was excited via a plane wave excitation. A collimating or hemispherical lens along with their associated ray-tracing diagrams, are depicted in Figure 4.32. The emission angle $\emptyset$ and the internal-incidence angle $\theta$ have a simple relation;

$$(\boldsymbol{d} - \boldsymbol{R}) \sin \emptyset = \boldsymbol{R} \boldsymbol{sin}\, \boldsymbol{\theta} \qquad (\mathbf{4.7})$$

where *(d)* is the distance from the spherical end to the focal point at the flat end of the lens and *(R)* is the radius of the lens. Because the wavelength of the THz radiation is not negligible compared with the size of the lenses (> 5 mm), diffraction can strongly affect the THz beam propagation. Ray-tracing analysis may overly simplify the realistic THz emission pattern emerging from the substrate lenses. Nevertheless, this simple picture provides some salient features of different lens designs.

The distance between the focal point and the tip of a collimating lens has the relation;

$$\boldsymbol{d} = \boldsymbol{R}\left(\mathbf{1} + \frac{\mathbf{1}}{\boldsymbol{n} - \mathbf{1}}\right) \qquad (\mathbf{4.8})$$

where (n) is the refractive index of the lens material. The refractive index of high resistivity polymer PDMS is 1.4 over the broad THz spectral range [13], which leads to d = 3.5R for the collimating hemispherical lens.

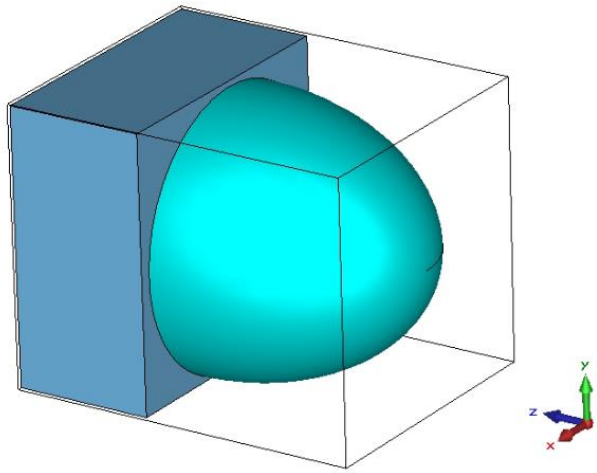

**Figure 4.31a) 3D semi spherical Lens with vacuum box on the left side**

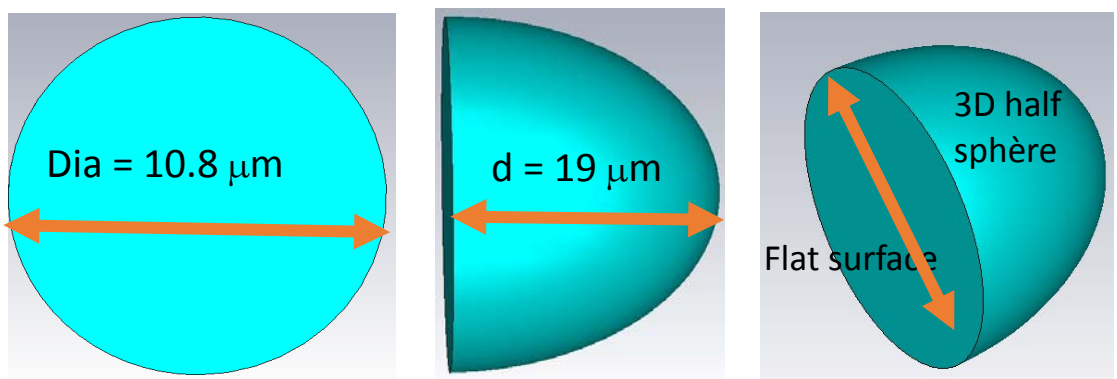


**Figure 4.31 b) 3D semi spherical Lens dimensions**

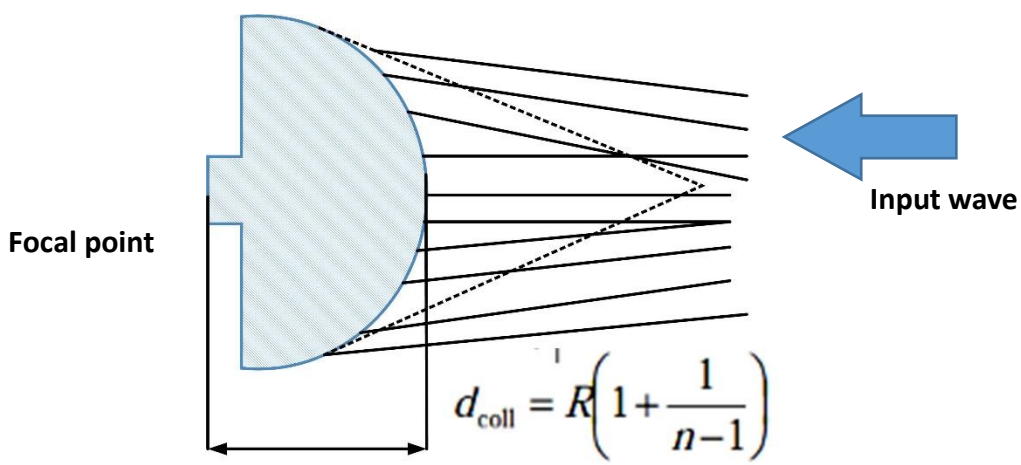


**Figure 4.32 Distance equation for collimated hemispherical lens.**

The simulated lens antenna was analyzed in terms of E-field concentration at the z-axis. After plane wave excitation, the flow of fields were analyzed to find the correct spot size or focal point as per the equations 4.7 and 4.8. Figure 4.33 shows the best optimized distance for concentration of focal point in the vacuum. The best distance was 1.5 m from the lens to vacuum resulting in a concentrated focus point.

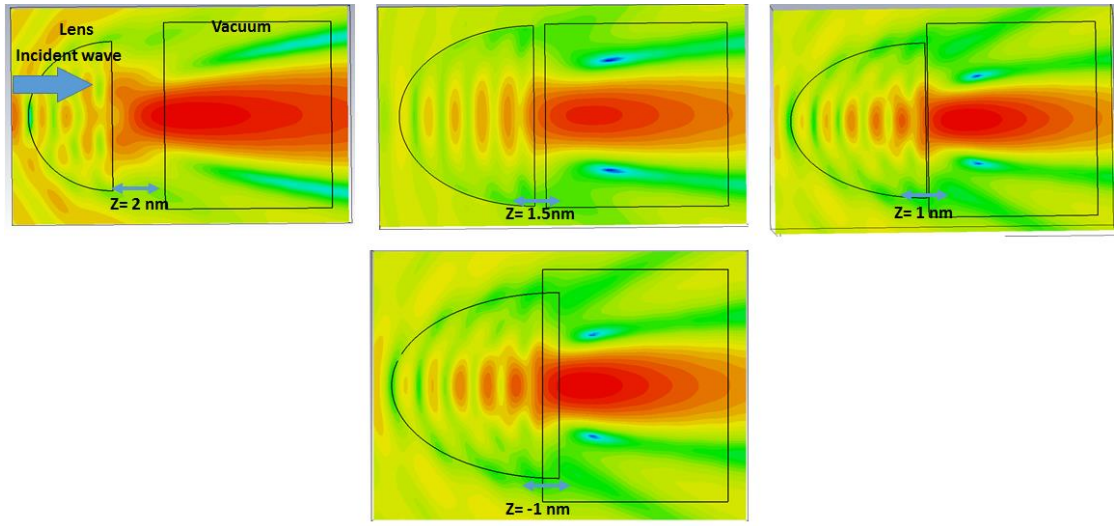


**Figure 4.33 Focus point of the incident beam at various distances of lens form the vacuum**

From Figure 4.33, the best focal point for the incident wave was seen at distance z= 1.5 m between the lens and the vacuum. The red spot was clearer and the waves or rays movement were much visible via the simulation of the E-field. The next phase was to make an array of the structure but as per limitation of mesh cells and hardware processing speed this task was not accomplished. The limitations in terms of fabrication were also halted as the diameter of the lenses were too small for the PDMS molding machine to cope with. Although the molds were simulated with various diameter sizes. This design technique is another option for concentrating light onto the photodiode. The simulation design of the mold array lens is shown in Figure 4.34.

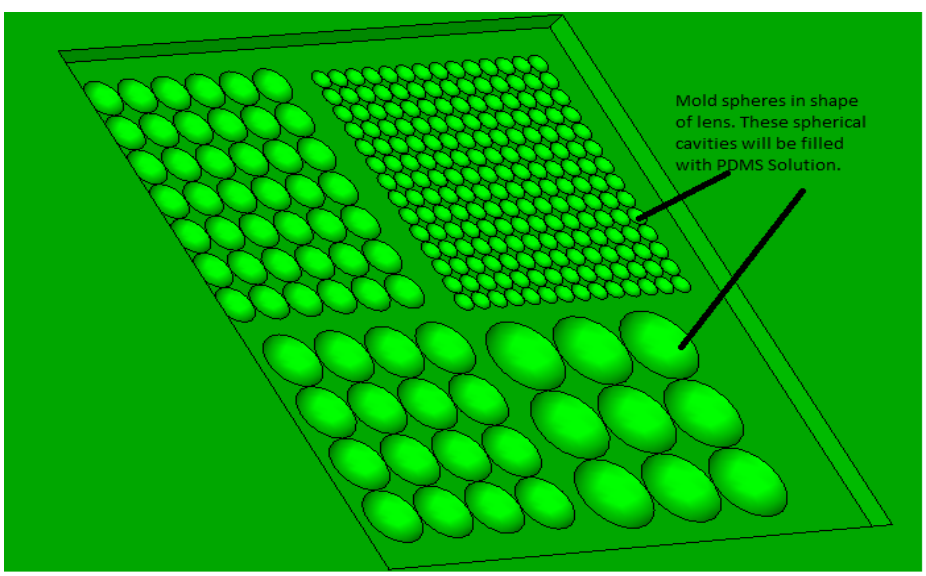


**Figure 4.34 Molds for PDMS deposition into the lenses with various diameter shapes.**

## 4.5 Optical Antenna Design III: Thermopile Antenna

In this section, third design technique for optical antennas will be presented. This technique is based on thermal radiation detection. The proposed optical antenna will capture the infrared light having heat signatures and will convert the received thermal waves into output voltage. The intended frequency band or wavelength of the antenna will lie in the 193.5 THz frequency or its equivalent 1550 nm optical communication window. The principle of thermal detection is based on the well-known seebeck effect [9] which will be discussed. The geometry of various proposed designs will be presented and realization of a working Yagi-uda thermopile nantenna will be shown along with the results it achieved. Figure 4.35 shows the general depiction of the experimental setup of the proposed thermopile array technique for harvesting solar energy.

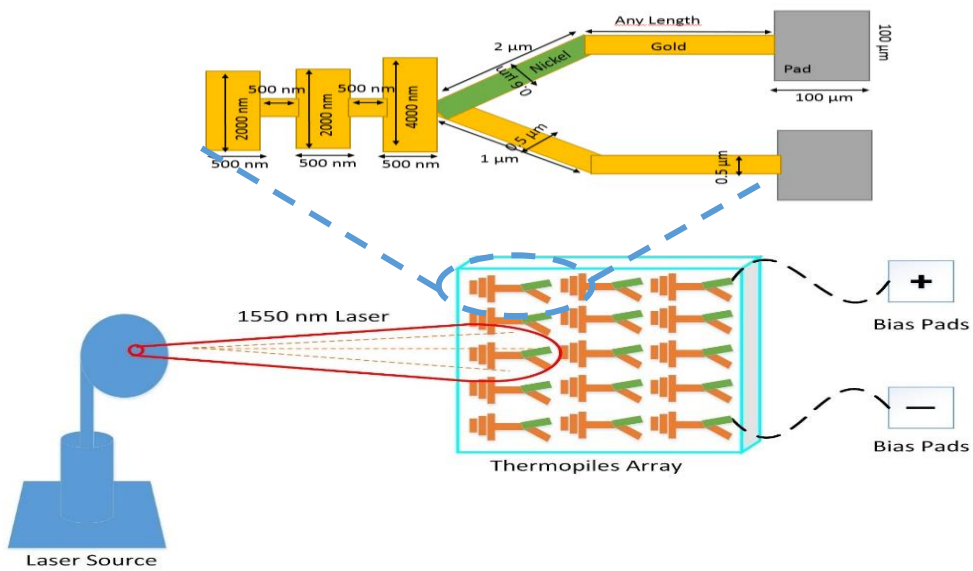


**Figure 4.35 Proposed experimental setup for the thermopile technique for harvesting energy.**

### 4.5.1 Thermopile Antenna detector and geometric designs

**(a) Principle of Thermocouples:** One of the oldest radiation detection device [8], thermocouples are electronic devices that convert thermal radiation into output voltage. A number of thermocouples connected in series or parallel are called thermopiles. Although thermopiles are not as temperature sensitive as bolometers and pyro-detectors but they offer much more in terms of reliable characteristics and good cost/performance ratio. The working principle of thermocouple is based on the seebeck effect [9] where a change in temperature across a conductor produces a change in voltage as shown in Figure 4.36 (a). When a temperature difference of 100 degrees, which is called a thermal gradient is applied over the conductor, it will generate a voltage gradient. This generated voltage is very small and often measured in microvolts – $\mu V$. This is one of the reasons thermocouple temperature ranges are for higher temperatures in order to generate higher output voltages in *Volts.*

To produce maximum output voltage between the two dissimilar metals, Figure 4.36 (b), following equations assist in calculating an estimate for the voltages,

$$\Delta V = \alpha_s \Delta T \qquad (4.9)$$

where $(\alpha_s)$ is the Seebeck coefficient commonly expressed in μV/K. The coefficient $(\alpha_s)$ is the effective or relative Seebeck coefficient of the thermocouple composed of two dissimilar conductors *"a"* and *"b"* by electrically joining one set of their ends. Consequently, a thermovoltage is equal to

$$\Delta V = \alpha_s \Delta T = (\alpha_a - \alpha_b)\Delta T \qquad (4.10)$$

where $(\alpha_a)$ and $(\alpha_b)$ are the absolute Seebeck coefficients of the material a and b. The output voltage of a single thermocouple is usually not sufficient; therefore, a number of thermocouples are connected in series to form a so-called thermopile. An important factor for obtaining a large output voltage from a thermopile is to obtain a high thermal isolation in order to maximize the temperature difference between hot cold junctions, *(ΔT)*, for a specific absorber power. Corresponding to eq 4.18, the totalized output voltage will be *(N)* times as high as for a single element;

$$\Delta V = N(\alpha_a - \alpha_b)\Delta T \qquad (4.11)$$

with N as the number of joined thermocouples.

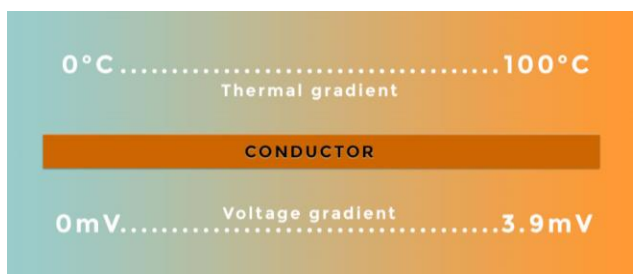


(a)

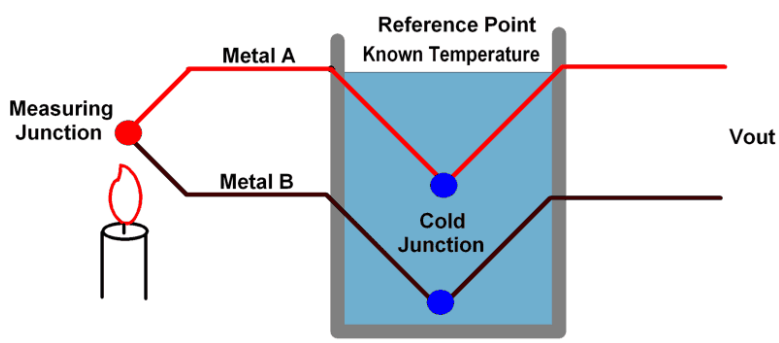


(b)

**Figure 4.36 Seebeck effect (a) When thermal gradient is applied to a conductor a voltage gradient will be generated. b) Thermocouple principle – How the thermocouple works [9].**

**(b) Proposed geometric designs and experimental realization:**

In order to test the thermopile effect, various geometric designs were presented and realized. No specific simulations were performed since the available full wave electromagnetic software (CST MWS) currently lacks features of optical wave excitations and thermal gradient analysis for voltage detection. From the knowledge of earlier realization of yagi-uda nantennas, these thermopile designs were proposed with their relevant geometric values inspired form literature [39-40]. Figure 4.37 shows the geometric design of the single element and array thermopiles while the realized single elements are shown in Figure 4.38. The designs are made using gold (Au) and nickel (Ni) as conducting materials. E-beam lithography, as described in section 4.3.3 and Figure 4.26, was used to realize the optical antennas.

For all the realized thermopile designs, an initial testing was done using a uniform thermal heating base. Figure 4.39 shows the experimental setup and testing of the thermopile designs. The optical thermopile antennas were placed one by one onto the golden colored heating base. Only the quasi Yagi-uda optical antenna produced some encouraging results. The output was monitored via probes connected to a Keysight B1500A semiconductor Device Parameter Analyzer/Semiconductor Characterization System Mainframe allowing Current-voltage (IV) measurement capabilities of spot, sweep, sampling and pulse measurement. To correctly position the probes, a Bosch & Lomb Micro-zoom-II high performance microscope was used. But no variations were observed in the voltage readings. Figure 4.39 shows the results of the quasi Yagi-uda thermopile optical antenna when heated uniformly. It was observed from the results that the proposed antenna was reacting to the temperature variation. Initially temperature was risen from 2-15 ºC, but no response was observed as the temperature difference between metals were no reached, Then a sudden spike was seen around 37 ºC giving output voltage of a few microvolts i.e. 20 uV. When the temperature was further increased the output voltage also increased showing a linear relationship. Finally the maximum voltage achieved was 48 uV at temperature of 120 ºC. After that the voltage started decreasing after the heating source was turned off which also meant that the maximum temperature potential difference was met for the metals as they started to lose their temperature effect. The initial experiment gave me the confident that the proposed design is reactive to heat change and was following the Seebeck and Peltier effect as well.

In order to test the quasi Yagi-uda thermopile optical antennas performance as per temperature change, laser sources of various wavelengths were utilized. Since tuneable laser was not available, an in-house solution was presented where the modulation of laser was done with a low modulated square signal of 1 Hz using a Keysight 33500B series signal generator connected to a breadboard. Four lasers with wavelengths 532 nm (green), 650 nm (red), 940 nm and 1550 nm were used to excite the realized quasi Yagi-uda antenna. . The output power of all lasers is a maximum about 5mW. The optical antenna was placed inside a special casing that was bonded with wires connected to the probes of the analyzer for measuring the output voltages. Figure 4.41 shows the experimental setup and laser signal generator.

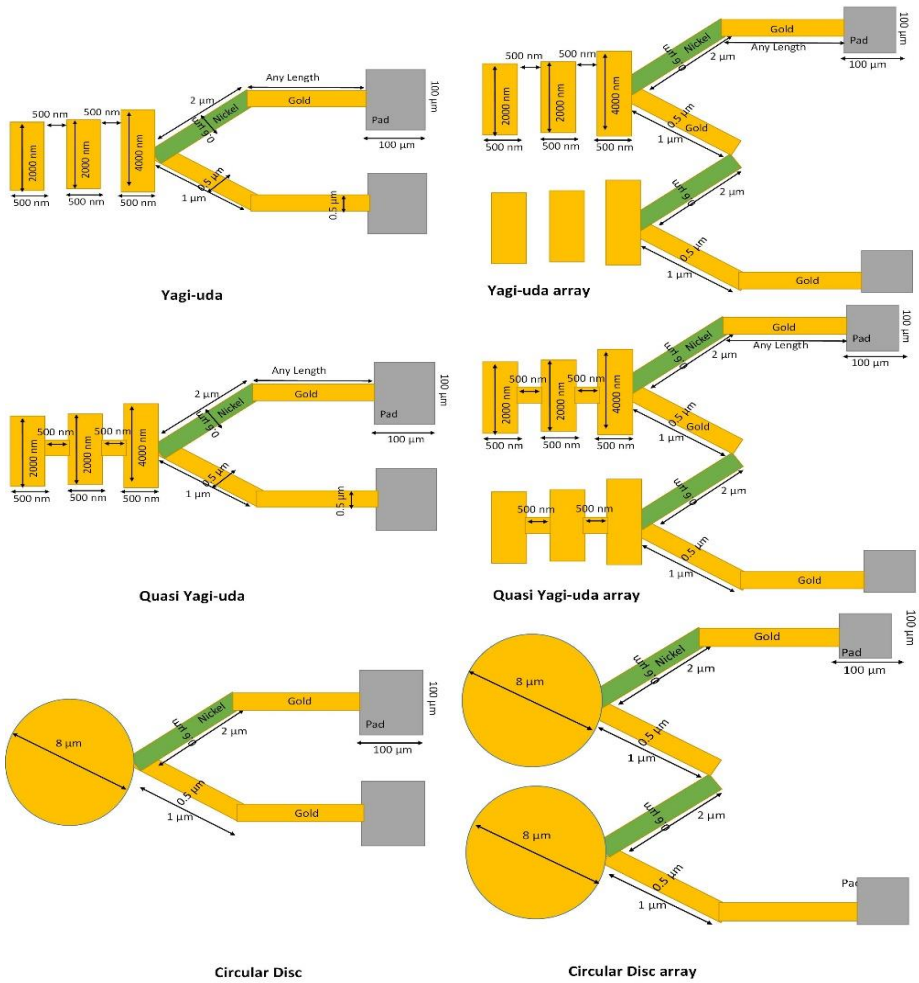


**Figure 4.37 Various geometric designs, single element and array, of nantennas for testing the thermopile effect**

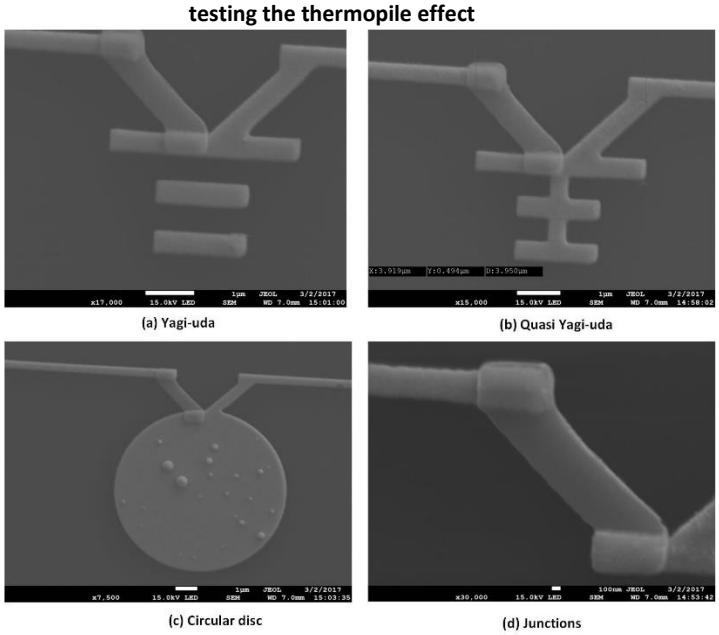


**Figure 4.38 Realized single element nantenna designs using gold and nickel for thermopile testing (a) yagi-uda, (b) Quasi Yagi-uda and (c) Circular disc and (d) Junctions**

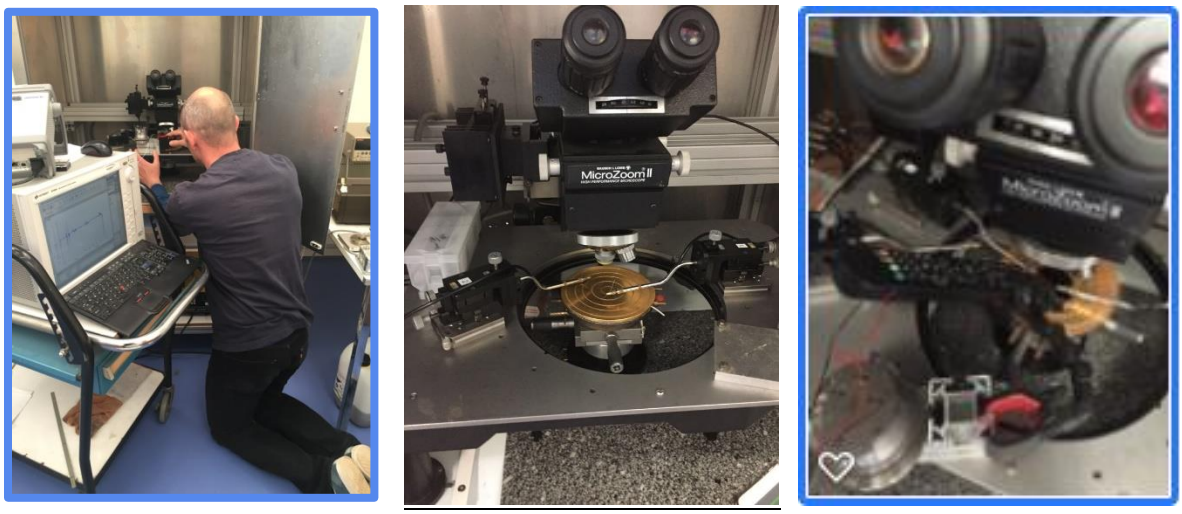


**Figure 4.39 Experimental setup and measurement apparatus for the realized Yagi-uda design**

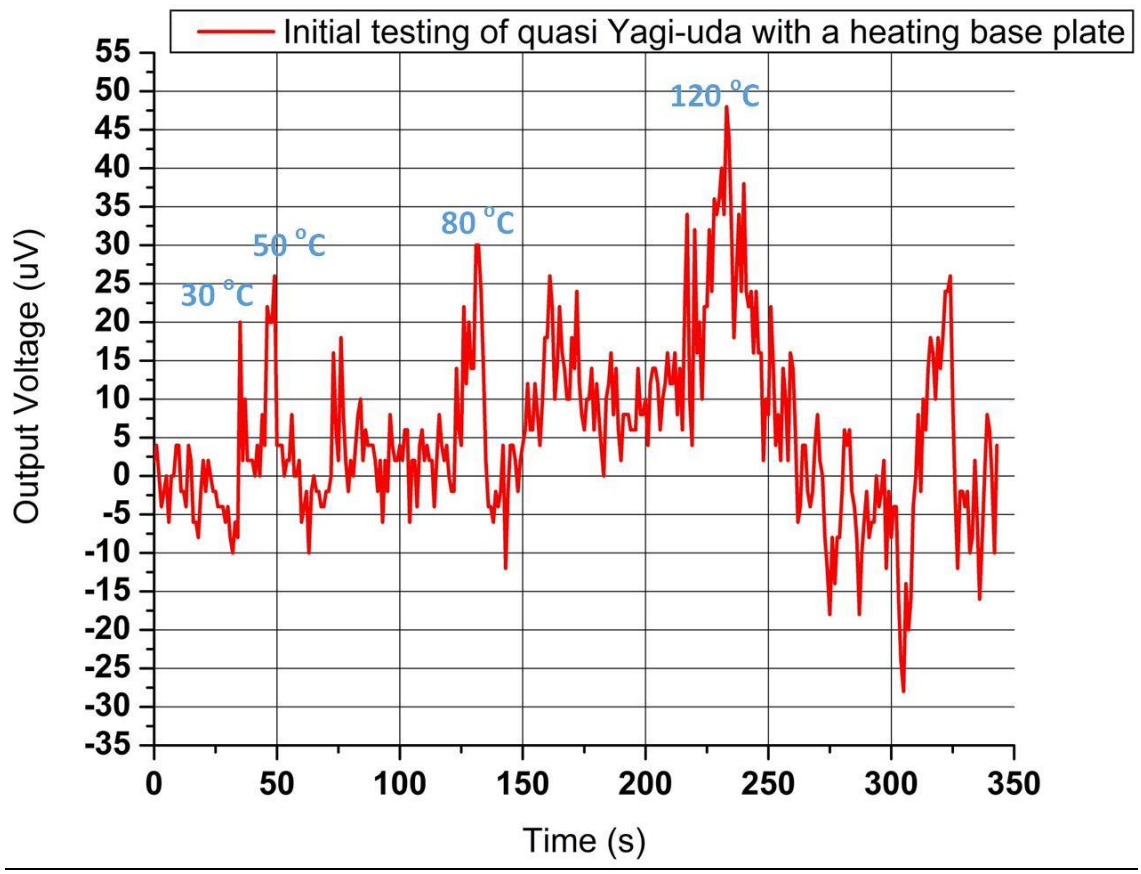


**Figure 4.40 Output voltage of the quasi Yagi-uda thermopile as per temperature gradient from a uniform heating source**

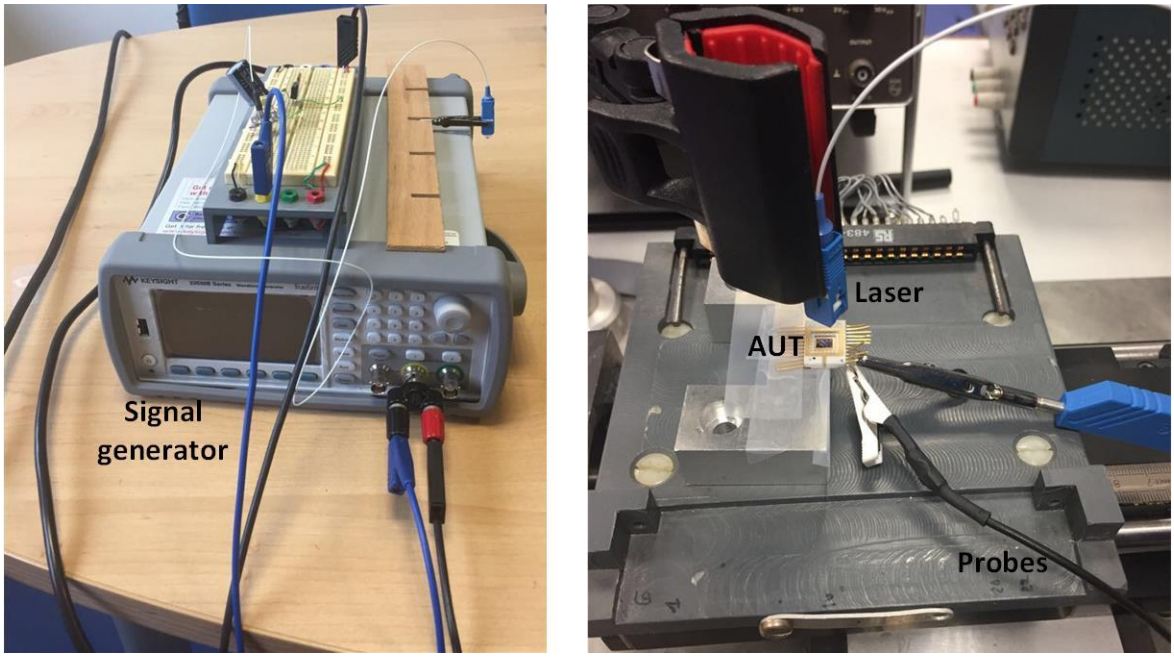


**Figure 4.41 Signal generator and testing of quasi Yagi-uda thermopile optical antenna with output probes uniform heating source**

Results of the quasi Yagi-uda optical thermopile antenna with excitation from three different wavelength laser sources are shown from Figure 4.42 to Figure 4.44. For the excitation of the antenna with the green laser at 532 nm, the excitation was timely controlled and the readings were taken just for a few seconds i.e. 30 seconds. It was observed that with initial excitation there was an abrupt jump in the voltage scale from 0 to 5 V. Then no variations were noted in the whole spectrum for the course of 30 seconds. The short pulses indicated that the noise factor was more involved and no temperature difference among the antenna elements reacted to the excitation. It was concluded that the design is not so operational at 532 nm laser. Figure 4.42(a) shows the measured results with zoomed in version in 4.42(b).

The quasi Yagi-uda antenna was next excited with a red laser operating at 650 nm. The duration of excitation was also for 30 seconds with its results and zoomed in version shown in Figure 4.43. It was observed from the results that the red laser excitation made the antenna resonate and produce some output voltage. Since the antenna is very sensitive to testing and the surrounding lab environment, before the excitation began, noise played a factor in the measurements and gave us a base line of 0.3 V. The excitation produced some results after 5seconds where variations in voltage peaks or rise and fall of voltage was observed. The voltage produced confirms the seebeck effect that the two metals have variating temperature and the dissipation of temperature gradient is affecting the optical antenna thus producing certain voltages. When the junction is heated, and due to the difference dissipation of temperature the junction create positive voltage but after short time the temperature become similar for both metals and the voltage decrease to zero. After sometimes the excitation is halted, the temperature decrease but both metal haven't the same dissipation temperature then the negative voltage is created for short time, after the temperature

become similar for both metals and the voltage decrease to zero. The level of negative pulse is lower to the positive one due probably to the dissipation of temperature. The maximum output voltage achieved for the 650 nm excitation was recorded around 0.7 V. Similarly, the antenna was then excited via the 940 nm laser and the results are shown in Figure 4.43. Same behaviour of peak voltages were observed for this stage of excitation. The only difference was in terms of the results where the 940 nm produced around 0.36 V of output voltage as per temperature difference among the two conducting metals i.e. Au and Ni.

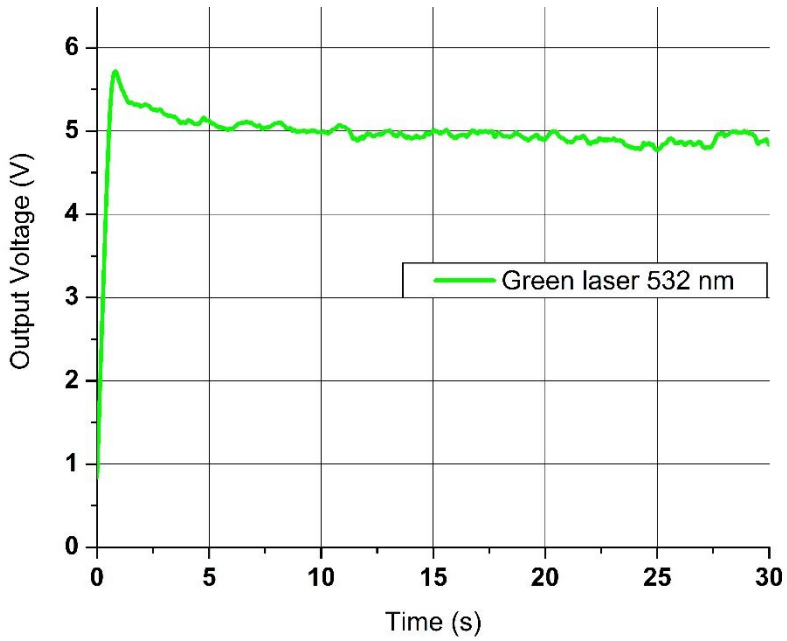


**(a) Output voltage of quasi Yagi-uda antenna**

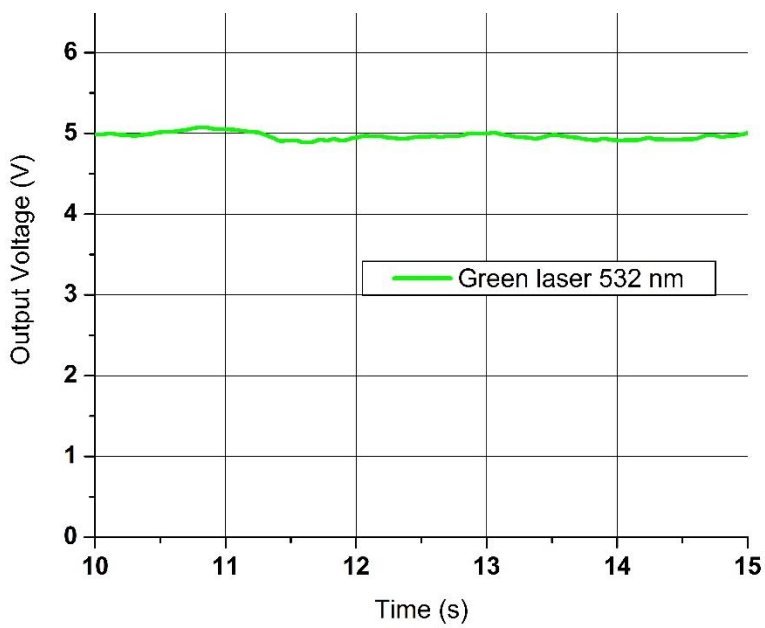


**(b) Zoomed in version**

**Figure 4.42 Measurements of excitation from 532 nm laser**

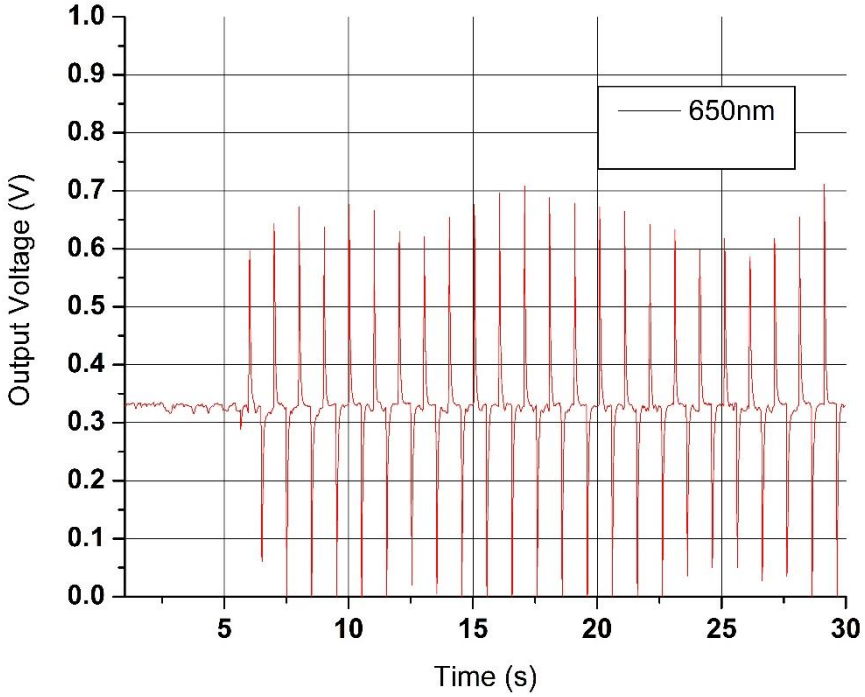


**(a) Output voltage of quasi Yagi-uda antenna**

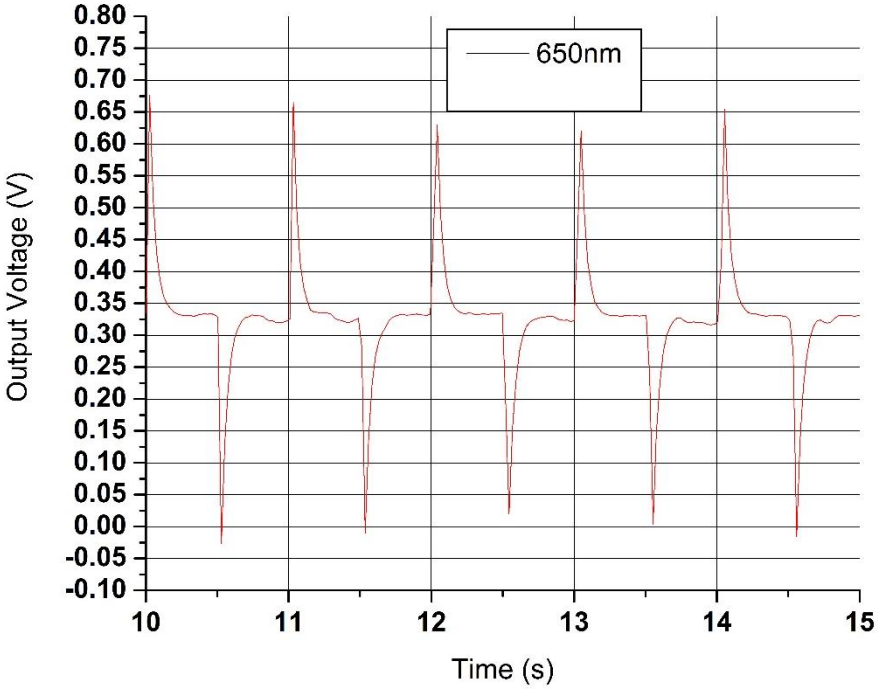


**(b) Zoomed in version**

**Figure 4.43 Measurements of excitation from 650 nm laser**

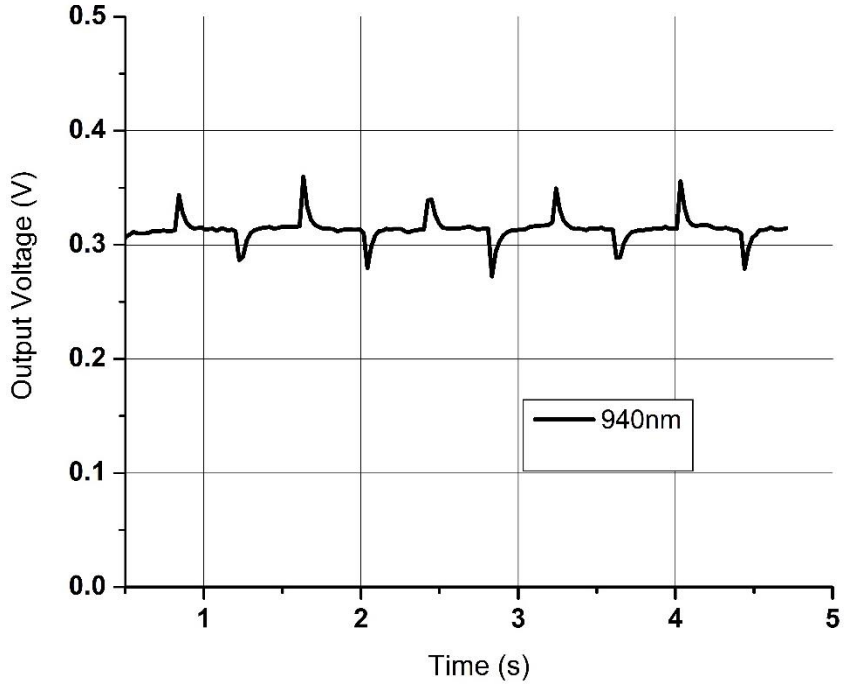


**(a) Output voltage of quasi Yagi-uda antenna**

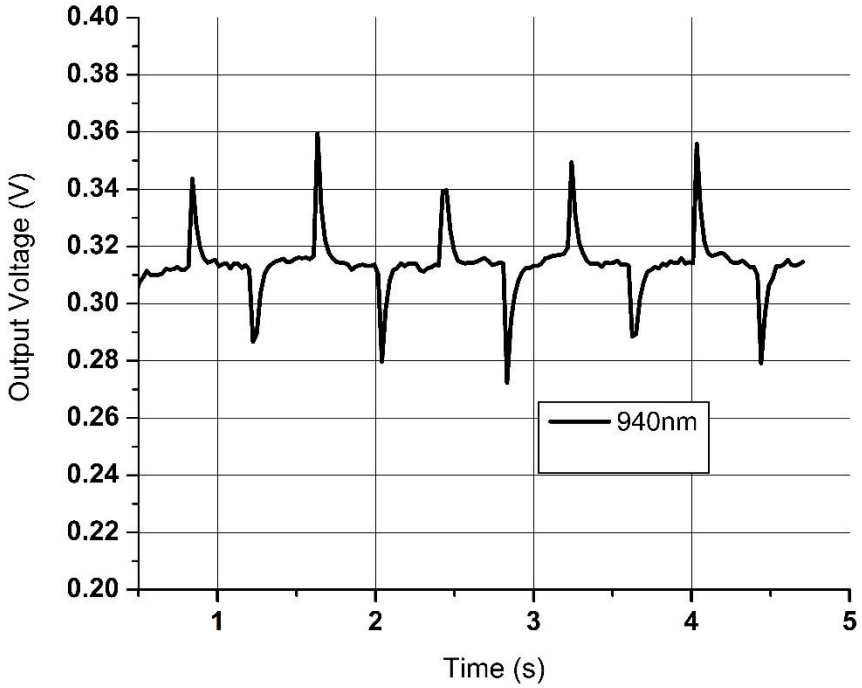


**(b) Zoomed in version**

**Figure 4.44 Measurements of excitation from 940 nm laser**

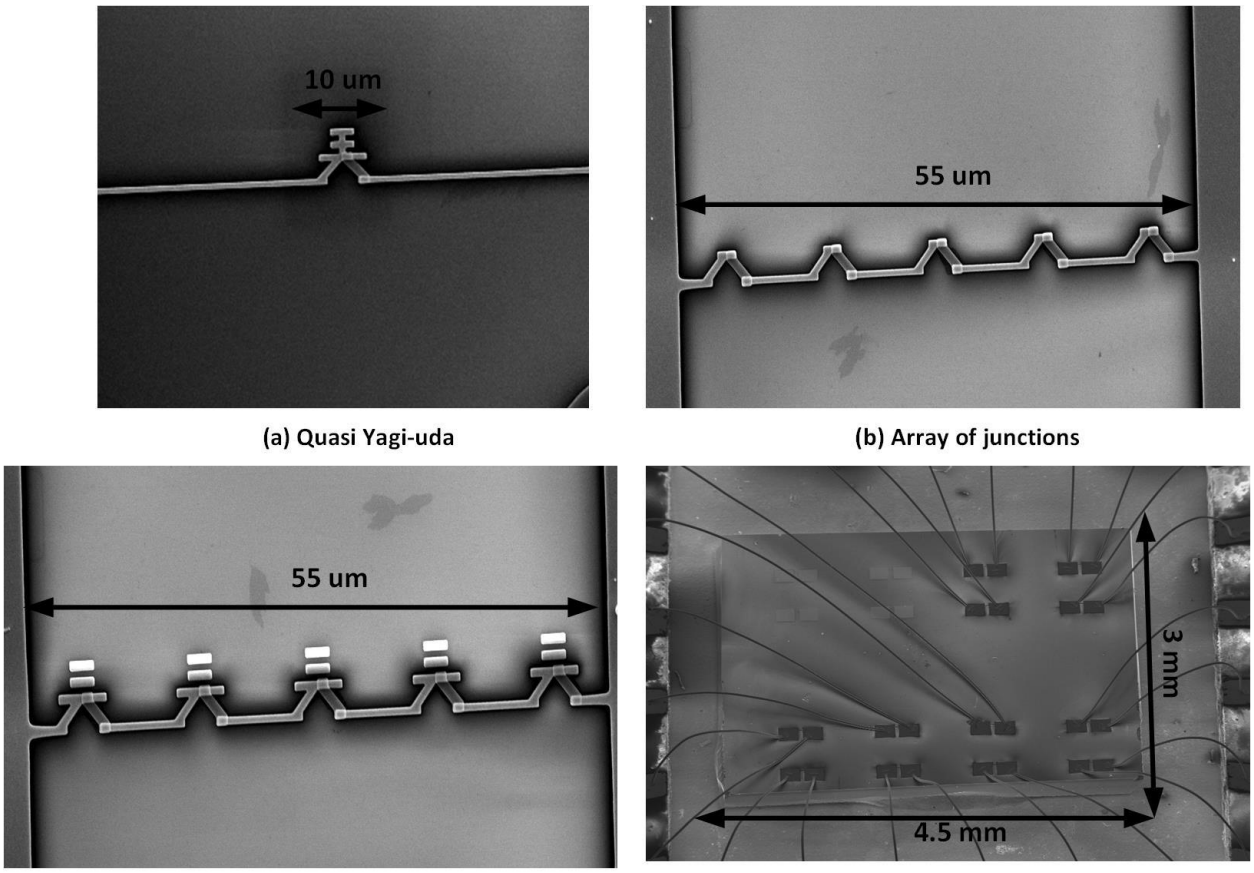


(a) Quasi Yagi-uda (b) Array of junctions

(c) Array of traditional Yagi-uda (d) Back side of casing with bonding wires

**Figure 4.45 Realized structures for 1550 nm laser excitation**

For the final testing of the optical thermopile antenna based on 1550 nm laser, it was decided to once again realize the traditional Yagi-uda antenna along with the junctions in array form. Since it was observed that increasing the laser wavelength produced certain appreciable output voltages, why not try refabricating the traditional Yagi-uda design and in the process check its temperature reaction to the excitation at 1550 nm. Figure 4.45 shows the three realized structures that were tested via laser excitation. One structure was the initial quasi Yagi-uda single element with others as 1x5 element array based on traditional Yagi-uda design and the junctions' of thermopiles. Figure 4.46 shows the results of the three structures with excitation done till 10 minutes. It was observed from the results that the single element quasi Yagi-uda produced maximum voltages around 0.75 V while the junction array (Peltier) produced 0.79 V with traditional Yagi-uda producing 0.82 V of output voltage. The resonance behave in the same manner as with earlier laser excitation where the positive voltage or peak appears due to thermal difference among the metals and the lowest peaks appear when the discharging happens when excitation is halted.

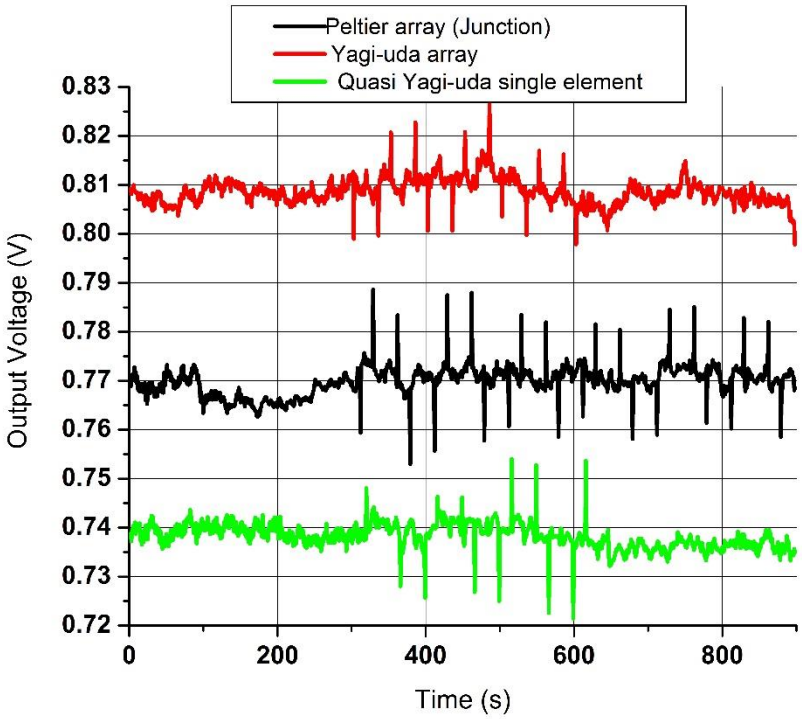


**(a) Output voltage of three designs**

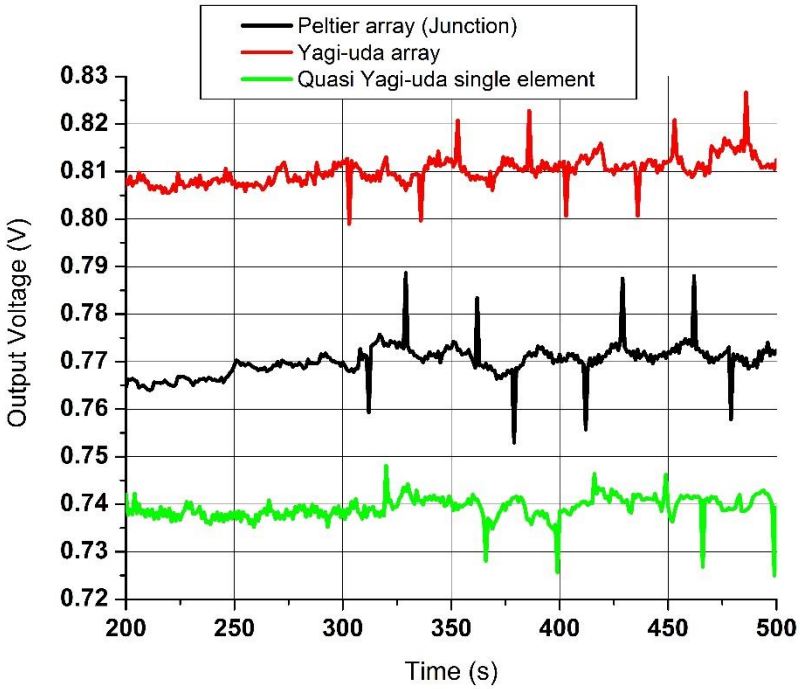


**(b) Zoomed in version**

**Figure 4.45 Measurement of excitating the three designs with 1550 nm laser**

## 4.6 Summary and Conclusion

In this chapter optical antenna designs based on three different techniques were presented. The first design technique used commercial photodiode to convert the received light into output voltage. The design for this antenna was based on quasi Yagi-uda design where array of 100 x 100 elements were fabricated using electron beam lithography process. The antenna array integrated with fermionics photodiode was illuminated via a visible and infrared laser. The visible light incidence produced 0.15 V on the Yagi fermionics integration. The laser light excitation produced 0.52 V of output voltage. The second design technique was based on simulations where the idea was to further focus or capture the incident light via a lens and project it onto the antenna. Simulations presented the exact design dimensions but limitation of fabrication facilities halted the remaining part of the experiment. The third and final design was based on generating output voltage using temperature difference among dissimilar metals. This process was based on the known seebeck or Peltier effect. In this technique various designs were fabricated and tested via lasers of different wavelengths i.e. 532 nm, 650nm, 940 nm and 1550 nm. The designs proved to be acceptable to these wavelengths and generated output voltages. The results produced were noted for single element quasi Yagi-uda antenna and an array of traditional Yagi-uda antenna. Both the designs were excited with 1550 nm lasers producing 0.75 V and 0.82 V of output voltage respectively.

Due to the difficulties of realizing the antenna and the rectifier part at THz band, we consider all the proposed structures as preliminary study. These designs deserve to be continued in order to perform the efficiency and the reliability of this kind of proposed solutions. The last solution proposed using the Peltier effect can be improved by opting for a multilayer structure. This will allow better management of the temperature dissipation and can maintain the stable output voltage for as long as possible.

# Bibliography


[1] Rudan Massimo, Physics of semiconductor devices, *Springer verlag*, NewYork, 2016.
[2] Sze, S. M, and Kwok Kwok Ng. *Physics Of Semiconductor Devices*. New Jersey: John Wiley & Sons, 2007.
[3] Dennis, P. N. J. Photodetectors: An introduction to current technology. *Springer Science & Business Media*, 2012.
[4] Wang J., Lee S.J., Ge-Photodetectors for Si-Based Optoelectronic Integration, *Sensors*,vol. 11, pp 696-718., 2011.
[5] Pavesi L., Guillot G., Optical Interconnects: The Silicon Approach (*Springer Series in Optical Sciences*), New York: Springer 2006.
[6] Langley, S.P., The "bolometer". The Society. New York: Published by *The Society. Gregory Bros*. Printers, 34 Carmine St., 1881.
[7] Kraus, H. "Superconductive bolometers and calorimeters." *Superconductor Science and Technology* vol. 9, pp.10 1996.
[8] Jarman, Jarman T., Essam E. Khalil, and Elsayed Khalaf. "Energy analyses of thermoelectric renewable energy sources." *Open Journal of Energy Efficiency*, vol.2, pp.04, 2013.
[9] Velmre, E. "Thomas Johann Seebeck and his contribution to the modern science and technology." *Electronics Conference (BEC), 2010 12th Biennial Baltic*, 2010.
[10] Lang, Sidney B. "Pyroelectricity: from ancient curiosity to modern imaging tool." *Physics today* vol.58, 2005.
[11] Elif Gul Arsoy, Mesut Inac, Atia Shafique, Meric Ozcan, Yasar Gurbuz, "The metal-insulator-metal diodes for infrared energy harvesting and detection applications *", Proc. SPIE 9819, Infrared Technology and Applications XLII*, (20 May 2016.
[12] Yang L.J., Wang S., Zeng Q.S., Zhang Z.Y., Peng L.M., Carbon Nanotube photoelectronic and photovoltaic devices and their applications in infrared detection, *Small* ,vol. 9,pp. 1225-1236, 2013.
[13] Bai P., Gu M.X., Wei X.C., Li E.P., Electrical Detection of Plasmonic Waves Using an Ultra-compact Structure via a Nanocavity, *Optics Express, vol.* 17,pp. 24349-24357, 2009.
[14] D. Corcos et al., "Antenna-Coupled MOSFET Bolometers for Uncooled THz Sensing," *in IEEE Transactions on Terahertz Science and Technology*, vol. 5, no. 6, pp. 902-913, Nov. 2015.
[15] Lu, Feng, Jongwon Lee, Aiting Jiang, Seungyong Jung, and Mikhail A. Belkin. "Thermopile detector of light ellipticity." *Nature communications*, vol. 7, 2016.
[16] Kuznetsov, Sergei A., Andrey G. Paulish, Miguel Navarro-Cía, and Andrey V. Arzhannikov. "Selective pyroelectric detection of millimetre waves using ultra-thin metasurface absorbers." *Scientific reports,* vol.6 pp. 21079, 2016.
[17] M. Schiselski et al., "A planar Schottky diode based integrated THz detector for fast electron pulse diagnostics," *2016 IEEE MTT-S International Microwave Symposium (IMS)*, San Francisco, CA, pp. 1-4, 2016.
[18] Arsoy, Elif Gul, Mesut Inac, Atia Shafique, Meric Ozcan, and Yasar Gurbuz. "The metal-insulator-metal diodes for infrared energy harvesting and detection applications*." In Proc. of SPIE* , vol. 9819, pp. 98190F-1. 2016.
[19] Sharma, Asha, Virendra Singh, Thomas L. Bougher, and Baratunde A. Cola. "A carbon nanotube optical rectenna." *Nature nanotechnology 10*, Vol no. 12,pp. 1027-1032, 2015.
[20] Balanis, C. A. Antenna Theory (John Wiley & Sons, 2005).
[21] Novotny L. Effective wavelength scaling for optical antennas. *Phys Rev Lett*, 98, 266802–4, 2007.
[22] Czack, Gerhard, and Leopold Gmelin. Molybdenum: Mo. Berlin: *Springer-Verlag*, 1988.
[23] Palik, Edward D., and Gorachand Ghosh. Handbook of Optical Constants of Solids Five-volume Set. London: Academic, 1998.
[24] James P. B. Johnson and R. W. Christy, "Optical constants of the noble metals," *Phys. Rev. B6*,pp 4370–4379, 1972.
[25] Dregely D, Taubert R, Dorfm¨uller J, Vogelgesang R, Kern K, Giessen H. 3D optical Yagi–Uda nanoantenna array. *Nat Commun* 2011, 2, 267–7.
[26] Lin, Yi-Cheng, W. T. Yen, and L. Q. Wang. "Effect of Substrate Temperature on the Characterization of Molybdenum Contacts Deposited by DC Magnetron Sputterings." *Chinese Journal of Physics* 50.1 (2012): 82-88.
[27] "Fermionics." Fermionics.com. N.p., 2017. Web. 8 July 2017.
[28] Brewer, George, ed. Electron-beam technology in microelectronic fabrication. *Elsevier,* 2012.
[29] Y. Fainman, L. P. Lee, D. Psaltis, and C. Yang, *Optofluidics: Fundamentals, Devices, and Applications* (McGraw-Hill, 2010).
[30] C. Kerbage, P. Steinvurzel, P. Reyes, P. S. Westbrook, R. S. Windeler, A. Hale, and B. J. Eggleton, "Highly tunable birefringent microstructured optical fiber," *Opt. Lett.* 27(10), 842–844 (2002).

[31] B. T. Kuhlmey, B. J. Eggleton, and D. K. C. Wu, “Fluid-filled solid-core photonic bandgap fibers,” *J. Lightwave Technol*. 27(11), 1617–1630 (2009).
[32] Markos, C., K. Vlachos, and G. Kakarantzas. "Thermo-optic effect of an index guiding photonic crystal fiber with elastomer inclusions." *21st International Conference on Optical Fiber Sensors*. Vol. 7753. 2011.
[33] Srinivasan, Arvind, et al. "Infrared dielectric function of polydimethylsiloxane and selective emission behavior." *Applied Physics Letters* 109.6 (2016): 061905.
[34] F. Schneider, J. Draheim, R. Kamberger, and U. Wallrabe, “Process and material properties of polydimethylsiloxane (PDMS) for Optical MEMS,” *Sens. Actuators A Phys*. 151(2), 95–99 (2009).
[35] Alqadami, Abdulrahman Shueai Mohsen, et al. "Assessment of PDMS technology in a MIMO antenna array." *IEEE Antennas and Wireless Propagation Letters* 15 (2016): 1939-1942.
[36] Elobaid, Husameldin Abdelrahman Elmobarak, et al. "A Transparent and Flexible Polymer-Fabric Tissue UWB Antenna for Future Wireless Networks." *IEEE Antennas and Wireless Propagation Letters* 16 (2017): 1333-1336.
[37] Ee, Ho-Seok, and Ritesh Agarwal. "Tunable metasurface and flat optical zoom lens on a stretchable substrate." *Nano letters* 16.4 (2016): 2818-2823.
[38] Park, Hyunsung, and Kenneth B. Crozier. "Multispectral imaging using polydimethylsiloxane (PDMS) embedded vertical silicon nanowires." CLEO: Applications and Technology. *Optical Society of America*, 2013.
[39] Lu F, Lee J, Jiang A, Jung S, Belkin MA, “Thermopile detector of light ellipticity”, *Nature communications,* vol 7, 2016.
[40] Szentpáli, Béla, Gábor Matyi, Péter Fürjes, Endre László, Gábor Battistig, István Bársony, Gergely Károlyi, and Tibor Berceli. "Thermopile-based THz antenna." *Microsystem technologies* 18, no. 7-8, 849-856 2012.

# Chapter 5
# Conclusion, challenges and Future Work

## 5.1 Summary of contributions:

This thesis has made the following contributions to the field of optical antennas being nominal candidates for harvesting solar radiation energy especially in the infra-red domain of the electromagnetic spectrum. The research work started with investigations of energy harvesting circuits at the lower bands of electromagnetic spectrum and then eventually transitioning to higher bands of the spectrum.

1. **Presented a hexaband monopole antenna for capturing various commercial bands i.e. GSm, CDMA, LTE, DCS and WLAN.**
   For the energy harvesting applications in the lower radio frequency domain, first a hexaband monopole printed antenna was presented and experimentally realized. This antenna was capable of capturing frequency signals in the known commercial bands of LTE, CDMA, GSM and WLAN. The antenna provided with omnidirectional gains of 1.83 dB, 3.17 dB, 3.23 dB and 5.82 dB at frequency of interests i.e. 0.9 GHz, 1.8 GHz, 2.45 GHz and 5.8 GHz respectively.

2. **Proposed a wideband rectifier using voltage doubler rectification technique.**
   Next step in the energy harvesting involved a rectifier circuit. To receive the multiband signals, a wideband rectifier was designed and optimized in terms of impedance matching, filtering load values via a commercially available circuit simulator called advanced design system (ADS). The rectifier design was based on Cockroft-Walton voltage doubling technique using HSMS 2860 schottky diodes. The rectifier was able to produce maximum DC output voltages (8V) and efficiencies (80 %) for input power levels ranging from -20 dBm to 20 dBm.

3. **Experimental prototype of a rectenna capable of capturing ambient electromagnetic signals in lab environment.**
   Finally, both the hexaband antenna and the wideband rectifier were integrated to form a complete rectenna system. Lab environment was used to test the rectenna placed at a distance of 1m from the transmitting source. At various frequencies of interest (0.9 GHz, 1.8 GHz, 2.45 GHz and 5.8 GHz), the realized rectenna produced an output voltage in the range of 0.024 V to 0.63 V when the input power was varied form 0 dBm to 20 dBm.

4. **Proposed simulation based equilateral triangular dielectric resonator nantenna (ETDRNA) working in the infrared regime of 1550 nm wavelength (193.5 THz).**
   Presented a simulation based design of an equilateral triangular dielectric resonator optical antenna. Due to less losses at the THz band, the dielectric material was selected for operating in the infrared domain. The proposed ETDRNA resonated with wide bandwidth of 5 THz (192.5 THz – 197.3 THz) and acceptable directivity of 8.6 dBi at the band of interest i.e. 193.5 THz (1550 nm wavelength). Various optimizations based on drude model characteristics of the conducting material and analysis on the axis rotation of the tringle were performed in order to get the required results in the infrared band.

5. **Proposed another nantenna based on hexagonal shaped dielectric resonator (HDRN) for the same 1550 nm wavelength (193.5 THz).**
   A hexagonal shaped based dielectric resonator was also presented for the center frequency of 193.5 THz. This HDRN presented better bandwidth compared to ETDRNA i.e. 7 THz (190 THz-198 THz) with similar directivity of 8.6 dBi. Also transmission modes analysis for the hexagonal DR were done in comparison to the simulated hexagonal dielectric resonator at the lower frequency of 3 GHz.

6. **Simulation and realization of a Yagi-uda based optical antenna made from molybdenum material.**
   For detection of infrared light at 1550 nm wavelength, a realized structure based on the Yagi-uda design was presented. Simulations suggested the optical antenna to be resonating in a wideband at 0.3 THz (193.37 THz to 193.71 THz) with gain and directivity of 12.9 dB and 16.6 dBi. The optical antenna was realized on a silicon substrate with conducting materials made from molybdenum material using the traditional e-beam lithography. After many trials the antenna was fabricated covering an area of 1000 x 1000 $\mu m^2$. Unfortunately its characterization was not done as per lacking of relevant apparatus in our lab.

7. **Realization of an array of Yagi-uda nantenna to be connected to a fermionics diode for generating output voltages.**
   Learning from the experiences of the first trial, especially the high temperature dependency of molybdenum material (around 2400 $^0$C) which caused sputtering of atoms to adhere rather than remain separate, it was decided to use a less temperature (600 $^0$C) dependent material for fabrication, i.e. Aluminum. The Yagi-uda nantenna was designed to resonate at 193.5 THz (1550 nm wavelength) where it was then connected to a commercially available fermionics diode in order to have rectification of the received light on the optical nantenna. Various array configuratins were simulated to get ideal resonance in the band of interest. Finally the realization of an array of Yagi-uda nantennas on a silicon based substrate having dimensions of 2 x2 $mm^2$ was achieved. It was tested via excitation of a 1550 nm laser in lab environment at a certain distance (3 cm). The nantenna array with integration of the commercial fermionics diode produced 0.52 V maximum output voltage.

8. **Proposed a polydimethylesilixone (PDMS) lens based design for capturing light waves and possibly convert them into output voltages.**
   It was observed from the previous nantenna design that the infrared light needs to be more focused onto the fermionics diode in order to obtain more output voltage. Few design techniques were surveyed and it was released that using a transparent lens might increase the intensity of light being projected onto the fermionics diode. A micro-fluid polymer material called polydimethylesilixone (PDMS) was used as it offers more transmission at the infrared band. Various spherical lens shaped were designed and simulated, in order to find the correct focus point for the beam which was achieved at a distance to 1.5 m. Unfortunately the size of lens (10-20 μm) was difficult to realize which halted the fabrication process.

9. **Experimental realization of thermopile nantenna for detection of light waves and generating output voltages.**
   The core of the research work was concluded with the experiments based on thermal generation resulting in output voltages. Various thermocouple designs (Yagi-uda, circular disc, peltier junction and bevel shaped) were proposed for this experiment. The design materials were based on a combination of gold (Au) and Nickel (Ni) printed on a silicon substrate. The design (Yagi-uda) produced successful results upon excitation with four kinds of wavelength lasers i.e. 532 nm, 650 nm, 940 nm and 1550 nm. The maximum output voltage obtained, via excitation from the 1550 nm laser, for the single Yagi-uda element and 1x5 element array was 0.75 V and 0.82 V respectively.

## 5.2 Challenges faced during research:

Working in a new field of optical antennas, for harvesting solar energy, with limited literature, a researcher is always faced with difficulties and challenges along the way. Following are the challenges faced at each stage of design and implementation during the course of this research work.

1. **Hexaband monopole rectenna**
   Impedance matching between schottky diode and the hexaband monopole antenna was a difficult challenge. Since hexabands were resonated by the antenna, the diode had to be matched with each band in terms of impedance so that maximum rectification could be achieved by the rectenna. Also the handling of schottky diodes during the measurements created some difficulties as most of them got burned out due to electrostatic infusion from human fingers. So care had to be taken when performing these rectenna measurements.

2. **Dielectric resonators (Triangular and Hexagonal) simulations**
   Limited full wave electromagnetic solvers are available when performing simulations in the THz domain. It was the first time that CST MWS studio was used to perform high

frequency simulations as only a few successful simulations were done in the range from 1 THz-10 THz. The designs based on dielectric resonators had to be optimized in term of geometric dimensions and material assigning at 193.5 THz central frequency. The problem came during the optimization stages as the mesh cells generated were around 2 billion which slowed the process for days. Another problem associated with the simulations were to correctly assign ports to the optical antennas as 50 ohm impedance was not a feasible option.

3. **Simulation and realization of Yagi-uda nantenna (Molybdenum or Aluminum)**
   The design again faced troubles during the simulation stages. Time consumption was another factor for delayed results, as optimization would take a lot of processing time. Also the design optimization for the Yagi-uda nantenna were not based on conventional or traditional microwave designs, so approximations were done in order to get the desired resonances around 193.5 THz central frequency. Another limitation associated with the simulation design was linked to the thickness of silicon substrate. The general economical silicon substrate available comes in the thickness of 380 µm, which caused simulations to end in error. The next challenge which this research work faced was in the fabrication of the yagi-uda nantenna. Various trials were done in order to get the correct sputtering of the molybdenum and later on Aluminum conductors to be deposited on the silicon substrate. All the process took months of work but in the end we had something in hand to be proud of.

4. **Characterization for the realized Yagi-uda nantenna and its bonding with fermioncs diode**
   The realized Yagi-uda nantenna array was not characterized as its measurement apparatus was not available or in our access. Since measuring the optical antennas require special optical apparatus, we had no resources or access to them. Secondly, in order to test the rectification of the proposed Yagi-uda array with fermioncs diode, we had difficulty in connecting them together. This was done many times to correctly bond the two elements together with the help of microscope and steady hands.

5. **Realization of polydimethylesilixone (PDMS) Lens**
   Another optical antenna design proposed for harvesting infrared energy was based on a transparent lens made from polydimethylesilixone (PDMS) material. This micro fluid polymer can easily be molded into any arbitrary shape and has shown progress in the microwave ranges. Unfortunately the dimension for our proposed lens was way too small to be realized, thus we only presented with the simulation results.

6. **Thermopile nantennas**
   The realization process for this design took a lot of time. The first prototype was fabricated using the e-beam lithography technique but was not accurate. The second time was a

charm as more attention was given to the details in terms of widths and lengths of the resonators. The material used was gold/nickel for the process so the sputtering had to be done correctly. The measurements was a little bit troublesome as a tubeable laser was not available to excite the antenna. The solution was home based where a low frequency signal modulator was used to provide modulation to the laser via a fiber. This took time and also no power control was possible for the laser during the process. Various readings at different occasions were taken until the satisfactory and stable output voltages were observed.

## 5.3 Future Work:

Although the objective of this research has been achieved, there are some future research topics and areas that may further enhance the concept. Some improvements to the following tasks achieved in this work can open doors to other potential researchers;

1. **Hexaband monopole rectenna**
   The current rectenna with its single voltage doubler circuit produces around 0.5-0.63 V output voltage. This can be experimented on further to add more rectification stages or other rectification topologies in order to generate more output voltage.

2. **Yagi-uda nantenna array**
   Appropriate excitation and characterization of the Yagi-uda nantenna array is a challenge and a good topic for further research, since nano technology is progressing and more ideas are being proposed to accomplish this task.

3. **Thermopile nantenna**
   Current realizations have provided us the know-how on how to tackle the fabrication details and this can be useful for continuing or proposing new designs for the thermopile antennas. The current realized single element Yagi-uda produced 0.75 V output voltage and its 1x5 array produced 0.82 V with excitation from a 1550 nm laser. This output voltage can further be increased by designing a larger array of 100 x 100 elements and exciting them individually or as a whole to generate more output voltage.

# List of Publications

## Peer-reviewed international journals

Waleed Tariq Sethi, Hamsakutty Vettikalladi, Habib Fathallah and Mohamed Himdi, Hexa-band printed monopole antenna for wireless applications, *Microw Opt Technol Lett*, v.59, p.2816–2822, 2017.

Waleed Tariq Sethi, Hamsakutty Vettikalladi, Habib Fathallah and Mohamed Himdi, "Optimizing a Nantenna Array at 1550 nm Band", *IET micro and nano letters*, v.11, p. 779-782, 19 Aug, 2016.

Waleed Tariq Sethi, Hamsakutty Vettikalladi, Habib Fathallah and Mohamed Himdi, "Nantenna for Standard 1550 nm Optical Communication Systems", *International Journal of Antennas and Propagation Hindawi,* v.2016, 9 pages*,* July 2016.

Waleed Tariq Sethi, Hamsakutty Vettikalladi, Habib Fathallah, and Mohamed Himdi, "Equilateral Triangular Dielectric Resonator Nantenna at Optical Frequencies for Energy Harvesting," *International Journal of Antennas and Propagation*, vol. 2015, 10 pages, 2015.

## Book chapter publications

Waleed Tariq Sethi, Hamsakutty Vettikalladi, Habib Fathallah, and Mohamed Himdi, "Dielectric Resonator Nantennas for Optical Communication", *in Optical Communication Technology*, p.29, InTech Publisher, Aug 2017.

## Peer-reviewed international conferences

Waleed Tariq Sethi, Hamsakutty Vettikalladi, Habib Fathallah and Mohamed Himdi, "1x2 Equilateral Triangular Dielectric Resonator Nantenna Array for Optical Communication", presented at *the 7th International Conference on Sciences of Electronics, Technologies of Information and Telecommunications (SETIT),* Hammamat, Tunisia, 18-20 Dec, 2016.

Waleed Tariq Sethi, Hamsakutty Vettikalladi, Habib Fathallah and Mohamed Himdi, "Hexagonal Dielectric Loaded Nantenna for Optical ITU-T C-Band Communication", *11th IEEE International Conference on Wireless and Mobile Computing, Networking and Communications, WiMob, Abu-Dhabi,* 19-21 Oct 2015.

Waleed Tariq Sethi, Hamsakutty Vettikalladi and Habib Fathallah, "Dielectric Resonator Nanoantenna at Optical Frequencies", *2015 International Conference on Information and Communication Technology Research (ICTRC)*, Abu-Dhabi,UAE, 17-19 May, 2015.

# List of Figures

Figure 1.1 Solar Radiation Energy Distribution on Earth [6] ..... 3
Figure 1.2 Solar radiation spectrum for direct light at Earth's atmosphere and at sea level [7]..... 4
Figure 1.3 Working Principle of Photovoltaic Cell ..... 4
Figure 1.4 Principle of surface plasmon resonance:[13]..... 6
Figure 1.5 The Roman Lycurgus Cup..... 7
Figure 2.1 Various RF energy sources with respective frequencies and power levels ..... 13
Figure 2.2 General block diagram of the RF energy harvesting system (Rectenna) [4]..... 14
Figure 2.3 Antenna Equivalent Circuit ..... 15
Figure 2.4 Various Matching Configurations (a) Transformer (b) Shunt Inductor (c) LC Net ..... 16
Figure 2.5 RF Energy Harvesting at 2.45 GHz: All elements on a single PCB [14] ..... 16
Figure 2.6 (a) Multiplier Stages (b) Output Voltage vs Efficiency [20] ..... 17
Figure 2.7 Multiplier equivalent circuit [21] ..... 18
Figure 2.8 Patch antenna and Rectifier [24] ..... 18
Figure 2.9 DC Output voltage produces from the rectenna [24]..... 19
Figure 2.10 (a) Paper based annular slot antenna [25]..... 19
Figure 2.11 Rectenna measurement: output DC voltage [25]..... 20
Figure 2.12 (a) Implemented antenna [26]..... 21
Figure 2.13 The implemented rectenna system are highlighted [27]..... 21
Figure 2.14 The rectified voltage at the rectenna output over frequency for three[27]……..22
Figure 2.15 Rectenna (a) Front view (b) Back view [28] ..... 22
Figure 2.16 Measured output voltage versus input power of only-rectifier and rectenna [28]..... 23
Figure 2.17 Fabricated prototype of rectenna [29]..... 23
Figure 2.18 Experimental setup and measured efficiency [29]..... 23
Figure 2.19 Antenna and rectifier [30]..... 24
Figure 2.20 Measured received power versus frequency and measured voltage rectenna [30]..... 24
Figure 2.21 Experimental setup of cell phone using 2 element array for a load of 4.3kΩ [31]..... 25
Figure 2.22 Fabricated Solar panel Vivaldi antenna [32]. ..... 26
Figure 2.23 Fabricated Rectenna [33]..... 26
Figure 2.24 Batteryless temperature-sensor prototype [33]..... 27
Figure 2.25 Geometry of the proposed Hexaband Antenna..... 29
Figure 2.26 Photograph of fabricated hexaband antenna..... 30

Figure 2.27 Measured and Simulated |S11| of the proposed hexaband antenna ..... 30
Figure 2.28 Surface current distributions for the proposed hexaband antenna…… 31
Figure 2.29 3D gain patterns of proposed hexaband antenna ..... 31
Figure 2.30 Measured E-Plane and H-Plane radiation patterns of proposed hexaband antenna.... 32
Figure 2.31 (a) Conventional Single Series rectifying circuit configuration ..... 34
Figure 2.31 (b) Voltage Doubler rectifier circuit configuration ..... 34
Figure 2.32 Voltage doubler design with multiple tones ..... 36
Figure 2.33 Input impedances for voltage doubler for various frequencies of interest..... 36
Figure 2.34 (a) Matching circuit at 0.9 GHz frequency ..... 37
Figure 2.34 (b) Results at 0.9 GHz frequency; ..... 37
Figure 2.35 (a) Matching circuit at 1.8 GHz frequency ..... 38
Figure 2.35 (b) Results at 1.8 GHz frequency; ..... 38
Figure 2.36 (a) Matching circuit at 2.45 GHz frequency ..... 39
Figure 2.36(b) Results at 2.45 GHz frequency ..... 39
Figure 2.37 (a) Matching circuit at 5.8 GHz frequency ..... 40
Figure 2.37 (b) Results at 5.8 GHz frequency ..... 40
Figure 2.38 Rload vs DC output voltages ..... 41
Figure 2.39 Multiband rectifier based on lumped components LC network ..... 42
Figure 2.40 Simulated matched results of multiband rectifier using lumped components ..... 42
Figure 2.41 Multiband rectifier based on distributed components..... 43
Figure 2.42 Geometric design of multiband rectifier in CST-MWS ……43
Figure 2.43 Realized multiband rectifier on RT-5880 substrate..... 44
Figure 2.44 Multiband rectifier measured s-parameters ..... 44
Figure 2.45 Multiband Rectifier measured voltages and efficiency ..... 45
Figure 2.46 Power levels received on hexaband antenna measured via a spectrum analyzer ..... 46
Figure 2.47 Hexaband Antenna and multiband rectifier together as a rectenna system……47
Figure 2.48 Experimental setup of the rectenna system ..... 47
Figure 2.49 Experimental results of output voltages and efficiency on rectenna ..... 48
Figure 3.1 Electromagnetic spectrum with THz range [10]..... 54
Figure 3.2 Applications for Terahertz Band (Nano scale antennas) [15]…….. 54
Figure 3.3 The basic principles of nantenna operation (exemplified by a nanodipole) [25] ..... 55
Figure 3.4 The electromagnetic spectrum with focus on visible light region [20] ..... 59
Figure 3.5 SPP at the interface between a metal and a dielectric [33]..... 62
Figure 3.6 Antenna Geometry of proposed nantenna design based on (ETDRNA) ..... 67

Figure 3.7 Optimized Parameters: (a) Length of Feed Line (b) Width of Feed Line ..... 69
Figure 3.8 Optimized Parameters: (a) Length of Ground Plane (b) Width of Ground Plane ..... 70
Figure 3.9 Height of the ETDRN antenna ..... 71
Figure 3.10 Angular Rotation of Triangular DR..... 71
Figure 3.11 Optimized Parameters: Effect of Angular Rotation of Resonant Frequency ..... 72
Figure 3.12 Simulated Return Loss and Directivity of ETDRNA ..... 73
Figure 3.13 3D end-fire Radiation Pattern at a) 192 THz (b) 193.5 THz (c) 197 THz……..74
Figure 3.14 Geometry of Hexagonal Dielectric Loaded Nantenna (HDLN)..... 76
Figure 3.15 Optimized Parameters: (a) Length of Feed Line (b) Width of Feed Line ..... 78
Figure 3.16 Optimized Parameters: (a) Length of Ground Plane (b) Width of Ground Plane ..... 79
Figure 3.17 Optimized Parameters: Height of Hexagonal DR..... 80
Figure 3.18 E-Field Propagation..... 81
Figure 3.19 Simulated return loss and Directivity of proposed HDLN ..... 82
Figure 3.20 E-field distribution as shown via the magnitude at 193.5 THz with HE20δ mode. ... 82
Figure 3.21 3D radiation pattern: (a) 191 THz (b) 193.5 THz (c) 198 THz ..... 83
Figure 3.22 Geometry of proposed 1x2 Array: (a) Front View (b) Side View..... 84
Figure 3.23 Return Loss and Directivity of 1x2 ETDRN Array..... 86
Figure 3.24 3D radiation pattern at 193.5 THz ..... 86
Figure 3.25 Rotation scenario of triangular DR's for spectral shifts ..... 87
Figure 3.26 Return Loss and Directivity as per Rotation (a) T1 Rotated (b) T2 Rotated (c) Both T1 and T2 simultaneously rotated ..... 88
Figure 3.27 3D radiation pattern of directivity at 193.5 THz ..... 89
Figure 3.28 Effect of Tuneability on Directivity and fractional bandwidth..... 89
Figure 4.1 The photoelectric effect ..... 95
Figure 4.2 Proposed experimental setup for the first technique for harvesting energy……99
Figure 4.3 Generic dimensions and layout of a Yagi-uda antenna [1]……..101
Figure 4.4 Geometry and dimensions of Yagi-uda optical antenna……..101
Figure 4.5 Simulated s-parameters of proposed Yagi-uda anntenna…….....103
Figure 4.6 Near Field Current Distributions ……...103
Figure 4.7 Gain and Directivity at 193.5 THz (a) 12.9 dB Gain; (b) 16.6 dB Directivity……...104
Figure 4.8 Fabricated Yagi-uda nantenna using [CVD] technology……104
Figure 4.9 Geometry and dimensions (Al) based of Yagi-uda nantenna…….105
Figure 4.10 Simulated return loss of proposed Yagi-uda nantenna……..106
Figure 4.11 Simulated gain of proposed Yagi-uda nantenna……....106

Figure 4.12 Fermionics Photodiode FD100L with lens cap [8]…….……..107
Figure 4.13 Geometry and dimensions of Yagi-uda nantenna with slot for fermionic diode…..…108
Figure 4.14 Simulated return loss of Yagi-uda nantenna with slot for fermionic diode……..…108
Figure 4.15 Simulated gain of proposed Yagi-uda nantenna with slot for fermionics diode…..…109
Figure 4.16 Current Distribution of Yagi-uda with slot for photodiode……..…109
Figure 4.17 Geometry and dimensions of Yagi-uda nantenna 1x2 array with slot fermionic ……110
Figure 4.18 Simulated return loss of oposed 1x2 Yagi-uda nantenna with slot fermionic diode…110
Figure 4.19 Simulated gain of proposed 1x2 Yagi-uda nantenna with slot for fermionics diode ..111
Figure 4.20 Current distributions of 1x2 Yagi-uda array with slot for fermionics diode ……..…111
Figure 4.21 Geometry of 1x4 Yagi-uda nantennas array ……112
Figure 4.22 Simulated return loss propose 1x4 Yagi-uda nantenna with slot for fermionic diode..112
Figure 4.23 Simulated gain of proposed 1x4 Yagi-uda nantenna with slot for fermionic…. …..…113
Figure 4.24 Current distributions at 193.5 THz of 1x4 Yagi-uda nantenna fermionics diode…....109
Figure 4.25 Large array of 8x20 elements of Yagi-uda design with slots……..……. ……115
Figure 4.26 E-beam lithography process of realized yagi-uda nantenna array ……...…117
Figure 4.27 Realized Yagi-uda nantenna array……. ..118
Figure 4.28 Yagi-uda array under test with visible light from microscope ……119
Figure 4.29 Experimental setup of nantenna with infra-red laser …….……..120
Figure 4.30 Proposed experimental setup for second technique based on PDMS lenses……..121
Figure 4.31 3D hemoispherical lens……. ……...123
Figure 4.32 Distance equation for collimated hemispherical lens …….……123
Figure 4.33 Focus point of the incident beam at various distances of lens …..……124
Figure 4.34 Molds for PDMS deposition into the lenses with various diameter ……....124
Figure 4.35 Experimental setup for the thermopile technique for harvesting energy ……. ……125
Figure 4.36 Seebeck effect.. ……..…126
Figure 4.37 Various geometric designs, single array, for testing the thermopile …….……128
Figure 4.38 Realized single elements using gold and nickel for thermopile testing ……..……..128
Figure 4.39 Experimental setup and measurement apparatus for Yagi-uda design ……..…...129
Figure 4.40 Output from Yagi-uda antenna from a uniform heating source…….. ……..…...129
Figure 4.41 Signal generator and testing of quasi Yagi-uda thermopile optical antenna …....…...130
Figure 4.42 Measurements of excitation from 532 nm laser……..……..…...131
Figure 4.43 Measurements of excitation from 650 nm laser……. ……..…...132
Figure 4.44 Measurements of excitation from 940 nm laser……. ……..…...133

Figure 4.45 Realized structures for 1550 nm laser excitation……..134
Figure 4.46 Measurement of excitating the three designs with 1550 nm laser….. ……..…...135

# List of Tables

Table 1.1 Efficiency of PV technology over the years [8].....2
Table 1.2 Comparison between two technologies [11].....5
Table 2.1 Output voltage obtained via 2-element array from a cell phone [31].....25
Table 2.2 Measured results for various input power levels [32].....26
Table 2.3. Comparison among state-of-the-art presented in the literature review section.....27
Table 2.4 Optimized hexaband antenna parameters (MM).....29
Table 2.5 Frequency bands supported by hexaband antenna.....33
Table 2.6 Input impedance of voltage doubler at various frequencies.....36
Table 2.7 LC values for matching network at various frequencies.....42
Table 2.8 Power received on the hexaband antenna with various input power levels pin.....46
Table 2.9 Output voltage produced at various frequencies as per input power levels.....47
Table 3.1 Coefficients of the Drude model for gold (Au) and silver (Ag) [24].....60
Table 3.2 Different material response as per characterization of reflect array [40].....64
Table 3.3 Optimized parameters of the proposed ETDRN.....73
Table 4.1 Comparison among state-of-the-art in thermal and semiconductor optical detectors....98
Table 4.2 n k values for noble metals and si substrate [3-4]..... 101
Table 4.3 Optical and Electrical parameters of Photodiode FD100L [27]... ..... 107

# Abstract

Recent years have witnessed an increased interest by the scientific community to acquire green and clean renewable sources of energy compared to traditional fossil fuels. Solar radiation is one particular abundant source of renewable energy that has been widely applied in vehicles, machines, and buildings, among others. There are generally two different ways in which solar energy is used – heat and electricity. The main motivation of this thesis work is to utilize that abundant source of energy in producing a small fraction of output DC voltage and current. Since the solar spectrum lies in the nano scale wavelengths or terahertz band, optical antennas as a novel nano fabrication technology will be used to capture and harvest the solar energy. Optical antennas have properties similar to their microwave counterparts, but the advantage they have is in terms of unprecedented means to tailor electromagnetic fields in all its aspects and applications. Therefore, with the aforementioned details, the main idea of this thesis is to capture the solar infrared radiation and utilize it for producing output DC voltage. The first part of this thesis is dedicated to understanding the working of radio frequency (RF) energy harvesting and presenting a rectenna design. The second part deals with the introduction and simulation of optical antennas based of dielectric resonators (DR) as they offer fewer losses at the THz band. Two different DR designs are proposed working at the center frequency of 193.5 THz (1550 nm wavelength). The third part discusses the main contribution to this work in terms of design, simulation and fabrication of a high gain and wideband Yagi-uda optical antenna. E-beam lithography technique is used to realize the proposed structure. Apart for the single element Yagi-uda design, various array configurations have been simulated with realization of a 100 x 100 elements array fabricated on a silicon substrate. To produce a certain amount of output voltage, two techniques were deployed in testing the realized Yagi-uda optical antenna array. The first technique involved integration of the Yagi-uda array with a commercial fermionic diode that produced output voltage of 0.15 V via excitation from a visible light and 0.52 V with direct excitation from a 1550 nm laser. The second technique is based on thermal dissipation among dissimilar metals producing an output voltage. Four different wavelength (532 nm, 650 nm, 940 nm and 1550 nm) lasers excited three realized nantenna designs. Among these designs, the maximum output voltage of 0.82 V was produced by the Yagi-uda array when excited via 1550 nm laser.

# Résumé

Au cours des dernières années, la communauté scientifique s'est intéressée de plus en plus à l'acquisition de sources d'énergie renouvelables vertes et propres par rapport aux combustibles fossiles traditionnels. Le rayonnement solaire est une source particulièrement abondante d'énergie renouvelable qui a été largement utilisée dans les véhicules, les machines et les bâtiments, entre autres. Il y a généralement deux manières différentes d'utiliser l'énergie solaire: la chaleur et l'électricité. La principale motivation de ce travail de thèse est d'utiliser cette abondante source d'énergie pour produire une petite fraction de la tension et du courant continu de sortie. Puisque le spectre solaire se situe dans les longueurs d'onde à l'échelle nanométrique ou dans la bande térahertz, les antennes optiques seront utilisées comme une nouvelle technologie de nanotechnologie pour capter et récolter l'énergie solaire. Les antennes optiques ont des propriétés similaires à celles de leurs homologues micro-ondes, mais leur avantage réside dans des moyens sans précédent pour adapter les champs électromagnétiques dans tous leurs aspects et applications. Par conséquent, avec les détails mentionnés ci-dessus, l'idée principale de cette thèse est de capturer le rayonnement infrarouge solaire et l'utiliser pour produire une tension continue de sortie. La première partie de cette thèse est consacrée à la compréhension du fonctionnement de la collecte d'énergie par radiofréquence (RF) et à la présentation d'un concept de rectenna. La deuxième partie traite de l'introduction et de la simulation d'antennes optiques à base de résonateurs diélectriques (DR) car elles offrent moins de pertes à la bande THz. Deux conceptions de DR différentes sont proposées fonctionnant à la fréquence centrale de 193,5 THz (longueur d'onde 1550 nm). La troisième partie traite de la contribution principale à ce travail en termes de conception, simulation et fabrication d'une antenne optique Yagi-uda à haut gain et large bande. La technique de lithographie par faisceau d'électrons est utilisée pour réaliser la structure proposée. En dehors de la conception de l'élément unique Yagi-uda, diverses configurations de réseau ont été simulées avec la réalisation d'un réseau d'éléments 100 x 100 fabriqué sur un substrat de silicium. Pour produire une certaine quantité de tension de sortie, deux techniques ont été utilisées pour tester le réseau d'antennes optiques Yagi-uda. La première technique impliquait l'intégration du réseau Yagi-uda avec une diode fermionique du commerce qui produisait une tension de sortie de 0,15 V par excitation à partir d'une lumière visible et de 0,52 V par excitation directe à partir d'un laser à 1550 nm. La deuxième technique est basée sur la dissipation thermique entre des métaux dissemblables produisant une tension de sortie. Quatre lasers à longueurs d'onde différents (532 nm, 650 nm, 940 nm et 1550 nm) ont excité trois conceptions de nantenna réalisées. Parmi ces conceptions, la tension de sortie maximale de 0,82 V a été produite par le réseau Yagi-uda lorsqu'il est excité via un laser de 1550 nm.